Computing the energetic component of the charge-transfer symmetry factor

Christof Drechsel-Grau
Wolfson College

This dissertation is submitted for the degree of Doctor of Philosophy

Preface

Je pense, donc je suis.

René Descartes (1596-1650) in *Discours de la méthode* (1637)

My interest in reaction dynamics was initiated by Professor Hynes's lecture on *reactivity* at Ecole normale supérieure in 2004. My subsequent studies and research projects were in the general area of theoretical physical chemistry and chemical dynamics. The present work focuses on electron-transfer dynamics and the activation parameters involved, as motivated in chapter 1. Therefore, chapter 2 describes theories of classical reaction rate constants and their relation to dynamically relevant activation parameters. The methods used to compute the activation parameters are outlined in chapter 3. Because I first encountered extensive computer simulations during this project, I also include the basics of the classical molecular simulation techniques, molecular dynamics and Monte Carlo methods, in this chapter. The model systems and the simulation details are briefly described in chapter 4, whereas I present the results for the activation parameters in chapter 5 and conclusions in chapter 6. I attempted to make this work as self-contained as possible so that relevant background material is given in the appendices. However, some depth and several topics had to be left out due to limitations in space and time.

I feel that this work would not be complete without a statement about my relation to it. Without doubt, I have learned a bit about general physical chemistry and about rate constant descriptions and activation parameters in particular. I have also learned something about the technical aspects involved, and it has been a pleasure to think about the specific problems encountered. This work has also been a constant source of self-doubt. However,

it has thereby provided an excellent opportunity for personal development, and I regard it as an important step in my life-long learning process. During this process I have benefitted from interactions with many people, whose input I would like to acknowledge next.

Acknowledgements

I would like to thank Michiel Sprik for his advice, guidance and helpful as well as clarifying discussions. Financial support from the EuroSim program in the framework of an Early Stage Research Training of the Marie Curie actions is gratefully acknowledged. I also wish to thank the administrative staff and the computer officers in the Department of Chemistry for their assistance. Warm thanks go to Wolfson college and my tutors, Lesley MacVinish and Sally Church, for providing support throughout my PhD.

Nick MacLaran is thanked for providing a reliable pseudo-random number generator. I am particular thankful to Peter Bolhuis, David Chandler and Christoph Dellago for insightful discussions on the transition path sampling method. Christoph Dellago and Phillip Geissler are also thanked for providing an initial version of the transition path sampling code. I would like to express my gratitude to Regla Ayala, Ruth Lynden-Bell, Marialore Sulpizi, Christopher Adriaanse, Robert Best, Jochen Blumberger, Alexander Büll, Dwaipayan Chakrabarti, Szilard Fejer and Harald Oberhofer for helpful and stimulating discussions. Also, I am very grateful to Anne Dhulesia, Carme Gabernet-Castello, Zsuzsanna Jenei, Christian Füllgrabe, Simon Lacoste-Julien and Nicolas Uhlich for their time, help and support as friends.

It is my greatest pleasure to thank my parents, Martine and Edgar Drechsel-Grau, my sister, Astrid Drechsel-Grau, and my fiancée, Julia Tränka, for their patience, encouragement and continuous support, without which this work could not have been accomplished. I dedicate this work to them.

Declaration

This dissertation is the result of my own work and includes nothing which is the outcome of work done in collaboration except where specifically indicated in the text. The research described was carried out between October 2006 and August 2010 in the Theoretical Sector of the Department of Chemistry at the University of Cambridge under the supervision of Professor Michiel Sprik. The contents are my original work except where indicated directly or by reference. This dissertation has not been submitted in whole or in part for any other degree or diploma at this or any other university, and it does not exceed 60,000 words in length.

Christof Drechsel-Grau
August 2010

Computing the energetic component of the charge-transfer symmetry factor

Christof Drechsel-Grau

Summary

The oxidation half-reaction of the aqueous ferrous ion serves as a model to investigate electron-transfer dynamics. The present classical model consists of two empirical valence bond states and a control parameter that effectively determines the reaction free energy. The model mimics an outer-sphere electron-transfer reaction that obeys Marcus theory to a good approximation. This theory uses the energy difference between the two empirical valence bond states as the reaction coordinate and quantitatively predicts the location of the transition state and activation parameters. The knowledge of the reaction coordinate is exploited in two ways: to compute activation parameters from umbrella integration (UI) and Marcus theory (MT) based simulations assuming linear response and to test the accuracy of transition path sampling (TPS) for the calculation of activation energies. Activation energies from transition path sampling ($10.2\,\mathrm{kJ\,mol^{-1}}$) agree within statistical uncertainty with reference calculations (UI: $15.2\,\mathrm{kJ\,mol^{-1}}$; MT: $15.7\,\mathrm{kJ\,mol^{-1}}$) and are lower than activation free energies (UI: $25.8\,\mathrm{kJ\,mol^{-1}}$; MT: $31.8\,\mathrm{kJ\,mol^{-1}}$), indicating substantial activation entropies. The variation of the activation free energy with the reaction free energy defines the charge-transfer symmetry factor (UI: 0.47; MT: 0.49). The latter is larger than its energetic (TPS: 0.39; UI: 0.23; MT: 0.38) and entropic (UI: 0.25; MT: 0.13) components, given by the variation of the activation energy and entropy with the reaction free energy. The charge-transfer symmetry factor also describes the location of the transition state, which is verified by a committor analysis, thereby supporting the validity of Marcus theory.

Contents

List of Figures

List of Tables

List of Symbols

$\nabla_{\boldsymbol{\xi}}\mathcal{A}$	Gradient of the dynamical variable $\mathcal{A}$ with respect to the set of canonical variables $\boldsymbol{\xi}$
$\dot{\mathcal{A}}$	Total time derivative of $\mathcal{A}$
$\frac{d\mathcal{A}}{dt}$	Total time derivative of $\mathcal{A}$
$\frac{\partial\mathcal{A}}{\partial t}$	Partial time derivative of $\mathcal{A}$
$\langle\mathcal{A}\rangle$	Equilibrium average, expected value or population mean of $\mathcal{A}$
$\langle\mathcal{A}\rangle_{ne}$	Non-equilibrium average of $\mathcal{A}$
$\{u,y\}_{\boldsymbol{\xi}}$	Poisson bracket of the variables u and y with respect to the set of canonical variables $\boldsymbol{\xi}$
$\imath$	Imaginary unit $\sqrt{-1}$
α	A parameter
β	$(k_B\,T)^{-1}$
β_{ct}	Charge-transfer symmetry factor
$\beta_{ct,S}$	Entropic component of the charge-transfer symmetry factor
$\beta_{ct,U}$	Energetic component of the charge-transfer symmetry factor
$\delta(y)$	Dirac δ-distribution of a variable y
ϵ_0	Vacuum permittivity $8.854187817\times10^{-12}\,\mathrm{A\,s\,V^{-1}\,m^{-1}}$ (after [1])
ϵ_r	Relative permittivity of a medium
$\epsilon_{LJ,jk}$	Energy parameter of the Lennard-Jones pair potential characterizing the interaction between species j and k
ε	Nosé-Hoover heat bath variable
ϕ	Time evolution operator
$\phi_{\mathfrak{R}}$	Angle in spherical coordinates
φ	Dynamical forward transition probability

$\bar{\varphi}$	Dynamical backward transition probability
γ_j	Activity coefficient of species $j = R, P$
γ_{el}	Electronic coupling mixing the diabatic states
$\theta(y)$	Heaviside function of argument y
$\theta_{\mathfrak{R}}$	Angle in spherical coordinates
κ	Phase space compressibility
κ_b	Force constant of the harmonic restraining potential
κ_k^c	k^{th} cumulant of a probability distribution
κ_{tr}	Transmission coefficient
κ_r	Transmission coefficient of reactive trajectories
λ	Reorganization free energy
λ_L	Lagrange multiplier
μ	Effective energy of the virtual electron shifting the diabatic states with respect to each other
μ_0	Shifting energy value for which the effective reaction free energy $\Delta\mu$ vanishes
$\Delta\mu$	Effective reaction free energy $\Delta\mu = \mu - \mu_0$
$\mu_k^{(r)}$	k^{th} raw moment of a probability distribution
$\mu_k^{(c)}$	k^{th} central moment of a probability distribution
ν	Frequency
π	3.14159265358... (after [2])
χ	Response function
$\hat{\rho}$	Density operator
ρ	Equilibrium phase space density
$\rho(x)$	Restricted equilibrium phase space density
ρ_c	Charge density
ρ_n	Number density
ρ_b	Generalized phase space density
σ	Standard deviation
σ_c	Holonomic constraint
$\sigma_{LJ,jk}$	Length parameter of the Lennard-Jones pair potential characterizing the interaction between species j and k
τ_{mol}	Molecular relaxation time

τ_{rxn}	Reaction time
$\tau_{LJ,Ar}$	Timescale associated with the Lennard-Jones interaction potential of the argon model
τ_{NH}	Nosé-Hoover thermostat relaxation time
$\boldsymbol{\upsilon}$	Set of canonical phase space variables υ_j
ω	Probability density of a continuous random variable
ω_b	Biasing weight
$\boldsymbol{\xi}$	Set of canonical phase space variables ξ_j
$\delta\boldsymbol{\xi}$	Infinitesimal phase space displacement
$d\boldsymbol{\xi}$	Differential phase space displacement
$\boldsymbol{\xi}(t)$	Phase space trajectory of length t
$\boldsymbol{\xi}_t$	Phase space point at time t
ψ	Distance-dependent part of the electrostatic potential
ζ	Coupling parameter
Δ	Difference operator
Φ	Functional
Γ	Γ-function
Θ	Path functional
Υ	Time integral of the phase space compressibility
Λ	Thermal wavelength
Π	Product symbol
Σ	Sum symbol
Ω_Y	Probability distribution function of a continuous random variable Y
$\Xi_{N\mathcal{V}E}$	Microcanonical partition function
Ξ	Generalized partition function
Ψ	Electrostatic potential
$\lvert\Psi_k\rangle$	Pure quantum state corresponding to the kth eigenvalue
$\lvert\Psi_1\rangle$	Electron-transfer adiabatic state
$\lvert\Psi_j\rangle$	Electron-transfer diabatic state with $j = R, P$
a_j	Activity of species $j = R, P$
(a)	Superscript for adiabatic
A	Electron acceptor species

A_r	Arrhenius pre-exponential factor
Ar	Argon
b	Subscript for backward
B	Radius
BR	Barrier region
c_j	Concentration of species $j = R, P$
c^0	Standard concentration
$c_{(j)}$	Coefficient of a diabatic state $j = R, P$ in an adiabatic state
$\mathcal{D}c_j$	Deviation from equilibrium concentration of species $j = R, P$
C	Correlation function
C_c	Conserved quantity
CP	Indicates crossing point
dy	Differential of y
d_{jk}	Constrained distance between particles j and k
(d)	Superscript for diabatic
D	Electron donor species
e	2.718281828459045235360287 . . . (after [2])
e_0	Elementary charge $1.60217646 \times 10^{-19}$ A s (after [1])
e^-	Electron
eq	Subscript for equilibrium
E	Total energy
ΔE	Diabatic energy gap
$\Delta E'(\boldsymbol{\xi})$	Diabatic energy gap as dynamical variable
ΔE_{max}	Diabatic gap value at the barrier top of the free energy profile
$\Delta E_{R,min}$	Boundary diabatic gap value of the reactant state
$\Delta E_{P,max}$	Boundary diabatic gap value of the product state
E_a	(Adiabatic) activation energy
$E_{a,ctr}$	Activation energy from transition path sampling and central finite difference scheme
$E_{a,fwd}$	Activation energy from transition path sampling and forward finite difference scheme
$E_{solvation}$	Born solvation (free) energy
$f(y)$	A function of a variable y; its value is denoted by f

f	Subscript for forward
F	Helmholtz free energy
$F_L(x)$	Landau free energy as a function of an order parameter x
ΔF	Free energy difference
$\Delta_r F$	Reaction free energy
$\Delta_r F_{SR}$	Reaction free energy according to Simpson's rule
$\Delta_r F_L$	Landau free energy of reaction
$\Delta F_L(x)$	Landau free energy difference at a given order parameter value x
$\Delta_\ddagger F$	Activation free energy (also denoted by $\Delta_\# F$ in graphs)
$\Delta_\ddagger F^{(a)}$	Adiabatic activation free energy
$\Delta_\ddagger F^{(d)}$	Diabatic activation free energy
Fe	Iron
$Fe^{2+}_{(aq)}$	Ferrous ion in aqueous solution
$Fe^{3+}_{(aq)}$	Ferric ion in aqueous solution
$g_r(r)$	Radial distribution function depending on the interparticle distance r
$\sqrt{g}$	Metric determinant factor
h	Planck's constant $6.6260688 \times 10^{-34}\,\mathrm{J\,s}$ (after [1])
H_{NH}	Energy conserved by the Nosé-Hoover thermostat
I	Identity matrix
j	Index
$\lvert j\rangle$	Member of a complete set of functions in Hilbert space
J	Antisymmetric matrix
k	Index
$\boldsymbol{k}$	Reciprocal space vector
k_B	Boltzmann's constant $1.380650 \times 10^{-23}\,\mathrm{J\,K^{-1}}$ (after [1])
k_+	Rate constant of the forward reaction
k_-	Rate constant of the backward reaction
$k_{+,\mathrm{TST}}$	Transition state theory (TST) expression for the forward rate constant
$k_{+,\mathrm{ET}}$	Rate constant of the forward electron-transfer reaction
K	Kinetic energy

l	index
ln	Neperian logarithm
L	Box length
m	Index
m_j	Mass of species j
MD	Molecular dynamics
mol	6.0221420×10^{23} (after [1])
MT	Marcus theory
M	Sample mean
$\boldsymbol{n}$	Integer triple
n	Superscript for new
n	n-sphere related number
N	Number of particles
o	Superscript for old
O	Indicates order of
$\boldsymbol{p}$	Set of canonical momenta p_j
$\boldsymbol{p}_C$	Set of Cartesian momenta $p_{C,j}$
$\boldsymbol{p}_C^{'}$	Cartesian momentum variable in the centre-of-mass frame
$p_{C,j}^{(m)}$	Scaled mass-weighted Cartesian momentum
p_ε	Nosé-Hoover heat bath variable "conjugate" to ε
P	Indicates product state
$\boldsymbol{q}$	Set of canonical coordinates q_j
$\boldsymbol{q}_{a,j}$	Auxiliary velocity of particle j in the RATTLE algorithm
Q	Canonical partition function
$Q(x)$	Restricted canonical partition function
r	Distance between two points or interaction sites
$\boldsymbol{r}$	Set of distances $r_{jk} = \lvert\boldsymbol{r}_{C,j} - \boldsymbol{r}_{C,k}\rvert$
r_w	Width of double-well potential
r_{12}	Distance between particles 1 and 2 of the argon model
r_x	Configuration with order parameter value x
$\boldsymbol{r}_C$	Set of Cartesian coordinates $r_{C,j}$ or particle positions $\boldsymbol{r}_{C,j}$
$\boldsymbol{r}_C^{'}$	Cartesian coordinate in the centre-of-mass frame
R	Indicates reactant state

s	Subscript for shooting slice
$\boldsymbol{s}$	Instantaneous approximation to the distance between particles j and k in the RATTLE algorithm
s^2	Sample variance
S	Entropy
$\Delta_{\ddagger} S$	Activation entropy
$\Delta_{\ddagger} S^{(a)}$	Adiabatic activation entropy
$\Delta_{\ddagger} S^{(d)}$	Diabatic activation entropy
ΔS_{λ}	Reorganization entropy
t	Time; also trajectory length
δt	Time step
Δt	Time interval
Δt_s	Shifting length in a shifting move
t_{ft}	Length of fleeting trajectories
t_{tr}	Transition time
t_0	Reference time
t'	Another time variable
T	Thermodynamic or absolute temperature
TPS	Transition path sampling
TS	Indicates transition state
u	A variable
U	Internal energy
$\Delta_{\ddagger} U$	Internal energy of activation
$\Delta_{\ddagger} U^{(a)}$	Adiabatic internal energy of activation
$\Delta_{\ddagger} U^{(d)}$	Diabatic internal energy of activation
UI	Umbrella integration
v	Rate of chemical reaction
V	Potential energy
$V^{(a)}$	Adiabatic potential energy
$V^{(d)}$	Diabatic potential energy
V_{ES}	Electrostatic or Coulomb potential
V_{LJ}	Lennard-Jones potential
V_b	Biasing potential

V_{dw}	Double-well potential
V_h	Potential energy barrier height of the double-well potential for the argon model
V_{WCA}	Weeks-Chandler-Andersen potential
w	Probability distribution of a discrete random variable
w_{eq}	Equilibrium probability distribution of a discrete random variable
w_t	Transition probability
w_a	Acceptance probability
w_g	Generation probability
$w_a^{'}$	Acceptance probability of a lower-level Monte Carlo move
w_{shoot}	Shooting probability
w_P	Committor
w_{RP}	Path probability
W_Y	Probability distribution function of a discrete random variable Y
x	An order parameter
$x^{'}(\boldsymbol{\xi})$	Order parameter as dynamical variable
y	A variable
Y	A random variable
z	Charge
Z	Partition function characterizing a path ensemble
$\mathcal{A}$	A dynamical variable or observable
$\mathcal{A}_{obs}$	Observable mean $\langle\mathcal{A}\rangle$ of a dynamical variable $\mathcal{A}$
$\mathcal{A}_j$	j^{th} value of the dynamical variable $\mathcal{A}$
$\mathcal{B}$	Another dynamical variable
$\mathcal{C}_j$	A set of constants or coefficients
$\boldsymbol{\mathcal{C}_{\mathcal{P}}}$	A vector of constant total linear momenum components
$\mathcal{D}\mathcal{A}$	Deviation from equilibrium average
$\mathcal{D}_p\langle\mathcal{A}\rangle$	Difference between the averages of perturbed and unperturbed Hamiltonians
$\mathcal{D}_{ne}\mathcal{A}$	Deviation from non-equilibrium average
$\mathcal{D}_{ne}\langle\mathcal{A}\rangle$	Difference between non-equilibrium and equilibrium averages

$\mathcal{F}$	A field acting as a perturbation
$\boldsymbol{\mathcal{F}}_j$	Force on particle j
$\boldsymbol{\mathcal{G}}_j$	Constraint force on particle j
$\mathcal{H}$	Hamiltonian
$\mathcal{H}_p$	Perturbed Hamiltonian
$\boldsymbol{\mathcal{J}}$	Jacobian matrix of a transformation ($\boldsymbol{\upsilon} \rightarrow \boldsymbol{\xi}$) with elements $\mathcal{J}_{jk} = \frac{\partial \xi_j}{\partial \upsilon_k}$
$\mathcal{J}(\boldsymbol{\xi}; \boldsymbol{\upsilon})$	Determinant of the Jacobian matrix $\boldsymbol{\mathcal{J}}$
$\lvert\mathcal{J}\rvert$	Absolute value of the determinant of the Jacobian matrix
$\widetilde{\boldsymbol{\mathcal{J}}}$	Transpose of the Jacobian matrix $\boldsymbol{\mathcal{J}}$
$\mathcal{K}$	Equilibrium constant
$\mathcal{L}$	Classical Liouville operator
$\mathcal{L}_u$	Lagrangian of the unconstrained system
$\mathcal{L}_c$	Lagrangian of the constrained system
$\mathcal{M}$	Total mass
$\mathcal{N}$	Index of the last time slice of a reactive trajectory; $\mathcal{N}+1$ denotes the trajectory's number of time slices
$\mathcal{N}_{bin}$	Number of bins for umbrella integration analysis
$\mathcal{N}_c$	Number of constraints
$\mathcal{N}_d$	Number of data points
$\mathcal{N}_f$	Number of (physical) degrees of freedom
$\mathcal{N}_{ft}$	Number of fleeting trajectories
$\mathcal{N}_{Fe}$	Number of iron atoms
$\mathcal{N}_H$	Number of hydrogen atoms
$\mathcal{N}_w$	Number of windows
$\mathcal{N}_O$	Number of oxygen atoms
$\mathcal{N}_r$	Number of interaction sites in the $Fe^{2+}_{(aq)}/Fe^{3+}_{(aq)}$ model system
$\mathcal{N}_s$	Number of modified time slices in a shifting move
$\mathcal{N}_{st}$	Number of stages in a free energy difference calculation
$\mathcal{N}_t$	Number of time steps
$\mathcal{N}_W$	Number of water molecules
$\mathcal{N}_\rho$	Number of phase space points
$\boldsymbol{\mathcal{P}}$	Set of canonical momenta $\mathcal{P}_j$

$\boldsymbol{\mathcal{P}_C}$	Total linear momentum
$\mathcal{P}_C$	Linearly independent component of the total linear momentum
$\boldsymbol{\mathcal{Q}}$	Set of canonical coordinates $\mathcal{Q}_j$
$\boldsymbol{\mathcal{R}_C}$	Centre-of-mass position
$\mathcal{V}$	Volume
$\mathcal{W}_{NH}$	Nosé-Hoover thermostat parameter
$\mathcal{X}$	Mole fraction
$\mathbb{A}$	An event
$\mathbb{B}$	Another event
$\mathbb{E}$	Certain event
$\mathbb{I}$	An integral
$\mathbb{I}_{tot}$	Another integral
$\mathbb{J}$	Another integral
$\mathbb{K}$	Cumulant-generating function
$\mathbb{M}$	Moment-generating function
$\mathbb{R}$	Radius of a hypersphere
$\mathbb{S}_n$	Hypersurface area of an n-sphere
$\boldsymbol{\mathfrak{R}}$	Real space vector of length $\mathfrak{R} = \lvert\boldsymbol{\mathfrak{R}}\rvert$

Chapter 1

Introduction

Thermally activated processes are of great importance in nature and technology. Examples include the freezing of water [3, 4], the corrosion of iron [5, 6] as well as the proton- and electron-transfer processes in the respiratory chain [7, 8]. These and other thermally activated processes are characterized by rare transitions between reactants and products [9–13]. The reactive events occur infrequently because the stable states are separated by activation barriers large compared to typical thermal fluctuations. This difference in energy scales results in a separation of timescales [9, 12]. Many reactive transitions take place on molecular timescales, whereas the average time between transitions is typically orders of magnitude longer because the fluctuations providing the required activation have a low probability. This separation of timescales leads to the existence of rate constants, which are macroscopic observables [9]. However, a detailed understanding of activated processes also requires unraveling their microscopic dynamics [14].

Understanding the reaction dynamics of an activated process involves detailed knowledge about the system's structural and energetic time evolution [14, 15]. This microscopic information must be consistent with macroscopic kinetic observables such as rate constants and activation energies. If transition state theory is assumed to hold, the activation free energy and entropy can also be obtained from kinetic measurements [15], which primarily yield rate constants and activation energies [15, 16]. For a series of related

reactions evolving according to the same mechanism, even the relative location of the transition state with respect to the stable states can be inferred from the Leffler-Hammond postulate [17,18]. In addition, time-resolved spectroscopy provides increasingly detailed information about reaction dynamics [19]. Nonetheless, information about the reaction coordinate and the transition state is usually difficult to obtain [20–22].

The identification of transition states and reaction coordinates generally becomes more difficult with increasing complexity of the system [20, 21, 23]. For instance, chemical reactions of small molecules in the gas phase generally involve relatively few degrees of freedom. In that case, the transition state often corresponds to a saddle point of the potential energy surface, and the reaction coordinate may be inferred by inspection or from the minimum energy path [15, 24]. Also, the reaction is typically controlled by energetic factors. In contrast, chemical reactions in solution take place in high-dimensional spaces [21, 22, 25]. This complexity greatly decreases the reliability of physical intuition for the identification of transition states and reaction coordinates [21, 22]. Furthermore, the activation barrier is now generally a free energy barrier[1] because entropic effects are rarely negligible in solution [9,29]. Thus, even unraveling the energy-entropy partitioning of the activation barrier remains a challenge and might lead to a better understanding of the reaction dynamics.

To investigate such activation parameters in the condensed phase, I shall focus on homogeneous outer-sphere electron-transfer reactions in aqueous solution. This is done for two reasons. First, these chemical reactions, which do not involve the formation or rupture of bonds [30–32], are prototypical for the investigation of solvent effects on chemical reactivity [25]. A detailed understanding of outer-sphere electron-transfer reactions is also relevant for more complex redox processes because the latter still involve charged species,

[1]Kinetic measurements of simple and elementary reactions yield the rate constant from the time-dependence of the concentrations [15]. The activation energy is obtained from the temperature-dependence of the logarithm of the rate constant, namely from the slope of an Arrhenius plot [15,26]. The activation free energy is defined theoretically [12,27,28] and becomes accessible once we assume a specific value for the pre-exponential frequency of the transition state theory rate constant expression (2.18).

which are stabilized by a polar solvent [33,34]. Second, outer-sphere electron-transfer reactions are well described by Marcus theory [30, 32, 35–42], which provides a quantitative expression for the activation free energy. This activation free energy is routinely determined [34, 43–50], whereas the computation of activation energies and entropies [51, 52] from classical molecular simulation techniques still poses substantial challenges, which motivates the present investigation. Marcus theory also identifies the transition state and the reaction coordinate of outer-sphere electron-transfer reactions. I exploit this knowledge about the reaction coordinate to pursue the following complex double objective.

On the one hand, I address a set of physical questions. In particular, I try to better understand the activation process and the nature of the transition state of a suitably chosen model system by means of computer simulations. The above-mentioned knowledge of the reaction coordinate allows for a computation not only of the activation free energy [20, 53], but also of the activation energy and entropy [29, 54]. I thus ask what the latter quantities, which are obtained from the temperature-dependence of the activation free energy, contribute to the activation barrier. Similarly, I compute the charge-transfer symmetry factor, which is defined as the derivative of the activation free energy with respect to the reaction free energy [55–60]. This charge-transfer symmetry factor is a measure of the location of the transition state relative to the stable states according to the Leffler-Hammond postulate [17, 18]. In addition, I determine the activation entropy and energy variation with the reaction free energy, namely the entropic and energetic components of the charge-transfer symmetry factor [61–64], from umbrella integration [65, 66] and Marcus theory based simulations [47, 67, 68].[2]

On the other hand, methodological alternatives for the investigation of electron-transfer reactions are explored. The methods mentioned above rely on transition state theory [9, 11–13, 27, 69–72] and the knowledge of the

[2]Marcus theory based equilibrium simulations in the canonical ensemble are also known as free energy perturbation method. However, I shall use the former term throughout this document because it employs expressions that are only valid if the assumptions underlying Marcus theory hold. In contrast, free energy perturbation is a more generally applicable method.

reaction coordinate to compute static activation parameters. Here, a dynamic viewpoint is emphasized. In particular, I employ transition path sampling [21, 23, 73–75], which provides a more general route to the computation of activation energies and rate constants. This method, which is based on the statistical mechanics of trajectories, requires neither prior knowledge of the reaction coordinate nor biased dynamics to obtain dynamical information. In addition, Dellago and Bolhuis [76] derived an expression for the activation energy as the temperature derivative of the logarithm of the exact classical rate constant. However, this activation energy formula is expected to exhibit large statistical uncertainties for complex systems because it involves differences of averages of the Hamiltonian [76]. I therefore assess the accuracy of activation energies from transition path sampling using activation energies computed from umbrella integration and Marcus theory based simulations as a reference. The former reference method relies on the knowledge of the reaction coordinate, whereas the latter further assumes knowledge of the transition state and the validity of the linear response approximation, discussed below. After the validation of the transition path sampling method for the computation of activation energies, the physical and methodological aspects of this work are combined to study the nature of the transition state. Specifically, I investigate whether the static transition state of Marcus theory, namely the maximum of the free energy profile, corresponds to dynamical transition state configurations in the committor sense. The committor is the probability to reach the products before the reactants [21–23, 73, 77–83]. In particular, transition state configurations have equal probability of reaching the reactants and products next. Because the committor has emerged as the ideal reaction coordinate, a committor analysis provides an alternative means of assessing the reaction coordinate, the transition state and thus the validity of Marcus theory.

In the following, I briefly describe the main features of Marcus theory and the model system to make the above-mentioned objectives more explicit. Then, I motivate the choice for using transition path sampling as the rare event method. More detailed accounts of reaction rate theory, Marcus theory and the computational methods employed are given in the main part of this

document.

Marcus theory of electron transfer has been remarkably successful despite its simple and elegant formulation [30, 32, 35–42]. Originally formulated as a macroscopic dielectric continuum theory [35, 84], Marcus theory was subsequently based on a more general statistical-mechanical framework [30, 38]. Below, I shall first describe the physical ideas and then turn to the mathematical framework of Marcus theory.

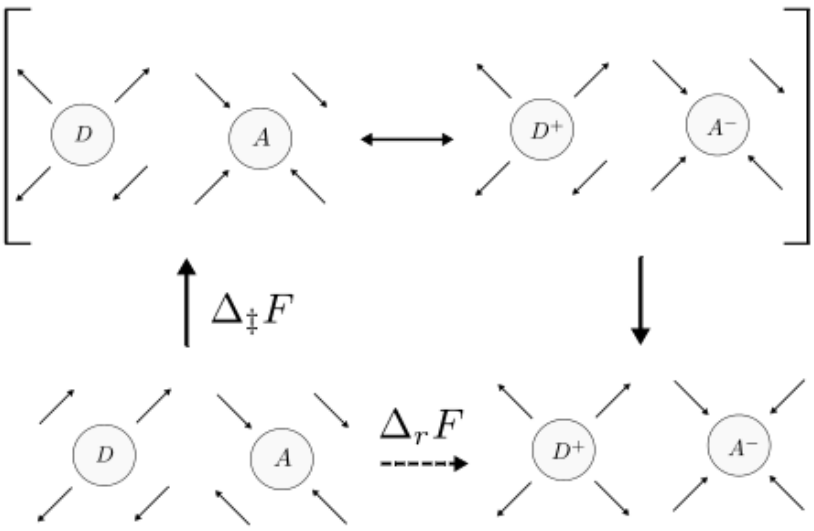

Figure 1.1: Schematic illustration of an outer-shere electron transfer from a donor D to an acceptor A. Due to the disparate timescales of electronic and nuclear motion the solvent has to rearrange prior to electron transfer, as indicated by the reaction process following the solid arrows. The square brackets contain the resonance between the degenerate solute charge distributions of the reactants and products at fixed nuclear configuration, which corresponds to the transition state. The direct transition from reactants to products (dashed arrow) is not allowed and only indicates the reaction free energy.

Marcus considered a thermally activated outer-sphere electron transfer between a donor (D) and an acceptor (A) species in a polar solvent:

$$D + A \rightarrow D^+ + A^-. \tag{1.1}$$

The reactants and products are characterized by the solvation of the fixed charge distributions of the solute [30, 35, 38, 85, 86]. Electronic states with a fixed charge distribution of the solute are one example of diabatic states, which are defined as electronic states that retain their physical character at all nuclear configurations [87]. In contrast, adiabatic states, which are the eigenstates of the electronic Hamiltonian [31, 33, 87], generally change their physical character as a function of nuclear geometry [31, 87]. For example, the dissociation of a NaI molecule involves the transition from a mainly ionic structure at short internuclear distances to a covalent structure at large internuclear distances [15, 87, 88]. The set of adiabatic eigenstates forms a unique basis in which the total wavefunction can be expanded. The coupling between electronic states then arises from the nuclear kinetic energy operator acting on the electronic states. In contrast, there is no unique diabatic basis [31, 87] because a basis in which the nuclear kinetic energy operator is diagonal cannot generally be found [87]. In a diabatic representation, the coupling or mixing between electronic states arises from off-diagonal potential energy terms [31]. Diabatic states in this document denote electronic states with a fixed charge distribution of the solute that is independent of the nuclear configuration. These diabatic states can be thought of as resonance forms of valence bond theory, in which electron pairs are localized either as a lone pair on one nuclear site or as a bonding electron pair between two nuclei [15, 31, 87, 89]. The ground-state electronic wavefunction is then obtained as a linear combination of the diabatic states or charge-localized resonance structures [33, 89, 90].

The diabatic and adiabatic states are obtained at a given nuclear configuration. If the electronic energies are computed for many geometries, diabatic and adiabatic potential energy surfaces are obtained from which the forces, needed for molecular dynamics simulations, can be derived [15].

Marcus described the electron transfer as a change of electronic state, that is, as a transition from the reactant diabatic state to the product diabatic state. As in optical spectroscopy, the Franck-Condon principle, which states that the electronic transition takes place in the presence of frozen nuclei because the electronic motion is usually faster than the nuclear one [15,

33], ensures that the radiationless electron transfer occurs at a fixed nuclear configuration. Because the electrons are assumed to be equilibrated to the nuclei, a fixed nuclear configuration entails a fixed total energy. Marcus thus realized that the electron transfer must occur at nuclear configurations with the same total energy of the diabatic reactant and product states to ensure sufficient electronic coupling between these states [30, 35, 38].

Outer-sphere electron-transfer reactions are characterized not only by an unaltered bonding pattern, but also by a first coordination shell that is relatively insensitive to a change in the solute's charge distribution [31]. Accordingly, changes in energy arise from changes in nuclear configurations of the solvent. Because electrons move faster than nuclei (within the Born-Oppenheimer and Franck-Condon approximations), electronic transitions require that the solvent rearranges first (see figure 1.1) and thereby provides the activation as follows [33,35,38]. Initially equilibrated to the reactants' charge distribution, the solvent fluctuates until it reaches a configuration for which the reactants and products are degenerate. This solvent configuration is in electrostatic equilibrium with the solute's charge distribution of neither the reactants nor the products. After the electron transfer the solvent relaxes to a configuration in equilibrium with the products' charge distribution [35,84]. Hence, outer-sphere electron transfer is driven by large thermal fluctuations of the solvent [33].

The mathematical formulation of the physical picture of Marcus theory drawn above is based on transition state theory. The reaction coordinate is the diabatic energy gap $\Delta E = \mathcal{H}_P - \mathcal{H}_R$, that is, the total energy difference between the product and reactant diabatic states [30, 38, 43]. The electron transfer occurs at the transition state, where the diabatic gap vanishes: $\Delta E = 0$. In addition, Marcus theory assumes that the solvent responds linearly to a (hypothetical) change in the solute's charge distribution [35,42]. As shown in section 2.2, the linear response property and the diabatic gap as reaction coordinate entail that the diabatic free energies, schematically shown in figure 1.2, are parabolas with equal curvatures [44,48,91–93]. With these ingredients, Marcus obtained the following elegant expressions for the

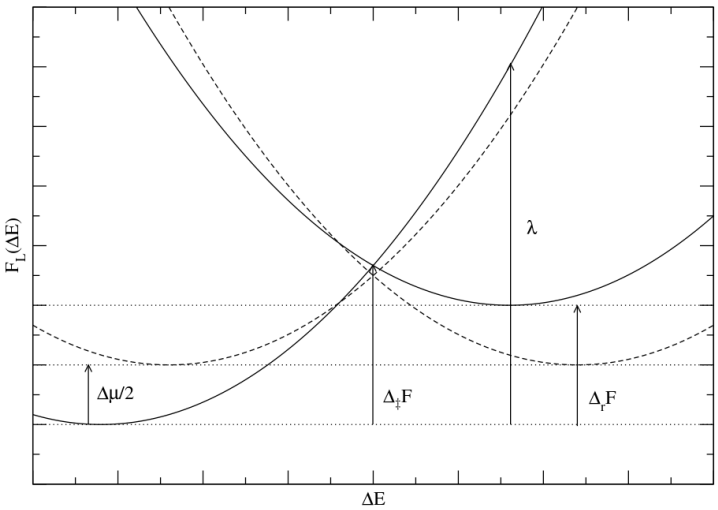

Figure 1.2: Schematic diabatic free energy profiles are displayed for vanishing (dashed lines) and positive (solid lines) reaction free energies $\Delta_r F$. The reorganization (λ) and activation ($\Delta_\ddagger F$) free energies are also shown for the asymmetric reaction. Furthermore, $\Delta\mu/2$ indicates the shift in the effective reaction free energy for the reactant state.

rate constant [38, 42, 94, 95],

$$k_{+,\mathrm{ET}} = \nu_R \, e^{-\beta \Delta_\ddagger F}, \tag{1.2}$$

and for the activation free energy[3] [25, 30, 42]:

$$\Delta_\ddagger F = \frac{(\lambda + \Delta_r F)^2}{4\,\lambda}. \tag{1.3}$$

Above, ν_R denotes a characteristic frequency in the reactant well [95], and $\beta^{-1} = k_B T$ is the product of the Boltzmann constant k_B and the absolute temperature T. The reaction free energy $\Delta_r F$ characterizes the thermody-

[3]In principle, the full activation free energy includes the work terms for bringing together the reactants and for separating the products. However, these terms are often of similar magnitude and cancel. In addition, the work terms are usually negligible compared to the activation barrier at the separation at which the reaction takes place [25, 55], and I shall use the simplified expression given in equation (1.3) throughout.

namics of the transformation, and the solvent effect is condensed into the single parameter λ [67], called reorganization free energy and shown in figure 1.2. The reorganization free energy is the reversible work to distort the solvent around the *fixed reactants' charge distribution* between two solvent configurations: one in equilibrium with the reactants' charge distribution and another that would be in equilibrium with the products' charge distribution [48, 96, 97]. Throughout this reversible work the system stays on the reactants' free energy surface. The required distortion around the reactants' charge distribution entails an intrinsic activation barrier of $\lambda/4$ even if the reaction free energy vanishes [55]. Like transition state theory, Marcus theory with its simple and elegant expressions has been remarkably robust and successful [34, 48].

An intriguing feature of Marcus theory is the quadratic dependence of the activation free energy on the free energy of reaction. This functional dependence leads to two kinetic regions: the normal region, in which the rate constant increases as the reaction free energy decreases ($-\Delta_r F < \lambda$), and the inverted region, in which the rate constant decreases as the reaction free energy becomes more negative ($-\Delta_r F > \lambda$). The maximum rate constant is obtained for barrierless reactions ($-\Delta_r F = \lambda$) [42, 48]. That the activation free energy depends quadratically on the reaction free energy also entails that the charge-transfer symmetry factor [59, 60],

$$\beta_{ct} = \frac{\partial \Delta_{\ddagger} F}{\partial \Delta_r F}, \tag{1.4}$$

depends on the reaction free energy in Marcus theory (MT) [30, 55, 56]:

$$\beta_{ct,MT} = \frac{1}{2} + \frac{\Delta_r F}{2\,\lambda}. \tag{1.5}$$

As a result, the location of the transition state, given by β_{ct}, is predicted to be in the middle of a symmetric barrier for $\Delta_r F = 0$ and $\beta_{ct,MT} = 1/2$ [56]. In contrast, the transition state becomes more reactant-like for negative reaction free energies and more product-like for positive $\Delta_r F$ in accordance with the Leffler-Hammond postulate [17, 18].

The Leffler-Hammond postulate states that two states involved in a reaction that are close in energy will exhibit similar structures [18]. In particular, the transition state of an elementary chemical reaction step can be considered intermediate between the reactants and the products. Moreover, it will be less product-like if it resembles the reactants more and less reactant-like if it is closer to the products [17].

Let us consider a series of electron-transfer reactions that follow the same mechanism. For instance, an electron donor might be oxidized by a series of electron acceptors. If we assume that the reaction free energy decreases along the series, the transition state will become more reactant-like because the activation free energy is expected to decrease according to the Leffler-Hammond postulate [17, 18]. However, if the overall change of the reaction free energy within the reaction series is small compared to the activation free energies, the transition state will be at a similar location relative to the reactants and products for all reactions within the series. Hence, the variation of the activation free energy with the reaction free energy can serve as a measure of how closely the transition state resembles the reactant state. In other words, the charge-transfer symmetry factor is an indicator of the location of the transition state relative to the reactants and products.

The same conclusion can be reached by a reasoning put forward by Hush [85, 86]. Hush considered an adiabatic electron transfer for which the solute charge distribution is always equilibrated to the solvent configuration [85, 86]. In his treatment, Hush introduced a parameter measuring the probability that the transferring electron resides on the acceptor [85, 86]. At the transition state, a fraction of the electron was assumed to have been transferred from the donor to the acceptor [85, 86]. The transition state value of Hush's parameter coincides with the charge-transfer symmetry factor of Marcus theory given by equation (1.5) [85, 86]. In other words, the charge distribution at the transition state influences the activation free energy. The latter will be lower if the charge distribution at the transition state resembles that of the reactants, whereas a higher activation free energy is obtained if the transition state charge distribution is closer to that of the products [86]. Marcus noted that the charge distribution of the so-

lute is not equilibrated to that of the solvent at all times for both adiabatc and non-adiabatic electron-transfer reactions [38]. Instead, the system will switch from the charge distribution of the reactants to that of the products at the transition state [35]. However, a picture involving an intermediate charge distribution between reactants and products can be formulated even from Marcus's point of view. In that case, an equivalent charge distribution can be introduced that corresponds to the one with which the instantaneous solvent configuration would be in equilibrium [38]. The equivalent transition state charge then also corresponds to the charge-transfer symmetry factor (1.5) [30]. We note that even in the (strong) adiabatic electron-transfer case considered by Hush, the change in the solute's charge distribution is largest at the transition state because the mixing between the charge-localized reactant and product state is at a maximum there due to the vanishing energy difference [85].

I can now enunciate the above-mentioned objectives more specifically. The validity of Marcus theory is tested in three ways. First, I compare the curvatures of the reactant and product free energy parabolas to test the linear response approximation, as has been done numerous times before [34, 43–48, 67, 91, 97–102] (see the review [32] for experimental investigations). Second, a committor analysis is used to test whether the diabatic energy gap is a suitable reaction coordinate. Third, I assess the quality of the Marcus theory prediction that the transition state corresponds to vanishing diabatic gap configurations by two means. On the one hand, the maximum of the free energy profile is compared to the free energy at $\Delta E = 0$. On the other hand, I compute the committor distribution of dynamically harvested configurations with gap values close to zero and test whether the mean is statistically close to 1/2. Anticipating the result that Marcus theory provides a robust description of the model system, I use the diabatic gap as the reaction coordinate to compute the activation free energy. The activation energy and entropy are obtained from the Gibbs-Helmholtz relation and the temperature derivative of the activation free energy [15]. The computation of the activation parameters is then repeated for a series of reaction free energies to obtain the charge-transfer symmetry factor as well as its energetic

and entropic components, defined below.

In the electrochemical literature, the variations of the activation energy and entropy with electrode potential have been termed the energetic and entropic components of the charge-transfer symmetry factor by some authors [58, 61–64]. By analogy, I shall call the dependence of the activation entropy and (internal) energy on the reaction free energy the entropic ($\beta_{ct,S}$) and energetic ($\beta_{ct,U}$) components of the charge-transfer symmetry factor:

$$T\beta_{ct,S} = -T\frac{\partial \Delta_{\ddagger} S}{\partial \Delta_r F}; \tag{1.6a}$$

$$\beta_{ct,U} = \frac{\partial \Delta_{\ddagger} U}{\partial \Delta_r F}. \tag{1.6b}$$

The above procedure is only partially analogous because the precise effects of electrode potential on reaction free energy and of temperature on electrode potential are difficult to quantify. Indeed, Gileadi has pointed out that the quantities $\beta_{ct,U}$ and $\beta_{ct,S}$ might depend on temperature [103, 104]. Below, I describe the model system employed and how the reaction free energy is controlled.

To investigate the nuclear dynamics and the activation parameters of outer-sphere electron-transfer reactions, I study the classical model oxidation half-reaction of the aqueous ferrous ion:

$$Fe^{2+}_{(aq)} \rightarrow Fe^{3+}_{(aq)} + e^{-}_{(\mu)}. \tag{1.7}$$

The ferrous (Fe^{2+}) and ferric (Fe^{3+}) ions are described by diabatic, charge-localized empirical valence bond states [105], which interact via a classical, non-polarizable force field characterized by Lennard-Jones and Coulomb potentials [106, 107]. A constant electronic coupling element mixes the diabatic states to yield an adiabatic potential energy surface, as in reference [108]. The electron is not treated explicitly. Rather, it acquires an effective energy μ, which is used as a control parameter to shift the potential and free energies of the diabatic states with respect to each other; this approach is similar to the virtual electrode treatment of Sprik and co-workers [67, 100]. As a

result, the control parameter μ provides a means of varying the reaction free energy $\Delta_r F$. The effective reaction free energy $\Delta\mu = \mu - \mu_0$ shown in figure 1.2 (between solid parabolas) is the μ value relative to the one (μ_0; $\Delta\mu = 0$ between dashed parabolas) for which the reaction free energy would vanish if Marcus theory applied *exactly*. The model consists of 64 simple point charge water molecules [109, 110], thus rendering the classical system moderately complex.

The study of a half-reaction instead of the full reaction is motivated by the following factors. First, the half-reaction allows for a smaller system size, thus reducing the computational cost of the investigation. Second, the study of a single ion avoids the additional complexity of the donor-acceptor distance, which influences the rate constant. Third, it is desirable to isolate a single redox pair and to study its properties, as can be done in electrochemical experiments [58]. Fourth, although the system size is decreased, the model remains relatively complex because half-reactions are typically asymmetric in the sense that even if the reaction free energy vanishes, the reaction entropy and internal energy are generally non-zero. Finally, the main feature of electron-transfer reactions, namely the activation due to the reorganization of the solvent, is included in the study of half-reactions.

Classical models have been used in numerous studies of electron-transfer reactions to determine reaction, activation and reorganization free energies or dynamical solvent effects, for example in references [34, 43, 44, 47–49, 51, 52, 97, 108, 111]. This approach is justified by two aspects. First, Marcus theory separates the electronic structure of the solute from the classical nuclear motion of the solvent [67]. It is thus assumed that the dynamics of the system can be accurately described by classical mechanics. Second, classical force fields are routinely used to study atomistic systems. This approach is possible if the connectivity of the constituents remains unaltered [112]. Because the present model only exhibits a change in the charge of the iron ion, the latter condition is fulfilled. In addition, if the water molecule is considered as an entity of its own, its mass and a study at room temperature guarantee that the first classical approximation above is reasonable [113].

The investigation of atomistic classical model systems can generally be

achieved by Monte Carlo or molecular dynamics simulations [106, 107]. I shall employ molecular dynamics simulations for the computation of static quantities such as activation and reaction free energies because I will need the system's time evolution to compute committor values and to generate reactive trajectories. Furthermore, I use umbrella integration [65, 66] to obtain the free energy profile because its analysis of the umbrella sampling data [114, 115] converges with the number of bins. This is in contrast to self-consistent histogram methods [116–118], as pointed out in references [65, 119]. Marcus theory based simulations can be considered as a special case of free energy perturbation [93, 120]. Alternatively, I shall regard the computation of the reaction free energy by unbiased molecular dynamics as thermodynamic integration [121] in the present work because this enables me to assess the accuracy of the linear response approximation in a straightforward way. To motivate the choice of the transition path sampling method, I shall briefly survey some rare events techniques below.

Over the last decades, a variety of computational tools has been devised to overcome the timescale problem [9, 10, 12], on the one hand, and to find answers to the reaction coordinate question, on the other hand [122, 123]. Because the literature is very extensive, I shall not attempt an exhaustive review. Instead, I focus on a selection of approaches proposed to tackle the problems of finding the reaction coordinate and of computing the rate constant in complex systems from the transition path ensemble, defined as a weighted set of reactive trajectories [21, 124].

The traditional approach to rate constant calculations follows the two-step procedure of the reactive flux formalism [9, 125–127]. This approach first identifies the free energy barrier along the known reaction coordinate, which gives the probability of being at the dividing surface compared to being in the reactant state. Then, dynamical trajectories are launched from the transition state to evaluate how long transitions between the stable states are [106] and how large the transmission coefficient is [23]. Alternative approaches are often based on an idea by Pratt [123] to use a Monte Carlo procedure for sampling trajectory space, where the endpoints of the trajectories constitute constraints. Examples include transition path sampling (TPS) [21, 23, 73–75]

and related approaches [22, 77, 128–133].

In particular, transition path sampling performs a biased random walk in trajectory space that does not alter the natural dynamics of the system's time evolution [21, 23]. Here, the rate constant is obtained from the time derivative of a time correlation function. In an attempt to improve the efficiency of rate constant calculations, the transition interface sampling method was developed [130], which uses a history-dependent definition of states in phase space and several interfaces or dividing surfaces in between the stable states. For diffusive dynamics, the loss of correlation along a given pathway was exploited in partial path transition interface sampling [131].

One challenging problem of transition path sampling techniques is collecting transition paths when the reactive events are long because the Lyapunov instability causes initially close trajectories to diverge [106, 134], which leads to low acceptance probabilities [21]. To overcome this problem, more efficient sampling was achieved by combining deterministic dynamics with an Andersen thermostat [129], on the one hand, and by precision shooting [132], on the other hand. The former method leads to increased efficiency because partial paths, propagated from a given time slice and combined with the remaining part of the trajectory, might yield a new reactive trajectory with the fraction of the cost of an entire pathway [129]. In the latter method, deterministic dynamics is preserved throughout by rescaling the divergence of a trial trajectory from a reference trajectory while the divergence is still in the linear regime. This procedure allows arbitrarily small momentum changes to be performed to increase the acceptance probability of long transition pathways [132].

Conventional transition path sampling schemes consider an activated process between two stable states. Recently, an extension to deal with multiple states including intermediate states was proposed [133]. There, the transitions between any two states were included in an extended path ensemble. For instance, trajectories that do not visit any other state before returning to the initial state are not taken into account; all other paths contribute to the extended path ensemble.

Hummer [22] and Best and Hummer [77] used transition path sampling

from any dividing surface with a given value of the order parameter to compute rate constants and to identify transition states. The transition state was defined as the collection of phase space points with the highest probability that trajectories containing these points connect the stable states.

The methods mentioned above require a stationary phase space density. For stochastic dynamics, non-equilibrium systems can be investigated by an extension of the transition path sampling method [128] or by forward flux sampling and related approaches [124,135,136]. The former changes the noise history of a randomly selected point along the path, whereas the latter grows transition paths from one interface to the next, thus generating the transition path ensemble and yielding the rate constant. The forward flux sampling technique also differs from transition path sampling based simulations in the sense that no initial reactive trajectory is required [124, 135, 136].

Although the computation of rate constants is more efficient if the order parameter chosen is close to a suitable reaction coordinate, the identification of the latter remains a major challenge in complex systems. A widely used approach is to generate the transition path ensemble and to analyse the reactive trajectories by means of a committor analysis. The committor, which is the probability of relaxing to the products prior to reaching the reactants, along the states of the reactive trajectories can indicate whether the order parameter characterizing the stable states is a suitable reaction coordinate [21, 23, 73]. A technique combining transition path sampling and likelihood maximization [137] was used in references [82, 83, 138] to extract the reaction coordinate from partial paths using aimless shooting. In this approach, the reaction coordinate is obtained as a linear combination of proposed order parameters. An alternative approach [78, 139] is to identify isocommittor surfaces, which contain configurations that have the same probability of reaching the product state before the reactant state [21–23, 79], as the ideal reaction coordinate directly by finding the minimum (free) energy path connecting reactants and products. Ma and Dinner [140] proposed to find the reaction coordinate automatically from a set of order parameters by means of a genetic neural network algorithm. Because the genetic neural network needs to be trained before it can be used [140], no fully automated

method to identify reaction coordinates seems to exist at present, and all approaches rely on partial physical insight.

In the present work, I employ transition path sampling to study rare events. This choice is motivated by the requirements of the system studied and by the objectives. As mentioned earlier, the computation of activation parameters and the identification of the reaction coordinate without prior knowledge of the latter are especially valuable for complex systems. An additional desirable feature of transition path sampling is the use of dynamically unbiased trajectories. This characteristic allows direct insight into the activation process and is not possible with biased or static free energy methods such as umbrella sampling or thermodynamic integration. Also, I investigate ultrafast electron-transfer dynamics so that deterministic dynamics are necessary. An important reason for choosing transition path sampling is the computation of the activation energy. Although transition interface sampling could also be used to evaluate the activation energy, reference data have been published in the case of transition path sampling [76], which was crucial during the development stage of the present work. Contrary to the problem of long transition pathways, the short reactive trajectories harvested here might suffer from too slow a divergence. Therefore, the temperature control for transition path sampling in the canonical ensemble reported in reference [141] was implemented to allow for large momentum changes with moderate variations of the kinetic energy. Hence, theoretical and practical considerations lead to the use of transition path sampling.

The remainder of this thesis is structured as follows. Chapter 2 outlines the theoretical frameworks of reaction rate theory, of Marcus theory and of the statistical mechanics of trajectories. Simulation techniques are described in chapter 3, whereas the characteristics of the model systems and the simulation details are presented in chapter 4. I present the outcomes of the simulations and their discussion in chapter 5. The main conclusions are summarized in chapter 6, whereas supporting material is presented in the appendices.

Chapter 2

Theory

The present chapter outlines the theoretical framework that underlies the dynamics and the energetics of electron-transfer reactions. Because electron-transfer reactions form an important class of chemical reactions, we briefly review the principles of chemical kinetics. Our presentation focuses on the central observable of chemical kinetics, namely the rate constant. Along the way, we describe thermodynamic properties, such as free energies of reaction and activation, that influence the rate constant of chemical reactions. The rate constant provides a link both to empirical quantities, such as the activation energy, and to theoretical formulations, such as transition state theory. This leads directly to our presentation of the classical theory of electron transfer by Marcus, which is based on transition state theory. On the other hand, the classical rate constant and the activation energy of electron-transfer reactions can be computed by transition path sampling. Hence, our description of the underlying statistical mechanics of trajectories provides a natural transition to chapter 3.

2.1 Classical reaction rate theory

2.1.1 Chemical kinetics

Chemical kinetics deals with the study of reaction rates, which determine the speed of a chemical transformation [15]. In principle, reaction rates depend

on the concentration of species, on temperature and on pressure. Here, we shall focus on condensed phase kinetics, for which the pressure dependence of the rate is negligible [142].

To measure the rate of a chemical reaction, we need an observable that changes in time [15]. However, all properties in thermodynamic equilibrium are time-independent except time-correlation functions [72]. Therefore, the system is perturbed from equilibrium, and we monitor its time-dependent relaxation from the non-equilibrium state back towards equilibrium [33]. In the realm of chemical kinetics, one example of a perturbation is to create non-equilibrium concentrations. The speed of the decay of the concentration deviations from equilibrium then yields the rate [9, 11, 143].

We now turn to the rate law. The rate law determines how the rate depends on the concentrations of each chemical species [15]. Two additional features reveal the importance of the rate law. First, any proposed mechanism for the reaction must be consistent with the rate law [15]. Second, the rate law enables us to determine the rate constant and thus the temperature dependence of the rate [15].

The rate constant is independent of the concentrations and carries the temperature dependence of the rate. Measuring the temperature dependence of the rate constant, we gain access to the activation energy [15]. For a given temperature and pressure the rate constant and the activation energy are intrinsic kinetic parameters of a chemical reaction. Hence, their determination provides quantitative insight into the dynamics of the process considered.

To make the treatment more quantitative, we consider the example of a reversible unimolecular reaction [72]:

$$R \underset{k_-}{\overset{k_+}{\rightleftharpoons}} P. \tag{2.1}$$

In reaction (2.1) above, reactants (R) transform into products (P) with rate constant k_+, and products convert to reactants with rate constant k_-. In equilibrium the concentrations of reactants ($\langle c \rangle_R$) and products ($\langle c \rangle_P$) remain unchanged, and the rate constants for the forward and backward reactions

are related by the equilibrium constant[4] [15, 72, 145, 146],

$$\mathcal{K} = \frac{k_+}{k_-} = \frac{\langle c \rangle_P}{\langle c \rangle_R}, \tag{2.2}$$

which determines the relative population of stable states. We proceed by introducing instantaneous time-dependent concentrations $c_j(t)$ of the states $j = R$ and $j = P$ [9, 72],

$$c_R(t) = \langle c \rangle_R + \mathcal{D}c_R(t); \tag{2.3}$$

$$c_P(t) = \langle c \rangle_P + \mathcal{D}c_P(t), \tag{2.4}$$

as the sum of equilibrium concentrations $\langle c \rangle_j$ and deviations $\mathcal{D}c_j(t) = c_j(t) - \langle c \rangle_j$ from them. Because the equilibrium concentrations are constant, the time dependence of the concentrations equals that of their deviations from equilibrium [9, 72, 145].

We are now in a position to define the rate of the unimolecular transformation given in equation (2.1). The rate v is determined by the speed with which product particles are formed at a given absolute temperature T [15, 146]:

$$v = \frac{d\mathcal{D}c_P(t)}{dt} = k_+\mathcal{D}c_R(t) - k_-\mathcal{D}c_P(t) \tag{2.5}$$

$$= -\left(k_+ + k_-\right)\mathcal{D}c_P(t). \tag{2.6}$$

The last equation follows if a closed system with constant particle number is considered. In that case, we have $\mathcal{D}c_R(t) + \mathcal{D}c_P(t) = 0$ [9, 72]. In addition, equation (2.5) is the rate law for reaction (2.1) because it relates the rate to

[4]The thermodynamic equilibrium constant $\mathcal{K}_{eq} = \frac{a_P}{a_R}$ at constant temperature and pressure involves the activities of reactants (a_R) and products (a_P) [15]. $\mathcal{K}_{eq}$ is related to the equilibrium constant obtained from the ratio of equilibrium populations (2.2) by $\mathcal{K}_{eq} = \mathcal{K}\,\frac{\gamma_P}{\gamma_R}$. The activity coefficient γ links the activity to the equilibrium concentration $\langle c \rangle$ via $a = \gamma\,\langle c \rangle / c^0$ [144], where c^0 denotes the standard concentration used to render the concentration dimensionless. Thus, activities can be regarded as effective mole fractions [15]. We shall consider sufficiently dilute solutions, for which activity coefficients approach unity and for which we may replace activities by (dimensionless) concentrations or mole fractions.

the concentration of each species.

Because the rate law given in equation (2.5) is linear in $\mathcal{D}c_P(t)$, it can be integrated to express the time-dependent deviation from equilibrium $\mathcal{D}c_P(t)$ as a function of its initial value $\mathcal{D}c_P(0)$ [9, 15, 72, 146]:

$$\mathcal{D}c_P(t) = \mathcal{D}c_P(0)\, e^{-\frac{t}{\tau_{rxn}}}. \tag{2.7}$$

Here, we have introduced the reaction time $\tau_{rxn} = (k_+ + k_-)^{-1}$ for future reference [9, 143]. We also note that the exponential decay of the non-equilibrium concentration holds for first-order kinetics discussed in the present document [15]. Until now, we have not given an explicit treatment of the rate constant. This is what we shall do next.

An empirical expression of the rate constant for many condensed phase reactions was first proposed by van't Hoff and Arrhenius at the end of the 19th century (according to reference [13]). It consists both of a temperature-independent frequency factor A_r (which measures the rate of collisions with suitable orientation) and of a temperature-dependent exponential term containing the activation energy E_a, which the system needs to acquire to overcome the barrier between reactant and product states [15]. The rate constant k_+ at absolute temperature T is then given by the *Arrhenius equation* [15, 146]:

$$k_+ = A_r\, e^{-\beta E_a}. \tag{2.8}$$

Above, $k_B T = \beta^{-1}$ denotes the product of the Boltzmann constant with temperature.

From an experimental point of view, the activation energy is obtained by measuring the rate constant at various temperatures [15, 26]. Then, a plot of the logarithm of the rate constant over inverse temperature yields the negative activation energy scaled by the inverse Boltzmann constant [15, 26]. Such a graph is called an Arrhenius plot [15]. Equivalently, the activation energy is defined by equation (2.9) [15, 146]:

$$E_a = -\frac{d\, ln\, k_+}{d\beta} = k_B T^2\, \frac{d\, ln\, k_+}{dT}. \tag{2.9}$$

In this section we have introduced the empirical expressions for the rate, the rate law, the rate constant and the activation energy. In the next sections we will relate these to microscopic theoretical concepts.

2.1.2 Classical reaction rate constant

The empirical form of the rate constant has been given in the previous section. In this section we introduce microscopic expressions for the rate constant. Our treatment will be classical. In particular, classical statistical mechanics and Hamiltonian dynamics are used throughout.

Restricting our attention to thermal chemical reactions in condensed phases, we first need to address the conditions under which a rate constant exists. According to Chandler [9], a rate constant only exists if a rate law can be written. For this to be possible the process under consideration must be activated [9]. In other words, the chemical transformation must be characterized by a separation of timescales to be described in more detail later. Chandler states in reference [9] that the derivation of a macroscopic rate law from microscopic principles seems impossible. We shall therefore assume that the rate law of equation (2.5) is accurate and that a rate constant exists. In that sense, the experimental information guides the theoretical approach [9].

Our starting point is the fluctuation-dissipation theorem discussed below (and in appendix E) [33, 72]. The fluctuation-dissipation theorem applies to many condensed phase processes and is particularly suited to describe relaxation phenomena as the one discussed in the previous section. We shall assume that it holds for chemical kinetics of the type considered here. It then provides a direct link between the macroscopic expressions of the previous section and the microscopic ones that we will present below [72].

The fluctuation-dissipation theorem states that the relaxation of a macroscopic non-equilibrium state towards equilibrium occurs on the same timescale as the decay of spontaneous equilibrium fluctuations [33,72,145,147]. In other words, for small deviations from equilibrium we cannot distinguish whether the initial state of the system has been arrived at by a spontaneous fluctuation or by a systematic perturbation [145].

One mathematical form of the fluctuation-dissipation theorem for the observable $\mathcal{A}$ is given by equation (2.10) [9, 33, 72]:

$$\frac{\langle \mathcal{D}_{ne}\mathcal{A}(t)\rangle_{ne}}{\langle \mathcal{D}_{ne}\mathcal{A}(0)\rangle_{ne}} = \frac{\langle \mathcal{D}\mathcal{A}(0)\mathcal{D}\mathcal{A}(t)\rangle}{\langle \mathcal{D}\mathcal{A}(0)\mathcal{D}\mathcal{A}(0)\rangle}. \tag{2.10}$$

Above, angular brackets denote population mean values of a given probability distribution, and the subscript ne indicates non-equilibrium averages.[5] Deviations from the mean values are written as $\mathcal{D}\mathcal{A}(t) = \mathcal{A}(t) - \langle \mathcal{A}\rangle$ in the case of equilibrium fluctuations and as $\mathcal{D}_{ne}\mathcal{A}(t) = \mathcal{A}(t) - \langle \mathcal{A}\rangle_{ne}$ in the non-equilibrium case. The theoretical foundation of the fluctuation-dissipation theorem is linear response theory, a brief account of which is given in appendix E.

To proceed, two questions have to be dealt with. First, we identify the observable that enters equation (2.10) for the fluctuation-dissipation theorem [72]. Second, we discuss the timescales involved and the times for which the fluctuation-dissipation theorem holds [72]. Because our aim is to arrive at an expression for the rate constant that describes the intrinsic rate of transformation, the relevant observables are the concentrations of the species involved in reaction (2.1). For ensembles with constant volume $\mathcal{V}$ and particle number N concentrations can be replaced by the corresponding particle numbers $N_j = c_j\,\mathcal{V}$ or mole fractions $\mathcal{X}_j = \frac{N_j}{N} = \langle \theta_j\rangle$. Here, $N = \sum_j N_j$ is the total number of particles in the system, and $j = R, P$ indicates the chemical species. The characteristic function θ is defined by relation (2.12). Combining equations (2.7) and (2.10), we arrive at equation (2.11) [72]:

$$\frac{\langle \mathcal{D}_{ne}N_P(t)\rangle_{ne}}{\langle \mathcal{D}_{ne}N_P(0)\rangle_{ne}} = \frac{\langle \mathcal{D}N_P(0)\mathcal{D}N_P(t)\rangle}{\langle \mathcal{D}N_P(0)\mathcal{D}N_P(0)\rangle} = e^{-\frac{t}{\tau_{rxn}}}. \tag{2.11}$$

As mentioned previously, we see that the fluctuation-dissipation theorem

[5] Contrary to stationary equilibrium averages, non-equilibrium averages are not unique [72, 148] because they depend on the specific way they are prepared. The distribution of initial conditions of a non-equilibrium state can be thought of as corresponding to that obtained from a specific application of an external force that is absent in equilibrium. This external force will cause a non-equilibrium average value of an observable macroscopically characterizing the non-equilibrium state. The resulting non-equilibrium average is generally time-dependent [33, 72].

provides a connection between the macroscopic rate law and a microscopic time-correlation function in the canonical ensemble.

To aid the subsequent derivation, we rewrite equation (2.11) in terms of characteristic functions. The characteristic function for the product state is defined as [2, 149]

$$\theta_P(x) = \begin{cases} 1 & \text{for } x \geq 0; \\ 0 & \text{for } x < 0. \end{cases} \tag{2.12}$$

Here, x is a scalar order parameter that separates the phase space unambiguously into reactant ($x < 0$) and product ($x \geq 0$) regions [72]. In principle, the order parameter $x = x(\boldsymbol{\xi})$, which may not be easily identified, is a function of all phase space variables [22, 81, 150]:

$$\boldsymbol{\xi} = \{q_1, q_2, \ldots, q_{3N}, p_1, p_2, \ldots, p_{3N}\}. \tag{2.13}$$

Here, the q_j and p_j denote canonically conjugate coordinates and momenta, and N is the number of particles in the system. With the above definition, the characteristic function of the reactant state is $\theta_R(x) = 1 - \theta_P(x)$, and the canonical ensemble average of the characteristic function of any stable state corresponds to the equilibrium mole fraction of that state [9]. We also have $\langle \theta^2 \rangle = \langle \theta \rangle$. This property is used to express equation (2.11) as[6]

$$\begin{aligned} e^{-\frac{t}{\tau_{rxn}}} &= \frac{\langle \mathcal{D}\theta_P(x_0)\mathcal{D}\theta_P(x_t)\rangle}{\langle \mathcal{D}\theta_P(x_0)\mathcal{D}\theta_P(x_0)\rangle} \\ &= \frac{\langle \theta_P(x_0)\theta_P(x_t)\rangle - \langle \theta_P\rangle^2}{\langle \theta_P^2\rangle - \langle \theta_P\rangle^2} \\ &= 1 - \frac{\langle \theta_R(x_0)\theta_P(x_t)\rangle}{\langle \theta_R\rangle\langle \theta_P\rangle}. \end{aligned} \tag{2.15}$$

[6]Throughout this document the equilibrium ensemble average of an observable $\mathcal{A}$ in the framework of classical statistical mechanics (outlined in appendix D) is written as

$$\langle \mathcal{A} \rangle = \int \mathcal{A}(\boldsymbol{\xi})\, \rho(\boldsymbol{\xi})\, d\boldsymbol{\xi}. \tag{2.14}$$

Here, $\rho(\boldsymbol{\xi})$ is the equilibrium phase space density, and the notation $d\boldsymbol{\xi} = \prod_{j=1}^{6\,N} d\xi_j$ indicates integration over the entire set of canonical phase space variables.

Above, the order parameter value at time t is denoted by x_t. Expanding the exponential to first order in t, taking time derivatives and using $\tau_{rxn}^{-1} = k_+ + k_- = k_+ \left(1 + \frac{\langle\theta_R\rangle}{\langle\theta_P\rangle}\right)$ yields an expression for the rate constant of the forward reaction [9, 12, 70, 72]:

$$k_+(t) = \frac{\left\langle \theta_R(x_0)\dot{\theta}_P(x_t)\right\rangle}{\langle\theta_R\rangle}. \tag{2.16}$$

According to Miller [70], the classical rate constant defined above is the equilibrium reactive flux out of the reactant well through the dividing surface (separating reactants and products) into the product well. To see this, we rearrange equation (2.16) as follows. First, the time derivative can be transferred to the first factor in the average using properties of equilibrium time-correlation functions (see appendix F) [33, 72]. Second, noting that the derivative of the characteristic function is the δ-distribution, we obtain [9, 11, 12, 70]

$$\begin{aligned} k_+(t) &= -\frac{\langle\dot{\theta}_R(x_0)\theta_P(x_t)\rangle}{\langle\theta_R\rangle} \\ &= \frac{\langle\delta(x_0)\dot{x}_0\theta_P(x_t)\rangle}{\langle\theta_R\rangle}. \end{aligned} \tag{2.17}$$

The interpretation of equation (2.17) is as follows. The δ-distribution locates the system at the dividing surface at time $t = 0$, and the initial "velocity" $\dot{x}_0$ correspond to the equilibrium distribution in the reactant state because of the denominator. Then, the characteristic function selects those trajectories that have reached the product state after time t. The factor $\theta_P(x_t)$ thus contains the dynamical information [70]; in particular, it describes the correlation of the system with its initial state after time t, obeying $\tau_{mol} \ll t \ll \tau_{rxn}$. On this timescale the system relaxes to one of the stable states so that the plateau value of the rate constant is established as described below [11, 12, 151].

We now turn to the description of timescales involved in the discussion of chemical reaction dynamics to assess under which circumstances equation (2.16) is valid [9, 12, 72]. The rate constant describes the dynamics of a slow

variable [9]. In the present case, the slow variable is the time-dependent population of the product state (or of the reactant state because both are coupled in a closed system) [9, 12]. This means that the number of particles in the product state changes appreciably only on a timescale of the order of the reaction time τ_{rxn}, the average time the system spends in a stable state between infrequent transitions [11]. All other relevant motions of the system must occur on much shorter timescales for a rate constant to exist [9, 12]. In particular, the time for the system to equilibrate in the new stable state after a transition and the time needed for that transition are of the order of molecular times τ_{mol}. We thus have a separtation of timescales $\tau_{mol} \ll \tau_{rxn}$ that characterizes the chemical reaction as an activated process [9, 11].

It follows from the above considerations that the rate constant expression of equation (2.16) is valid for times t such that $\tau_{mol} \ll t \ll \tau_{rxn}$ [9]. To see this, consider times of the order of τ_{rxn}. In that case, a given particle has made at least one transition on average, and the correlation with its initial state has been lost [11]. In contrast, for times comparable to τ_{mol} the system's motion is inertial and strongly correlated to its initial condition. On this timescale the experimentally measured exponential decay cannot hold. In other words, the rate constant reaches a plateau value after a transient time of the order of t [9, 12].

2.1.3 Transition state theory

Having discussed the classical reaction rate constant in the previous section, we now introduce one of the most successful and most widely used concepts in chemical dynamics: transition state theory. We shall present the assumptions made in going from the exact classical rate constant to that of transition state theory and outline its range of validity. Two complementary treatments of transition state theory are encountered in the literature: a dynamical and a thermodynamic one. Both treatments are statistical and will be outlined below. First, Wigner's dynamical transition state theory is described [69, 150]. Subsequently, the thermodynamic version of Eyring [27] is given to make the connection to the empirical rate constant and the activation energy

in equations (2.8) and (2.9).

Wigner's work [69] involves three assumptions. The first states that the chemical reaction occurs on the adiabatic ground state potential energy surface. Second, classical mechanics is assumed to provide an accurate description of the nuclear motion. Wigner's third or *fundamental assumption* [70] states that all trajectories reaching the bottleneck region from the reactant side are reactive and form product species [69]. In addition, because transitions between reactants and products are infrequent, thermal equilibrium prevails in the metastable states [9, 12, 33, 70, 71]. According to Wigner [69], the rate constant is the average velocity of reactant phase space points through the dividing surface normalized by the total number of reactant phase space points.

Clearly, the assumption that trajectories do not recross the dividing surface enables us to make the transition from the exact classical rate constant to the one given by transition state theory. In mathematical terms, we let the time t approach zero from the positive side [9]. This is equivalent to replacing $\theta_P(x_t)$ in equation (2.17) by $\theta(\dot{x}_0)$, yielding the transition state theory rate constant [9, 12, 70]:

$$k_{+,\mathrm{TST}} = \frac{\langle \delta(x_0)\dot{x}_0\theta(\dot{x}_0)\rangle}{\langle \theta_R \rangle}. \tag{2.18}$$

In other words, a system at the dividing surface with a positive velocity in the reactive direction is assumed to proceed to the product state. As a consequence, the rate constant is determined by a statistical average of properties at the dividing surface that are uncorrelated [33, 72]. In particular, transition state theory allows us to obtain dynamical information without having to propagate trajectories. [9, 70] This is in contrast to the exact classical expression for the rate constant (2.17), where the fate of a trajectory depends on the velocities and positions at its initial and final times [9, 70].

As can be seen from equation (2.18), the transition state theory rate constant is given by the probability density of finding the system at the transition state (or at the dividing surface) compared to the probability that the system is in the reactant well multiplied by the thermally averaged velocity in the

reactive direction at the transition state [33]. This very attractive feature of only involving static properties comes at a price. The transition state theory rate constant depends on the location of the dividing surface and thus on the choice of the reaction coordinate [9, 152]. In contrast, the exact classical rate constant is independent of the location of the dividing surface, as follows from Liouville's theorem (discussed in section 3.1) [70]. Even if the transition state could be located correctly, the rate constant of transition state theory would still overestimate the exact classical rate constant because of the no-recrossing rule [152]. The difference between the exact classical rate constant and that from transition state theory is accounted for by the transmission coefficient [12, 27, 69, 153]:

$$\kappa_{tr} = \frac{k_+}{k_{+,\mathrm{TST}}}. \tag{2.19}$$

Given an adiabatic ground state potential energy surface and classical forces derived from it acting on the nuclei, transition state theory is based on two key assumptions [9, 12, 33, 70, 71]. First, equilibrium prevails in the reactant state. Second, trajectories crossing the bottleneck from the reactants transform to products with certainty. According to Nitzan [33], these two assumptions are incompatible with each other. The second assumption can only be fulfilled if motion across the dividing surface is inertial so that no collisions can reverse the trajectory of the system. However, for thermal equilibrium to exist within the whole reactant region up to the dividing surface according to the first assumption, collisions with the environment are necessary and thus contradict the second assumption.

Wigner's dynamical transition state theory emphasizes the second of the above assumptions, namely that the system does not recross the dividing surface. In contrast, Eyring's work [27] stresses the equilibrium within the reactant state governing the probability of reaching the transition state or activated complex. The activated complex is the state of the system at the bottleneck and decomposes along the reaction coordinate. If the motion in the reaction coordinate is approximated by a harmonic mode in the classical

limit, we obtain the transition state theory rate constant [12, 33, 71, 154]:

$$k_{+,\mathrm{TST}} = \nu_R \, e^{-\beta \Delta_\ddagger F}. \tag{2.20}$$

Above, ν_R is a characteristic relaxation frequency in the reactant well, and $\Delta_\ddagger F$ denotes the activation free energy[7] that determines the probability of finding the system at the transition state compared to finding it in the reactant region.

We are now in a position to relate the transition state theory rate constant (2.20) to the empirical rate constant (2.8). In particular, using the definition of the Helmholtz free energy change [15],

$$\Delta_\ddagger F = \Delta_\ddagger U - T \Delta_\ddagger S, \tag{2.22}$$

we obtain

$$k_{+,\mathrm{TST}} = \nu_R \, e^{-\beta \Delta_\ddagger U} \, e^{\frac{\Delta_\ddagger S}{k_B}}. \tag{2.23}$$

For reactions in solution the activation energy and the activation internal energy are related by equation (2.24) [15, 95]:

$$E_a = \Delta_\ddagger U + k_B T. \tag{2.24}$$

Hence, we can identify the pre-exponential factor A_r in equation (2.8) as [15, 36, 95]

$$A_r = e \, \nu_R \, e^{\frac{\Delta_\ddagger S}{k_B}}. \tag{2.25}$$

[7] In principle, the quantity denoted by $\Delta_\ddagger F$ (denoted by Marcus as ΔF^* [95]) in equation (2.20) has one degree of freedom less in the partition function of the reactants than that in the Eyring equation [27]:

$$k_{+,\mathrm{TST}} = \frac{k_B T}{h} \, e^{-\beta \, \Delta_\ddagger F}. \tag{2.21}$$

However, the numerical difference is small in practice [38, 95], and we shall not introduce another symbol to distinguish between the two activation free energies.

The above equation can thus be interpreted as the product of a collision factor in condensed phase ν_R and a factor determining the fraction of systems suitably prepared for reaction via the relative accessible phase space volume to do so. The connection between activation parameters and the rate constant closes our discussion about transition state theory. Next, we present Marcus theory, which uses the framework of transition state theory described above.

2.2 Marcus theory of electron transfer

2.2.1 Electron-transfer reactions

Before we describe the mechanism and dynamics of electron-transfer reactions, a brief account of redox reactions, their nature and their classification is given. Electron-transfer reactions involve the transfer of one or more electrons from an electron donor D to an electron acceptor A, as in equation (2.26) [15, 86]. For notational brevity we shall focus on reactions involving the transfer of a single electron (e^-). The reduced form of the donor D and the oxidized form of the acceptor A correspond to the reactants R, whereas the products P consist of the oxidized form of the donor D^+ and the reduced form of the acceptor A^-:

$$D + A \rightleftharpoons D^+ + A^-. \tag{2.26}$$

From a theoretical point of view, we can divide the above-given full redox reaction into two half-reactions.[8] The first half-reaction consists of the oxidized and reduced forms of the donor D^+/D, whereas the second one is formed by the oxidized and reduced forms of the acceptor A/A^-. The

[8]Dividing the full reaction into half-reactions is a hypothetical operation for homogeneous redox reactions. In heterogeneous redox processes the oxidation and reduction are spatially separated and take place at different electrodes [15].

corresponding half-reactions read

$$D \rightarrow D^{+} + e^{-}; \tag{2.27a}$$

$$A + e^{-} \rightarrow A^{-}. \tag{2.27b}$$

As will be seen below, the decomposition of the full reaction into half-reactions allows for computationally less expensive schemes to evaluate redox free energies [68].

Redox reactions are fundamental chemical transformations and can be found in diverse environments and under various conditions. Consequently, several types of redox reactions can be distinguished. First, homogeneous redox reactions involve electron transfer between donor and acceptor species that are in the same phase, often in a polar solvent [15]. In contrast, heterogeneous redox processes are transformations in which the electron donor or acceptor is an electrode. In this case, the electron transfer occurs across an interface [15]. Second, the electron transfer can be light-induced as in photosystem II of plants or thermally activated as in the respiratory chain [155]. In the former case, the system must dissipate excess energy effectively, whereas the latter case requires an environment capable of providing the activation for the electron transfer. Third, if the first solvation shell around an electroactive species remains unaltered during the reaction, the process is called an outer-sphere electron transfer [30]. On the other hand, inner-sphere electron-transfer reactions are characterized by significant changes in the first solvation shell, such as variations in the number of ligands or shared ligands between donor and acceptor species [30]. Fourth, as most condensed phase reactions, redox processes can be divided into the following sequence of steps: encounter, reaction, separation [33]. The first step involves the encounter of the reactants via diffusion, and possibly adsorption, to reach a distance suitable for reaction. Then, the chemical transformation takes place, and the products diffuse away from each other, conceivably after desorption from a surface. It is assumed here that the diffusion steps are fast compared to the chemical reaction so that the chemical transformation is rate-limiting [15,33]. Also, to restrict the scope of the present document, the investigation will

focus on homogeneous, thermally activated outer-sphere electron-transfer reactions.

After the brief description of redox reactions above the physical view of electron transfer according to Marcus theory will be presented [35]. It is first noted that outer-sphere electron-transfer reactions are special transformations because no chemical bond involving the electroactive species is being broken or formed [42]. Thus, the electronic coupling between the solute states is usually weak, and diabatic or charge-localized states can be employed to describe the solutes' charge distribution [35]. Because the reactant and product solute states usually exhibit charges, redox processes generally take place in polar solvents capable of stabilizing these charges [34].

The next observation pertains to the overall stable states including solutes and solvent. Because the solute's charge distribution of the reactants differs from that of the products, the equilibrium solvent configuration around the reactant state of the solute will typically be different from the most probable solvent configuration stabilizing the products' solute [33]. Because electrons commonly move faster than nuclei, the following mechanism of electron transfer is proposed within the framework of Marcus theory [35, 42].

The actual electron transfer occurs at a fixed nuclear configuration of the solutes and the solvent, thereby obeying the Franck-Condon principle [35,42]. Because attention is restricted to thermal processes, the total energies of the reactant and product states must be equal at the transition state for electron transfer to occur [35, 42]. As a consequence, the activation involves nuclear rearrangement of the solvent prior to electron transfer. The solvent distorts from a configuration equilibrated to the reactants' charge distribution to a solvent configuration at the transition state that is in equilibrium with neither the reactants' nor the products' charge distribution [35,84]. After the charge transfer the solvent relaxes to a configuration that is in equilibrium with the products' charge distribution. In summary, thermal fluctuations of the polar solvent away from the most probable regions of the reactant well, making reactant and product states degenerate, allow for and drive electron transfer [33].

After the physical and qualitative aspects the quantitative features of Marcus theory will next be described within the microscopic framework of statistical mechanics [38].

2.2.2 Rate constant and activation free energy

As mentioned earlier, the expression of the rate constant for electron-transfer reactions is based on transition state theory [38, 42, 94, 95]:

$$k_{+,\mathrm{ET}} = \nu_R \, e^{-\beta \Delta_\ddagger F}. \tag{2.28}$$

Here, $\beta^{-1} = k_B T$ is the Boltzmann constant times the absolute temperature, and $\Delta_\ddagger F$ denotes the Helmholtz free energy of activation. The value of the pre-exponential factor ν_R corresponds to a typical frequency in the reactant well if the adiabatic version of the rate constant is employed. In contrast, the non-adiabatic formulation, derived from Fermi's golden rule in a quantum treatment or from a semi-classical Landau-Zener approach, identifies $\nu_R = \frac{2\pi}{\hbar} \gamma_{el}^2 \, (4\pi \, \lambda \, k_B T)^{-1/2}$ in the high temperature limit [43, 48, 92, 156, 157]. Here, $\hbar$ is Planck's constant divided by 2π. The electronic coupling element between the reactant and product states is denoted by γ_{el}, and λ is the reorganization free energy defined below.

As usual, the exponential factor gives the probability density for finding the system at the transition state compared to finding it in the reactant region. According to Marcus theory [25, 30, 42], the (diabatic) activation free energy is (see also the footnotes on page 8)[9]

$$\Delta_\ddagger F = \Delta_\ddagger F^{(d)} = \frac{(\Delta_r F + \lambda)^2}{4 \, \lambda}. \tag{2.29}$$

Above, $\Delta_r F$ denotes the Helmholtz free energy of reaction, hereafter referred

[9] We shall distinguish between diabatic (d) and adiabatic (a) activation parameters ($\Delta_\ddagger F$; $\Delta_\ddagger U$; $\Delta_\ddagger S$), for which the difference due to the electronic coupling γ_{el} between diabatic states is expected to be largest. In contrast, reaction parameters ($\Delta_r F$; $\Delta_r U$; $\Delta_r S$) as well as the charge-transfer symmetry factor and its components (β_{ct}; $\beta_{ct,U}$; $\beta_{ct,S}$) are expected to be less sensitive to γ_{el}. Whenever a statement applies to the diabatic and adiabatic cases, no distinction in notation will be made.

to as the reaction free energy. The reaction free energy is a quantity involving both reactant and product states, whereas the reorganization free energy λ is a property of only one diabatic state characterized by a fixed charge distribution of the solute. The reorganization free energy of the reactants is the reversible work to distort the solvent from a configuration equilibrated to the reactants' charge distribution to a configuration that would be in equilibrium with the products' charge distribution [48, 96, 97]. The reorganization free energy of the products is specified in an analogous manner.

As seen from the equations above, Marcus theory provides an elegant way of describing electron-transfer dynamics [48, 50]. This picture rests on two crucial assumptions discussed below. The first assumption involves the choice of the reaction coordinate [91], whereas the second one is the linear response approximation for the solvent [42]. The implications of these assumptions will be described, and the quantitative relations following from them will be used to derive equation (2.29). We shall start with the choice of the reaction coordinate.

2.2.3 Reaction coordinate and transition state

According to the physical picture of electron transfer given earlier, the transition state of redox reactions is characterized by degenerate total energies of the reactants and products [35, 42, 48, 92]. Equivalently, the difference in energy between the products and reactants, called the diabatic energy gap,[10,11]

[10]Throughout this document we interchangeably call the diabatic energy gap diabatic gap, energy gap or gap. As seen from equation (2.30), the diabatic gap is a dynamical variable that depends on the phase space variables $\boldsymbol{\xi}$. We shall denote the function $\Delta E(\boldsymbol{\xi})$ and its value ΔE. This value represents all phase space points for which the dynamical variable $\Delta E(\boldsymbol{\xi})$ is ΔE. In the case of δ-distribution arguments, the function will be written $\Delta E^{'}(\boldsymbol{\xi})$.

[11]Some authors [48, 92] define ΔE as a solvation or solvent coordinate because it describes the configuration of the solvent. This solvent coordinate is the difference in interaction energy of the solvent with the reactants' and products' charge distribution. In that case, the solvent coordinate need not vanish at the transition state because the gas phase energies of the reactant and product states are generally different. The total energy difference is also zero at the transition state in that case, and the description is equivalent to the one given here.

given in equation (2.30), vanishes at the transition state.

$$\Delta E(\boldsymbol{\xi}) = \mathcal{H}_P(\boldsymbol{\xi}) - \mathcal{H}_R(\boldsymbol{\xi}) \tag{2.30}$$

In 1960 Marcus proposed the diabatic gap as the reaction coordinate [38]. This choice leads to the correspondence of the transition state to the crossing point of the free energy curves displayed in figure 1.2 as a special case of the following relation [47, 91]:

$$\Delta F_L\left(\Delta E\right) = F_{L,P}\left(\Delta E\right) - F_{L,R}\left(\Delta E\right) = \Delta E. \tag{2.31}$$

In words, the difference in Landau free energy F_L between the product and reactant states for a given value of the diabatic energy gap equals precisely that gap value.

The consequences of equation (2.31) are far-reaching, and we shall therefore derive it below. Our starting point is the expression for the Landau free energy of state $j = R, P$ (also discussed in appendix D) [47, 48, 68, 93],

$$\begin{aligned} F_{L,j}(\Delta E) &= -\beta^{-1}\, ln\, \left(h^{3N} N!\right)^{-1} \int \delta(\Delta E^{'}(\boldsymbol{\xi}) - \Delta E)\, e^{-\beta \mathcal{H}_j(\boldsymbol{\xi})}\, d\boldsymbol{\xi} \\ &= F_j - \beta^{-1}\, ln\, \left\langle\, \delta(\Delta E^{'}(\boldsymbol{\xi}) - \Delta E)\, \right\rangle_j \\ &= F_j - \beta^{-1}\, ln\, \rho_j(\Delta E), \end{aligned} \tag{2.32}$$

where $\beta^{-1} = k_B T$, h is Planck's constant, N denotes the number of particles and $\delta(y)$ is the Dirac δ-distribution, whose properties are given in appendix C.2. The free energy [113]

$$F_j = -\beta^{-1}\, ln\, (h^{3N} N!)^{-1} \int e^{-\beta \mathcal{H}_j(\boldsymbol{\xi})}\, d\boldsymbol{\xi} \tag{2.33}$$

of state j is introduced to express the Landau free energy in terms of a canonical ensemble average, indicated by angular brackets. The third line defines the restricted phase space density $\rho_j(\Delta E)$ in state j. Next, we use the explicit phase space integrals introduced above to obtain the Landau free

energy difference:

$$\begin{aligned}
\Delta F_L(\Delta E) &= -\beta^{-1}\, ln \frac{\int \delta(\Delta E'(\boldsymbol{\xi}) - \Delta E)\, e^{-\beta \mathcal{H}_P(\boldsymbol{\xi})}\, d\boldsymbol{\xi}}{\int \delta(\Delta E'(\boldsymbol{\xi}) - \Delta E)\, e^{-\beta \mathcal{H}_R(\boldsymbol{\xi})}\, d\boldsymbol{\xi}} \\
&= -\beta^{-1}\, ln\, \frac{\int \delta(\Delta E'(\boldsymbol{\xi}) - \Delta E)\, e^{-\beta \Delta E'(\boldsymbol{\xi})}\, e^{-\beta \mathcal{H}_R(\boldsymbol{\xi})}\, d\boldsymbol{\xi}}{\int \delta(\Delta E'(\boldsymbol{\xi}) - \Delta E)\, e^{-\beta \mathcal{H}_R(\boldsymbol{\xi})}\, d\boldsymbol{\xi}} \\
&= -\beta^{-1}\, ln\, e^{-\beta \Delta E} \\
&= \Delta E. \qquad (2.34)
\end{aligned}$$

Above, we use the definition of the diabatic gap (2.30) to reach the second line. The δ-distribution selects the same phase space points in the denominator and in the numerator except that the latter contains an additional constant weight factor $e^{-\beta \Delta E}$, which can be extracted from the integral, thus yielding the third line. Hence, equation (2.31) is established.

We note that equation (2.31) is specific to the energy gap as the reaction coordinate [91, 93]. Furthermore, the transition state is indeed predicted to coincide not only with degenerate energies but also with degenerate free energies according to this relation. Until now, we have not specified any functional form of the gap probability density. We shall do so next in our discussion of the linear response approximation.

2.2.4 Linear response approximation

The linear response approximation consists in assuming that the environment surrounding the electroactive species distorts harmonically. In particular, the solvent responds linearly to a change in the solute's charge distribution [30, 42]. From a mathematical point of view, the linear response approximation corresponds to assuming that the probability density of the diabatic gap is Gaussian [99].

The linear response approximation together with choosing the diabatic gap as the reaction coordinate results in simple and powerful expressions for the reaction and reorganization free energies used in equation (2.29) for the activation free energy. To obtain the reaction and reorganization free

energies, we proceed as follows. First, the Gaussian gap probability density is used in the expression for the Landau free energy (2.32). We then compute the Landau free energy difference. Finally, the prefactors of the powers of the diabatic gap are compared to those in equation (2.31), yielding the expressions for the reaction and reorganization free energies [68, 93].

We start with the Landau free energy (2.32) of state $j = R, P$ with the Gaussian probability density (B.17) in terms of the diabatic gap [68]:

$$\begin{aligned}
F_{L,j}(\Delta E) =& F_j - \beta^{-1}\, ln\, \rho_j\,(\Delta E) \\
=& F_j - \beta^{-1}\, ln\, \left(2\pi\sigma_j^2\right)^{-\frac{1}{2}}\, e^{-\frac{\left(\Delta E - \langle \Delta E\rangle_j\right)^2}{2\sigma_j^2}} \\
=& F_j + \frac{\beta^{-1}}{2}\, ln\, \left(2\pi\sigma_j^2\right) + \frac{\beta^{-1}}{2}\frac{\left(\Delta E - \langle \Delta E\rangle_j\right)^2}{\sigma_j^2} \\
=& \frac{\beta^{-1}}{2\sigma_j^2}(\Delta E)^2 - \frac{\beta^{-1}\langle \Delta E\rangle_j}{\sigma_j^2}\Delta E \\
&+ F_j + \frac{\beta^{-1}}{2}\, ln\, \left(2\pi\sigma_j^2\right) + \frac{\beta^{-1}}{2\sigma_j^2}\left(\langle \Delta E\rangle_j\right)^2 .
\end{aligned} \tag{2.35}$$

Above and below, the mean and the variance of the diabatic gap of state j are denoted by $\langle \Delta E\rangle_j$ and σ_j^2.

For the difference in the Landau free energy of the stable states we obtain

$$\begin{aligned}
\Delta F_L(\Delta E) &= F_{L,P}(\Delta E) - F_{L,R}(\Delta E) \\
&= \frac{\beta^{-1}}{2}\left(\frac{1}{\sigma_P^2} - \frac{1}{\sigma_R^2}\right)(\Delta E)^2 - \beta^{-1}\left(\frac{\langle \Delta E\rangle_P}{\sigma_P^2} - \frac{\langle \Delta E\rangle_R}{\sigma_R^2}\right)\Delta E \\
&\quad + \Delta_r F + \beta^{-1}\, ln\left(\frac{\sigma_P}{\sigma_R}\right) + \frac{\beta^{-1}}{2}\left(\frac{(\langle \Delta E\rangle_P)^2}{\sigma_P^2} - \frac{(\langle \Delta E\rangle_R)^2}{\sigma_R^2}\right).
\end{aligned} \tag{2.36}$$

The term $\Delta_r F = F_P - F_R$ in the last line denotes the unrestricted equilibrium Helmholtz free energy of reaction. For an arbitrary, normally distributed reaction coordinate $\Delta_r F$ is related to the Landau free energy of reaction (2.37) [68],

$$\Delta_r F_L = F_{L,P}(\langle \Delta E\rangle_P) - F_{L,R}(\langle \Delta E\rangle_R), \tag{2.37}$$

by [48, 68]

$$\Delta_r F = \Delta_r F_L - k_B T \, ln \frac{\sigma_P}{\sigma_R}. \tag{2.38}$$

We note that equations (2.35), (2.36) and (2.38) are independent of the reaction coordinate. However, choosing the diabatic gap as the reaction coordinate enables us to exploit equation (2.31), which demands that the coefficients vanish for the second and zeroth power in the diabatic gap. Also, the coefficient of the linear term must be unity [68]. These constraints lead to the following results.

First, setting the coefficient of the quadratic term to zero yields equal variances for the product and reactant states:

$$\sigma_R^2 = \sigma_P^2 = \sigma^2. \tag{2.39}$$

Second, comparison of the coefficients of the linear term in the diabatic gap in equations (2.31) and (2.36) yields

$$\beta\sigma^2 = \langle \Delta E \rangle_R - \langle \Delta E \rangle_P. \tag{2.40}$$

This relation (2.40) is now inserted into the last term of equation (2.36) to yield a remarkable expression for the reaction free energy [50, 68, 93]:

$$\Delta_r F = \frac{\langle \Delta E \rangle_R + \langle \Delta E \rangle_P}{2}. \tag{2.41}$$

Having determined the reaction free energy above, we now seek an expression for the reorganization free energy [68]:

$$\lambda_R = F_{L,R}(\langle \Delta E \rangle_P) - F_{L,R}(\langle \Delta E \rangle_R); \tag{2.42a}$$

$$\lambda_P = F_{L,P}(\langle \Delta E \rangle_R) - F_{L,P}(\langle \Delta E \rangle_P). \tag{2.42b}$$

From equations (2.35), (2.39) and (2.42) it follows that the reorganization free energies for the product and reactant states are equal $\lambda_R = \lambda_P = \lambda$

[52, 68]:

$$\lambda = \frac{(\langle \Delta E \rangle_R - \langle \Delta E \rangle_P)^2}{2\beta\sigma^2} = \frac{\langle \Delta E \rangle_R - \langle \Delta E \rangle_P}{2} = \frac{\beta\sigma^2}{2}. \tag{2.43}$$

Here, the third and fourth expressions are obtained from the second one by substituting equation (2.40) in the denominator and in the numerator.

The mean diabatic gaps in the reactant and product states can be expressed as the sum and the difference of equations (2.41) and (2.43) [44, 68]:

$$\langle \Delta E \rangle_R = \Delta_r F + \lambda; \tag{2.44a}$$

$$\langle \Delta E \rangle_P = \Delta_r F - \lambda. \tag{2.44b}$$

Approximating the activation free energy as the Landau free energy difference between the transition state and the reactant well [68],

$$\Delta_\ddagger F = F_{L,R}(0) - F_{L,R}(\langle \Delta E \rangle_R), \tag{2.45}$$

we obtain for the diabatic case [30, 68]

$$\Delta_\ddagger F^{(d)} = \frac{(\langle \Delta E \rangle_R)^2}{2\beta\sigma^2}. \tag{2.46}$$

Above, we have used equation (2.35). Substituting relations (2.43) and (2.44a) into equation (2.46) yields the familiar expression for the (diabatic) activation free energy [25, 30, 42]:

$$\Delta_\ddagger F^{(d)} = \frac{(\Delta_r F + \lambda)^2}{4\lambda}.$$

For completeness, an alternative route to obtaining the expressions for the reaction and reorganization free energies is discussed next. The thermodynamic perturbation result for the reaction free energy between diabatic

states $j = R, P$ is presented below [68, 120]:

$$\Delta_r F = -\beta^{-1} ln \frac{\int e^{-\beta \mathcal{H}_P(\boldsymbol{\xi})}\, d\boldsymbol{\xi}}{\int e^{-\beta \mathcal{H}_R(\boldsymbol{\xi})}\, d\boldsymbol{\xi}}; \tag{2.47a}$$

$$\Delta_r F = -\beta^{-1} ln \left\langle e^{-\beta \Delta E(\boldsymbol{\xi})} \right\rangle_R; \tag{2.47b}$$

$$\Delta_r F = \beta^{-1} ln \left\langle e^{\beta \Delta E(\boldsymbol{\xi})} \right\rangle_P. \tag{2.47c}$$

Using the cumulant expansions of equations (2.47b) and (2.47c) for the normally distributed random variable ΔE (see appendix B), we obtain [68, 93]

$$\Delta_r F = \langle \Delta E \rangle_R - \frac{1}{2}\beta\sigma_R^2; \tag{2.48a}$$

$$\Delta_r F = \langle \Delta E \rangle_P + \frac{1}{2}\beta\sigma_P^2. \tag{2.48b}$$

For equal variances the sum and difference of equations (2.48a) and (2.48b) multiplied by one half reduce to relations (2.41) and (2.43).

It is worth pointing out that equations (2.41), (2.43) and (2.29) for the reaction, reorganization and activation free energies only hold if the diabatic energy gap is the reaction coordinate *and* normally distributed. A Gaussian probability density of another reaction coordinate would yield parabolic Landau free energy curves, but not necessarily the same variance for product and reactant states. The equality of the Marcus parabola curvatures is a specific feature of the normally distributed diabatic gap, for which equation (2.31) applies [48, 91].

2.2.5 Activation parameters

In this section we obtain the energetic and entropic contributions to the diabatic activation free energy. We then consider the effect of the electronic coupling on the activation parameters. In other words, expressions for adiabatic activation parameters are derived.

The internal energy of activation is given by the Gibbs-Helmholtz equa-

tion [15]:

$$\Delta_{\ddagger} U = \left(\frac{\partial \frac{\Delta_{\ddagger} F}{T}}{\partial \frac{1}{T}} \right)_{N,\mathcal{V}} . \tag{2.49}$$

Equivalently, we can use equation (2.22) to obtain the internal energy of activation from the activation free energy and activation entropy. The activation entropy in the framework of Marcus theory is given by equation (2.50) [37]:

$$\begin{aligned} \Delta_{\ddagger} S^{(d)} &= - \left(\frac{\partial \Delta_{\ddagger} F^{(d)}}{\partial T} \right)_{N,\mathcal{V}} \\ &= \left(\frac{1}{2} + \frac{\Delta_r F}{2\,\lambda} \right) \Delta_r S + \left(\frac{1}{4} - \left(\frac{\Delta_r F}{2\,\lambda} \right)^2 \right) \Delta S_{\lambda}. \end{aligned} \tag{2.50}$$

Above, we have defined the reorganization entropy [52]:

$$\Delta S_{\lambda} = - \left(\frac{\partial \lambda}{\partial T} \right)_{N,\mathcal{V}} . \tag{2.51}$$

The internal energy of activation then follows from equation (2.22):

$$\Delta_{\ddagger} U^{(d)} = \frac{(\Delta_r F + \lambda)^2}{4\,\lambda} + \left(\frac{1}{2} + \frac{\Delta_r F}{2\,\lambda} \right) T \Delta_r S + \left(\frac{1}{4} - \left(\frac{\Delta_r F}{2\,\lambda} \right)^2 \right) T \Delta S_{\lambda}. \tag{2.52}$$

We note that the entropy and internal energy of activation contain both an intrinsic contribution due to the reorganization of the environment and a contribution due to the asymmetry of the reaction. The above expressions are valid if the diabatic states do not interact, whereas the effect of the electronic coupling will be summarized below.

Brunschwig and Sutin derived the following approximate expression for the adiabatic activation free energy [158]:

$$\Delta_{\ddagger} F^{(a)} = \frac{\lambda}{4} + \frac{\Delta_r F}{2} + \frac{\Delta_r F^2}{4\,(\lambda - 2\,\gamma_{el})} - \gamma_{el} + \frac{\gamma_{el}^2}{\lambda + \Delta_r F}. \tag{2.53}$$

The equation above assumes that the free energy profile has two minima separated by a local maximum [158]. The effect of the electronic coupling γ_{el}

consists in lowering the free energy of the transition state by γ_{el} compared to the non-interacting case. In addition, the minima of the free energy profile approach each other and are lower in energy [158]. The reaction free energy $\Delta_r F$ is that of the diabatic case. The fourth term on the right-hand side of equation (2.53) represents the dominant effect in going from the diabatic to the adiabatic activation free energy for small to moderate coupling elements γ_{el}.

Neglecting terms of order $(\gamma_{el}/\lambda)^2$ and assuming that γ_{el} is temperature-independent, we obtain the following approximate relations from equation (2.53) for $\gamma_{el} \ll \lambda/2$ and $|\Delta_r F| < \lambda$. The adiabatic activation entropy is given by equation (2.54):

$$\begin{aligned}\Delta_{\ddagger} S^{(a)} &= -\left(\frac{\partial \Delta_{\ddagger} F^{(a)}}{\partial T}\right)_{N,\mathcal{V}} \\ &= \left(\frac{1}{2} + \frac{\Delta_r F}{2\,(\lambda - 2\,\gamma_{el})}\right)\Delta_r S + \left(\frac{1}{4} - \left(\frac{\Delta_r F}{2\,(\lambda - 2\,\gamma_{el})}\right)^2\right)\Delta S_\lambda. \quad (2.54)\end{aligned}$$

Similarly, we obtain the adiabatic internal energy of activation:

$$\begin{aligned}\Delta_{\ddagger} U^{(a)} =& \frac{\lambda}{4} + \frac{\Delta_r F}{2} + \frac{\Delta_r F^2}{4\,(\lambda - 2\,\gamma_{el})} - \gamma_{el} + \frac{\gamma_{el}^2}{\lambda + \Delta_r F} \\ &+ \left(\frac{1}{2} + \frac{\Delta_r F}{2\,(\lambda - 2\,\gamma_{el})}\right) T\Delta_r S + \left(\frac{1}{4} - \left(\frac{\Delta_r F}{2\,(\lambda - 2\,\gamma_{el})}\right)^2\right) T\Delta S_\lambda \\ =& \frac{\lambda}{4} + \frac{\Delta_r U}{2} + \frac{\Delta_r F^2}{4\,(\lambda - 2\,\gamma_{el})} - \gamma_{el} + \frac{\gamma_{el}^2}{\lambda + \Delta_r F} \\ &+ \frac{\Delta_r F}{2\,(\lambda - 2\,\gamma_{el})} T\Delta_r S + \left(\frac{1}{4} - \left(\frac{\Delta_r F}{2\,(\lambda - 2\,\gamma_{el})}\right)^2\right) T\Delta S_\lambda. \quad (2.55)\end{aligned}$$

In the small coupling limit, considered in the present work, the diabatic expressions for the activation parameters are close to the adiabatic ones.

2.2.6 Charge-transfer symmetry factor

The activation parameters given in equations (2.29), (2.50) and (2.52) are valid for an electron-transfer reaction under specific conditions. If the reac-

tion free energy is changed, for example by modifying the chemical nature of the acceptor species, the derivatives of the activation parameters with respect to the reaction free energy can be obtained. The variation of the activation free energy with the reaction free energy defines the charge-transfer symmetry factor β_{ct}, which describes the relative location of the transition state relative to the reactants and products in accordance with the Leffler-Hammond postulate [17,18]. Under restrictions given in the introduction, the charge-transfer symmetry factor [55–60] can be formally decomposed into an energetic ($\beta_{ct,U}$) and entropic ($T\beta_{ct,S}$) component [61–64]:

$$\beta_{ct} = \frac{\partial \Delta_{\ddagger} F}{\partial \Delta_r F} = \frac{\partial \left(\Delta_{\ddagger} U - T\Delta_{\ddagger} S\right)}{\partial \Delta_r F} = \beta_{ct,U} + T\beta_{ct,S}. \tag{2.56}$$

For a simple and elementary electron-transfer step in the framework of Marcus theory $\beta_{ct,MT}$ becomes [30, 85, 86]

$$\beta_{ct,MT} = \frac{1}{2} + \frac{\Delta_r F}{2\lambda}. \tag{2.57}$$

Its temperature dependence is given by equation (2.58):

$$\frac{\partial \beta_{ct,MT}}{\partial T} = \frac{-\Delta_r S}{2\lambda} + \Delta S_\lambda \frac{\Delta_r F}{2\lambda^2}. \tag{2.58}$$

The temperature dependence is seen to be related to the entropic component of the symmetry factor:

$$T\beta_{ct,S,MT} = -T\frac{\partial \Delta_{\ddagger} S^{(d)}}{\partial \Delta_r F} = -\,T\frac{\Delta_r S}{2\,\lambda} + T\Delta S_\lambda \frac{\Delta_r F}{2\,\lambda^2}. \tag{2.59}$$

The energetic component of the charge-transfer symmetry factor is

$$\beta_{ct,U,MT} = \frac{\partial \Delta_{\ddagger} U^{(d)}}{\partial \Delta_r F} = \frac{1}{2} + \frac{\Delta_r U}{2\,\lambda} - T\Delta S_\lambda \frac{\Delta_r F}{2\,\lambda^2}. \tag{2.60}$$

The above expression for the charge-transfer symmetry factor and its components apply in the diabatic case. The corresponding adiabatic expressions are obtained by replacing λ by $\lambda - 2\,\gamma_{el}$. As a result, the diabatic and adiabatic

expressions are close for $\gamma_{el} \ll \lambda$, and we shall use the diabatic expressions for the charge-transfer symmetry factor and its components in subsequent discussions.

After this outline of elements of classical electron-transfer theory the statistical mechanics of trajectory space will be presented below.

2.3 Statistical mechanics of trajectories

Classical rate theory and transiton state theory provide key dynamical information about chemical transformations, such as rate constants and activation (free) energies. As already pointed out, transition state theory relies on the knowledge of the reaction coordinate to compute rate constants and activation parameters [65,159–161]. Although this is not necessary for the classical rate constant expression, its evaluation is more efficient if the dividing surface is close to the transition state [9,143,152,153]. However, the mechanism of a complex transformation is often unknown [159,162].

Transition path sampling [21, 23, 74] is a method that does not require the knowledge of the reaction coordinate. It enables us to calculate rate constants and activation energies of chemical reactions if the stable reactant and product states can be identified. Transition path sampling focuses on the infrequent transitions between the stable states and is based on the statistical mechanics of trajectories in phase space [73]. Its theoretical foundations are described next, thereby laying the ground for expressions of the rate constant and the activation energy.

From a methodological point of view, transition path sampling employs a Monte Carlo procedure to sample trajectory space [73]. The individual pathways are generated by molecular dynamics simulation [73]. Details of the method are deferred to section 3.3.

As stated above, transition path sampling focuses on the actual dynamical transitions from reactants to products or on reactive trajectories.[12] Akin to classical rate theory, transition path sampling expresses the rate constant as

[12]The terms trajectory, pathway and path are used interchangeably throughout this work to describe the time evolution of a phase space point.

an average over reactive trajectories. To proceed, it is necessary to define the probability of a trajectory and the appropriate ensemble. Following Chandler and co-workers [21, 23, 74], we will turn to both aspects below, starting with the path probability.

2.3.1 Probability distribution of trajectories

In classical (statistical) mechanics, the (dynamical) state of a system is represented by a point in phase space [113]. This corresponds to specifying all positions and momenta of all particles in the system. In addition, the phase space density gives the probability of finding the system at each point in phase space given the external constraints defining the ensemble under consideration [113].

When we consider a reactive trajectory, we also need to specify the time evolution of the system for a given time t. Because we focus on rare events, the chosen time will satisfy $\tau_{mol} \ll t \ll \tau_{rxn}$. Thus, the dynamics captures the entire transition from reactants to products, but avoids the equilibrium fluctuations in the stable states [11, 21, 23].

In principle, the time evolution of a system is continuous [21]. However, in the realm of computer simulations time is represented in a discrete manner [163]. Following reference [21], we define a trajectory $\boldsymbol{\xi}(t)$ as an ordered sequence of phase space points $\boldsymbol{\xi}_{j\Delta t}$ at time $j\Delta t$ and write the trajectory as $\boldsymbol{\xi}(t) = \{\boldsymbol{\xi}_0, \boldsymbol{\xi}_{\Delta t}, \boldsymbol{\xi}_{2\Delta t}, \ldots, \boldsymbol{\xi}_t\}$ [21]. A pathway of length t is thus characterized by $t/\Delta t+1$ phase space points or time slices. The continuous path is recovered in the limit of vanishing time intervals Δt.

We now present the probability $w[\boldsymbol{\xi}(t)]$ associated with a particular pathway $\boldsymbol{\xi}(t)$. This probability depends on the weight of the initial conditions $\rho(\boldsymbol{\xi}_0)$ and the probability to reach the subsequent phase space points from the first time slice [21]. We restrict our attention to Markovian transition probabilities, for which the probability to reach the next time slice from the current one depends on the current phase space point only [33, 113]. The probability to reach a subsequent time slice is thus independent of the history of the trajectory [33, 113]. In that case, the probability to go from the

first to the last phase space point of the trajectory is the product of transition probabilities for reaching the next time slice $(j+1)$ from the current one (j): $w_t\left(\boldsymbol{\xi}_{j\Delta t} \to \boldsymbol{\xi}_{(j+1)\Delta t}\right)$. The overall path probability then reads as follows [21]:

$$w[\boldsymbol{\xi}(t)] = \rho(\boldsymbol{\xi}_0) \prod_{j=0}^{\frac{t}{\Delta t}-1} w_t\left(\boldsymbol{\xi}_{j\Delta t} \to \boldsymbol{\xi}_{(j+1)\Delta t}\right). \tag{2.61}$$

The above treatment has been given with deterministic dynamics in mind. For deterministic dynamics the time evolution of the system is known if one point along its trajectory is specified completely [33]. In that case, the individual transition probabilities become unity and the path weight reduces to the probability of observing the first phase space point $w[\boldsymbol{\xi}(t)] = \rho(\boldsymbol{\xi}_0)$ [21]. For this special case the length of the trajectory does not influence its weight. We shall turn to path ensembles below.

2.3.2 Path ensembles and their partition functions

The set of all trajectories of length t defines a path ensemble characterized by the partition function $Z(t) = \int \rho(\boldsymbol{\xi}_0) \prod_{j=0}^{\frac{t}{\Delta t}-1} w_t\left(\boldsymbol{\xi}_{j\Delta t} \to \boldsymbol{\xi}_{(j+1)\Delta t}\right) d\boldsymbol{\xi}_j$. Because the probability of finding a given trajectory, whose time evolution is governed by Hamiltonian dynamics, depends on its initial time slice only, all *unrestricted* path ensembles are equivalent, and the trajectory length is unimportant. As a consequence, the partition function characterizing the path ensemble reduces to $Z = \int \rho(\boldsymbol{\xi}_0)\, d\boldsymbol{\xi}_0$. In contrast, when restrictions are placed on the trajectories, the path length is crucial, and the resulting restricted path ensembles become time-dependent [21]. As already mentioned in section 2.1, restrictions in phase space can be introduced by the use of characteristic functions (2.12). The shorthand notation $x_t = x(\boldsymbol{\xi}_t)$ is again used to refer to the value of the order parameter x at the phase space point $\boldsymbol{\xi}_t$ at time t. Examples relevant for the future development of this work are displayed in figure 2.1, and analytical expressions are given below.

One way of restricting the path ensemble is to place a condition on the initial phase space point. As above, the resulting path ensemble is indepen-

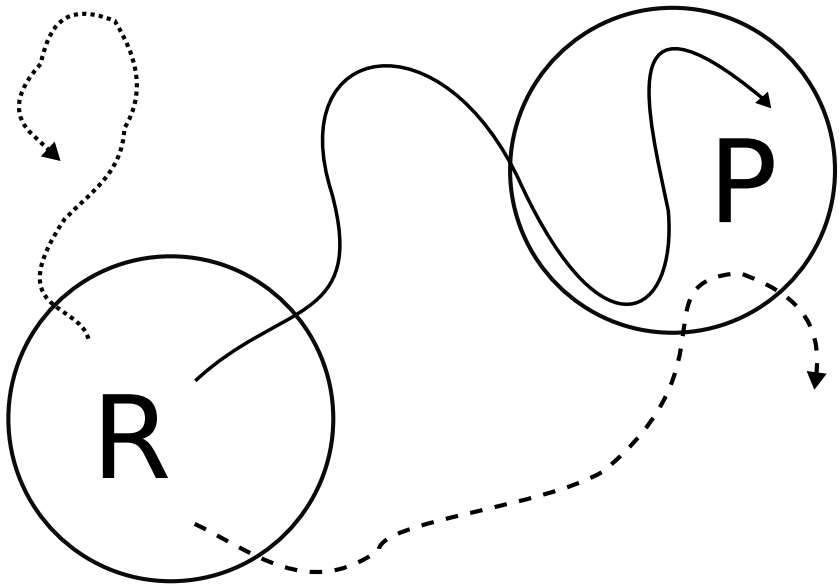

Figure 2.1: Representative schematic trajectories of length t are shown for the following path ensembles. The solid trajectory is a member of the path ensemble that requires paths to start in R and to end in P, whereas the dashed trajectory belongs to the path ensemble in which trajectories start in R and visit P within time t. The dotted trajectory represents the path ensemble that fixes the starting point in R. All three trajectories are members of the path ensemble Z_R (2.62), whereas only the solid path belongs to $Z_{RP}(t)$ (2.63). The path ensemble Z^*_{RP} (2.64) contains the dashed and the solid trajectories.

dent of path length because the time evolution is determined by the initial time slice. For instance, the ensemble of all paths required to start in the reactant state is given by [21, 73]

$$Z_R = \int \theta_R(x_0)\, \rho(\boldsymbol{\xi}_0)\, d\boldsymbol{\xi}_0. \tag{2.62}$$

A different type of restricted path ensemble is obtained when both ends of a trajectory are subject to conditions. As an example, *reactive* trajectories are required to start in the reactants at time $t = 0$ and end in the product region at time t, the length of the trajectory. The resulting *transition path*

ensemble reads [73]

$$Z_{RP}(t) = \int \theta_R(x_0)\, \theta_P(x_t)\, \rho(\boldsymbol{\xi}_0)\, d\boldsymbol{\xi}_0. \tag{2.63}$$

The final example of restricted path ensembles comprises trajectories that start in the reactants and visit the product state within the path length t. This ensemble is formally obtained by introducing the path functional $\Theta_P(x_0; \boldsymbol{\xi}(t))$ that depends on the entire trajectory. It is unity if the indicator function for the state P is unity for at least one phase space point along the trajectory and vanishes if the trajectory is not reactive. The path ensemble obeying these boundary conditions is [21]

$$Z^*_{RP}(t) = \int \theta_R(x_0)\, \Theta_P\left(x_0; \boldsymbol{\xi}(t)\right)\, \rho(\boldsymbol{\xi}_0)\, d\boldsymbol{\xi}_0. \tag{2.64}$$

As already mentioned, the preceding partition functions characterize the path ensembles introduced above. Furthermore, we define the path average of a dynamical variable $\mathcal{A}$ in the path ensemble $Z^*_{RP}(t)$ [164]:

$$\langle \mathcal{A}(t) \rangle^*_{RP} = \frac{\int \mathcal{A}(\boldsymbol{\xi}_0)\, \theta_R(x_0)\, \Theta_P\left(x_0; \boldsymbol{\xi}(t)\right)\, \rho(\boldsymbol{\xi}_0)\, d\boldsymbol{\xi}_0}{\int \theta_R(x_0)\, \Theta_P\left(x_0; \boldsymbol{\xi}(t)\right)\, \rho(\boldsymbol{\xi}_0)\, d\boldsymbol{\xi}_0}. \tag{2.65}$$

2.3.3 Classical rate constant expression

With the path ensembles introduced above we can express the classical rate constant (2.16) in terms of path ensembles [21, 75]:

$$\begin{aligned} k_+(t) &= \frac{\langle \theta_R(x_0) \dot{\theta}_P(x_t) \rangle}{\langle \theta_R \rangle} = \frac{\dot{Z}_{RP}(t)}{Z_R} \\ &= \frac{\int \theta_R(x_0)\, \dot{\theta}_P(x_t)\, \rho(\boldsymbol{\xi}_0)\, d\boldsymbol{\xi}_0}{\int \theta_R(x_0)\, \rho(\boldsymbol{\xi}_0)\, d\boldsymbol{\xi}_0} = \langle \dot{\theta}_P(x_t) \rangle_R. \end{aligned} \tag{2.66}$$

The last equality uses the path ensemble restricted to start in the reactant state Z_R as a new weight, namely $\rho_R(\boldsymbol{\xi}_0) = \frac{\theta_R(x_0)\, \rho(\boldsymbol{\xi}_0)}{\int \theta_R(x_0)\, \rho(\boldsymbol{\xi}_0)\, d\boldsymbol{\xi}_0}$. We note that this

expression for the rate constant is exact in the canonical ensemble if classical mechanics describes the dynamics of the system accurately. In practice, the rate constant is computed according to an equivalent, but computationally more convenient, expression [21, 164]:

$$\begin{aligned} k_+(t) &= \frac{\int \theta_R(x_0)\,\dot{\theta}_P(x_t)\,\rho(\boldsymbol{\xi}_0)\,d\boldsymbol{\xi}_0}{\int \theta_R(x_0)\,\rho(\boldsymbol{\xi}_0)\,d\boldsymbol{\xi}_0} \\ &= \frac{\int \theta_R(x_0)\,\dot{\theta}_P(x_t)\,\rho(\boldsymbol{\xi}_0)\,d\boldsymbol{\xi}_0}{\int \theta_R(x_0)\,\theta_P(x_{t'})\,\rho(\boldsymbol{\xi}_0)\,d\boldsymbol{\xi}_0} \times \frac{\int \theta_R(x_0)\,\theta_P(x_{t'})\,\rho(\boldsymbol{\xi}_0)\,d\boldsymbol{\xi}_0}{\int \theta_R(x_0)\,\rho(\boldsymbol{\xi}_0)\,d\boldsymbol{\xi}_0} \\ &= \frac{\langle \dot{\theta}_P(x_t)\rangle^*_{RP}}{\langle \theta_P(x_{t'})\rangle^*_{RP}} \times \frac{\langle \theta_R(x_0)\theta_P(x_{t'})\rangle}{\langle \theta_R\rangle}. \end{aligned} \tag{2.67}$$

Above, the first line is the definition of the classical rate constant in the transition path ensemble (2.66). The second line is obtained by multiplying by unity, thereby introducing a path ensemble that requires trajectories to start in the reactant state and to end in the product state at time $t^{'}$. To reach the third line, we insert the path functional $\Theta_P(x_0; \boldsymbol{\xi}(t))$ into the numerator and denominator of the first ratio on the right-hand side of the second line of equation (2.67). This operation leaves the integrals concerned unchanged because the path functional vanishes if the weight of the path is zero; otherwise, the path functional is unity and does not alter the path weight. We also normalize both the numerator and the denominator of that same first fraction of the second line of equation (2.67) by the path ensemble (2.64).

The advantage of equation (2.67) is the appearance of path averages of the form (2.65) for which reactive trajectories are required to visit the product state, but need not end there. In particular, reactive trajectories are not rejected if they end outside the product region. In contrast, the second fraction on the right-hand side of the last line of equation (2.67) requires trajectories to end in the product state. This second factor corresponds to a ratio of path partition functions $Z_{RP}(t^{'})/Z_R$, which is related to the reversible work of constraining the endpoints of trajectories to the product state provided that they started in the reactant state [21, 73, 164]. Standard free energy methods, such as umbrella sampling, can be used to compute this reversible work. This approach divides the entire phase space into windows of overlap-

ping order parameter ranges. A single transition path sampling simulation is then carried out to sample trajectories required to start in the reactant state and to end in a specific window. This is repeated for all windows to determine the probability of finding the end point of a path in a given order parameter range provided that it started in the reactants. The probability that a trajectory ends in the products is then obtained as an integral over the windows spanning the product region [21,73,164]. Because this computation of the reversible work involves several transition path sampling simulations, it is computationally demanding. As a result, the procedure becomes more efficient than that for computing the rate constant according to equation (2.66) if a path length $t^{'}$ shorter than t can be employed to compute the second factor of the last line of equation (2.67). In that case, the first ratio on the right-hand side of the last line of equation (2.67) is obtained from a single transition path sampling simulation with trajectories of length t and enables us to compute the rate constant for all times up to t. We shall only need to compute path averages of the form (2.65), such as the numerator and denominator of the first fraction on the right-hand side of the last line of equation (2.67).

It can be seen from equations (2.66) and (2.67) that the computation of the rate constant requires a derivative with respect to time. In this work the time derivative of a path average, such as that given by equation (2.65) or the one appearing in the last line of equation (2.66), is evaluated by means of two finite difference schemes. The first is the central finite difference scheme for a dynamical variable $\mathcal{A}$ [2],

$$\dot{\mathcal{A}} = \frac{d\mathcal{A}}{dt} \approx \frac{\mathcal{A}(t+\Delta t) - \mathcal{A}(t-\Delta t)}{2\Delta t}, \tag{2.68}$$

and the second is the forward finite difference scheme [2]:

$$\dot{\mathcal{A}} = \frac{d\mathcal{A}}{dt} \approx \frac{\mathcal{A}(t+\Delta t) - \mathcal{A}(t)}{\Delta t}. \tag{2.69}$$

Above, Δt denotes a small time interval between different realizations of the dynamical variable.

2.3.4 Activation energy expression

Following Dellago and Bolhuis [76], we now derive an expression for the activation energy. As pointed out in equation (2.9), the activation energy is obtained by measuring the rate constant as a function of temperature. This leads us to take the derivative of the logarithm of the rate constant given in equation (2.66) with respect to $\beta = (k_B T)^{-1}$ if the canonical probability function $\rho(\boldsymbol{\xi}_0) = \frac{e^{-\beta\mathcal{H}(\boldsymbol{\xi}_0)}}{\int e^{-\beta\mathcal{H}(\boldsymbol{\xi}_0)} d\boldsymbol{\xi}_0}$ is used. The activation energy thus reads [76]

$$
\begin{aligned}
E_a(t) &= -\frac{\partial}{\partial\beta}\left(ln\, k_+(t)\right) \\
&= -\frac{\partial}{\partial\beta}\left(ln\, \frac{\int \theta_R(x_0)\, \dot{\theta}_P(x_t)\, e^{-\beta\mathcal{H}(\boldsymbol{\xi}_0)}\, d\boldsymbol{\xi}_0}{\int \theta_R(x_0)\, e^{-\beta\mathcal{H}(\boldsymbol{\xi}_0)}\, d\boldsymbol{\xi}_0}\right) \\
&= -\frac{\frac{\partial}{\partial\beta}\int \theta_R(x_0)\, \dot{\theta}_P(x_t)\, e^{-\beta\mathcal{H}(\boldsymbol{\xi}_0)}\, d\boldsymbol{\xi}_0}{\int \theta_R(x_0)\, \dot{\theta}_P(x_t)\, e^{-\beta\mathcal{H}(\boldsymbol{\xi}_0)}\, d\boldsymbol{\xi}_0} + \frac{\frac{\partial}{\partial\beta}\int \theta_R(x_0)\, e^{-\beta\mathcal{H}(\boldsymbol{\xi}_0)}\, d\boldsymbol{\xi}_0}{\int \theta_R(x_0)\, e^{-\beta\mathcal{H}(\boldsymbol{\xi}_0)}\, d\boldsymbol{\xi}_0} \\
&= \frac{\int \theta_R(x_0)\, \dot{\theta}_P(x_t)\, \mathcal{H}(\boldsymbol{\xi}_0)\, e^{-\beta\mathcal{H}(\boldsymbol{\xi}_0)}\, d\boldsymbol{\xi}_0}{\int \theta_R(x_0)\, \dot{\theta}_P(x_t)\, e^{-\beta\mathcal{H}(\boldsymbol{\xi}_0)}\, d\boldsymbol{\xi}_0} - \frac{\int \theta_R(x_0)\, \mathcal{H}(\boldsymbol{\xi}_0)\, e^{-\beta\mathcal{H}(\boldsymbol{\xi}_0)}\, d\boldsymbol{\xi}_0}{\int \theta_R(x_0)\, e^{-\beta\mathcal{H}(\boldsymbol{\xi}_0)}\, d\boldsymbol{\xi}_0} \\
&= \frac{\int \theta_R(x_0)\, \Theta_P(x_0;\boldsymbol{\xi}(t))\, \dot{\theta}_P(x_t)\, \mathcal{H}(\boldsymbol{\xi}_0)\, e^{-\beta\mathcal{H}(\boldsymbol{\xi}_0)}\, d\boldsymbol{\xi}_0}{\int \theta_R(x_0)\, \Theta_P(x_0;\boldsymbol{\xi}(t))\, \dot{\theta}_P(x_t)\, e^{-\beta\mathcal{H}(\boldsymbol{\xi}_0)}\, d\boldsymbol{\xi}_0} - \langle\mathcal{H}(\boldsymbol{\xi}_0)\rangle_R \\
&= \frac{\langle\dot{\theta}_P(x_t)\, \mathcal{H}(\boldsymbol{\xi}_0)\rangle^*_{RP}}{\langle\dot{\theta}_P(x_t)\rangle^*_{RP}} - \langle\mathcal{H}(\boldsymbol{\xi}_0)\rangle_R. \qquad (2.70)
\end{aligned}
$$

Above, the first line defines the activation energy; the second line uses the expression for the classical rate constant in the transition path ensemble; the third line evaluates the derivative of the logarithm of a fraction; in the fourth line the derivative introduces the total energy at the initial phase space point. In going from the fourth to the fifth line, we add the path functional $\Theta_P(x_0;\boldsymbol{\xi}(t))$ to those integrands that contain the time derivative of the characteristic function $\theta_P(x_t)$. This does not alter the integral because $\Theta_P(x_0;\boldsymbol{\xi}(t))$ is less restrictive than $\theta_p(x_t)$; if the latter vanishes, the former does not contribute anything; if the latter is unity, the former equals one as well. We see that the integral remains unchanged in both cases. In going to the last line, we divide both the numerator and the denominator of the first term on the right-hand side by the partition function $Z^*_{RP}(t)$

to introduce averages over the transition path ensemble characterized by pathways starting in the reactant region and visiting the product state within the path length t.

Chapter 3

Methods

The present chapter outlines the methods used to evaluate the properties introduced in the previous chapter. First, we describe the standard techniques for treating classical atomistic systems: molecular dynamics and Monte Carlo simulations. In the present work molecular dynamics simulations are employed to compute equilibrium properties such as the average total energy of the system at a given temperature. We then discuss the Monte Carlo method because it provides a means for controlling the temperature in a molecular dynamics simulation. In addition, it is essential for the transition path sampling procedure, which combines molecular dynamics and Monte Carlo simulations to generate ensembles of trajectories from which the activation energy is obtained. Later, the activation energy will be compared to the activation free energy. Hence, we close this chapter with a discussion on biased molecular dynamics simulations and umbrella integration, which are employed to evaluate free energy differences and free energy profiles.

3.1 Molecular dynamics simulations

Our outline of the molecular dynamics technique follows reference [106]. Molecular dynamics simulations are a means to obtain static and dynamic equilibrium properties of classical molecular systems [163]. The idea is to follow the time evolution of a system and to extract observable quantities

in analogy to a physical experiment [106]. The method is based on classical mechanics and, through the ergodic hypothesis, on classical statistical mechanics. In particular, it is assumed that time averages correspond to ensemble averages for long observation times (see appendix D). Furthermore, we assume that the time evolution of a given system, namely its (simulated) trajectory in phase space, is close to the physical trajectory of that system. In other words, the outcome of the computer experiment is believed to be representative of the physical system investigated [106].

In general, a molecular dynamics simulation requires three main ingredients [163]. First, a model for the interactions between the particles in the system has to be chosen, which we shall do in the next chapter. Second, an ensemble is selected that determines the thermodynamic control parameters. Third, we need to integrate the classical equations of motion to obtain a molecular dynamics trajectory from which ensemble averages are computed.

Because the equations of motion depend on the ensemble, we shall present the integration of the equations of motion in the microcanonical and canonical ensembles. We use molecular dynamics simulations in the canonical ensemble to obtain reference equilibrium properties in the stable states. In contrast, pathways in the microcanonical ensemble are used in the transition path sampling method.

Because the Hamiltonian formulation of classical mechanics provides both a link to classical statistical mechanics and insight into desirable features of an integration algorithm [106], we shall discuss it below, following reference [165]. We start with the microcanonical ensemble because it is the natural ensemble for a system's time evolution. Subsequently, we turn to the canonical ensemble.

3.1.1 Hamilton's equations of motion and canonical variables

Before we discuss the Hamiltonian form of the equations of motion, we introduce the Hamiltonian function. To this end, we restrict ourselves to conservative systems. In classical mechanics a conservative system is characterized

by forces that can be obtained from the gradient of a scalar potential energy function V with respect to particle positions [165]. Furthermore, we shall only consider Hamiltonians that do not explicitly depend on time t. In that case, the Hamiltonian of a conservative N-particle system corresponds to the total energy of that system [165]. In Cartesian coordinates it reads [106, 165]

$$\mathcal{H}(\boldsymbol{r}_C, \boldsymbol{p}_C; t) = \mathcal{H}(\boldsymbol{r}_C(t), \boldsymbol{p}_C(t)) = \sum_{j=1}^{\mathcal{N}_f} \frac{p_{C,j}(t)^2}{2m_j} + V(\boldsymbol{r}_C(t)). \tag{3.1}$$

Above, m_j denotes the mass associated with the degree of freedom j. The number of degrees of freedom is $\mathcal{N}_f$, and the set of positions of all particles is denoted by $\boldsymbol{r}_C = \{r_{C,1}, r_{C,2}, \ldots, r_{C,\mathcal{N}_f}\}$. Likewise, we abbreviate the variables for all momenta by $\boldsymbol{p}_C = \{p_{C,1}, p_{C,2}, \ldots, p_{C,\mathcal{N}_f}\}$. As mentioned above, the Hamiltonian depends on time only implicitly via the time dependence of the positions and momenta. This implicit time dependence is indicated by the notation $\mathcal{H}(\boldsymbol{r}_C, \boldsymbol{p}_C; t)$, in which the semicolon separates explicit from implicit arguments of the Hamiltonian function.

Having introduced the Hamiltonian function above, we now turn to the Hamiltonian equations of motion in Cartesian coordinates [165]:

$$\frac{dr_{C,j}}{dt} = \dot{r}_{C,j} = \frac{\partial \mathcal{H}}{\partial p_{C,j}}; \tag{3.2a}$$

$$\frac{dp_{C,j}}{dt} = \dot{p}_{C,j} = -\frac{\partial \mathcal{H}}{\partial r_{C,j}}. \tag{3.2b}$$

The equations of motion (3.2) are derived from the Hamiltonian function (3.1), and Cartesian coordinates thus constitute a special case of canonical variables. In particular, *canonical phase space variables* satisfy the equations of motion in the Hamiltonian form (3.3) [165]:

$$\frac{dq_j}{dt} = \dot{q}_j = \frac{\partial \mathcal{H}}{\partial p_j}; \tag{3.3a}$$

$$\frac{dp_j}{dt} = \dot{p}_j = -\frac{\partial \mathcal{H}}{\partial q_j}. \tag{3.3b}$$

We shall denote a set of canonical phase space variables consisting of gen-

eralized coordinates q_j and their conjugate momenta p_j by $\boldsymbol{\xi} = \{\boldsymbol{q}, \boldsymbol{p}\} = \{q_1, q_2, \ldots, q_{\mathcal{N}_f}, p_1, \ldots, p_{\mathcal{N}_f}\}$.

In the Hamiltonian formulation of classical mechanics the canonical variables are independent of each other. Consequently, the terms canonical coordinates and conjugate momenta for the variables q_j and p_j might be misleading. In particular, the canonical coordinates need not refer to positions, and the conjugate momenta need not be mechanical momenta. The requirements for a pair of canonical variables are that their product has dimension energy times time and that they fulfill the canonical equations of motion (3.3). The latter condition implies that the functional dependence of the Hamiltonian on the canonical variables is such that Hamilton's equations of motion can be obtained from it [165].

3.1.2 Canonical transformations and Poisson brackets

We have seen above that the Hamiltonian function (3.1) leads to equations of motion of the form (3.3). As already mentioned, Cartesian coordinates $\{\boldsymbol{r}_C, \boldsymbol{p}_C\}$ are one example of canonical variables $\{\boldsymbol{q}, \boldsymbol{p}\}$. Now, the physical state of a system does not depend on the mathematical representation used to describe it. Specifically, the value of the Hamiltonian will not change if it is expressed by a different set of variables $\{\boldsymbol{\mathcal{Q}}, \boldsymbol{\mathcal{P}}\}$. However, the functional dependence may alter, and the equations of motion might not be derivable from the Hamiltonian any longer. In contrast, a change of variables is called a canonical transformation if the new equations of motion are also in the canonical form of equation (3.3). If the transformation equations do not involve time explicitly, we have a restricted canonical transformation [165]:

$$\mathcal{Q}_k = \mathcal{Q}_k(\boldsymbol{q}, \boldsymbol{p}; t); \tag{3.4a}$$

$$\mathcal{P}_k = \mathcal{P}_k(\boldsymbol{q}, \boldsymbol{p}; t). \tag{3.4b}$$

For restricted canonical transformations the Hamiltonian still represents the total energy of the system after the new variables have been introduced.

In addition, the equations of motion are in the Hamiltonian form [165]:

$$\frac{d\mathcal{Q}_j}{dt} = \dot{\mathcal{Q}}_j = \frac{\partial \mathcal{H}}{\partial \mathcal{P}_j}; \tag{3.5a}$$

$$\frac{d\mathcal{P}_j}{dt} = \dot{\mathcal{P}}_j = -\frac{\partial \mathcal{H}}{\partial \mathcal{Q}_j}. \tag{3.5b}$$

Canonical transformations thus do not alter the form of the Hamiltonian equations of motion. In the following, we shall introduce Poisson brackets and the symplectic condition to describe canonical transformations in a mathematically more concise way. We start with the Poisson brackets below.

Let us consider two functions $\mathcal{A}$ and $\mathcal{B}$ and a set of canonical variables $\{\boldsymbol{q}, \boldsymbol{p}\}$. Then, the Poisson bracket of $\mathcal{A}$ and $\mathcal{B}$ with respect to the canonical variables $\{\boldsymbol{q}, \boldsymbol{p}\}$ is given by [165]

$$\{\mathcal{A}, \mathcal{B}\}_{\boldsymbol{q},\boldsymbol{p}} = \sum_j \left(\frac{\partial \mathcal{A}}{\partial q_j} \frac{\partial \mathcal{B}}{\partial p_j} - \frac{\partial \mathcal{A}}{\partial p_j} \frac{\partial \mathcal{B}}{\partial q_j} \right). \tag{3.6}$$

If we use the ordered set of canonical phase space variables $\boldsymbol{\xi} = \{\boldsymbol{q}, \boldsymbol{p}\} = \{q_1, q_2, \ldots, q_{\mathcal{N}_f}, p_1, \ldots, p_{\mathcal{N}_f}\}$ introduced earlier,[13]

$$\xi_j = q_j; \qquad \xi_{j+\mathcal{N}_f} = p_j; \qquad j \leq \mathcal{N}_f, \tag{3.7}$$

we can write equation (3.6) in matrix form [165]:

$$\{\mathcal{A}, \mathcal{B}\}_{\boldsymbol{\xi}} = \frac{\widetilde{\partial \mathcal{A}}}{\partial \boldsymbol{\xi}} J \frac{\partial \mathcal{B}}{\partial \boldsymbol{\xi}}. \tag{3.8}$$

In equation (3.8) J designates the $2\mathcal{N}_f \times 2\mathcal{N}_f$ antisymmetric matrix [2] whose building blocks are unit and zero matrices of size $\mathcal{N}_f \times \mathcal{N}_f$. The constituting building blocks are arranged as in equation (3.9) [106, 165]:

$$J = \begin{pmatrix} 0 & 1 \\ -1 & 0 \end{pmatrix}. \tag{3.9}$$

[13] Throughout this document we denote a set by braces $\{\cdots\}$. In contrast, a Poisson bracket always carries the relevant set of phase space variables as a subscript, as in $\{\cdots\}_{\boldsymbol{\xi}}$.

Furthermore, the matrix $\frac{\partial \mathcal{B}}{\partial \boldsymbol{\xi}}$ of size $2\mathcal{N}_f \times 1$ contains the partial derivatives of $\mathcal{B}$ with respect to all canonical variables [165]:

$$\left(\frac{\partial \mathcal{B}}{\partial \boldsymbol{\xi}}\right)_j = \frac{\partial \mathcal{B}}{\partial q_j}; \qquad \left(\frac{\partial \mathcal{B}}{\partial \boldsymbol{\xi}}\right)_{j+\mathcal{N}_f} = \frac{\partial \mathcal{B}}{\partial p_j}; \qquad j \leq \mathcal{N}_f. \tag{3.10}$$

The transpose of a similar matrix of size $1 \times 2\mathcal{N}_f$ is denoted by $\widetilde{\frac{\partial \mathcal{A}}{\partial \boldsymbol{\xi}}}$. Using this symplectic notation [106, 165], we can write the canonical equations of motion as

$$\dot{\boldsymbol{\xi}} = J\frac{\partial \mathcal{H}}{\partial \boldsymbol{\xi}}. \tag{3.11}$$

Equivalently, substituting $\boldsymbol{\xi}$ for $\mathcal{A}$ and $\mathcal{H}$ for $\mathcal{B}$ into equation (3.8), we obtain Hamilton's equation of motion in terms of Poisson brackets [165]:

$$\begin{aligned}
\dot{\boldsymbol{\xi}} &= J\frac{\partial \mathcal{H}}{\partial \boldsymbol{\xi}} = \{\boldsymbol{\xi}, \mathcal{H}\}_{\boldsymbol{\xi}} \\
&= \sum_{j=1}^{j=\mathcal{N}_f} \sum_{k=1}^{k=2\mathcal{N}_f} \left(\frac{\partial \xi_k}{\partial q_j}\frac{\partial \mathcal{H}}{\partial p_j} - \frac{\partial \xi_k}{\partial p_j}\frac{\partial \mathcal{H}}{\partial q_j}\right) \\
&= \sum_{j=1}^{j=\mathcal{N}_f} \sum_{k=1}^{k=2\mathcal{N}_f} \left(\frac{\partial \xi_k}{\partial \xi_j}\frac{\partial \mathcal{H}}{\partial \xi_{j+\mathcal{N}_f}} - \frac{\partial \xi_k}{\partial \xi_{j+\mathcal{N}_f}}\frac{\partial \mathcal{H}}{\partial \xi_j}\right).
\end{aligned} \tag{3.12}$$

Having introduced the Poisson bracket above, we return to our discussion of canonical transformations. First, we consider the special case for which the functions $\mathcal{A}$ and $\mathcal{B}$ in equation (3.8) are replaced by the set of canonical variables $\boldsymbol{\xi}$. This yields the fundamental Poisson bracket [165]:

$$\{\boldsymbol{\xi}, \boldsymbol{\xi}\}_{\boldsymbol{\xi}} = \widetilde{\frac{\partial \boldsymbol{\xi}}{\partial \boldsymbol{\xi}}} J \frac{\partial \boldsymbol{\xi}}{\partial \boldsymbol{\xi}} = J. \tag{3.13}$$

Next, let us examine a set of new variables $\boldsymbol{\upsilon}$,

$$\upsilon_j = \mathcal{Q}_j; \qquad \upsilon_{j+\mathcal{N}_f} = \mathcal{P}_j; \qquad j \leq \mathcal{N}_f, \tag{3.14}$$

whose elements are obtained from the transformation given in equation (3.4). If the new variables $\boldsymbol{\upsilon}$ are introduced as arguments of the Poisson bracket

with respect to the old canonical variables, we obtain [165]

$$\{\boldsymbol{\upsilon}, \boldsymbol{\upsilon}\}_{\boldsymbol{\xi}} = \widetilde{\frac{\partial \boldsymbol{\upsilon}}{\partial \boldsymbol{\xi}}} J \frac{\partial \boldsymbol{\upsilon}}{\partial \boldsymbol{\xi}} = \widetilde{\boldsymbol{\mathcal{J}}} J \boldsymbol{\mathcal{J}}. \tag{3.15}$$

In going to the last equation, we have introduced the Jacobian matrix $\boldsymbol{\mathcal{J}}$ whose elements are the partial derivatives associated with the variable transformation from $\boldsymbol{\xi}$ to $\boldsymbol{\upsilon}$ [165]:

$$\mathcal{J}_{jk} = \frac{\partial \upsilon_j}{\partial \xi_k}. \tag{3.16}$$

If the transformation is canonical, the set $\boldsymbol{\upsilon}$ constitutes another set of canonical variables. In that case, we have [165]

$$\{\boldsymbol{\upsilon}, \boldsymbol{\upsilon}\}_{\boldsymbol{\xi}} = \widetilde{\boldsymbol{\mathcal{J}}} J \boldsymbol{\mathcal{J}} = J = \{\boldsymbol{\upsilon}, \boldsymbol{\upsilon}\}_{\boldsymbol{\upsilon}}. \tag{3.17}$$

In words, the fundamental Poisson bracket of the canonical variables $\boldsymbol{\upsilon}$ is the same with respect to any set of canonical variables and thus invariant under canonical transformation [165]. As can be shown [165], any Poisson bracket is a canonical invariant:

$$\{\mathcal{A}, \mathcal{B}\}_{\boldsymbol{\xi}} = \widetilde{\frac{\partial \mathcal{A}}{\partial \boldsymbol{\xi}}} J \frac{\partial \mathcal{B}}{\partial \boldsymbol{\xi}} = \widetilde{\frac{\partial \mathcal{A}}{\partial \boldsymbol{\upsilon}}} J \frac{\partial \mathcal{B}}{\partial \boldsymbol{\upsilon}} = \{\mathcal{A}, \mathcal{B}\}_{\boldsymbol{\upsilon}}. \tag{3.18}$$

From equation (3.17) we see that canonical transformations satisfy the symplectic condition [106, 165]:

$$\widetilde{\boldsymbol{\mathcal{J}}} J \boldsymbol{\mathcal{J}} = J = \boldsymbol{\mathcal{J}} J \widetilde{\boldsymbol{\mathcal{J}}}. \tag{3.19}$$

Hence, a transformation is canonical if it leaves Poisson brackets unaltered and satisfies the symplectic condition (3.19). The symplectic condition and canonical invariance of Poisson brackets are completely equivalent to stating that Hamilton's equation of motion keep the same form under canonical transformation [165].

3.1.3 Time evolution and Liouville's theorem

Until now, we have considered canonical transformations as changing from one set of canonical variables to another set of canonical variables. Instead, we can also view a canonical transformation as bringing a set of canonical variables from time t to time $t + \Delta t$ [165]. In that case, the canonical variables at time t correspond to the initial set, and the canonical variables at time $t + \Delta t$ correspond to the new set of canonical variables. Dividing the time interval Δt into infinitesimal time intervals dt, we see that the overall transformation will be canonical if the transformation from t to $t + dt$ is canonical. This situation is similar to viewing a rotation in space as a sequence of infinitesimal rotations. Hence, such transformations are called infinitesimal canonical transformations [165]. In the case of interest here, time is the continuous parameter for an infinitesimal canonical transformation. In the following, we consider the transformation from $\boldsymbol{\xi}(t)$ to the new set of canonical variables $\boldsymbol{\upsilon}$:

$$\boldsymbol{\upsilon} = \boldsymbol{\xi}(t + dt) = \boldsymbol{\xi}(t) + \delta\boldsymbol{\xi}. \tag{3.20}$$

To proceed, we employ another way of describing canonical transformations, namely in terms of generating functions [165]. As shown in reference [165], an infinitesimal change in canonical variables can be expressed in terms of the generating function $\mathcal{H}$ and the infinitesimal time difference dt as

$$\delta\boldsymbol{\xi} = dt\, J\, \frac{\partial \mathcal{H}}{\partial \boldsymbol{\xi}} = dt\, \{\boldsymbol{\xi}, \mathcal{H}\}_{\boldsymbol{\xi}} = dt\, \dot{\boldsymbol{\xi}} = d\boldsymbol{\xi}. \tag{3.21}$$

As a finite time evolution is composed of a sequence of infinitesimal canonical transformations, the values of a set of canonical variables at a given time t result from their values at an earlier time t_0 via a canonical transformation that is continuous in time. We thus see that the Hamiltonian $\mathcal{H}$ generates the motion of the system [106, 165].

As a consequence, the time evolution of any dynamical variable $\mathcal{A}$ be-

comes [165]

$$\begin{aligned}\frac{d\mathcal{A}}{dt} &= \frac{\partial \mathcal{A}}{\partial t} + \sum_{j=1}^{\mathcal{N}_f}\left(\frac{\partial \mathcal{A}}{\partial q_j}\frac{\partial q_j}{\partial t} + \frac{\partial \mathcal{A}}{\partial p_j}\frac{\partial p_j}{\partial t}\right)\\ &= \frac{\partial \mathcal{A}}{\partial t} + \sum_{j=1}^{\mathcal{N}_f}\left(\frac{\partial \mathcal{A}}{\partial q_j}\frac{\partial \mathcal{H}}{\partial p_j} - \frac{\partial \mathcal{A}}{\partial p_j}\frac{\partial \mathcal{H}}{\partial q_j}\right)\\ &= \frac{\partial \mathcal{A}}{\partial t} + \{\mathcal{A}, \mathcal{H}\}_{\boldsymbol{\xi}}. \end{aligned} \tag{3.22}$$

Hence, the Poisson bracket of the dynamical variable under consideration with the (time-independent) Hamiltonian determines the implicit time-dependence of that dynamical variable through its parametric dependence on time.

As a special case, the time evolution of the total energy of a system with time-independent Hamiltonian vanishes [165]:

$$\begin{aligned}\frac{d\mathcal{H}}{dt} &= \frac{\partial \mathcal{H}}{\partial t} + \{\mathcal{H}, \mathcal{H}\}_{\boldsymbol{\xi}}\\ &= \frac{\partial \mathcal{H}}{\partial t} = 0. \end{aligned} \tag{3.23}$$

Another important property of canonical transformations is the invariance of a volume element in phase space. More precisely, the magnitude of the volume element is preserved [165], whereas the shape of the volume element under consideration may vary [33]. Let us denote the volume element of the new set of canonical variables $d\boldsymbol{\upsilon}$ and that of the old canonical variables $d\boldsymbol{\xi}$. Then, the absolute value of the determinant of the Jacobian matrix $|\mathcal{J}|$ (see equation (3.16)) relates the volume element of *any* new set of variables to that of the old set by [2]

$$d\boldsymbol{\upsilon} = |\mathcal{J}(\boldsymbol{\upsilon}; \boldsymbol{\xi})| d\boldsymbol{\xi}. \tag{3.24}$$

Now, for canonical transformations, the symplectic condition (3.19) holds. Given that the determinant of a matrix product equals the product of the determinants of the individual matrices [2], the determinants of both sides

of equation (3.19) are related by [106, 165]

$$|\boldsymbol{\mathcal{J}}|\,|J|\,|\widetilde{\boldsymbol{\mathcal{J}}}| = |J| = |\boldsymbol{\mathcal{J}}|^2\,|J|; \tag{3.25a}$$

$$\mathcal{J}(\boldsymbol{\upsilon};\boldsymbol{\xi})\,|J|\,\widetilde{\mathcal{J}}(\boldsymbol{\xi};\boldsymbol{\upsilon}) = |J| = \mathcal{J}^2\,|J|. \tag{3.25b}$$

The last equality follows because the determinant of the transpose $\widetilde{\boldsymbol{\mathcal{J}}}$ equals the determinant of the original Jacobian matrix $\boldsymbol{\mathcal{J}}$ [2]. We see from equation (3.25) that the absolute value of the determinant of the Jacobian matrix, which enters equation (3.24), is unity for canonical transformations. As a result, the magnitude of a volume element in phase space is invariant under canonical transformation [165].

We are now in a position to discuss the time dependence of the probability density in phase space: Liouville's theorem [33, 113, 165]. Liouville's theorem states that the probability density around any given point in phase space is constant in time. To see this, we note that trajectories in phase space are completely determined by their initial conditions [165].

Let us consider a small volume element in phase space whose boundary is composed of phase space points. As the volume element evolves in phase space, so do the phase space points constituting the boundary. Following reference [165], we shall show that the number of phase space points in the volume considered does not change. In other words, phase space points cannot enter or leave the volume element specified. Any phase space point entering or leaving the volume element would have to cross the boundary. In that case, the phase space point would coincide with one at the boundary, and its time evolution would be the same as that of the phase space point at the boundary. Hence, the phase space point would stay on the boundary and could neither enter nor leave the volume element considered. As a consequence, the number of phase space points $d\mathcal{N}_\rho$ within the volume element remains constant. Because we know from the symplectic condition for canonical transformations (see equation (3.19)) that the volume element $d\mathcal{V}$ in phase space does not evolve in time, it follows that the phase space point

density ρ is also a canonical invariant [33, 113, 165]:

$$\frac{d\rho}{dt} = \frac{d}{dt}\left(\frac{d\mathcal{N}_\rho}{d\mathcal{V}}\right) = 0. \tag{3.26}$$

Equivalently, we can consider the phase space density ρ as a dynamical variable and use equation (3.22) to obtain [113, 165]

$$\frac{d\rho}{dt} = \frac{\partial\rho}{\partial t} + \{\rho, \mathcal{H}\}_{\boldsymbol{\xi}}. \tag{3.27}$$

Using equation (3.27) above, we can express Liouville's theorem as [165]

$$\frac{\partial\rho}{\partial t} = -\{\rho, \mathcal{H}\}_{\boldsymbol{\xi}}. \tag{3.28}$$

In words, the explicit time dependence of the phase space density is governed by the negative Poisson bracket of the probability density with the Hamiltonian. As a result, the time evolution arising from the implicit time dependence cancels that stemming from the explicit one.

In thermodynamic equilibrium, the explicit time dependence of the phase space density must vanish because the number of phase space points representing a given state of the system is constant in time. Hence, we can write the condition for thermodynamic equilibrium using equation (3.28) as [165]:

$$\{\rho, \mathcal{H}\}_{\boldsymbol{\xi}} = 0. \tag{3.29}$$

Furthermore, any constant of the motion that does not explicitly depend on time has a vanishing Poisson bracket with the Hamiltonian [165]. Consequently, any function of such constants of the motion can be chosen as phase space density to guarantee that the system is in equilibrium [165]. For conservative systems considered here any function ρ of the Hamiltonian obeys the equilibrium condition (3.29) [165]. In particular, the microcanonical and canonical probability densities are examples of equilibrium phase space densities.

3.1.4 Molecular dynamics in the microcanonical ensemble

As we have seen in the previous section, the Hamiltonian is the generator of the system's motion. Equivalently, integrating Hamilton's canonical equations of motion provides a means of obtaining the system's trajectory in phase space. Consequently, the time evolution of the system would be known if the initial conditions could be determined [33, 165].

In practice, numerical integration of the equations of motion requires that time is discretized, which leads to inaccuracies [163]. However, it is desirable to employ an algorithm that satisfies the symplectic condition [106]; in other words, the integration algorithm would be correct, in principle, if the integration time step could be made arbitrarily small.

One way to approach this challenge is to recognize that the time evolution of any dynamical variable that does not depend on time explicitly is given by the Poisson bracket of that property with the Hamiltonian, as discussed in equation (3.22) above. Because the underlying canonical transformation obeys the symplectic condition, we can construct an algorithm that is symplectic [106]. This approach is also known as the Liouville formulation for symplectic integrators [106].

Given a not explicitly time-dependent function $\mathcal{A}$ in terms of a set of canonical phase space variables $\boldsymbol{\xi} = \{q_1, \ldots, p_{\mathcal{N}_f}\}$, its time evolution can be expressed as [106, 163, 165]

$$\frac{d\mathcal{A}}{dt} = \dot{\mathcal{A}} = \{\mathcal{A}, \mathcal{H}\}_{\boldsymbol{\xi}} = \imath\mathcal{L}\mathcal{A}. \tag{3.30}$$

Above, we have defined the Liouville operator $\mathcal{L}$ [106, 113, 163]:

$$\imath\mathcal{L} = \{\cdots, \mathcal{H}\}_{\boldsymbol{\xi}} = \sum_j \left(\frac{\partial \mathcal{H}}{\partial p_j} \frac{\partial}{\partial q_j} - \frac{\partial \mathcal{H}}{\partial q_j} \frac{\partial}{\partial p_j} \right). \tag{3.31}$$

We can formally integrate equation (3.30) to obtain [106, 113, 163]

$$\mathcal{A}(t) = e^{\imath\mathcal{L}t}\mathcal{A}(0). \tag{3.32}$$

If the canonical variables above are identified as Cartesian coordinates and mechanical momenta, the Liouville operator contains operators that do not commute. However, to construct a discrete timestep integrator, we can split the Liouville operator into two parts $\mathcal{L} = \mathcal{L}_1 + \mathcal{L}_2$ and use the Trotter expansion [106, 163]:

$$\begin{aligned} e^{\imath\mathcal{L}t} &= e^{\imath(\mathcal{L}_1+\mathcal{L}_2)t} \\ &= \lim_{\mathcal{N}_t\to\infty} \left(e^{\frac{\imath\mathcal{L}_1 t}{2\mathcal{N}_t}} e^{\frac{\imath\mathcal{L}_2 t}{\mathcal{N}_t}} e^{\frac{\imath\mathcal{L}_1 t}{2\mathcal{N}_t}} \right)^{\mathcal{N}_t}. \end{aligned} \tag{3.33}$$

In practice, the simulation time t is split into a finite number $\mathcal{N}_t$ of timesteps of length $\delta t = t/\mathcal{N}_t$. Hence, the effect of propagating the system for one timestep is [106, 163]

$$\mathcal{A}(\delta t) = e^{\imath\mathcal{L}\delta t}\mathcal{A}(0) \approx e^{\imath\mathcal{L}_1\delta t/2} e^{\imath\mathcal{L}_2\delta t} e^{\imath\mathcal{L}_1\delta t/2}. \tag{3.34}$$

In particular, we choose the two parts of the Liouville operator as $\imath\mathcal{L}_2 = \sum_j \dot{r}_{C,j}\frac{\partial}{\partial r_{C,j}}$, only depending on position variables, and as $\imath\mathcal{L}_1 = \sum_j \dot{p}_{C,j}\frac{\partial}{\partial p_{C,j}}$, only depending on momentum variables. To proceed, we consider the effect of the operator $e^{\alpha\frac{d}{dy}}$ on any function $f(y)$ [163]:

$$\begin{aligned} e^{\alpha\frac{d}{dy}} f(y) &= \sum_{j=0}^{\infty} \frac{\alpha^j}{j!} \frac{d^{(j)}}{dy^j} f(y) \\ &= \sum_{j=0}^{\infty} \frac{\alpha^j}{j!} f^{(j)}(y) \\ &= f(y+\alpha). \end{aligned} \tag{3.35}$$

Applying the operator $e^{\alpha\frac{d}{dy}}$ to a function $f(y)$ corresponds to shifting the argument of f by α, which is independent of y [106, 163]. For the special choice for $\mathcal{L}_1$ and $\mathcal{L}_2$ above the effect of one timestep is to first shift the momenta by half a timestep, then to shift the positions by one timestep, and

again, to shift the momenta for half a timestep [106]:

$$
\begin{aligned}
&e^{\imath\mathcal{L}_1\delta t/2}\mathcal{A}\left(\boldsymbol{r}_C(t),\boldsymbol{p}_C(t)\right)\\
&\qquad=\mathcal{A}\left(\boldsymbol{r}_C(t),\boldsymbol{p}_C(t+\delta t/2)\right)\\
&\qquad=\mathcal{A}\left(\boldsymbol{r}_C(t),\boldsymbol{p}_C(t)+\dot{\boldsymbol{p}}_C(t)\delta t/2\right) \qquad (3.36)\\
&e^{\imath\mathcal{L}_2\delta t}\mathcal{A}\left(\boldsymbol{r}_C(t),\boldsymbol{p}_C(t+\delta t/2)\right)\\
&\qquad=\mathcal{A}\left(\boldsymbol{r}_C(t+\delta t),\boldsymbol{p}(t+\delta t/2)\right)\\
&\qquad=\mathcal{A}\left(\boldsymbol{r}_C(t)+\dot{\boldsymbol{r}}_C(t+\delta t/2)\delta t,\boldsymbol{p}_C(t)+\dot{\boldsymbol{p}}_C(t)\delta t/2\right) \qquad (3.37)\\
&e^{\imath\mathcal{L}_1\delta t/2}\mathcal{A}\left(\boldsymbol{r}_C(t+\delta t),\boldsymbol{p}_C(t+\delta t/2)\right)\\
&\qquad=\mathcal{A}\left(\boldsymbol{r}_C(t+\delta t),\boldsymbol{p}_C(t+\delta t)\right)\\
&\qquad=\mathcal{A}\left(\boldsymbol{r}_C(t)+\dot{\boldsymbol{r}}_C(t+\delta t/2)\delta t,\boldsymbol{p}_C(t)+\dot{\boldsymbol{p}}_C(t)\delta t/2+\dot{\boldsymbol{p}}_C(t+\delta t)\delta t/2\right)\\
&\qquad\qquad (3.38)
\end{aligned}
$$

We see that the overall effect of applying the Liouville operator on positions and velocities corresponds to that of employing the Verlet algorithm in the velocity form [106, 163, 166, 167]:

$$r_{C,j}(t+\delta t)=r_{C,j}(t)+\frac{p_{C,j}(t)}{m_j}\delta t+\frac{\dot{p}_{C,j}(t)}{m_j}\frac{(\delta t)^2}{2}; \qquad (3.39)$$

$$p_{C,j}(t+\delta t)=p_{C,j}(t)+\frac{\dot{p}_{C,j}(t+\delta t)+\dot{p}_{C,j}(t)}{2\,m_j}\delta t. \qquad (3.40)$$

3.1.5 Molecular dynamics with constraints

So far, we have considered the time evolution of an isolated system, and we have seen how the equations of motion can be integrated by means of the velocity Verlet algorithm in the previous section. Regarding the molecular dynamics technique we shall discuss two further situations of interest. On the one hand, we shall place the system in contact with a heat bath in the next section; the resulting system then serves to describe the canonical ensemble. On the other hand, we shall treat constraints and how to incorporate them into simulations in this section.

Constraints are conditions that limit the motion of the system under consideration [165]. A constraint could arise from the vessel in which a chemical reaction takes place. In that case, the motion of the particles is restricted to the volume inside the vessel. The limited motion is enforced by forces of constraint, which are generally not explicitly known. What is known about the forces of constraint is the effect they have on the motion of the system [165].

In the realm of molecular simulations constraints are often introduced for practical purposes. In particular, the timestep used in an integration algorithm should be a small fraction of the fastest motion or shortest relaxation time [106]. Because intramolecular vibrations are typically much faster than the remaining (translational and rotational) motions of the system, they are usually decoupled from the slower motions and can be replaced by rigid bonds [168]. It then becomes possible to employ a larger timestep than if the fast internal degrees of freedom were not frozen [106]. In that case, the effect of the constraints is to keep the bond lengths constant.

In the following we shall discuss how to incorporate constraints combined with the velocity Verlet algorithm [167, 169]. In doing so we focus on holonomic constraints. Holonomic constraints σ_c introduce a relation between the particle positions $\boldsymbol{r}_C = \{\boldsymbol{r}_{C,1}, \ldots, \boldsymbol{r}_{C,N}\} = \{r_{C,1}, \ldots, r_{C,\mathcal{N}_f}\}$ and possibly time and can be expressed as in equation (3.41) [165]:

$$\sigma_c(\boldsymbol{r}_C, t) = 0. \tag{3.41}$$

Imposing holonomic constraints leads two difficulties. First, the conditions of constraint result in a functional relationship between the physical degrees of freedom. Hence, the variables become coupled and cannot be varied independently any more [2, 113, 165]. Second, as mentioned above, the forces of constraint are typically unknown. Yet, their determination is required to solve the equations of motion for the system of interest [106, 165].

To proceed, we introduce Lagrange's equations of motion, which are convenient for the treatment of constraints. As in the case of Hamilton's equations of motion in section 3.1.1, we focus on conservative systems. In that

case (and for certain more general cases), the Lagrangian $\mathcal{L}_u$ of the unconstrained system can be expressed as [165]

$$\mathcal{L}_u(\boldsymbol{r}_C, \dot{\boldsymbol{r}}_C, t) = \sum_{j=1}^{j=\mathcal{N}_f} \frac{m_j \left(\dot{r}_{C,j}(t)\right)^2}{2} - V(\boldsymbol{r}_C(t)). \tag{3.42}$$

By means of the calculus of variations Lagrange's equations of motion can be derived from a variational principle: Hamilton's principle [165, 170]. Hamilton's principle states that the integral $\mathbb{I}$ of the Lagrangian along a trajectory from an initial time t_i to a final time t_f with fixed endpoints is an extremum [165]:

$$\mathbb{I} = \int_{t=t_i}^{t=t_f} \mathcal{L}_u(\boldsymbol{r}_C, \dot{\boldsymbol{r}}_C, t)\, dt. \tag{3.43}$$

To derive Lagrange's equations of motion, we consider a family of one-parameter functions $\overline{r}_{C,j}(t, \alpha)$ and seek the set of test functions that extremizes the integral [170]

$$\mathbb{I}(\alpha) = \int_{t=t_i}^{t=t_f} \mathcal{L}_u(\overline{\boldsymbol{r}}_C(t, \alpha), \dot{\overline{\boldsymbol{r}}}_C(t, \alpha), t)\, dt. \tag{3.44}$$

We request (i) that the test functions $\overline{r}_{C,j}(t, \alpha)$ reduce to the desired extremizing functions $r_{C,j}(t)$ for $\alpha = 0$, (ii) that the endpoint of the functions is independent of α and (iii) that they have continuous first and second derivatives with respect to t and α [170]. Then, an extremum of $\mathbb{I}(\alpha)$ requires [165, 170]

$$\left.\frac{d\mathbb{I}(\alpha)}{d\alpha}\right|_{\alpha=0} = \int_{t=t_i}^{t=t_f} \sum_{j=1}^{j=\mathcal{N}_f} \left(\frac{\partial \mathcal{L}_u}{\partial \overline{r}_{C,j}} \frac{d\overline{r}_{C,j}}{d\alpha} + \frac{\partial \mathcal{L}_u}{\partial \dot{\overline{r}}_{C,j}} \frac{d\dot{\overline{r}}_{C,j}}{d\alpha} \right) dt = 0. \tag{3.45}$$

Using condition (iii) we obtain [170]

$$\frac{d\mathbb{I}(\alpha)}{d\alpha} = \int_{t=t_i}^{t=t_f} \sum_{j=1}^{j=\mathcal{N}_f} \left(\frac{\partial \mathcal{L}_u}{\partial \overline{r}_{C,j}} \frac{d\overline{r}_{C,j}}{d\alpha} + \frac{\partial \mathcal{L}_u}{\partial \dot{\overline{r}}_{C,j}} \frac{d}{dt} \frac{d\overline{r}_{C,j}}{d\alpha} \right) dt, \tag{3.46}$$

which can be transformed into

$$\frac{d\mathbb{I}(\alpha)}{d\alpha} = \int_{t=t_i}^{t=t_f} \sum_{j=1}^{j=\mathcal{N}_f} \left(\frac{\partial \mathcal{L}_u}{\partial \overline{r}_{C,j}} - \frac{d}{dt} \frac{\partial \mathcal{L}_u}{\partial \dot{\overline{r}}_{C,j}} \right) \frac{d\overline{r}_{C,j}}{d\alpha}\, dt, \tag{3.47}$$

where we have integrated the second term by parts and where the boundary term vanishes because of condition (ii) [170]. By construction, $\mathbb{I}$ is an extremum for $\alpha = 0$ and all test functions $\overline{y}(t, \alpha)$ can be replaced by the desired functions $y(t)$. Defining

$$\chi_j(t) = \left. \frac{d\overline{r}_{C,j}}{d\alpha} \right|_{\alpha=0} \tag{3.48}$$

we obtain [170]

$$\left. \frac{d\mathbb{I}(\alpha)}{d\alpha} \right|_{\alpha=0} = \int_{t=t_i}^{t=t_f} \sum_{j=1}^{j=\mathcal{N}_f} \left(\frac{\partial \mathcal{L}_u}{\partial r_{C,j}} - \frac{d}{dt} \frac{\partial \mathcal{L}_u}{\partial \dot{r}_{C,j}} \right) \chi_j(t)\, dt = 0. \tag{3.49}$$

Because the functions $\chi_j(t)$ are independent and arbitrary as long as they satisfy conditions (i) and (iii) above, equation (3.49) vanishes if [165, 170]

$$\frac{d}{dt} \frac{\partial \mathcal{L}_u}{\partial \dot{r}_{C,j}} - \frac{\partial \mathcal{L}_u}{\partial r_{C,j}} = 0 \tag{3.50}$$

holds for all degrees of freedom j. The set of equations (3.50) corresponds to the Euler-Lagrange equations extremizing the integral $\mathbb{I}$ and here become Lagrange's equations of motion [165, 170].

We are now in a position to deal with a system with $\mathcal{N}_c$ holonomic constraints:

$$\sigma_{c,k}(\boldsymbol{r}_C, t) = 0. \tag{3.51}$$

From a mathematical point of view constraints introduce a relation between variables so that they are not independent any more. There are two ways to approach this situation [165, 170, 171]. First, we could eliminate $\mathcal{N}_c$ variables by means of the constraint equations, thereby reducing the number of degrees

of freedom from $\mathcal{N}_f$ to $\mathcal{N}_f - \mathcal{N}_c$ [165,171]. However, this approach might not be practical for complex systems [168]. In addition, the original variables are not treated in a symmetrical way [165]. Second, we could use the method of Lagrange multipliers, as we shall do below.

The idea of the method of Lagrange multipliers is to increase the number of variables to $\mathcal{N}_f + \mathcal{N}_c$ and to find the extremum of a function that has this number of variables. In that case, the problem of finding the extremum can be cast in the usual form. We shall achieve this goal by using a family of two-parameter functions $\overline{r}_{C,j}(t, \alpha_1, \alpha_2)$ and again seek those test functions that extremize the integral [170]

$$\mathbb{I} = \int_{t=t_i}^{t=t_f} \mathcal{L}_u(\boldsymbol{r}_C, \dot{\boldsymbol{r}}_C, t)\, dt \tag{3.52}$$

subject to the $\mathcal{N}_c$ conditions of constraint ($k = 1, \ldots, \mathcal{N}_c$)

$$\sigma_{c,k}(\boldsymbol{r}_C, t) = 0. \tag{3.53}$$

As above, the test functions $\overline{r}_{C,j}(t, \alpha_1, \alpha_2)$ reduce to the extremizing functions $r_{C,j}(t)$ for $\alpha_1 = \alpha_2 = 0$. In addition, they have fixed endpoints for any values of α_1 and α_2 as well as continuous derivatives up to second order [170]. In the same way as the test functions reduce to the extremizing functions the integral

$$\mathbb{I}(\alpha_1, \alpha_2) = \int_{t=t_i}^{t=t_f} \mathcal{L}_u(\overline{\boldsymbol{r}}_C, \dot{\overline{\boldsymbol{r}}}_C, t)\, dt \tag{3.54}$$

becomes the desired integral $\mathbb{I}$ for $\alpha_1 = \alpha_2 = 0$ [170]. The set of equations (3.53) constitutes a set of local constraints, which hold at any point t between the endpoints [170]. These constraint conditions can be transformed into an equivalent integral form by first multiplying by an arbitrary function $y(t)$ and then integrating from $t = t_i$ to $t = t_f$. This procedure yields [170]

$$\mathbb{J}(\alpha_1, \alpha_2) = \int_{t=t_i}^{t=t_f} \sum_{k=1}^{k=\mathcal{N}_c} y(t)\sigma_{c,k}(\overline{\boldsymbol{r}}_C(t, \alpha_1, \alpha_2), t)\, dt. \tag{3.55}$$

Next, we form the overall function to extremize [170]

$$\mathbb{I}_{tot}(\alpha_1, \alpha_2) = \mathbb{I}(\alpha_1, \alpha_2) + \sum_{k=1}^{k=\mathcal{N}_c} \lambda_{L,k} \mathbb{J}(\alpha_1, \alpha_2), \tag{3.56}$$

and we impose the necessary condition for an extremum [170]:

$$\left.\frac{\partial \mathbb{I}_{tot}}{\partial \alpha_1}\right|_{\alpha_1=0;\alpha_2=0} = 0 = \left.\frac{\partial \mathbb{I}_{tot}}{\partial \alpha_2}\right|_{\alpha_1=0;\alpha_2=0}. \tag{3.57}$$

Specifically, we have for $m = 1, 2$ [170]

$$\frac{\partial \mathbb{I}_{tot}}{\partial \alpha_m} = \int_{t=t_i}^{t=t_f} \sum_{j=1}^{j=\mathcal{N}_f} \left(\frac{\partial \mathcal{L}_u}{\partial \overline{r}_{C,j}} \frac{d\overline{r}_{C,j}}{d\alpha_m} + \frac{\partial \mathcal{L}_u}{\partial \dot{\overline{r}}_{C,j}} \frac{d\dot{\overline{r}}_{C,j}}{d\alpha_m} + \sum_{k=1}^{k=\mathcal{N}_c} \lambda_{L,k} y(t) \frac{\partial \sigma_{c,k}}{\partial \overline{r}_{C,j}} \frac{d\overline{r}_{C,j}}{d\alpha_m} \right) dt. \tag{3.58}$$

If we again integrate by parts the second term on the right-hand side, we obtain [170]

$$\frac{\partial \mathbb{I}_{tot}}{\partial \alpha_m} = \int_{t=t_i}^{t=t_f} \sum_{j=1}^{j=\mathcal{N}_f} \left(\frac{\partial \mathcal{L}_u}{\partial \overline{r}_{C,j}} - \frac{d}{dt} \frac{\partial \mathcal{L}_u}{\partial \dot{\overline{r}}_{C,j}} + \sum_{k=1}^{k=\mathcal{N}_c} \lambda_{L,k} y(t) \frac{\partial \sigma_{c,k}}{\partial \overline{r}_{C,j}} \right) \frac{d\overline{r}_{C,j}}{d\alpha_m} dt. \tag{3.59}$$

We now define the derivative of a test function $\overline{r}_{C,j}$ with respect to the parameter α_m for $m = 1, 2$ at the extremum as [170]

$$\chi_{m,j}(t) = \left.\frac{d\overline{r}_{C,j}}{d\alpha_m}\right|_{\alpha_1=0;\alpha_2=0}. \tag{3.60}$$

It is at this point that the difference between extremizing an integral with and without constraints becomes apparent. In the absence of constraints, the functions $\chi_j(t)$ were independent of each other. In the present case with constraints, the conditions of constraint lead to functional relationships between the test functions $\overline{r}_{C,j}$ and thus $\chi_{m,j}(t)$ so that the functions $\overline{r}_{C,j}$ and $\chi_{m,j}$ cannot be varied independently [170]. However, we have not specified the set of Lagrange multipliers $\lambda_{L,k}$ yet. We can formally choose the $\mathcal{N}_c$ Lagrange multipliers $\lambda_{L,k}$ in such a way that the prefactors of $\mathcal{N}_c$ functions $\chi_{m,j}$ for

$j = 1, \ldots, \mathcal{N}_c$ vanish [165, 170]. Then, the remaining $\mathcal{N}_f - \mathcal{N}_c$ functions $\chi_{m,j}$ with $j = \mathcal{N}_c + 1, \ldots, \mathcal{N}_f$ can be varied independently [165, 170]. The overall effect of this procedure is that all variables are treated in a symmetrical way because the choice of the first $\mathcal{N}_c$ variables is arbitrary. We therefore have for all variables $\chi_{m,j}$ [165, 170]

$$\frac{\partial \mathcal{L}_u}{\partial r_{C,j}} - \frac{d}{dt}\frac{\partial \mathcal{L}_u}{\partial \dot{r}_{C,j}} + \sum_{k=1}^{k=\mathcal{N}_c} \lambda_{L,k} y(t) \frac{\partial \sigma_{c,k}}{\partial r_{C,j}} = 0, \tag{3.61}$$

where we have used the condition that the test functions $\overline{r}_{C,j}$ become the desired functions $r_{C,j}$ at the extremum ($\alpha_1 = \alpha_2 = 0$). Together with the $\mathcal{N}_c$ conditions of constraint (3.53) the equations (3.61) constitute a set of $\mathcal{N}_f + \mathcal{N}_c$ equations for $\mathcal{N}_f + \mathcal{N}_c$ variables.

In principle, the set of linear equations given by equations (3.53) and (3.61) could be solved by matrix inversion [106]. In practice, however, the differential equations are approximated by difference equations during a molecular dynamics simulation. As a consequence, the constraints are not rigorously satisfied due to the error of the integration algorithm [106, 168, 169]. As a result, the Lagrange multipliers are approximated in such a way that the constraint conditions (3.53) are satisfied arbitrarily closely at every timestep [106,168,169]. Below we shall focus on the RATTLE algorithm, which enables us to treat holonomic constraints with the velociy Verlet algorithm [167, 169].

Following reference [169], we define the Lagrangian $\mathcal{L}_c$ of the constrained system as [168]

$$\mathcal{L}_c(\boldsymbol{r}_C, \dot{\boldsymbol{r}}_C, t) = \mathcal{L}_u(\boldsymbol{r}_C, \dot{\boldsymbol{r}}_C, t) - \sum_{k=1}^{k=\mathcal{N}_c} \lambda_{L,k}(t) \sigma_{c,k}(\boldsymbol{r}_C). \tag{3.62}$$

Then, the equations of motion read [165]

$$\frac{d}{dt}\frac{\partial \mathcal{L}_u}{\partial \dot{r}_{C,j}} - \frac{\partial \mathcal{L}_u}{\partial r_{C,j}} = -\sum_{k=1}^{k=\mathcal{N}_c} \lambda_{L,k}(t) \frac{\partial \sigma_{c,k}}{\partial r_{C,j}}. \tag{3.63}$$

Switching to a description that is based on particle positions $\boldsymbol{r}_{C,j}$ instead

of Cartesian degrees of freedom $r_{C,j}$, we obtain the following equations of motion for the constrained dynamics [169]:

$$m_j \ddot{\boldsymbol{r}}_{C,j} = \boldsymbol{\mathcal{F}}_j + \boldsymbol{\mathcal{G}}_j, \tag{3.64}$$

where m_j is the mass associated with particle j. The force on particle j due to the remaining particles is $\boldsymbol{\mathcal{F}}_j = -\nabla_{\boldsymbol{r}_{C,j}} V$, and the force on particle j due to the conditions of constraints reads [169]

$$\boldsymbol{\mathcal{G}}_j = -\sum_{k=1}^{k=\mathcal{N}_c} \lambda_{L,k}(t) \nabla_{\boldsymbol{r}_{C,j}} \sigma_{c,k}. \tag{3.65}$$

If we focus on bond constraints, the force due to constraints involves only those constraints defining bonds connecting another particle k to particle j, and we have [169]

$$\boldsymbol{\mathcal{G}}_j = -\sum_{k \text{ bt } j} \lambda_{L,jk}(t) \nabla_{\boldsymbol{r}_{C,j}} \sigma_{c,jk}, \tag{3.66}$$

where the sum is over all particles k bonded to (bt) particle j and the Lagrange multiplier $\lambda_{L,jk} = \lambda_{L,kj}$ is associated with the constraint $\sigma_{c,jk} = \sigma_{c,kj}$ below. The bond constraints appearing in equation (3.66) are expressed as follows [169]

$$\sigma_{c,jk} = (\boldsymbol{r}_{C,j} - \boldsymbol{r}_{C,k})^2 - d_{jk}^2 = 0. \tag{3.67}$$

With the above framework and the specific choice for the constraints we obtain the velocity Verlet prescription for updating the particle positions [167, 169]

$$\boldsymbol{r}_{C,j}(t+\delta t) = \boldsymbol{r}_{C,j}(t) + \dot{\boldsymbol{r}}_{C,j}(t)\delta t + \frac{(\delta t)^2}{2m_j}\left(\boldsymbol{\mathcal{F}}_j(t) + \boldsymbol{\mathcal{G}}_j^r(t)\right), \tag{3.68}$$

where δt is the timestep. The velocity of particle j is updated using the forces $\boldsymbol{\mathcal{F}}_j$ at times t and $t+\delta t$ as well as the forces due to the constraints $\boldsymbol{\mathcal{G}}_j^r$

and $\boldsymbol{\mathcal{G}}_j^v$ [169]

$$\dot{\boldsymbol{r}}_{C,j}(t+\delta t) = \dot{\boldsymbol{r}}_{C,j}(t) + \frac{\delta t}{2m_j}\left(\boldsymbol{\mathcal{F}}_j(t) + \boldsymbol{\mathcal{G}}_j^r(t) + \boldsymbol{\mathcal{F}}_j(t+\delta t) + \boldsymbol{\mathcal{G}}_j^v(t+\delta t)\right). \tag{3.69}$$

The force of constraint $\boldsymbol{\mathcal{G}}_j^r$ reads [169]

$$\boldsymbol{\mathcal{G}}_j^r(t) = -2\sum_{k \text{ bt } j} \lambda_{L,jk}^r(t)\,(\boldsymbol{r}_{C,j} - \boldsymbol{r}_{C,k}). \tag{3.70}$$

According to reference [169], the time derivative of the conditions of constraint (3.67) impose constraints on the velocities

$$(\boldsymbol{r}_{C,j} - \boldsymbol{r}_{C,k})\,(\dot{\boldsymbol{r}}_{C,j} - \dot{\boldsymbol{r}}_{C,k}) = 0. \tag{3.71}$$

Andersen's choice for the forces of constraint for satisfying the velocity constraints (3.71) is as follows [169]

$$\boldsymbol{\mathcal{G}}_j^v(t+\delta t) = -2\sum_{k \text{ bt } j} \lambda_{L,jk}^v(t+\delta t)\,(\boldsymbol{r}_{C,j}(t+\delta t) - \boldsymbol{r}_{C,k}(t+\delta t)). \tag{3.72}$$

Given the formal expressions (3.70) and (3.72) for the forces of constraint and writing $\boldsymbol{r}_{C,jk} = \boldsymbol{r}_{C,j} - \boldsymbol{r}_{C,k}$, we have the following explicit expressions for the update of the position and velocity of each particle j [169]:

$$\begin{aligned}\boldsymbol{r}_{C,j}(t+\delta t) =& \boldsymbol{r}_{C,j}(t) + \dot{\boldsymbol{r}}_{C,j}(t)\delta t \\ &+ \frac{(\delta t)^2}{2m_j}\left(\boldsymbol{\mathcal{F}}_j(t) - 2\sum_{k \text{ bt } j} \lambda_{L,jk}^r(t)\boldsymbol{r}_{C,jk}(t)\right); \end{aligned} \tag{3.73a}$$

$$\begin{aligned}\dot{\boldsymbol{r}}_{C,j}(t+\delta t) =& \dot{\boldsymbol{r}}_{C,j}(t) + \frac{\delta t}{2m_j}\Bigg(\boldsymbol{\mathcal{F}}_j(t) - 2\sum_{k \text{ bt } j} \lambda_{L,jk}^r(t)\boldsymbol{r}_{C,jk}(t) \\ &+ \boldsymbol{\mathcal{F}}_j(t+\delta t) - 2\sum_{k \text{ bt } j} \lambda_{L,jk}^v(t+\delta t)\boldsymbol{r}_{C,jk}(t+\delta t)\Bigg). \end{aligned} \tag{3.73b}$$

The RATTLE algorithm then uses an iterative scheme to generate ap-

proximations to the Lagrange multipliers $\lambda^r_{L,jk}(t)$ and $\lambda^v_{L,jk}(t+\delta t)$ so that the constraints (3.67) and (3.71) are satisfied at each timestep to within a desired tolerance [169]. We assume that the positions, velocities and forces are given at time t and that all constraints are satisfied. Our task is then to compute the positions and velocities satisfying the constraints at time $t+\delta t$. To proceed, we define the auxiliary quantity $\boldsymbol{q}_{a,j}$ [169]

$$\boldsymbol{q}_{a,j} = \dot{\boldsymbol{r}}_{C,j}(t) + \frac{\delta t}{2m_j}\boldsymbol{\mathcal{F}}_j(t) - \frac{\delta t}{m_j}\sum_{k \text{ bt } j} \lambda^r_{L,jk}(t)\boldsymbol{r}_{C,jk}(t). \tag{3.74}$$

We can then write equations (3.73) as [169]

$$\boldsymbol{r}_{C,j}(t+\delta t) = \boldsymbol{r}_{C,j}(t) + \delta t \boldsymbol{q}_{a,j}; \tag{3.75a}$$

$$\dot{\boldsymbol{r}}_{C,j}(t+\delta t) = \boldsymbol{q}_{a,j} + \frac{\delta t}{2m_j}\boldsymbol{\mathcal{F}}_j(t+\delta t) - \frac{\delta t}{m_j}\sum_{k \text{ bt } j} \lambda^v_{L,jk}(t+\delta t)\boldsymbol{r}_{C,jk}(t+\delta t). \tag{3.75b}$$

Now the equations of motion can be solved by constructing the set of $\boldsymbol{q}_{a,j}$ in such a way that the constraints are fulfilled. At the beginning all Lagrange multipliers are set to zero, and we have [169]

$$\boldsymbol{q}_{a,j} = \dot{\boldsymbol{r}}_{C,j}(t) + \frac{\delta t}{2m_j}\boldsymbol{\mathcal{F}}_j(t). \tag{3.76}$$

With this initial choice we check whether every pair of particles j and k subject to a constraint $\sigma_{c,jk}$ has the required distance d_{jk}. The instantaneous approximation $\boldsymbol{s}_{jk}$ to the particle distance between particles j and k is given by [169]

$$\boldsymbol{s}_{jk} = \boldsymbol{r}_{C,j}(t) + \delta t \boldsymbol{q}_{a,j} - \boldsymbol{r}_{C,k}(t) - \delta t \boldsymbol{q}_{a,k} \tag{3.77}$$

If $\boldsymbol{s}_{jk}$ differs from d_{jk} by more than a desired tolerance, new trial positions

$\boldsymbol{r}_{C,j}^T$ and $\boldsymbol{r}_{C,k}^T$ are generated as follows [169]:

$$\boldsymbol{r}_{C,j}^T(t) = \boldsymbol{r}_{C,j}(t) + \delta t \left(\boldsymbol{q}_{a,j} - \frac{\delta t}{m_j} \lambda_{L,jk}^r(t) \boldsymbol{r}_{C,jk}(t) \right); \tag{3.78a}$$

$$\boldsymbol{r}_{C,k}^T(t) = \boldsymbol{r}_{C,k}(t) + \delta t \left(\boldsymbol{q}_{a,k} + \frac{\delta t}{m_k} \lambda_{L,jk}^r(t) \boldsymbol{r}_{C,jk}(t) \right). \tag{3.78b}$$

The trial positions should satisfy the constraint [169]

$$\left(\boldsymbol{r}_{C,j}^T(t) - \boldsymbol{r}_{C,k}^T(t) \right)^2 = d_{jk}^2. \tag{3.79}$$

Inserting equations (3.78) into equation (3.79), we obtain [169]

$$\left(\boldsymbol{s}_{jk} - \left(m_j^{-1} + m_k^{-1} \right) (\delta t)^2 \lambda_{L,jk}^r(t) \boldsymbol{r}_{C,jk}(t) \right)^2 = d_{jk}^2. \tag{3.80}$$

We could in principle solve this quadratic equation for $\lambda_{L,jk}^r(t)$. However, adjusting one constraint typically leads to violating another one, requiring subsequent adjustments of particle positions in an interative manner [168]. In practice, only the linear term in $\lambda_{L,jk}^r(t)$ is therefore retained for computational efficiency [168, 169], leading to [169]:

$$\lambda_{L,jk}^r(t) = \frac{\boldsymbol{s}_{jk}^2 - d_{jk}^2}{2(\delta t)^2 \boldsymbol{s}_{jk} \boldsymbol{r}_{C,jk}(t) \left(m_j^{-1} + m_k^{-1} \right)}. \tag{3.81}$$

The approximate determination of the Lagrange multiplier is used to update $\boldsymbol{q}_{a,j}$ and $\boldsymbol{q}_{a,k}$ [169]:

$$\boldsymbol{q}_{a,j} \mapsto \boldsymbol{q}_{a,j} - \frac{\delta t}{m_j} \lambda_{L,jk}^r(t) \boldsymbol{r}_{C,jk}(t); \tag{3.82}$$

$$\boldsymbol{q}_{a,k} \mapsto \boldsymbol{q}_{a,k} + \frac{\delta t}{m_k} \lambda_{L,jk}^r(t) \boldsymbol{r}_{C,jk}(t). \tag{3.83}$$

This iterative adjustment of the particle positions is repeated until all bond distance constraints are satisfied simultaneously [169].

Now the positions at time $t + \delta t$ are known, and the forces $\boldsymbol{\mathcal{F}}_j(t + \delta t)$ in the absence of constraints can be computed to determine the velocities at $t + \delta t$ [169]. As in the case of particle positions, we start with vanishing

Lagrange multipliers $\lambda^v_{L,jk}(t+\delta t)$ [169]:

$$\dot{\boldsymbol{r}}_{C,j}(t+\delta t) = \boldsymbol{q}_{a,j} + \frac{\delta t}{2m_j}\boldsymbol{\mathcal{F}}_j(t+\delta t). \tag{3.84}$$

To test whether the constraints on the velocities are fulfilled, the dot product between $\boldsymbol{r}_{C,jk}(t)$ and $\dot{\boldsymbol{r}}_{C,jk}(t)$ is computed [169]. If it deviates from zero by more than the desired tolerance, trial velocities are generated as follows [169]:

$$\dot{\boldsymbol{r}}^T_{C,j}(t+\delta t) = \dot{\boldsymbol{r}}_{C,j}(t+\delta t) - \frac{\delta t}{m_j}\lambda^v_{L,jk}(t)\boldsymbol{r}_{C,jk}(t+\delta t); \tag{3.85a}$$

$$\dot{\boldsymbol{r}}^T_{C,k}(t+\delta t) = \dot{\boldsymbol{r}}_{C,k}(t+\delta t) + \frac{\delta t}{m_k}\lambda^v_{L,jk}(t)\boldsymbol{r}_{C,jk}(t+\delta t). \tag{3.85b}$$

Inserting the trial velocities (3.85) into the condition of constraint for velocities (3.71), we obtain [169]

$$\begin{aligned}\boldsymbol{r}_{C,jk}(t+\delta t)&\left(\dot{\boldsymbol{r}}^T_{C,j}(t+\delta t) - \dot{\boldsymbol{r}}^T_{C,k}(t+\delta t)\right)\\ =&\boldsymbol{r}_{C,jk}(t+\delta t)\big\{\dot{\boldsymbol{r}}_{C,j}(t+\delta t) - \dot{\boldsymbol{r}}_{C,k}(t+\delta t)\\ &- \delta t\lambda^v_{L,jk}(t)\boldsymbol{r}_{C,jk}(t+\delta t)\left(m_j^{-1}+m_k^{-1}\right)\big\} = 0.\end{aligned} \tag{3.86}$$

This results in the following choice for the Lagrange multiplier $\lambda^v_{L,jk}(t+\delta t)$ [169]:

$$\lambda^v_{L,jk}(t+\delta t) = \frac{\boldsymbol{r}_{C,jk}(t+\delta t)\left(\dot{\boldsymbol{r}}_{C,j}(t+\delta t) - \dot{\boldsymbol{r}}_{C,k}(t+\delta t)\right)}{\delta t d^2_{jk}\left(m_j^{-1}+m_k^{-1}\right)}. \tag{3.87}$$

We then update the particle velocities by the current trial velocities [169]:

$$\dot{\boldsymbol{r}}_{C,j}(t+\delta t) \mapsto \dot{\boldsymbol{r}}_{C,j}(t+\delta t) - \frac{\delta t}{m_j}\lambda^v_{L,jk}(t+\delta t)\boldsymbol{r}_{C,jk}(t+\delta t); \tag{3.88}$$

$$\dot{\boldsymbol{r}}_{C,k}(t+\delta t) \mapsto \dot{\boldsymbol{r}}_{C,k}(t+\delta t) + \frac{\delta t}{m_k}\lambda^v_{L,jk}(t+\delta t)\boldsymbol{r}_{C,jk}(t+\delta t). \tag{3.89}$$

Once all constraints on the velocities are satisfied, we proceed with the next timestep.

Having described how holonomic constraints can be combined with the velocity Verlet algorithm, we now turn to molecular dynamics simulations in the canonical ensemble.

3.1.6 Canonical molecular dynamics simulations

We shall restrict our attention to the extended-system approach [163] of the Nosé-Hoover [172–175] thermostat to generate a trajectory according to the canonical phase space distribution function. The original formulation of Nosé [172] contains a time scaling parameter leading to virtual variables satisfying the Hamiltonian form of the equations of motion. However, in this virtual formulation, the time intervals in real time are not equally spaced, which is inconvenient in a numerical simulation [174]. When transformed to real variables, the equations of motion are no longer canonical, and the theoretical framework of non-Hamiltonian dynamics [176,177], which is briefly described in appendix G, proves useful.

Although the Nosé-Hoover thermostat does not yield a canonical distribution of phase space variables for all systems, it does so for systems that conserve an energy specified below and whose centre of mass is at rest [177]. Because periodic boundary conditions are used in all simulations in this work, the total angular momentum is not conserved [107, 173], and the Nosé-Hoover thermostat is sufficient to obtain equilibrium properties in the canonical ensemble for the stable states [106]. If further conserved quantities are present or the total linear momentum does not vanish, Nosé-Hoover chains should be employed [112]. Our presentation will follow the discussion of references [106, 177].

The idea behind the Nosé-Hoover algorithm is to couple the physical system to a heat bath, consisting of an additional degree of freedom [172,173]. Hence, we obtain an extended system in which the energy of the physical system is allowed to fluctuate [172]. Later, the phase space of the extended system is projected back onto that of the physical system by integrating out the artificial degree of freedom [172, 173].

The equations of motion of the Nosé-Hoover thermostat can be written

in Cartesian coordinates as [106, 177]

$$\dot{r}_{C,j} = \frac{p_{C,j}}{m_j}; \tag{3.90a}$$

$$\dot{p}_{C,j} = -\nabla_{r_{C,j}} V - \frac{p_\varepsilon}{\mathcal{W}_{NH}} p_{C,j}; \tag{3.90b}$$

$$\dot{p}_\varepsilon = \sum_{j=1}^{\mathcal{N}_f} \frac{p_{C,j}^2}{m_j} - \mathcal{C}_n k_B T; \tag{3.90c}$$

$$\dot{\varepsilon} = \frac{p_\varepsilon}{\mathcal{W}_{NH}}. \tag{3.90d}$$

The heat bath is characterized by the variables ε and p_ε, and $\mathcal{N}_f$ is the number of physical degrees of freedom. $\mathcal{C}_n$ denotes a constant to be specified later, and $\mathcal{W}_{NH}$ is a parameter describing the relaxation time of the thermostat. According to reference [177], it reads

$$\mathcal{W}_{NH} = \mathcal{C}_n k_B T \tau_{NH}^2. \tag{3.91}$$

Above, τ_{NH} is a timescale of the physical system. We see that the total force on particle j has contributions from the potential V and from the heat bath via the term $p_\varepsilon / \mathcal{W}_{NH}\, p_{C,j}$.

As pointed out in references [173, 175], the above equations of motion are not Hamiltonian. However, they conserve the following energy [173, 177]:

$$H_{NH} = \sum_{j=1}^{\mathcal{N}_f} \frac{p_{C,j}^2}{2m_j} + V(\boldsymbol{r_C}) + \frac{p_\varepsilon^2}{2\,\mathcal{W}_{NH}} + \mathcal{C}_n k_B T \varepsilon. \tag{3.92}$$

To see this, we use the equations of motion (3.90) to obtain [173]

$$\begin{aligned}\frac{dH_{NH}}{dt} =& \frac{\partial H_{NH}}{\partial t} + \sum_{j=1}^{\mathcal{N}_f} \frac{p_{C,j}}{m_j} \dot{p}_{C,j} + \sum_j \dot{r}_{C,j} \nabla_{r_{C,j}} V + \frac{p_\varepsilon}{\mathcal{W}_{NH}} \dot{p}_\varepsilon + \mathcal{C}_n k_B T \dot{\varepsilon} \\ =& \sum_{j=1}^{\mathcal{N}_f} \frac{p_{C,j}}{m_j} \left(-\frac{p_\varepsilon}{\mathcal{W}_{NH}} p_{C,j} \right) + \frac{p_\varepsilon}{\mathcal{W}_{NH}} \left(\sum_j \frac{p_{C,j}^2}{m_j} - \mathcal{C}_n k_B T \right) \\ &+ \mathcal{C}_n k_B T \frac{p_\varepsilon}{\mathcal{W}_{NH}} = 0.\end{aligned} \tag{3.93}$$

Here, we shall follow the procedure for obtaining the phase space density from the non-Hamiltonian equations of motion (3.90) outlined in appendix G and in reference [177]. According to that scheme, all conserved quantities need to be identified. In addition to the energy H_{NH}, the total linear momentum $\boldsymbol{\mathcal{P}_C} = \sum_{j=1}^{j=N} \boldsymbol{p_{C,j}}$ of the N-particle system is conserved [172, 177]:

$$\frac{d\boldsymbol{\mathcal{P}_C}}{dt} = \sum_{j=1}^{N} \dot{\boldsymbol{p}}_{\boldsymbol{C,j}} = \sum_{j=1}^{\mathcal{N}_f} \left(-\nabla_{r_{C,j}} V\right) + \sum_{j=1}^{\mathcal{N}_f} \left(-\frac{p_\varepsilon}{\mathcal{W}_{NH}} p_{C,j}\right) = -\frac{p_\varepsilon}{\mathcal{W}_{NH}} \boldsymbol{\mathcal{P}_C}. \tag{3.94}$$

The last identity in equation (3.94) above follows from the definition of the total linear momentum and from the absence of external forces. Consequently, the sum of all internal forces vanishes. We see from equation (3.94) that the conserved quantity for non-vanishing total linear momentum is $\boldsymbol{\mathcal{P}_C} e^{\varepsilon} = \boldsymbol{\mathcal{C}_{\mathcal{P}}}$ [174, 177]:

$$\frac{d\boldsymbol{\mathcal{P}_C}}{dt} = -\dot{\varepsilon}\, \boldsymbol{\mathcal{P}_C}; \tag{3.95a}$$

$$\int_{\boldsymbol{\mathcal{P}_C}(0)}^{\boldsymbol{\mathcal{P}_C}(t)} d\, ln\, \boldsymbol{\mathcal{P}_C} = -\int_0^t \dot{\varepsilon}\, dt'; \tag{3.95b}$$

$$\frac{\boldsymbol{\mathcal{P}_C}(t)}{\boldsymbol{\mathcal{P}_C}(0)} = e^{-(\varepsilon(t)-\varepsilon(0))}; \tag{3.95c}$$

$$\boldsymbol{\mathcal{P}_C}(t)\, e^{\varepsilon(t)} = \boldsymbol{\mathcal{P}_C}(0)\, e^{\varepsilon(0)} = \boldsymbol{\mathcal{C}_{\mathcal{P}}}. \tag{3.95d}$$

As pointed out, for instance, in references [106, 177], a canonical distribution function is generated by the Nosé-Hoover equations of motion only if the constant vector $\boldsymbol{\mathcal{C}_{\mathcal{P}}}$ and the total linear momentum $\boldsymbol{\mathcal{P}_C}$ vanish. We restrict our attention to that special case because it is the only relevant one for the present work.

A conserved total linear momentum has two consequences. First, the individual components of the total linear momentum are linearly dependent [177]. As a result, only one component is a linearly independent degree of freedom for the phase space considered. Second, the centre-of-mass coordinates are cyclic [177]. This means that they are not present in the equations of motion and do not influence other variables. The physical meaning is that the state

of the system is independent of the position of its centre of mass if external forces are absent.

To eliminate cyclic and linearly dependent variables, we follow references [106, 177] and introduce a new set of coordinates $\{\boldsymbol{p'_C}, \boldsymbol{\mathcal{P}_C}, \boldsymbol{r'_C}, \boldsymbol{\mathcal{R}_C}\}$. The centre of mass is characterized by its position $\boldsymbol{\mathcal{R}_C} = 1/\mathcal{M} \sum_{j=1}^{j=N} m_j \, \boldsymbol{r_{C,j}}$ with total mass $\mathcal{M} = \sum_{j=1}^{j=N} m_j$ and momentum $\boldsymbol{\mathcal{P}_C} = \sum_{j=1}^{j=N} \boldsymbol{p_{C,j}}$. In addition, the primed variables denote the positions and momenta of particles relative to the centre of mass. Furthermore, the motion of the centre of mass is represented by the variable $\mathcal{P}_C = \sqrt{\sum_{j=1}^{j=3} \mathcal{P}_{C,j}^2}$. This yields the equations of motion in the new coordinate system [177]:

$$\dot{r}'_{C,j} = \frac{p'_{C,j}}{m_j}; \tag{3.96a}$$

$$\dot{p}'_{C,j} = -\nabla_{r_{C,j}} V - \frac{p_\varepsilon}{\mathcal{W}_{NH}} p'_{C,j}; \tag{3.96b}$$

$$\dot{\mathcal{P}}_C = -\frac{p_\varepsilon}{\mathcal{W}_{NH}} \mathcal{P}_C; \tag{3.96c}$$

$$\dot{p}_\varepsilon = \sum_{j=1}^{3N-3} \frac{\left(p'_{C,j}\right)^2}{m_j} + \frac{\mathcal{P}_C^2}{2\,\mathcal{M}} - \mathcal{C}_n k_B T; \tag{3.96d}$$

$$\dot{\varepsilon} = \frac{p_\varepsilon}{\mathcal{W}_{NH}}. \tag{3.96e}$$

Above, N is the number of physical particles in the system. The conserved quantities are the total linear momentum $\mathcal{P}_C \, e^\varepsilon = \mathcal{C}_\mathcal{P}$ and the energy H_{NH} [177]:

$$\begin{aligned} H_{NH} &= \sum_{j=1}^{3N-3} \frac{(p'_{C,j})^2}{2m_j} + \frac{\mathcal{P}_C^2}{2\,\mathcal{M}} + V(\boldsymbol{r'_C}) + \frac{p_\varepsilon^2}{2\,\mathcal{W}_{NH}} + \mathcal{C}_n k_B T \varepsilon \\ &= \mathcal{H}(\boldsymbol{r'_C}, \boldsymbol{p'_C}, \mathcal{P}_C) + \frac{p_\varepsilon^2}{2\,\mathcal{W}_{NH}} + \mathcal{C}_n k_B T \varepsilon. \end{aligned} \tag{3.97}$$

Having identified the conservation laws and having eliminated linearly dependent as well as cyclic variables, we now proceed to evaluate the generalized invariant measure. This requires the determination of the phase space compressibility and the phase space metric. Using the equations of

motion (3.96), we obtain the phase space compressibility given in equation (3.98) [177]:

$$\begin{aligned}\kappa &= \sum_{j=1} \nabla_{r'_{C,j}} \dot{r}'_{C,j} + \sum_{j=1} \nabla_{p'_{C,j}} \dot{p}'_{C,j} + \nabla_{\mathcal{P}_C} \dot{\mathcal{P}}_C + \nabla_{\varepsilon} \dot{\varepsilon} + \nabla_{p_\varepsilon} \dot{p}_\varepsilon \\ &= -(3(N-1)+1)\dot{\varepsilon}. \end{aligned} \tag{3.98}$$

The phase space metric follows immediately from the phase space compressibility via equations (G.7) and (G.6) of appendix G, as discussed in references [176, 177]:

$$\sqrt{g} = e^{(3(N-1)+1)\varepsilon}. \tag{3.99}$$

The invariant measure is obtained from combining the phase space metric with the differential volume element $d\mathcal{V}$ describing the set of phase space variables [176, 177]:

$$\sqrt{g}\, d\mathcal{V} = e^{(3(N-1)+1)\varepsilon}\, d\boldsymbol{r}'_{\boldsymbol{C}}\, d\boldsymbol{p}'_{\boldsymbol{C}}\, d\mathcal{P}_C\, d\varepsilon dp_\varepsilon. \tag{3.100}$$

We now proceed to construct the generalized microcanonical partition function (G.12), denoting the constants for the conserved quantities H_{NH} and $\mathcal{P}_C e^{\varepsilon}$ by $\mathcal{C}_H$ and $\mathcal{C}_{\mathcal{P}}$. As pointed out above, the latter will later be set to zero. For the Nosé-Hoover thermostat system equation (G.12) can be written as [176, 177]

$$\begin{aligned}\Xi(\mathcal{C}_H, \mathcal{C}_{\mathcal{P}}) &= \int \delta\left(H_{NH} - \mathcal{C}_H\right) \delta\left(\mathcal{P}_C e^{\varepsilon} - \mathcal{C}_{\mathcal{P}}\right) \sqrt{g}\, d\mathcal{V} \\ &= \int \delta\left(\mathcal{H}\left(\boldsymbol{r}'_{\boldsymbol{C}}, \boldsymbol{p}'_{\boldsymbol{C}}, \mathcal{P}_C\right) + \frac{p_\varepsilon^2}{2\,\mathcal{W}_{NH}} + \mathcal{C}_n k_B T \varepsilon - \mathcal{C}_H\right) \\ &\quad \times \delta\left(\mathcal{P}_C e^{\varepsilon} - \mathcal{C}_{\mathcal{P}}\right) e^{(3(N-1)+1)\varepsilon}\, d\boldsymbol{r}'_{\boldsymbol{C}}\, d\boldsymbol{p}'_{\boldsymbol{C}}\, d\mathcal{P}_C\, d\varepsilon\, dp_\varepsilon. \end{aligned} \tag{3.101}$$

If we set $\mathcal{C}_{\mathcal{P}}$ to zero, $\mathcal{P}_C$ vanishes, and the integration over $\mathcal{P}_C$ yields

[176, 177]

$$\begin{aligned}\Xi(\mathcal{C}_H,0) &= \int \delta\left(\mathcal{H}\left(\boldsymbol{r}_{\boldsymbol{C}}^{'},\boldsymbol{p}_{\boldsymbol{C}}^{'},\mathcal{P}_C\right)+\frac{p_\varepsilon^2}{2\,\mathcal{W}_{NH}}+\mathcal{C}_n k_B T\varepsilon-\mathcal{C}_H\right)\\ &\quad\times\delta\left(\mathcal{P}_C e^{\varepsilon}\right)e^{(3(N-1)+1)\varepsilon}\,d\boldsymbol{r}_{\boldsymbol{C}}^{'}\,d\boldsymbol{p}_{\boldsymbol{C}}^{'}\,d\mathcal{P}_C\,d\varepsilon\,dp_\varepsilon\\ &= \int \delta\left(\mathcal{H}\left(\boldsymbol{r}_{\boldsymbol{C}}^{'},\boldsymbol{p}_{\boldsymbol{C}}^{'},0\right)+\frac{p_\varepsilon^2}{2\,\mathcal{W}_{NH}}+\mathcal{C}_n k_B T\varepsilon-\mathcal{C}_H\right)\\ &\quad\times e^{-\varepsilon}\,e^{(3(N-1)+1)\varepsilon}\,d\boldsymbol{r}_{\boldsymbol{C}}^{'}\,d\boldsymbol{p}_{\boldsymbol{C}}^{'}\,d\varepsilon\,dp_\varepsilon. \end{aligned} \tag{3.102}$$

Here, the factor $e^{-\varepsilon}$ in the last line arises from property (C.6) of the δ-distribution. The remaining restriction in phase space determines ε:

$$\varepsilon = -\frac{1}{\mathcal{C}_n k_B T}\left(\mathcal{H}\left(\boldsymbol{r}_{\boldsymbol{C}}^{'},\boldsymbol{p}_{\boldsymbol{C}}^{'},0\right)+\frac{p_\varepsilon^2}{2\,\mathcal{W}_{NH}}-\mathcal{C}_H\right). \tag{3.103}$$

Hence, integrating over ε, we obtain [106]

$$\begin{aligned}\Xi(\mathcal{C}_H,0) &= \int e^{-\frac{3(N-1)}{\mathcal{C}_n k_B T}\left(\mathcal{H}\left(\boldsymbol{r}_{\boldsymbol{C}}^{'},\boldsymbol{p}_{\boldsymbol{C}}^{'},0\right)+\frac{p_\varepsilon^2}{2\,\mathcal{W}_{NH}}-\mathcal{C}_H\right)}\,dr_C^{'}\,dp_C^{'}\,dp_\varepsilon\\ &= e^{\frac{3(N-1)}{\mathcal{C}_n k_B T}\mathcal{C}_H}\int e^{-\frac{3(N-1)}{\mathcal{C}_n k_B T}\left(\mathcal{H}\left(\boldsymbol{r}_{\boldsymbol{C}}^{'},\boldsymbol{p}_{\boldsymbol{C}}^{'},0\right)\right)}\,dr_C^{'}\,dp_C^{'}\\ &\quad\times\int e^{-\frac{3(N-1)}{\mathcal{C}_n k_B T}\frac{p_\varepsilon^2}{2\,\mathcal{W}_{NH}}}\,dp_\varepsilon. \end{aligned} \tag{3.104}$$

If we choose $\mathcal{C}_n = 3N-3$, the physical variables are distributed (within constant prefactors) according to the canonical ensemble for a system consisting of $N-1$ particles. The ensemble averages obtained from the Nosé-Hoover equations of motion are thus canonical if the total linear momentum vanishes and the energy H_{NH} is conserved [106, 174, 177].

3.2 Monte Carlo simulations

One aim of Monte Carlo (MC) simulations is to evaluate ensemble averages of static equilibrium properties [72,106,107,178]. For instance, the average of an observable $\mathcal{A}$ in the canonical ensemble can be computed as the Boltzmann

weighted integral of instantaneous values $\mathcal{A}(\boldsymbol{\xi})$ over phase space [106, 107]:

$$\langle \mathcal{A} \rangle = \frac{\int \mathcal{A}(\boldsymbol{\xi})\, e^{-\beta \mathcal{H}(\boldsymbol{\xi})} d\boldsymbol{\xi}}{\int e^{-\beta \mathcal{H}(\boldsymbol{\xi})} d\boldsymbol{\xi}}. \tag{3.105}$$

Contrary to the molecular dynamics technique, the Monte Carlo method in its original form does not involve velocities or physical time [72, 106, 107, 178]. Instead, it uses random numbers to evolve a system through phase space [72, 106, 107, 178]. In the following, we discuss the theoretical foundations of Monte Carlo simulations. Subsequently, we turn our attention to few technical aspects. The spirit of the presentation is to provide the basis for the description of the transition path sampling technique in the next section. The basis of our exposition can be found in references [33, 72, 106, 107, 178].

3.2.1 Importance sampling

The Monte Carlo method evaluates the ensemble average $\langle \mathcal{A} \rangle$ using importance sampling. The idea behind importance sampling is to visit states in configuration space according to their (relative) equilibrium probabilities [72, 106, 107, 178]. In that case, the sample mean $\langle \mathcal{A} \rangle$, used as an unbiased estimate for the ensemble mean, is obtained from the unweighted average of data points [72, 106, 107]:

$$\langle \mathcal{A} \rangle = \frac{1}{\mathcal{N}_d} \sum_{j=1}^{\mathcal{N}_d} \mathcal{A}(t_j). \tag{3.106}$$

Here, $\mathcal{N}_d$ is the size of the sample, and t_j denotes the Monte Carlo time, which labels the random variables $\mathcal{A}(t_j)$. The weighting is included by the rules for visiting states in configuration space [72, 106, 107].

Importance sampling differs from random sampling in the following way. In the case of random sampling, states in configuration space are sampled with a uniform probability [106]. In particular, configurations with a low statistical weight are visited with the same likelihood as configurations with a high probability of occurrence [106]. Although the contribution of configurations with low statistical weight to the ensemble average is usually small,

the computational effort to sample such configurations by means of random sampling can be substantial for non-uniform probability functions. This use of resources is undesirable, and importance sampling, which preferentially visits configurations of large statistical weight, is thus the sampling method of choice [72, 106].

3.2.2 Markovian stochastic processes

To determine the rules for visiting states in configuration space according to their equilibrium probabilities, we first need to introduce the concept of a stochastic process. A stochastic process is a time series of random variables [33, 178]. In other words, it is a sequence of random variables ordered by the parameter time. In the present case, the stochastic process $\mathcal{A}(t)$ consists of the ordered sequence of random variables $\mathcal{A}(t_j)$ whose values are the instantaneous values of the observable $\mathcal{A}$.

To proceed, we need to identify how the stochastic process evolves from one random event to the next. This evolution is discussed below for the important class of stochastic processes that have the Markov property.

Let us consider a stochastic process $\mathcal{A}(t)$. If the probability $w(\mathcal{A}(t_{j+1}))$ of finding the system at time t_{j+1} depends on the state $\mathcal{A}(t_j)$ at the present time t_j only, the stochastic process is Markovian [33, 113]. In other words, only the present affects the immediate future of the stochastic process; its past has no influence. Mathematically, this corresponds to expressing the transition probability $w_t(\mathcal{A}(t_j) \to \mathcal{A}(t_{j+1}))$ of going from state $\mathcal{A}(t_j)$ to state $\mathcal{A}(t_{j+1})$ as a conditional probability [33, 113, 178]:

$$\begin{aligned} w_t\left(\mathcal{A}(t_j) \to \mathcal{A}(t_{j+1})\right) &= w\left(\mathcal{A}(t_{j+1})|\mathcal{A}(t_j)\right) \\ &= \frac{w\left(\mathcal{A}(t_{j+1}) \cap \mathcal{A}(t_j)\right)}{w\left(\mathcal{A}(t_j)\right)}. \end{aligned} \tag{3.107}$$

As a consequence, the probability of observing the series of outcomes $\mathcal{A}(t) =$

$\{\mathcal{A}(t_1), \ldots, \mathcal{A}(t_N)\}$ is [33]

$$\begin{aligned} w\left(\mathcal{A}(t)\right) &= w\left(\mathcal{A}(t_1) \cap \mathcal{A}(t_2) \cap \cdots \cap \mathcal{A}(t_{\mathcal{N}_d-1}) \cap \mathcal{A}(t_{\mathcal{N}_d})\right) \\ &= w\left(\mathcal{A}(t_1)\right) \prod_{j=1}^{\mathcal{N}_d-1} w\left(\mathcal{A}(t_{j+1})|\mathcal{A}(t_j)\right). \end{aligned} \tag{3.108}$$

In summary, a Markovian stochastic process is characterized by the transition probabilities w_t connecting the current state to the next. Put differently, the transition probabilities generate the Markovian stochastic process, an example of which is the random walk [33, 178]. Next, we consider what requirements the transition probabilities have to fulfill so that the random walk generates configurations according to their equilibrium distribution.

3.2.3 Conditions for the random walk and detailed balance

Two requirements for the transition probability of a random walk can be identified: ergodicity and generating the desired probability distribution [106, 178]. We shall discuss ergodicity first. Given any initial state with non-zero probability according to the target weight function, the random walk must ensure that any state belonging to the ensemble under consideration can be reached in principle [106, 178]. In practice, this requirement means that any point in configuration space must be accessible in a finite number of steps. Also, the time series of random events generated must not contain periodically reoccurring sequences [178].

We now turn our attention to the generation of the desired probability function. At the beginning of the Markovian stochastic process the probability distribution $w(t)$ will depend on time. For a sufficiently large random walk the probability function should become stationary and identical to the equilibrium distribution w_{eq} sought [106, 178].

One condition the transition probabilities must satisfy is that they maintain the equilibrium distribution once it has been reached [106]. Consequently, the number of systems going from state j to any other state k must

be balanced exactly by the number of systems moving from any state k to state j [106, 107]. This condition corresponds to the balance of occupation numbers for any state in an ensemble [107]:

$$\sum_k w(j)\, w_t(j \to k) = \sum_k w(k)\, w_t(k \to j). \tag{3.109}$$

In practice, one usually imposes the stricter constraint of detailed balance, which requires that the number of systems leaving state j to state k is equal to the number of systems going from state k to state j at any given time. This establishes a dynamical equilibrium according to the following expression [106, 107]:

$$w(j)\, w_t(j \to k) = w(k)\, w_t(k \to j). \tag{3.110}$$

If the transition probabilities are ergodic, satisfying detailed balance guarantees that the equilibrium distribution is reached asymptotically [106, 178].

3.2.4 Metropolis acceptance rule

The detailed balance condition (3.110) states that the ratio of transition probabilities underlying the random walk equals the ratio of equilibrium probabilities of the states involved [106, 178]. Hence, only relative probabilities are needed to generate a sequence of random events according to the desired probability distribution [106, 178]. In particular, the normalization factor, which is related to the (accessible) phase space volume, need not be computed [106, 178]. This is the reason why Monte Carlo procedures can be employed to evaluate ensemble averages [106, 178].

In practice, it is common to decompose the transition probability $w_t(j \to k)$ of going from state j to state k into two factors: the probability of proposing or generating a trial move $w_g(j \to k)$ and the probability of accepting the trial move $w_a(j \to k)$ [106, 178]:

$$w_t(j \to k) = w_g(j \to k)\, w_a(j \to k). \tag{3.111}$$

As a consequence, the ratio of acceptance probabilities according to the de-

tailed balance criterion becomes [72, 106, 178]

$$\frac{w_a(j \to k)}{w_a(k \to j)} = \frac{w(k)}{w(j)} \frac{w_g(k \to j)}{w_g(j \to k)}. \tag{3.112}$$

In a computer simulation we need to have a rule for the acceptance probability $w_a(j \to k)$ of going from state j to state k. The choice of Metropolis and co-workers [179] is

$$w_a(j \to k) = \min \left\{ \frac{w(k)}{w(j)} \frac{w_g(k \to j)}{w_g(j \to k)}, 1 \right\}. \tag{3.113}$$

To show that the Metropolis criterion for acceptance probabilities obeys detailed balance, we consider the two possible cases for the acceptance probability ratio [178]:

1. $\frac{w(k)}{w(j)} \frac{w_g(k \to j)}{w_g(j \to k)} \geq 1$ so that:

$$\begin{aligned} w_a(j \to k) &= 1; \\ w_a(k \to j) &= \frac{w(j)}{w(k)} \frac{w_g(j \to k)}{w_g(k \to j)}; \\ \frac{w_a(j \to k)}{w_a(k \to j)} &= \frac{w(k)}{w(j)} \frac{w_g(k \to j)}{w_g(j \to k)}; \end{aligned}$$

2. $\frac{w(k)}{w(j)} \frac{w_g(k \to j)}{w_g(j \to k)} < 1$ so that:

$$\begin{aligned} w_a(j \to k) &= \frac{w(k)}{w(j)} \frac{w_g(k \to j)}{w_g(j \to k)}; \\ w_a(k \to j) &= 1; \\ \frac{w_a(j \to k)}{w_a(k \to j)} &= \frac{w(k)}{w(j)} \frac{w_g(k \to j)}{w_g(j \to k)}. \end{aligned}$$

For the canonical ensemble and symmetric generation probilities the Metropolis criterion becomes [72, 106, 107]

$$w_a(j \to k) = \min \left\{ e^{-\beta(E_k - E_j)}, 1 \right\}. \tag{3.114}$$

Flexibility can be added to the Monte Carlo method by using asymmetric generation probabilities [106]. One such example used in this work will be presented in our treatment of transition path sampling below.

3.3 Transition path sampling

Transition path sampling [21, 23, 73–75] performs an importance sampling in trajectory space [21, 23]. In analogy to the Monte Carlo method presented in the previous section for configuration space a biased random walk is carried out in path space [21, 23]. Hence, pathways are visited according to their weight in the transition path ensemble [23, 73].

As in our presentation of the theoretical foundations of transition path sampling, we restrict attention to deterministic dynamics and equilibrium probability functions. The latter are reached asymptotically in an ergodic Markovian stochastic process as pointed out earlier. Our discussion follows references [21, 23, 73].

Transition path sampling generates a random walk in trajectory space by imposing detailed balance [73]. In path space the detailed balance condition implies that the ratio of transition probabilities w_t equals the ratio of reactive path weights w_{RP} of trajectories $x(t)$ [21, 73]:

$$\frac{w_t(\boldsymbol{\xi}^o(t) \to \boldsymbol{\xi}^n(t))}{w_t(\boldsymbol{\xi}^n(t) \to \boldsymbol{\xi}^o(t))} = \frac{w_{RP}[\boldsymbol{\xi}^n(t)]}{w_{RP}[\boldsymbol{\xi}^o(t)]}. \tag{3.115}$$

Here, properties associated with the current trajectory $\boldsymbol{\xi}^o(t)$ carry the superscript o, whereas the superscript n indicates quantities related to the proposed new trajectory $\boldsymbol{\xi}^n(t)$. For instance, $w_t(\boldsymbol{\xi}^o(t) \to \boldsymbol{\xi}^n(t))$ is the transition probability to move from the current trajectory to the new one. The probability $w_{RP}[\boldsymbol{\xi}^o(t)]$ of observing the current pathway is related to the weight $w[\boldsymbol{\xi}^o(t)]$ of any path given in equation (2.61) by [21, 73]

$$w_{RP}[\boldsymbol{\xi}^o(t)] = \theta_R(x_0^o)\, \theta_P(x_t^o)\, w[\boldsymbol{\xi}^o(t)]. \tag{3.116}$$

Hence, the indicator functions select reactive trajectories by probing whether

the system is in the reactants at the initial time slice ($t = 0$) and whether it is in the product state at the final time slice ($t = t$) [73].

To proceed, we express the transition probability as a product of generation (w_g) and acceptance (w_a) probabilities [21, 73]:

$$w_t(\boldsymbol{\xi}^o(t) \to \boldsymbol{\xi}^n(t)) = w_a(\boldsymbol{\xi}^o(t) \to \boldsymbol{\xi}^n(t))\, w_g(\boldsymbol{\xi}^o(t) \to \boldsymbol{\xi}^n(t)). \tag{3.117}$$

The ratio of acceptance probabilities is obtained from the detailed balance relation (3.115) [21, 73]:

$$\frac{w_a(\boldsymbol{\xi}^o(t) \to \boldsymbol{\xi}^n(t))}{w_a(\boldsymbol{\xi}^n(t) \to \boldsymbol{\xi}^o(t))} = \frac{w_{RP}[\boldsymbol{\xi}^n(t)]}{w_{RP}[\boldsymbol{\xi}^o(t)]} \frac{w_g(\boldsymbol{\xi}^n(t) \to \boldsymbol{\xi}^o(t))}{w_g(\boldsymbol{\xi}^o(t) \to \boldsymbol{\xi}^n(t))}. \tag{3.118}$$

As in the case of configurations, the Metropolis criterion is used to generate trajectories according to their weight in trajectory space [21, 73]:

$$w_a(\boldsymbol{\xi}^o(t) \to \boldsymbol{\xi}^n(t)) = \min\left\{1, \frac{w_{RP}[\boldsymbol{\xi}^n(t)]}{w_{RP}[\boldsymbol{\xi}^o(t)]} \frac{w_g(\boldsymbol{\xi}^n(t) \to \boldsymbol{\xi}^o(t))}{w_g(\boldsymbol{\xi}^o(t) \to \boldsymbol{\xi}^n(t))}\right\}. \tag{3.119}$$

We now turn to the question how trial pathways are generated. Transition path sampling usually uses two types of trial moves to propose a trial trajectory: shooting and shifting moves [21, 23, 74]. We shall discuss these in turn below.

3.3.1 Shooting moves

Given a current reactive trajectory $\boldsymbol{\xi}^o(t)$, shooting moves provide a means to generate a trial trajectory $\boldsymbol{\xi}^n(t)$ that is accepted according to the Metropolis criterion (3.119) stated above. Shooting moves are essential for ergodic sampling because shifting moves, described in the next section, do not exhibit this property [21, 106].

The generation of a trial pathway involves the modification of a randomly chosen phase space point, called shooting point, and the subsequent propagation of the system forward and backward in time. For Hamiltonian dynamics the shooting point is commonly modified by changing the momenta [21]. As a result, the initial conditions are different, leading to different phase space

trajectories [33, 165].[14]

We now discuss how large the momentum change should be. This issue is affected by the Lyapunov instability. We have seen in section 3.1 that the equations of motion of a Hamiltonian system are deterministic. In other words, the time evolution of a system is known for all future and past times if a single phase space point along the system's trajectory is known *exactly* [165]. This implies that trajectories in phase space do not cross if their initial phase space points are different [165]. The above remarks relate to the determinism of dynamical trajectories [180]. However, although Hamiltonian dynamics are deterministic, phase space trajectories might not be predictable [180]. The lack of predictability is due to the possible instability of the trajectories [180]. Stability of the solution of the dynamical differential equations implies that two trajectories that are initially close will deviate from one another more slowly than a function linear in time [180]. If a system's time evolution is not stable in the above sense, the system is sensitive to the initial conditions and its time evolution cannot be predicted [180]. This so-called Lyapunov instability leads to an exponential divergence of initially close trajectories after a characteristic time [21, 106, 134, 180–183].

In practice, the numerical precision on a computer implies that we cannot know the initial state of the system exactly. It therefore follows that the time evolution of a complex system becomes unpredictable in practice [180]. As a result, if the momentum change is too large, the Lyapunov instability causes the trial trajectory to be very different from the original one. Hence, the probability that the trial pathway is reactive will be low, resulting in a low acceptance probability. On the other hand, if the momentum change is too small, the new trajectory will be very similar to the current one. Consequently, the sampling through trajectory space will be slow [21].

The present work reports transition path sampling simulations in the microcanonical and canonical ensembles. We employ symmetric generation probabilities for trial trajectories in the microcanonical ensemble and an

[14]The modification of the shooting point can be omitted if stochastic dynamics is employed. In that case, the stochastic elements of the propagation dynamics yield different trajectories even for identical initial conditions [21].

asymmetric generation probability [141] in the canonical ensemble. This asymmetric generation probability and the motivation for employing it are outlined in the next section. Here, we describe the shooting procedure for the microcanonical ensemble and indicate where it differs from that for the canonical ensemble.

As mentioned above, a shooting move consists of four steps: selecting a shooting slice, modifying the shooting slice, dynamically propagating the system, accepting or rejecting the trial move [21]. The only difference between ensembles involves the modification of the shooting slice. Below, we describe the four steps of the shooting procedure in more detail.

In the first step a phase space point along the trajectory is selected at random. The present work employs a uniform distribution to select the shooting slice. The second step, namely the modification of the shooting slice, is divided into three stages. First, we add a small momentum change drawn from a normal distribution to the old momenta of the shooting slice [184]. Subsequently, possible constraints need to be satisfied, and the centre-of-mass motion is removed [184]. We then scale the velocities to the desired kinetic energy [184].

It is at this point that the procedure differs depending on the ensemble. For the microcanonical ensemble the velocities are scaled in such a way that the new kinetic energy equals the old one. On the other hand, the velocities are scaled to a kinetic energy determined by the Maxwell-Boltzmann distribution in the canonical ensemble. Hence, the kinetic energies differ between the shooting points of the current trajectory and the trial pathway [21, 73]. As a result, another acceptance criterion is introduced for the shooting point when the canonical ensemble is sampled. If the shooting point is rejected, we reject the shooting move. If the shooting point is accepted, the procedures for the canonical and microcanonical ensembles become identical again and continue with the third step.

In particular, the trial pathway is propagated forwards in time from the shooting slice up to time t of the path length. If the end point $\boldsymbol{\xi}_t$ is in the product state, we pursue the trial move; otherwise, the shooting move is rejected. To proceed, the trial path is grown backwards in time to the

initial time slice $\boldsymbol{\xi}_0$ at time $t = 0$. This is done by inverting the momenta of the shooting slice, propagating forwards in time, and inverting the momenta of the added path segment. This ensures that the momenta of the entire trajectory are in the forward propagation direction of time [21, 73].

The last step is the acceptance or rejection of the trial trajectory. If the initial phase space point belongs to the reactant region and if the final time slice lies in the product region, the trial trajectory is accepted. It is rejected otherwise [21, 73].

In summary, we accept a trial trajectory if the shooting point is accepted, and if the new trajectory is reactive. The reactive trajectory then becomes the current trajectory. If the shooting move is aborted at any time, the old trajectory is kept as the current one, and a new trial move is attempted [21, 73].

Below, we quantify the criterion (3.119) for accepting a trial trajectory. To do so, we write out the path weight $w_{RP}[\boldsymbol{\xi}(t)]$ and note that the probability for generating a new trajectory from an old one is the probability of generating a new shooting slice times the probability of dynamically growing a new pathway [21]:

$$w_g(\boldsymbol{\xi}^o(t) \to \boldsymbol{\xi}^n(t)) = w_g(\boldsymbol{\xi}^o_s \to \boldsymbol{\xi}^n_s) \prod_{j=s}^{\mathcal{N}-1} \varphi(\boldsymbol{\xi}^n_{j\Delta t} \to \boldsymbol{\xi}^n_{(j+1)\Delta t}) \times \prod_{j=1}^{s} \bar{\varphi}(\boldsymbol{\xi}^n_{j\Delta t} \to \boldsymbol{\xi}^n_{(j-1)\Delta t}). \tag{3.120}$$

We denote the dynamical forward and backward transition probabilities by φ and $\bar{\varphi}$. Also, s indicates the shooting slice. The time slices carry indices from 0 to $\mathcal{N}$ so that the total trajectory consists of $\mathcal{N} + 1 = t/\Delta t + 1$ phase space points. Using a similar expression for the generation probability of the old trajectory from the new one yields for the last term in the min-function

of the Metropolis acceptance criterion (3.119) [21, 73]

$$
\begin{aligned}
&\frac{w_{RP}[\boldsymbol{\xi}^n(t)]}{w_{RP}[\boldsymbol{\xi}^o(t)]}\frac{w_g(\boldsymbol{\xi}^n(t)\to\boldsymbol{\xi}^o(t))}{w_g(\boldsymbol{\xi}^o(t)\to\boldsymbol{\xi}^n(t))}\\
&\quad=\theta_R(x_0^n)\,\theta_P(x_t^n)\frac{\rho(\boldsymbol{\xi}_0^n)}{\rho(\boldsymbol{\xi}_0^o)}\frac{\prod_{j=0}^{\mathcal{N}-1}\varphi(\boldsymbol{\xi}_{j\Delta t}^n\to\boldsymbol{\xi}_{(j+1)\Delta t}^n)}{\prod_{j=0}^{\mathcal{N}-1}\varphi(\boldsymbol{\xi}_{j\Delta t}^o\to\boldsymbol{\xi}_{(j+1)\Delta t}^o)}\\
&\qquad\times\frac{w_g(\boldsymbol{\xi}_s^n\to\boldsymbol{\xi}_s^o)\prod_{j=s}^{\mathcal{N}-1}\varphi(\boldsymbol{\xi}_{j\Delta t}^o\to\boldsymbol{\xi}_{(j+1)\Delta t}^o)\prod_{j=1}^{s}\bar{\varphi}(\boldsymbol{\xi}_{j\Delta t}^o\to\boldsymbol{\xi}_{(j-1)\Delta t}^o)}{w_g(\boldsymbol{\xi}_s^o\to\boldsymbol{\xi}_s^n)\prod_{j=s}^{\mathcal{N}-1}\varphi(\boldsymbol{\xi}_{j\Delta t}^n\to\boldsymbol{\xi}_{(j+1)\Delta t}^n)\prod_{j=1}^{s}\bar{\varphi}(\boldsymbol{\xi}_{j\Delta t}^n\to\boldsymbol{\xi}_{(j-1)\Delta t}^n)}\\
&\quad=\theta_R(x_0^n)\,\theta_P(x_t^n)\frac{\rho(\boldsymbol{\xi}_0^n)}{\rho(\boldsymbol{\xi}_0^o)}\frac{w_g(\boldsymbol{\xi}_s^n\to\boldsymbol{\xi}_s^o)}{w_g(\boldsymbol{\xi}_s^o\to\boldsymbol{\xi}_s^n)}\\
&\qquad\times\frac{\prod_{j=0}^{s-1}\varphi(\boldsymbol{\xi}_{j\Delta t}^n\to\boldsymbol{\xi}_{(j+1)\Delta t}^n)}{\prod_{j=0}^{s-1}\varphi(\boldsymbol{\xi}_{j\Delta t}^o\to\boldsymbol{\xi}_{(j+1)\Delta t}^o)}\frac{\prod_{j=0}^{s-1}\bar{\varphi}(\boldsymbol{\xi}_{(j+1)\Delta t}^o\to\boldsymbol{\xi}_{j\Delta t}^o)}{\prod_{j=0}^{s-1}\bar{\varphi}(\boldsymbol{\xi}_{(j+1)\Delta t}^n\to\boldsymbol{\xi}_{j\Delta t}^n)}.
\end{aligned}
\tag{3.121}
$$

To reach the last equality, we have shifted the index by one unit and simplified terms common in the path weight and the generation probabilities [21].

To proceed, we seek a relation between the transition probabilities for dynamical forward and backward propagation. For Hamiltonian dynamics this relation becomes [21, 165]

$$
\frac{\varphi(\boldsymbol{\xi}_{j\Delta t}\to\boldsymbol{\xi}_{(j+1)\Delta t})}{\bar{\varphi}(\boldsymbol{\xi}_{(j+1)\Delta t}\to\boldsymbol{\xi}_{j\Delta t})}=1. \tag{3.122}
$$

This result can be understood as follows. Let us write the time evolution operator $\phi_{\Delta t}(\boldsymbol{\xi})=e^{\imath\mathcal{L}\Delta t}$ propagating the system from time slice j to $j+1$ and its inverse $\phi_{-\Delta t}(\boldsymbol{\xi})=e^{-\imath\mathcal{L}\Delta t}$ according to equation (3.123) [21]:

$$
\boldsymbol{\xi}_{(j+1)\Delta t}=\phi_{\Delta t}(\boldsymbol{\xi}_{j\Delta t}); \tag{3.123a}
$$

$$
\boldsymbol{\xi}_{j\Delta t}=\phi_{-\Delta t}(\boldsymbol{\xi}_{(j+1)\Delta t}). \tag{3.123b}
$$

Then, equation (3.122) can be written as [21]

$$
\frac{\varphi(\boldsymbol{\xi}_{j\Delta t}\to\boldsymbol{\xi}_{(j+1)\Delta t})}{\bar{\varphi}(\boldsymbol{\xi}_{(j+1)\Delta t}\to\boldsymbol{\xi}_{j\Delta t})}=\frac{\delta(\boldsymbol{\xi}_{(j+1)\Delta t}-\phi_{\Delta t}(\boldsymbol{\xi}_{j\Delta t}))}{\delta(\boldsymbol{\xi}_{j\Delta t}-\phi_{-\Delta t}(\boldsymbol{\xi}_{(j+1)\Delta t}))}=\left|\frac{\partial\phi}{\partial\boldsymbol{\xi}}\right|^{-1}=1. \tag{3.124}
$$

To arrive at the third term, we have regarded the argument of the δ-distribution

in the numerator as a function of $\boldsymbol{\xi}_{j\Delta t}$ and used property (C.6) for δ-distributions. The final equation results if we consider the time evolution of the system from phase space point $\boldsymbol{\xi}_{j\Delta t}$ to $\boldsymbol{\xi}_{(j+1)\Delta t}$ as a coordinate transformation between two sets of variables. For Hamiltonian dynamics this coordinate transformation is canonical [165]. Consequently, the absolute value of the Jacobian determinant is unity [165].

Another way of obtaining equation (3.122) considers the principle of microscopic reversibility [21, 107]:

$$\frac{\varphi(\boldsymbol{\xi}_{j\Delta t} \to \boldsymbol{\xi}_{(j+1)\Delta t})}{\bar{\varphi}(\boldsymbol{\xi}_{(j+1)\Delta t} \to \boldsymbol{\xi}_{j\Delta t})} = \frac{\rho(\boldsymbol{\xi}_{(j+1)\Delta t})}{\rho(\boldsymbol{\xi}_{j\Delta t})} = 1. \tag{3.125}$$

Because the Hamiltonian is conserved along a trajectory, the probabilities $\rho(\boldsymbol{\xi})$ of being at time slices j and $j+1$ are equal, and equation (3.122) follows [21,165]. Hence, equation (3.119) for an arbitrary generation probability ratio of shooting points reduces to [21]

$$w_a(\boldsymbol{\xi}^o(t) \to \boldsymbol{\xi}^n(t)) = \theta_R(x_0^n)\,\theta_P(x_t^n)\min\left\{1, \frac{\rho(\boldsymbol{\xi}_0^n)}{\rho(\boldsymbol{\xi}_0^o)}\frac{w_g(\boldsymbol{\xi}_s^n \to \boldsymbol{\xi}_s^o)}{w_g(\boldsymbol{\xi}_s^o \to \boldsymbol{\xi}_s^n)}\right\}. \tag{3.126}$$

Until now, the quantification above has been general for Hamiltonian dynamics. Below, we distinguish between the microcanonical and canonical procedures used in the present document. In the microcanonical ensemble we use symmetric shooting point generation probabilities. Furthermore, the weight of the initial phase space point is the same for the old and new trajectories because all allowed phase space points are equally likely in the microcanonical ensemble [72, 113]. Consequently, equation (3.126) simplifies to [21]

$$w_a(\boldsymbol{\xi}^o(t) \to \boldsymbol{\xi}^n(t)) = \theta_R(x_0^n)\,\theta_P(x_t^n). \tag{3.127}$$

A trial trajectory is therefore accepted if it is reactive.

For the canonical case we note that the probability of finding the system at any phase space point along a given trajectory is the same because the system's dynamics is Hamiltonian and Liouville's theorem is satisfied. We can therefore shift the ratio of phase space point weights from the initial slice

to the shooting slice $\boldsymbol{\xi}_s$ and obtain [21, 73]

$$w_a(\boldsymbol{\xi}^o(t) \to \boldsymbol{\xi}^n(t)) = \theta_R(x_0^n)\,\theta_P(x_t^n)\min\left\{1, \frac{\rho(\boldsymbol{\xi}_s^n)}{\rho(\boldsymbol{\xi}_s^o)}\frac{w_g(\boldsymbol{\xi}_s^n \to \boldsymbol{\xi}_s^o)}{w_g(\boldsymbol{\xi}_s^o \to \boldsymbol{\xi}_s^n)}\right\}. \quad (3.128)$$

In this work we employ an asymmetric shooting slice generation probability, described next.

3.3.2 Asymmetric generation probability for shooting moves

As in reference [141], the trajectories in our transition path ensemble are short. Hence, the Lyapunov instability is unlikely to produce sufficiently large deviations for small momentum changes. Larger momentum changes probably involve relatively large changes in energy and lead to low acceptance probabilities [21, 141]. This difficulty is overcome by a method capable of generating large momentum changes with moderate changes in the kinetic energy [141].

The method concerns the shooting slice modification step of a shooting trial move, as outlined in the preceding subsection. As mentioned there, the shooting slice manipulation consists of changing the momenta and selecting a new kinetic energy. The key feature of the method [141] is to propose a new shooting point with an asymmetric generation probability. In particular, we choose a symmetric generation probability for the momentum changes. However, a Monte Carlo procedure (additional to the one for the overall shooting attempt) is employed to obtain the new from the old kinetic energy in an asymmetric manner. This key asymmetric generation probability is summarized next and described in more detail below [21, 141].

Given a randomly chosen shooting point along an old reactive trajectory, the practical steps for obtaining the modified shooting slice are as follows:

1. Add a momentum displacement $\Delta p_{C,j} = \alpha\sqrt{m_j k_B T}$ (α governs the magnitude of the momentum change) drawn from a normal distribution to all Cartesian momentum components so that $p_{C,j}^{(0)} \to p_{C,j}^{(1)} = p_{C,j}^{(0)} + \Delta p_{C,j}$

2. Apply the constraint of vanishing total linear momentum component $p_{C,j}^{(1)} \rightarrow p_{C,j}^{(2)} = p_{C,j}^{(1)} - \frac{m_j}{\mathcal{M}} \sum_{j=1}^{j=N} p_{C,j}^{(1)}$

3. Satisfy the hidden constraints for the momenta resulting from the constraints for the bond lengths via the RATTLE algorithm $p_{C,j}^{(2)} \rightarrow p_{C,j}^{(3)}$

4. Select a new kinetic energy K_s^n according to the canonical distribution

   (a) Draw a random kinetic energy change $\Delta K = K_s^n - K_s^o$ from a normal distribution

   (b) Accept the new kinetic energy with probability $w_a^{'}\left(K_s^o \rightarrow K_s^n\right) = \min\left\{1, e^{-\beta(K_s^n - K_s^o)} \left(\frac{K_s^n}{K_s^o}\right)^{\mathcal{N}_f/2-1}\right\}$

5. Scale the momenta so that $p_{C,j}^{(3)} \rightarrow p_{C,j}^{(4)} = \sqrt{\frac{K_s^n}{K_s^o}} p_{C,j}^{(3)}$ if the proposed kinetic energy has been accepted

Our specific aim in this subsection is to compute the last term in the min-function of equation (3.128). As in reference [21], our choice for the ratio of the asymmetric generation probabilities is

$$\frac{w_g(\boldsymbol{\xi}_s^n \rightarrow \boldsymbol{\xi}_s^o)}{w_g(\boldsymbol{\xi}_s^o \rightarrow \boldsymbol{\xi}_s^n)} = \frac{\omega(K_s^o)}{\omega(K_s^n)} \frac{dK_s^o}{dK_s^n} \frac{\prod_{j=1}^{\mathcal{N}_f} \delta\left(p_{C,j,s}^o - \sqrt{\frac{K_s^o}{K_s^n}}\, p_{C,j,s}^n\right)}{\prod_{j=1}^{\mathcal{N}_f} \delta\left(p_{C,j,s}^n - \sqrt{\frac{K_s^n}{K_s^o}}\, p_{C,j,s}^o\right)}. \tag{3.129}$$

Here, the kinetic energy probability density at the shooting slice s is denoted by $\omega(K_s)$, and the δ-distributions impose constraints on the relationship between the old and new momenta.

We shall discuss the individual contributions to equation (3.129) in turn, namely the ratio of kinetic energy probability densities, the ratio of kinetic energy differentials and the ratio of products of δ-distributions.

Starting with the ratio of kinetic energy probability densities, we employ the above-mentioned additional Monte Carlo procedure of equation (3.130), which is indicated by primed acceptance probabilities $w_a^{'}$, to generate kinetic energies according to their equilibrium weight $\omega(K)$ (see equation (3.131)). Following reference [141], we denote the current kinetic energy by K_s^o. The

trial kinetic energy $K_s^n = K_s^o + \Delta K$ is obtained by adding a random kinetic energy ΔK drawn from a normal distribution. As a consequence, the generation probabilities for the trial kinetic energies are symmetric, and their ratio $\frac{w_g'(K_s^n \to K_s^o)}{w_g'(K_s^o \to K_s^n)} = 1$ can be omitted from equation (3.130) if detailed balance is imposed. The following acceptance probability ratio for the kinetic energy results [141]:

$$\frac{w_a'(K_s^o \to K_s^n)}{w_a'(K_s^n \to K_s^o)} = \frac{\omega(K_s^n)}{\omega(K_s^o)}. \tag{3.130}$$

To proceed, we use the kinetic energy probability density in the canonical ensemble, discussed in section C.3 [141]:

$$\omega(K) = \mathcal{C} e^{-\beta K} K^{\mathcal{N}_f/2-1}. \tag{3.131}$$

Above, $\mathcal{N}_f$ denotes the number of degrees of freedom, and $\mathcal{C}$ is a normalizing factor. Inserting the kinetic energy probability density (3.131) into equation (3.130) for the acceptance ratio of kinetic energies and employing the Metropolis acceptance criterion, we obtain [141]

$$w_a'(K_s^o \to K_s^n) = \min\left\{1,\, e^{-\beta(K_s^n - K_s^o)} \left(\frac{K_s^n}{K_s^o}\right)^{\mathcal{N}_f/2-1}\right\}. \tag{3.132}$$

Because the inverse of equation (3.130) enters equation (3.129), the contribution of the kinetic energy densities to the asymmetric kinetic energy generation probability is

$$\frac{\omega(K_s^o)}{\omega(K_s^n)} = e^{-\beta(K_s^o - K_s^n)} \left(\frac{K_s^o}{K_s^n}\right)^{\mathcal{N}_f/2-1}. \tag{3.133}$$

We now turn to the ratio of kinetic energy differentials whose contribution to equation (3.129) reads

$$\frac{dK_s^o}{dK_s^n} = \frac{K_s^o}{K_s^n}. \tag{3.134}$$

This result follows from the definition of the kinetic energy $K = \sum_{j=1}^{\mathcal{N}_f} \frac{p_{C,j}^2}{2\,m_j}$

and from the constraints imposed by the δ-distributions on the momenta:

$$p^o_{C,j,s} = \sqrt{\frac{K^o_s}{K^n_s}}\, p^n_{C,j,s}; \tag{3.135a}$$

$$dp^o_{C,j,s} = \sqrt{\frac{K^o_s}{K^n_s}}\, dp^n_{C,j,s}. \tag{3.135b}$$

To establish equation (3.134), we express the differential dK^o_s of the current kinetic energy at the shooting slice K^o_s in terms of the differential dK^n_s of the new kinetic energy:

$$\begin{aligned} dK^o_s &= \sum_{j=1}^{\mathcal{N}_f} \frac{\partial K^o_s}{\partial p^o_{C,j,s}} dp^o_{C,j,s} = \sum_{j=1}^{\mathcal{N}_f} \frac{p^o_{C,j,s}}{m_j} dp^o_{C,j,s} = \sum_{j=1}^{\mathcal{N}_f} \frac{K^o_s}{K^n_s} \frac{p^n_{C,j,s}}{m_j} dp^n_{C,j,s} \\ &= \sum_{j=1}^{\mathcal{N}_f} \frac{K^o_s}{K^n_s} \frac{\partial K^n_s}{\partial p^n_{C,j,s}} dp^n_{C,j,s} = \frac{K^o_s}{K^n_s} dK^n_s. \end{aligned} \tag{3.136}$$

Next, we consider the contribution arising from the ratio of products of δ-distributions to equation (3.129). To simplify the ratio of δ-distributions, we employ equation (C.6) for any function $f(y)$:

$$\int_{-\infty}^{\infty} \delta\left(f(y)\right)\, dy = \int_{-\infty}^{\infty} \sum_{y_j : f(y_j)=0} \frac{\delta(y - y_j)}{\left| \left.\frac{\partial f}{\partial y}\right|_{y_j} \right|}\, dy. \tag{3.137}$$

We obtain for one momentum degree of freedom with $f(p^o_{j,s}) = p^n_{j,s} - \sqrt{\frac{K^n_s}{K^o_s}} p^o_{j,s}$

$$\delta\left(p^n_{C,j,s} - \sqrt{\frac{K^n_s}{K^o_s}} p^o_{C,j,s}\right) = \frac{\delta\left(p^o_{C,j,s} - \sqrt{\frac{K^o_s}{K^n_s}} p^n_{C,j,s}\right)}{\left| -\sqrt{\frac{K^n_s}{K^o_s}} \right|}. \tag{3.138}$$

Because there are $\mathcal{N}_f$ degrees of freedom, the ratio involving δ-distributions contributes a factor $\left(\frac{K^n_s}{K^o_s}\right)^{\mathcal{N}_f/2}$ to equation (3.129) for the ratio of asymmetric generation probabilities. Collecting the contributions from all three ratios

considered, we have for the generation probability ratio [141]

$$\begin{aligned}\frac{w_g(\boldsymbol{\xi}_s^n \to \boldsymbol{\xi}_s^o)}{w_g(\boldsymbol{\xi}_s^o \to \boldsymbol{\xi}_s^n)} &= e^{-\beta(K_s^o - K_s^n)} \left(\frac{K_s^o}{K_s^n}\right)^{\mathcal{N}_f/2-1} \frac{K_s^o}{K_s^n} \left(\frac{K_s^n}{K_s^o}\right)^{\mathcal{N}_f/2} \\ &= e^{-\beta(K_s^o - K_s^n)}. \end{aligned} \tag{3.139}$$

We are now in a position to insert the ratio of generation probabilities (3.139) into the acceptance probability for a proposed shooting move (3.128) using the Metropolis criterion [21, 141]:

$$\begin{aligned} w_a(\boldsymbol{\xi}^o(t) \to \boldsymbol{\xi}^n(t)) &= \theta_R(x_0^n)\, \theta_P(x_t^n) \min\left\{1, \frac{\rho(\boldsymbol{\xi}_s^n)}{\rho(\boldsymbol{\xi}_s^o)} \frac{w_g(\boldsymbol{\xi}_s^n \to \boldsymbol{\xi}_s^o)}{w_g(\boldsymbol{\xi}_s^o \to \boldsymbol{\xi}_s^n)}\right\} \\ &= \theta_R(x_0^n)\, \theta_P(x_t^n) \min\left\{1, \frac{e^{-\beta\mathcal{H}(\boldsymbol{\xi}_s^n)}}{e^{-\beta\mathcal{H}(\boldsymbol{\xi}_s^o)}} \frac{e^{-\beta K(\boldsymbol{\xi}_s^o)}}{e^{-\beta K(\boldsymbol{\xi}_s^n)}}\right\} \\ &= \theta_R(x_0^n)\, \theta_P(x_t^n). \end{aligned} \tag{3.140}$$

The last equation results because the modification of the shooting slice affects momenta and kinetic energies only; the particle positions and the potential energy remain unaltered. The proposed shooting slice is thus accepted if we accept the kinetic energy proposed according to the asymmetric generation probability described above. Consequently, we accept a trial trajectory in the canonical ensemble if it is reactive.

3.3.3 Shifting moves

In this section we give a brief account of shifting moves following references [21, 164]. A shifting move consists in moving the time origin of a pathway by an amount Δt_s. If the path segment Δt_s is positive, we have a forward shifting move. In contrast, a backward shifting move has a negative Δt_s [73].

We shall next describe the practical implementation of shifting moves [21]. To start, let us consider a forward shifting move. In that case, a path segment of length Δt_s is appended at the end of the current trajectory. At the same time, the first time slices whose combined length equals Δt_s are removed from the trial trajectory. On the other hand, a backward shifting move deletes

the final segment Δt_s of the original path. Then, the new path segment is propagated backwards in time starting from the initial time slice [21]. In practice, this is done in the following way. The momenta at the initial time slice are inverted. Next, the equations of motion are integrated for a time Δt_s, and the momenta of all time slices of the newly grown trajectory segment are reversed.

Irrespective of the shifting direction, trial trajectories are accepted if they are reactive in the case of Hamiltonian dynamics [21]. To see this, we impose detailed balance between a given forward shifting move and the corresponding backward shifting move that reverts the effect of the former so that the final pathway corresponds to the initial trajectory. In mathematical terms, we have [21]

$$\frac{w_{a,f}(\boldsymbol{\xi}^o(t) \to \boldsymbol{\xi}^n(t))}{w_{a,b}(\boldsymbol{\xi}^n(t) \to \boldsymbol{\xi}^o(t))} = \frac{w_{RP}[\boldsymbol{\xi}^n(t)]}{w_{RP}[\boldsymbol{\xi}^o(t)]} \frac{w_{g,b}(\boldsymbol{\xi}^n(t) \to \boldsymbol{\xi}^o(t))}{w_{g,f}(\boldsymbol{\xi}^o(t) \to \boldsymbol{\xi}^n(t))}. \tag{3.141}$$

In the above equation the subscripts f and b indicate properties referring to forward and backward shifting moves. Here, we consider a pair of forward and backward shifting moves that involves $\mathcal{N}_s$ time slices and label all time slices in terms of the old pathway. In particular, the indices for the phase space points run from 0 to $\mathcal{N} + \mathcal{N}_s$. With this notational convention we obtain for equation (3.141) [21]

$$\begin{aligned}
\frac{w_{a,f}(\boldsymbol{\xi}^o(t) \to \boldsymbol{\xi}^n(t))}{w_{a,b}(\boldsymbol{\xi}^n(t) \to \boldsymbol{\xi}^o(t))} &= \theta_R(x_0^n)\theta_P(x_t^n) \frac{\rho(\boldsymbol{\xi}_0^n)}{\rho(\boldsymbol{\xi}_0^o)} \frac{\prod_{j=\mathcal{N}_s}^{\mathcal{N}-1+\mathcal{N}_s} \varphi(\boldsymbol{\xi}_{j\Delta t}^n \to \boldsymbol{\xi}_{(j+1)\Delta t}^n)}{\prod_{j=0}^{\mathcal{N}-1} \varphi(\boldsymbol{\xi}_{j\Delta t}^o \to \boldsymbol{\xi}_{(j+1)\Delta t}^o)} \\
&\times \frac{\prod_{j=\mathcal{N}_s}^{\mathcal{N}-1} \varphi(\boldsymbol{\xi}_{j\Delta t}^o \to \boldsymbol{\xi}_{(j+1)\Delta t}^o) \prod_{j=0}^{\mathcal{N}_s-1} \bar{\varphi}(\boldsymbol{\xi}_{(j+1)\Delta t}^o \to \boldsymbol{\xi}_{j\Delta t}^o)}{\prod_{j=\mathcal{N}_s}^{\mathcal{N}-1} \varphi(\boldsymbol{\xi}_{j\Delta t}^n \to \boldsymbol{\xi}_{(j+1)\Delta t}^n) \prod_{j=\mathcal{N}}^{\mathcal{N}-1+\mathcal{N}_s} \varphi(\boldsymbol{\xi}_{j\Delta t}^n \to \boldsymbol{\xi}_{(j+1)\Delta t}^n)} \\
&= \theta_R(x_0^n)\theta_P(x_t^n) \frac{\rho(\boldsymbol{\xi}_0^n)}{\rho(\boldsymbol{\xi}_0^o)} \frac{\prod_{j=0}^{\mathcal{N}_s-1} \bar{\varphi}(\boldsymbol{\xi}_{(j+1)\Delta t}^o \to \boldsymbol{\xi}_{j\Delta t}^o)}{\prod_{j=0}^{\mathcal{N}_s-1} \varphi(\boldsymbol{\xi}_{j\Delta t}^o \to \boldsymbol{\xi}_{(j+1)\Delta t}^o)}.
\end{aligned} \tag{3.142}$$

As mentioned in the section describing shooting moves, Hamiltonian dynamics conserves the total energy of the system and satisfy equation (3.122) [165]. Accordingly, the acceptance probabilities for forward and backward shifting moves reduce to equations (3.143), which state that a shifting move

is accepted if it still connects the reactant and product states [21]

$$w_{a,f}(\boldsymbol{\xi}^o(t) \to \boldsymbol{\xi}^n(t)) = \theta_R(x_0^n)\theta_P(x_t^n); \tag{3.143a}$$

$$w_{a,b}(\boldsymbol{\xi}^n(t) \to \boldsymbol{\xi}^o(t)) = \theta_R(x_0^o)\theta_P(x_t^o). \tag{3.143b}$$

Shifting moves are employed to reduce the statistical noise of transition path sampling simulations [73]. Shifting moves are not ergodic because they do not alter the nature of a given trajectory [21,106,164]. Hence, they should only be used in combination with shooting moves.

Having outlined shooting and shifting moves as part of a biased random walk in trajectory space, we close our discussion of tools to harvest reactive trajectories. In the following, we shall turn to the analysis of the transition path ensemble.

3.3.4 Committor, reaction coordinate and transition state

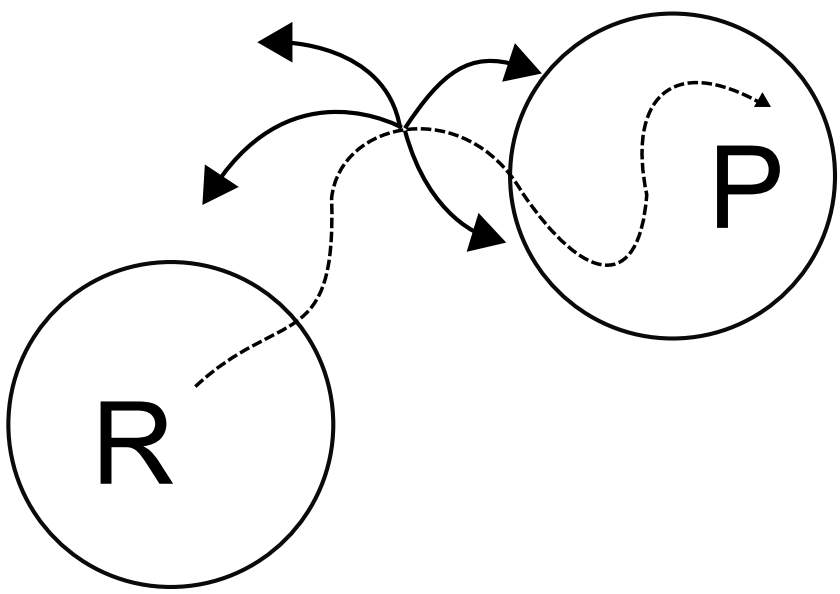

Figure 3.1: The committor calculation of equation (3.145) is illustrated as a set of fleeting trajectories (solid lines) from a configuration of a reactive path (dashed line) to estimate the relaxation probability to the product state (P).

Once a set of reactive trajectories has been obtained, this transition path ensemble can be analyzed to provide insight about the molecular mechanism of the activated process under consideration [21, 73]. A detailed understanding of the reaction mechanism requires identification of the reaction coordinate [21, 73, 82, 140], which consists of dynamically relevant physical degrees of freedom that drive the transition [21, 22, 73, 77, 82, 140]. Hence, motion along the reaction coordinate is necessary to pass the dynamical bottleneck of the reaction, namely the transition state, located between reactants and products [22, 77, 123]. This dynamical relevance distinguishes reaction coordinates from order parameters, used to separate (meta-)stable regions in phase space [21, 73, 140]. In addition, the reaction coordinate provides both a dynamical [22, 77, 140] and a statistical [21, 73, 77, 78, 81, 140, 185] measure for the progress of the reaction.

One such statistical measure for the advancement of the reaction is the committor [21, 73, 77–79, 81, 140, 185]. Two definitions of the committor are common. In the first definition, the committor is the probability of reaching the product state before reaching the reactant state if the system is launched from a configuration with momenta randomly drawn from the Maxwell-Boltzmann distribution [22, 77–79, 81–83, 140]. In that case, the committor is time-independent and defined in terms of a configuration although, in principle, it is a function of all phase space variables [22, 81, 140]. In the second definition, the committor is time-dependent and consists of the fraction of trajectories launched from a given configuration reaching the product state within a specified time t_{ft} [21, 73, 123]. If the specified time satisfies the plateau time property $\tau_{mol} \ll t_{ft} \ll \tau_{rxn}$ [9, 12] of an activated process, the two definitions are essentially identical because the latter becomes insensitive to the exact length t_{ft} of the fleeting trajectories [21]. The separation of timescales implies that the system relaxes to one of the stable states on a molecular timescale τ_{mol} [21], whereas subsequent spontaneous transitions typically require times of the order of the reaction time τ_{rxn} [21]. We shall therefore assume that the committor is independent of time for $\tau_{mol} < t_{ft} \ll \tau_{rxn}$.

Following references [21, 73], we define the committor as

$$w_P(r_x, t_{ft}) = \frac{\int \delta\left(r_x'(\boldsymbol{\xi}_0) - r_x\right)\, \theta_P(x_{t_{ft}})\, \rho(\boldsymbol{\xi}_0)\, d\boldsymbol{\xi}_0}{\int \delta\left(r_x'(\boldsymbol{\xi}_0) - r_x\right)\, \rho(\boldsymbol{\xi}_0)\, d\boldsymbol{\xi}_0} \approx w_P(r_x). \tag{3.144}$$

As illustrated in figure 3.1 and indicated above, the committor is approximated as the fraction $w_P(r_x)$ of $\mathcal{N}_{ft}$ fleeting trajectories that reaches the product state P from a configuration r_x [21, 73]:

$$w_P(r_x, t_{ft}) \approx \frac{1}{\mathcal{N}_{ft}} \sum_{j=1}^{\mathcal{N}_{ft}} \theta_P\left(x_{t_{ft},j}\right). \tag{3.145}$$

To estimate the statistical uncertainty of equation (3.145), we can regard the result of one fleeting trajectory as the outcome of a binomially distributed random variable [21, 73]. Furthermore, we assume that the fleeting trajectories are independent and identically distributed. If the number of fleeting trajectories is sufficiently large, the standard deviation of the mean of the committor can be estimated by the central limit theorem [21, 73, 137]:

$$\sigma\left(w_P(r_x)\right) \approx \sqrt{\frac{w_P(r_x)(1 - w_P(r_x))}{\mathcal{N}_{ft}}}. \tag{3.146}$$

Transition states are configurations with equal probability of relaxing to the reactant and product states [21, 73, 81–83, 140, 185]. In other words, transition state configurations have a committor value of one half. This criterion agrees with the expectation that the transition state is intermediate between reactants and products [22, 77, 123].

The committor is sometimes considered as an ideal reaction coordinate [77, 78, 81–83, 140]. However, although the committor is universal, it does not provide direct physical insight [21, 73, 82, 140]. What is needed to gain this insight, is an approximation to the committor in terms of few physical collective variables [82, 140]. In practice, we shall use the reverse route. Instead of parametrizing the committor in terms of collective variables, we usually propose a reaction coordinate and subsequently test its validity [21, 22, 73, 77, 81, 82, 140]. This test exploits the property that dynamically relevant

collective variables must closely approximate the statistically exact committor [77,82]. In particular, the configurations of the transition state according to the proposed reaction coordinate are harvested. Then, the committor w_P is computed for every member of this set, and a histogram of the computed committor values is constructed [21, 73, 81, 82, 140]. This histogram approximates the committor distribution $w(w_P)$ of equation (3.147), which describes the committor values observed for configurations characterized by a given value r_x of the collective variable $r_x^{'}$. If the committor distribution (3.147) [21, 73] is sharply peaked around $w_P(r_x) = 1/2$, the proposed collective variable r_x is considered a good approximation to the reaction coordinate [21, 73, 81, 82, 140].

$$w(w_P) = \frac{\left\langle \delta\left(w_P^{'}\left(r_x, t_{ft}\right) - w_P\right) \delta\left(r_x^{'}(\boldsymbol{\xi}) - r_x\right)\right\rangle}{\left\langle \delta\left(r_x^{'}(\boldsymbol{\xi}) - r_x\right)\right\rangle} \tag{3.147}$$

The test of transition states and reaction coordinates via committor evaluations and their distributions is not restricted to transition path sampling simulations. This procedure is generally applicable to microscopic configurations and therefore provides a transition to complementary simulation techniques for investigating activated processes, such as free energy calculations, described next.

3.4 Computation of free energy differences and profiles

The present section briefly discusses the challenge of evaluating free energy differences and free energy profiles. We then present the ideas behind a few techniques that address this challenge: thermodynamic perturbation [120], thermodynamic integration [121], umbrella sampling [114, 115]. The method we use to construct free energy profiles is called umbrella integration [65, 66]; it is based on umbrella sampling and thermodynamic integration and will be presented as a fourth method.

As briefly mentioned in section 3.2, (absolute) free energies cannot be

evaluated by simulation techniques [106]. The reason is that the Helmholtz free energy and other thermal quantities, such as the entropy, cannot be expressed as ensemble averages [106]. Instead, they are related to the phase space volume accessible to the system [106]. This situation is analogous to that for physical experiments; only free energy differences are measurable in a laboratory [106].

The free energy difference $\Delta F = F_1 - F_0$ between two regions in phase space separated by a large free energy barrier and characterized by the Hamiltonians $\mathcal{H}_0$ and $\mathcal{H}_1$ can be written as an ensemble average of the exponential of the energy difference $\Delta E = \mathcal{H}_1 - \mathcal{H}_0$ over the state 0 [106, 120, 186]:

$$\Delta F = -k_B T \, ln \langle e^{-\beta(\mathcal{H}_1 - \mathcal{H}_0)} \rangle_0. \tag{3.148}$$

Hence, the situation is formally the same as that for mechanical properties $\langle \mathcal{A} \rangle_0 = \int \mathcal{A}(\boldsymbol{\xi}) \rho_0(\boldsymbol{\xi}) \, d\boldsymbol{\xi}$ [114, 115]. However, evaluating ensemble averages in the case of free energy differences requires special techniques [114]. To see why, we compare the characteristics of ensemble averages for mechanical properties with those for free energy differences.

In both cases, the weight $\rho_0 = e^{-\beta \mathcal{H}_0(\boldsymbol{\xi})} / \int e^{-\beta \mathcal{H}_0(\boldsymbol{\xi})} \, d\boldsymbol{\xi}$ of a phase space point in the canonical ensemble is determined by the Boltzmann factor, which is a rapidly varying function of the phase space variables [114]. Also in both cases, the largest contributions to the ensemble average $\langle \mathcal{A} \rangle_0$ stem from phase space points where the weight and the property of interest are large simultaneously so that their product, the integrand $\mathcal{A}\rho_0$, is non-negligible [114]. Mechanical properties tend to be smooth and slowly varying functions of phase space variables [106, 114]. Accordingly, the major contributions to the ensemble average of mechanical properties are determined by those configurations whose statistical weight is large because ρ_0 determines the behaviour of $\mathcal{A}\rho_0$. Because equilibrium simulations preferentially sample configurations with large statistical weight, the evaluation of average mechanical properties is accessible to molecular simulation techniques [107, 115].

The evaluation of free energy differences is more challenging in the following way. The function $\mathcal{A} = e^{-\beta \Delta E}$ may change as rapidly with phase space

coordinates as ρ_0 [114]. This means that large contributions $e^{-\beta\Delta E}\rho_0$ to the ensemble average may not only arise from configurations with high statistical weight but also from phase space points with lower weight and correspondingly large values of $e^{-\beta\Delta E}$ [107]. As a consequence, it is typically necessary to sample configurations with relatively low values of ρ_0 to accurately estimate the free energy difference ΔF [107, 114]. In particular, we wish to sample phase space points that belong to both the reference state and the target state to include all large contributions of $e^{-\beta\Delta E}\rho_0$ to the ensemble average [115]. If the states are well separated in phase space, they will have few configurations in common [106]. As a result, configurations that have a high probability in one state will have negligible weight in the other state and vice versa [106]. Thus, if a free energy barrier prevents sampling both states, we cannot extract statistically firm information on the target state from sampling the reference state if the two states are too dissimilar [107].

To overcome the difficulty of disjoint probability distributions of the states involved, several strategies have been proposed. These strategies can be divided into non-equilibrium and equilibrium approaches. The former involve simulations evaluating the non-equilibrium work to connect the reference and target states [106, 187, 188]. The latter include thermodynamic perturbation [120], thermodynamic integration [121] and umbrella sampling [114, 115]. In this work we shall focus on equilibrium methods, which extract information from simulations of systems in equilibrium with respect to their current, possibly artificial, Hamiltonians.

We distinguish two types of free energy differences. On the one hand, we have free energy differences between two different systems characterized by different Hamiltonians. An example is the reversible work to charge a solute in a polar solvent [189]. On the other hand, we consider free energy differences between different regions of phase space of the same system. In that case, the Hamiltonian of the system is the same in all states, which are characterized by an order parameter [190]. The free energy of a given state corresponds to the projection of the free energy onto the relevant part of phase space [161] and is related to (an integral over) the Landau free energy [106].

In mathematical terms, the difference in Helmholtz free energy between two systems characterized by the Hamiltonians $\mathcal{H}_1$ and $\mathcal{H}_0$ and by the partition functions Q_1 and Q_0 reads [72, 106]

$$\Delta F = F_1 - F_0 = -k_B T \, ln \, \frac{Q_1}{Q_0} = -k_B T \, ln \, \frac{\int e^{-\beta \mathcal{H}_1(\boldsymbol{\xi})} \, d\boldsymbol{\xi}}{\int e^{-\beta \mathcal{H}_0(\boldsymbol{\xi})} \, d\boldsymbol{\xi}}. \tag{3.149}$$

In contrast, the free energy difference between two states R and P of a system characterized by the Hamiltonian $\mathcal{H}$ involves Landau free energies $F_L(x)$ and restricted partition functions $Q(x)$ as a function of the order parameter x, as discussed in reference [33]:

$$\begin{aligned} \Delta_r F = F_P - F_R &= -k_B T \, ln \, \frac{Q_P}{Q_R} \\ &= -k_B T \, ln \, \frac{\int Q(x) \, \theta_P(x) \, dx}{\int Q(x) \, \theta_R(x) \, dx} = -k_B T \, ln \, \frac{\int e^{-\beta F_L(x)} \, \theta_P(x) \, dx}{\int e^{-\beta F_L(x)} \, \theta_R(x) \, dx}. \end{aligned} \tag{3.150}$$

Above, we have used the definition of both the restricted partition function [33, 161],

$$Q(x) = \frac{1}{h^{3N} N!} \int \delta \left(x^{'}(\boldsymbol{\xi}) - x \right) \, e^{-\beta \mathcal{H}(\boldsymbol{\xi})} \, d\boldsymbol{\xi}, \tag{3.151}$$

and the Landau free energy, which is also called the potential of mean force [33, 161]:

$$\begin{aligned} F_L(x) &= -k_B T \, ln \, Q(x) \\ &= F - k_B T \, ln \, \rho(x) \\ &= F - k_B T \, ln \, \left\langle \delta \left(x^{'}(\boldsymbol{\xi}) - x \right) \right\rangle \\ &= F - k_B T \, ln \, \frac{\int \delta \left(x^{'}(\boldsymbol{\xi}) - x \right) e^{-\beta \mathcal{H}(\boldsymbol{\xi})} d\boldsymbol{\xi}}{\int e^{-\beta \mathcal{H}(\boldsymbol{\xi})} d\boldsymbol{\xi}}. \end{aligned} \tag{3.152}$$

Here, the Helmholtz free energy F serves as an arbitrary reference energy [118]. This reference energy is arbitrary because it cancels when free energy differences or free energy profiles are evaluated. We also note that the free energy difference (3.150) generally differs from the Landau free energy dif-

ference between the minima of the two stable states. The latter involves the differences between the free energies restricted to two single values of the order parameter, whereas the former free energies characterize two extended regions of phase space.

Whether we wish to compute free energy differences of the form (3.149) or of the form (3.150), we will typically have to bridge the sampling from the initial state to the final state. In the former case, equilibrium simulations are performed with respect to a series of intermediate Hamiltonians. In the latter case, the system is biased along the order parameter to reach the final state from the initial state. These procedures enable us to sample configurations with a large weight in different regions of phase space or for different systems, resulting in a path connecting initial and final states.

3.4.1 Thermodynamic perturbation

The method of thermodynamic perturbation [120, 191] aims at evaluating the free energy difference between the system of interest and the reference system, indicated by the subscripts 1 and 0. Accordingly, we denote the Hamiltonians of the target and reference systems by $\mathcal{H}_1$ and $\mathcal{H}_0$. The thermodynamic perturbation method exists as both a one-step and a multi-step procedure [191]. In the one-step version we sample phase space points distributed according to the reference system and evaluate the exponential of the difference in total energy between the target and the reference systems $\Delta\mathcal{H}(\boldsymbol{\xi}) = \mathcal{H}_1(\boldsymbol{\xi}) - \mathcal{H}_0(\boldsymbol{\xi})$ [53, 120, 192]:

$$\begin{aligned}\Delta F = F_1 - F_0 = -k_B T\, ln\, \frac{Q_1}{Q_0} &= -k_B T\, ln\, \frac{\int e^{-\beta\mathcal{H}_1(\boldsymbol{\xi})} d\boldsymbol{\xi}}{\int e^{-\beta\mathcal{H}_0(\boldsymbol{\xi})} d\boldsymbol{\xi}} \\ &= -k_B T\, ln\, \left\langle e^{-\beta\Delta\mathcal{H}(\boldsymbol{\xi})} \right\rangle_0 = k_B T\, ln\, \left\langle e^{\beta\Delta\mathcal{H}(\boldsymbol{\xi})} \right\rangle_1 . \end{aligned} \tag{3.153}$$

Consequently, we directly face the challenges described above. To avoid sampling configurations that have negligible weight in one or both of the states involved, the multi-step procedure can be used. In that case, the free energy difference between the target and reference states is written as a sum

over free energy differences involving $\mathcal{N}_{st} - 2$ intermediate states [191, 193]:

$$\begin{aligned}\Delta F_{1,0} = F_1 - F_0 &= \sum_{j=0}^{\mathcal{N}_{st}-2} \Delta F_{\frac{j+1}{\mathcal{N}_{st}-1},\frac{j}{\mathcal{N}_{st}-1}} \\ &= -k_B T\, ln \prod_{j=0}^{\mathcal{N}_{st}-2} \left\langle e^{-\beta\Delta\mathcal{H}_{j+1,j}} \right\rangle_j . \end{aligned} \tag{3.154}$$

The total number of states is $\mathcal{N}_{st}$, and the number of perturbation stages is $\mathcal{N}_{st} - 1$. For a linear variation of the parameter characterizing the system the states j are often characterized by a Hamiltonian $\mathcal{H}_{\frac{j}{\mathcal{N}_{st}-1}}$ [53, 191]:

$$\mathcal{H}_{\frac{j}{\mathcal{N}_{st}-1}}(\boldsymbol{\xi}) = \mathcal{H}_0(\boldsymbol{\xi}) + \frac{j}{\mathcal{N}_{st} - 1} \left(\mathcal{H}_1(\boldsymbol{\xi}) - \mathcal{H}_0(\boldsymbol{\xi})\right). \tag{3.155}$$

Starting from the reference system, we sample phase space points with non-vanishing weight for the first intermediate state. The free energy difference $F_{\frac{1}{\mathcal{N}_{st}-1}} - F_0$ can be estimated, and state $\frac{1}{\mathcal{N}_{st}-1}$ becomes the next reference state with respect to the intermediate state $\frac{2}{\mathcal{N}_{st}-1}$ and so on. With an arbitrary reference free energy of the reference state 0 a series of free energies as a function of the parameter j is constructed from the individual free energy differences $\Delta F_{\frac{j+1}{\mathcal{N}_{st}-1},\frac{j}{\mathcal{N}_{st}-1}}$.

3.4.2 Thermodynamic integration

The thermodynamic integration method [106, 121] introduces a control parameter ζ characterizing the Hamiltonian of the system:

$$\begin{aligned}\mathcal{H}(\boldsymbol{\xi}, \zeta) &= (1 - \zeta)\, \mathcal{H}(\boldsymbol{\xi}, 0) + \zeta\, \mathcal{H}(\boldsymbol{\xi}, 1) \\ &= \mathcal{H}(\boldsymbol{\xi}, 0) + \zeta\, \left(\mathcal{H}(\boldsymbol{\xi}, 1) - \mathcal{H}(\boldsymbol{\xi}, 0)\right). \end{aligned} \tag{3.156}$$

The parameter varies from zero to unity. The reference system corresponds to $\zeta = 0$, and the target system is represented by $\zeta = 1$. Intermediate values of ζ define artificial systems bridging between the reference and target systems. As the Hamiltonian of each system depends on ζ, so do the partition function

and the (Landau) free energy. The idea behind thermodynamic integration is now first to take the derivative of the free energy with respect to the control parameter and second to integrate the averages given below numerically over various values of the control parameter [191]. We have for the canonical partition function of an atomic N-particle system characterized by $\mathcal{H}(\boldsymbol{\xi}, \zeta)$ (compare appendix D) [106]

$$Q(\zeta) = \frac{1}{N!\, h^{3N}} \int e^{-\beta \mathcal{H}(\boldsymbol{\xi},\zeta)} d\boldsymbol{\xi}. \tag{3.157}$$

The derivative of the (Landau) free energy with respect to ζ reads [53, 106, 121]

$$\begin{aligned} \frac{\partial F(\zeta)}{\partial \zeta} &= -k_B T \frac{\partial ln\, Q(\zeta)}{\partial \zeta} \\ &= -k_B T \frac{1}{Q(\zeta)} \frac{\partial Q(\zeta)}{\partial \zeta} \\ &= \frac{\int \frac{\partial \mathcal{H}(\boldsymbol{\xi},\zeta)}{\partial \zeta} e^{-\beta \mathcal{H}(\boldsymbol{\xi},\zeta)}\, d\boldsymbol{\xi}}{\int e^{-\beta \mathcal{H}(\boldsymbol{\xi},\zeta)}\, d\boldsymbol{\xi}} \\ &= \left\langle \frac{\partial \mathcal{H}(\boldsymbol{\xi}, \zeta)}{\partial \zeta} \right\rangle_{\zeta}. \end{aligned} \tag{3.158}$$

We see that the derivative of the (Landau) free energy with respect to the control parameter ζ results in an ensemble average of the derivative of the Hamiltonian with respect to ζ. The ensemble average is performed over the generalized density $\rho_\zeta(\boldsymbol{\xi}) = \frac{e^{-\beta \mathcal{H}(\boldsymbol{\xi},\zeta)}}{\int e^{-\beta \mathcal{H}(\boldsymbol{\xi},\zeta)} d\boldsymbol{\xi}}$. Integrating the generalized force of equation (3.158) over all values of ζ yields the free energy difference between the system of interest and the reference state [53, 106, 121, 190, 191, 193]:

$$\Delta F = F(\zeta = 1) - F(\zeta = 0) = \int_{\zeta=0}^{\zeta=1} \left\langle \frac{\partial \mathcal{H}(\boldsymbol{\xi}, \zeta')}{\partial \zeta'} \right\rangle_{\zeta'} d\zeta'. \tag{3.159}$$

As in the case of thermodynamic perturbation, a series of free energy differences can be obtained from simulations at different values of ζ.

3.4.3 Umbrella sampling

Although umbrella sampling [114, 115] was first introduced to compute free energy differences of the type (3.149), its primary current use seems to be the evaluation of free energy profiles [118, 194]. In both cases, the central idea of the method consists in employing a non-Boltzmann weight function $\rho_b = \frac{\omega_b\, e^{-\beta\mathcal{H}(\boldsymbol{\xi})}}{\int \omega_b\, e^{-\beta\mathcal{H}(\boldsymbol{\xi})}\, d\boldsymbol{\xi}}$ to sample configurations pertaining to both the initial and final states [114, 115]. Then, the free energy difference between two systems $\mathcal{H}_1$ and $\mathcal{H}_0$ reads [114, 115]

$$\begin{aligned}\Delta F = F_1 - F_0 &= -k_B T\, ln\, \frac{\int e^{-\beta\mathcal{H}_1}\, d\boldsymbol{\xi}}{\int e^{-\beta\mathcal{H}_0}\, d\boldsymbol{\xi}} \\ &= -k_B T\, ln\, \frac{\int \frac{\omega_b}{\omega_b}\, e^{-\beta\mathcal{H}_1}\, d\boldsymbol{\xi}}{\int \frac{\omega_b}{\omega_b}\, e^{-\beta\mathcal{H}_0}\, d\boldsymbol{\xi}} = -k_B T\, ln\, \frac{\left\langle \frac{1}{\omega_b}\, e^{-\beta(\mathcal{H}_1-\mathcal{H}_0)} \right\rangle_b}{\left\langle \frac{1}{\omega_b} \right\rangle_b}. \end{aligned} \tag{3.160}$$

Above, the subscript b indicates that the ensemble average is computed with the weight function $\rho_b = \frac{\omega_b\, e^{-\beta\mathcal{H}(\boldsymbol{\xi})}}{\int \omega_b\, e^{-\beta\mathcal{H}(\boldsymbol{\xi})}\, d\boldsymbol{\xi}}$, where ω_b, which is often expressed as $e^{-\beta V_b}$ in terms of a biasing potential V_b, is a factor describing the deviation from the unbiased phase space density $\rho = \frac{e^{-\beta\mathcal{H}(\boldsymbol{\xi})}}{\int e^{-\beta\mathcal{H}(\boldsymbol{\xi})}\, d\boldsymbol{\xi}}$. Relation (3.160) implies that the biased simulations are unbiased by ω_b^{-1} to yield the Boltzmann-weighted averages sought [115].

The same strategy of introducing a bias potential and correcting for it applies for the computation of free energy profiles along an order parameter x [47, 118, 194, 195]. According to equation (3.152), the free energy profile is a function of the equilibrium probability density restricted to a given order parameter value $\rho(x)$. In a multi-stage umbrella sampling simulation the equilibrium probability density is expressed in terms of the order parameter densities from several biased simulations [114, 115, 118]. The biased simulations are performed along the order parameter, and the entire order parameter range is divided into segments or windows. The bias is introduced by adding the restraining potential $V_{b,j}(x)$ to the Hamiltonian $\mathcal{H}(\boldsymbol{\xi})$, resulting in the following Hamiltonian for window j [118]:

$$\mathcal{H}_j(\boldsymbol{\xi}, x) = \mathcal{H}(\boldsymbol{\xi}) + V_{b,j}(x). \tag{3.161}$$

We note that the order parameter is a function of the phase space variables $x = x(\boldsymbol{\xi})$; however, this dependence has been left implicit for notational convenience. With the above definition the biased probability density of the order parameter for window j becomes [118, 161]

$$\rho_{b,j}(x) = \frac{\int \delta\left(x'(\boldsymbol{\xi}) - x\right) e^{-\beta \mathcal{H}_j(\boldsymbol{\xi}, x')} d\boldsymbol{\xi}}{\int e^{-\beta \mathcal{H}_j(\boldsymbol{\xi}, x')} d\boldsymbol{\xi}} = \left\langle \delta\left(x'(\boldsymbol{\xi}) - x\right)\right\rangle_{b,j}. \tag{3.162}$$

The last equation defines the average over the biased density $\rho_{b,j}(\boldsymbol{\xi}) = \frac{e^{-\beta \mathcal{H}_j(\boldsymbol{\xi}, x')}}{\int e^{-\beta \mathcal{H}_j(\boldsymbol{\xi}, x')} d\boldsymbol{\xi}}$.

We now relate the equilibrium density $\rho(x)$ to the biased density $\rho_{b,j}(x)$ in window j [118]:

$$\begin{aligned}
\rho(x) &= \frac{\int \delta\left(x'(\boldsymbol{\xi}) - x\right) e^{-\beta \mathcal{H}(\boldsymbol{\xi})} d\boldsymbol{\xi}}{\int e^{-\beta \mathcal{H}(\boldsymbol{\xi})} d\boldsymbol{\xi}} \\
&= \frac{\int \delta\left(x'(\boldsymbol{\xi}) - x\right) e^{-\beta \mathcal{H}_j(\boldsymbol{\xi}, x')} e^{\beta V_{b,j}(x')} d\boldsymbol{\xi}}{\int e^{-\beta \mathcal{H}_j(\boldsymbol{\xi}, x')} e^{\beta V_{b,j}(x')} d\boldsymbol{\xi}} \\
&= \frac{\left\langle \delta\left(x'(\boldsymbol{\xi}) - x\right) e^{\beta V_{b,j}(x')}\right\rangle_{b,j}}{\left\langle e^{\beta V_{b,j}(x')}\right\rangle_{b,j}} \\
&= e^{\beta V_{b,j}(x)} \frac{\rho_{b,j}(x)}{\left\langle e^{\beta V_{b,j}(x')}\right\rangle_{b,j}} \\
&= e^{\beta V_{b,j}(x)} \rho_{b,j}(x) \left\langle e^{-\beta V_{b,j}(x')}\right\rangle.
\end{aligned} \tag{3.163}$$

To reach the second line, we have multiplied the integrand by one and used equation (3.161). To reach the third line, we divide numerator and denominator by $\int e^{-\beta \mathcal{H}_j(\boldsymbol{\xi}, x')} d\boldsymbol{\xi}$. We then obtain line four on noting that the order parameter is restricted to the value x so that the term $e^{\beta V_{b,j}(x)}$ is a constant and can be taken out of the integral over phase space variables. This procedure is the same as that used in the electron-transfer case (see equation (2.34) on page 37). The remaining integral is identified as relation (3.162). The last line follows from the thermodynamic perturbation result for the free energy difference between states characterized by Hamiltonians $\mathcal{H}_j$ and

$\mathcal{H}$ [120]:

$$\begin{aligned}\left\langle e^{\beta V_{b,j}(x)}\right\rangle_{b,j}^{-1} &= \frac{\int e^{-\beta\mathcal{H}(\boldsymbol{\xi})}e^{-\beta V_{b,j}(x)}d\boldsymbol{\xi}}{\int e^{-\beta\mathcal{H}(\boldsymbol{\xi})}e^{-\beta V_{b,j}(x)}e^{\beta V_{b,j}(x)}d\boldsymbol{\xi}} \\ &= \left\langle e^{-\beta V_{b,j}(x)}\right\rangle = e^{-\beta\Delta F_j} = e^{-\beta(F-F_j)}. \end{aligned} \tag{3.164}$$

With the above definitions and results the contribution to the free energy profile (3.152) from biased simulations in window j reads [118]

$$F_j(x) = F - k_B T\, ln\, \rho_{b,j}(x) - V_{b,j}(x) + \Delta F_j. \tag{3.165}$$

The free energy profile segments from each window need to be combined to construct the Landau free energy or potential of mean force, which represent the free energy subject to the constraint that the order parameter has a fixed value [118], over the entire order parameter range of interest. One popular way of doing so is to iteratively evaluate the unknown constants ΔF_j by using the weighted histogram analysis method [117, 118]. However, the value and the accuracy of the calculated potential of mean force depend on the bin size for the order parameter [65, 119]. Consequently, we shall not describe the construction of free energy profiles using self-consistent histogram methods. Instead, we consider an alternative that converges with the number of bins used for the order parameter, namely umbrella integration [65, 66].

3.4.4 Umbrella integration

Umbrella integration [65,66] uses biased molecular simulation (umbrella sampling) to sample phase space regions whose Boltzmann weight is vanishingly small. Thus, the first step is identical to an umbrella sampling simulation [106, 114, 115]. The methods differ when it comes to the reconstruction of the free energy profile from the simulation data.

Umbrella integration [65, 66] is inspired by thermodynamic integration [106,121]. Specifically, the generalized force (along an order parameter) from each window is integrated using the extended version of Simpson's rule [2,65, 66]. An important ingredient of the method is the assumption that the order

parameter in each window is normally distributed to a good approximation [65].

The equilibrium contribution to the potential of mean force from window j can be expressed in terms of the probability density from the biased simulation in window j as in equation (3.165). Following reference [65], we obtain the generalized force by taking the derivative of the free energy in window j with respect to the order parameter x:

$$\frac{\partial F_j(x)}{\partial x} = -k_B T \frac{\partial ln\, \rho_{b,j}(x)}{\partial x} - \frac{dV_{b,j}(x)}{dx}. \tag{3.166}$$

Relation (3.166) is generally valid. As in reference [65], we restrict the scope of equation (3.166) in two ways. First, we focus on harmonic restraining potentials around the centre of window j at x_j^c [65]:

$$V_{b,j}(x) = \frac{1}{2}\kappa_b \left(x - x_j^c\right)^2. \tag{3.167}$$

Second, we approximate the order parameter density in window j by a normal probability density with mean $\langle x \rangle_{b,j}$ and variance $\sigma_{b,j}^2$ [65]:

$$\rho_{b,j}(x) = \frac{1}{\sqrt{2\pi}\,\sigma_{b,j}}\, e^{-\frac{1}{2}\left(\frac{x-\langle x\rangle_{b,j}}{\sigma_{b,j}}\right)^2}. \tag{3.168}$$

Inserting equations (3.167) and (3.168) into equation (3.166) for the generalized force for window j yields [65, 66]

$$\frac{\partial F_j(x)}{\partial x} = k_B T \frac{x - \langle x \rangle_{b,j}}{\sigma_{b,j}^2} - \kappa_b \left(x - x_j^c\right). \tag{3.169}$$

Because the potential of mean force is constructed by integrating the generalized force, we need to combine the different windows to obtain the generalized force for the entire order parameter range. To do so, we divide the order parameter range into bins so that they are independent of the windows used to perform the biased simulations [65]. The generalized force at the order parameter value x results from a weighted average over contributions

from each window j [65]:

$$\left.\frac{\partial F(x)}{\partial x}\right|_x = \sum_{j=1}^{\mathcal{N}_w} w_j(x) \left(\frac{\partial F_j(x)}{\partial x}\right)_x . \tag{3.170}$$

The weight of each window j at the order parameter value x is given in terms of a histogram approximation $w_{b,j}$ to the biased density $\rho_{b,j}$ [65]:

$$w_j(x) = \frac{\mathcal{N}_{d,j}\, w_{b,j}(x)}{\sum_{k=1}^{\mathcal{N}_w} \mathcal{N}_{d,k}\, w_{b,k}(x)} . \tag{3.171}$$

In equation (3.171) above the number of data points sampled in window j is denoted by $\mathcal{N}_{d,j}$, and the number of windows is $\mathcal{N}_w$.

Finally, the Landau free energy difference $\Delta F_L = F_L(x_P) - F_L(x_R)$ along the free energy profile $F(x)$ is obtained by numerical integration according to the extended Simpson's rule [2, 66]:

$$\Delta F_L = F_L(x_P) - F_L(x_R) = \int_{x_R}^{x_P} \left.\frac{\partial F}{\partial x}\right|_x dx \approx \frac{\Delta x}{3} \sum_{k=1}^{\mathcal{N}_{bin}} \mathcal{C}_k \left(\frac{\partial F(x)}{\partial x}\right)_k . \tag{3.172}$$

The order parameter value characterizing the minimum of the reactant state is x_R, whereas x_P designates the minimum of the products. In addition, $\mathcal{N}_{bin}$ is the number of bins for the order parameter and needs to be odd. The order parameter interval reads $\Delta x = (x_R - x_P)/(\mathcal{N}_{bin} - 1)$, and the coefficients take the values $\mathcal{C}_k = 1$ for $k = 1$ and $k = \mathcal{N}_{bin}$, $\mathcal{C}_k = 2$ for odd k, and $\mathcal{C}_k = 4$ for even k. We thus see how the potential of mean force can be obtained without iterations in a reliable and efficient way [65, 66]. In practice, the numerical difference is negligible between the extended versions of Simpson's rule and the trapezoidal rule for the cases considered in the present work.

To obtain the free energy difference between the product and reactant states, we use a crude numerical approximation to equation (3.150):

$$\Delta_r F = F_P - F_R = -k_B T\, ln \frac{\int e^{-\beta F_L(x)}\, \theta_P(x)\, dx}{\int e^{-\beta F_L(x)}\, \theta_R(x)\, dx} . \tag{3.173}$$

This concludes our brief outline of methods (commonly) used to evaluate free energy differences and profiles. In the next section we shall describe the Ewald summation as a technique to overcome the difficulties associated with computing long-ranged forces.

3.5 Ewald summation for dealing with long-range interactions

Atomistic simulations of bulk properties of molecular systems are limited by their computational cost [196]. One way of obtaining an approximate description of a macroscopic system consists in simulating a small box with a limited number of particles with periodic boundary conditions [196, 197]. As a result, the use of periodic boundary conditions eliminates surface effects between the condensed phase and the surrounding vacuum [196, 197].

If the system of interest contains charges, the long-range nature of the Coulomb interaction requires special simulation techniques. In particular, a given charged site will generally not only interact with nearby charged sites but also with distant periodic images [197]. It is therefore not possible to use simple truncation schemes because the contribution to the total potential energy arising from interactions with distant image sites can be substantial [197].

An infinitely periodically replicated system requires that the overall charge within the simulation box vanishes [198]. Otherwise the interaction of one box with any image box would be positive, and the sum over all boxes would tend to infinity. In the following we shall focus on periodic boundary conditions for cubic simulation cells of side length L and volume $\mathcal{V} = L^3$. The distance from the central simulation cell will be governed by the integer triple $\boldsymbol{n} = (n_x, n_y, n_z)$. We further assume that the system has no net charge. The case in which the system of interest carries a net charge will be discussed afterwards.

The electrostatic contribution due to point charges to the potential energy

of a unit cell of a periodic lattice is given by [106, 199–201]

$$V_{ES}(\boldsymbol{r}) = V_{ES}(\boldsymbol{r}_C) = \frac{1}{2}\sum_{j=1}^{j=N} z_j \Psi(\boldsymbol{r}_{C,j}), \tag{3.174}$$

where the symbol $\boldsymbol{r}$ denotes the set of all distances $r_{jk} = |\boldsymbol{r}_{C,j} - \boldsymbol{r}_{C,k}| = |\boldsymbol{r}_{C,jk}|$ between interaction sites j and k. Furthermore, z_j is the charge of particle j and $\Psi(\boldsymbol{r}_{C,j})$ is the electrostatic potential at the position $\boldsymbol{r}_{C,j}$ of ion j. This electrostatic potential is due to all the remaining charged sites in the central simulation cell ($\boldsymbol{n} = \boldsymbol{0}$) and due to all charged sites in the image cells ($\boldsymbol{n} \neq \boldsymbol{0}$) [106, 107]:

$$\Psi(\boldsymbol{r}_{C,j}) = \Psi(\boldsymbol{r}_{C,jk}) = \sum_{k=1}^{k=N} \frac{z_k}{4\pi\epsilon_0} \sum_{\boldsymbol{n}=-\infty}^{\boldsymbol{n}=\infty_*} \frac{1}{|\boldsymbol{r}_{C,jk} + \boldsymbol{n}L|}. \tag{3.175}$$

Above, the asterisk indicates that the term for $j = k$ is omitted for $\boldsymbol{n} = \boldsymbol{0}$ to ensure that the ion j does not interact with itself [106]. For notational convenience we summarize the distance dependence of the Coulomb potential by introducing the following potential [201]:

$$\psi(\boldsymbol{r}_{C,jk}) = \sum_{\boldsymbol{n}=-\infty}^{\boldsymbol{n}=\infty_*} \frac{1}{|\boldsymbol{r}_{C,jk} + \boldsymbol{n}L|} \tag{3.176}$$

Using equation (3.176), we can write the potential energy due to Coulomb interactions as [106, 107]

$$\begin{aligned} V_{ES}(\boldsymbol{r}) &= \frac{1}{2}\sum_{j=1}^{N}\sum_{k=1}^{N} \frac{z_j z_k}{4\pi\epsilon_0} \psi(\boldsymbol{r}_{C,jk}) \\ &= \frac{1}{2}\sum_{j=1}^{N}\sum_{k=1}^{N} \frac{z_j z_k}{4\pi\epsilon_0} \sum_{\boldsymbol{n}=-\infty}^{\boldsymbol{n}=\infty_*} \frac{1}{|\boldsymbol{r}_{C,jk} + \boldsymbol{n}L|}. \end{aligned} \tag{3.177}$$

It is clear that the sum (3.177), which extends over an infinitely large system, cannot converge unless positive and negative contributions cancel [199]. Even in that case, however, the sum is only conditionally convergent;

the result depends on the order of summation [199]. Ewald proposed to partition the sum (3.177) in such a way that one part contains only short-ranged contributions and that the other part is long-ranged [199]. One way to choose the short-ranged and long-ranged parts is [202]

$$\sum_{\boldsymbol{n}=-\infty}^{\infty *} \frac{1}{|\boldsymbol{r}_{C,jk}+\boldsymbol{n}L|} = \sum_{\boldsymbol{n}=-\infty}^{\infty *} \left(\frac{erfc(\alpha|\boldsymbol{r}_{C,jk}+\boldsymbol{n}L|)}{|\boldsymbol{r}_{C,jk}+\boldsymbol{n}L|} + \frac{erf(\alpha|\boldsymbol{r}_{C,jk}+\boldsymbol{n}L|)}{|\boldsymbol{r}_{C,jk}+\boldsymbol{n}L|} \right), \tag{3.178}$$

where $erf(y)$ is the error function [106, 170, 202]

$$erf(y) = \frac{2}{\sqrt{\pi}} \int_0^y e^{-u^2} du, \tag{3.179}$$

and $erfc(y) = 1 - erf(y)$ denotes the error function complement. The numerical evaluation of the long-ranged part of the Coulomb potential is carried out in Fourier or reciprocal space [106, 107]. We will therefore discuss the Fourier representation of equation (3.178) below.

Let us consider any function $f(\boldsymbol{\mathfrak{R}})$ in real space. This function can be represented in terms of a Fourier series with Fourier coefficients $f(\boldsymbol{k})$ [106]:

$$f(\boldsymbol{\mathfrak{R}}) = \frac{1}{\mathcal{V}} \sum_{\boldsymbol{k}=-\infty}^{\infty} f(\boldsymbol{k}) e^{\imath \boldsymbol{k} \boldsymbol{\mathfrak{R}}} \tag{3.180}$$

$$f(\boldsymbol{k}) = \int_{\mathcal{V}} f(\boldsymbol{\mathfrak{R}}) e^{-\imath \boldsymbol{k} \boldsymbol{\mathfrak{R}}} d^3\mathfrak{R} \tag{3.181}$$

Above, $\boldsymbol{\mathfrak{R}}$ denotes a real space vector of length $\mathfrak{R}$, and $d^3\mathfrak{R}$ is the corresponding volume element. In Cartesian coordinates it reads $d^3\mathfrak{R} = d\mathfrak{R}_x d\mathfrak{R}_y d\mathfrak{R}_z$, whereas it becomes $d^3\mathfrak{R} = \mathfrak{R}^2 sin\theta_{\mathfrak{R}} d\mathfrak{R} d\theta_{\mathfrak{R}} d\phi_{\mathfrak{R}}$ in spherical coordinates [2].

To arrive at the Fourier representation of equation (3.178), we use Poisson's equation [1], which relates the electrostatic potential $\Psi(\boldsymbol{\mathfrak{R}})$ at a point $\boldsymbol{\mathfrak{R}}$ to the charge density $\rho_c(\boldsymbol{\mathfrak{R}})$ that causes the potential:

$$-\nabla^2 \Psi(\boldsymbol{\mathfrak{R}}) = \frac{\rho_c(\boldsymbol{\mathfrak{R}})}{\epsilon_0}. \tag{3.182}$$

We now represent the electrostatic potential and the charge density as a Fourier series and insert these expressions into the Poisson equation (3.182) to obtain [106]

$$-\nabla^2 \frac{1}{\mathcal{V}} \sum_{\boldsymbol{k}=-\infty}^{\infty} \Psi(\boldsymbol{k}) e^{\imath \boldsymbol{k}\mathfrak{R}} = \frac{1}{\epsilon_0} \frac{1}{\mathcal{V}} \sum_{\boldsymbol{k}=-\infty}^{\infty} \rho_c(\boldsymbol{k}) e^{\imath \boldsymbol{k}\mathfrak{R}} \tag{3.183}$$

$$\frac{1}{\mathcal{V}} \sum_{\boldsymbol{k}=-\infty}^{\infty} |\boldsymbol{k}|^2 \Psi(\boldsymbol{k}) e^{\imath \boldsymbol{k}\mathfrak{R}} = \frac{1}{\epsilon_0} \frac{1}{\mathcal{V}} \sum_{\boldsymbol{k}=-\infty}^{\infty} \rho_c(\boldsymbol{k}) e^{\imath \boldsymbol{k}\mathfrak{R}} \tag{3.184}$$

Comparison of coefficients then yields Poisson's equation in Fourier space [106]

$$|\boldsymbol{k}|^2 \Psi(\boldsymbol{k}) = \frac{\rho_c(\boldsymbol{k})}{\epsilon_0}. \tag{3.185}$$

Here, we consider a system of point charges, which can be represented as [106, 202]

$$\rho_c(\mathfrak{R}) = \sum_{k=1}^{N} z_k \sum_{\boldsymbol{n}=-\infty}^{\infty} \delta(\mathfrak{R} - \boldsymbol{r}_{C,k} + \boldsymbol{n}L). \tag{3.186}$$

We can then write the electrostatic potential in Fourier space representation because the term for $\boldsymbol{k} = \boldsymbol{0}$ vanishes on both sides of equation (3.183). The left-hand side is zero because $\boldsymbol{k} = \boldsymbol{0}$, and the right-hand side vanishes because the unit cell is neutral overall $\sum_{k=1}^{N} z_k = 0$. We thus obtain for the electrostatic potential in real space [106]

$$\begin{aligned} \Psi(\mathfrak{R}) &= \frac{1}{\epsilon_0} \frac{1}{\mathcal{V}} \sum_{\substack{\boldsymbol{k}=-\infty \\ \boldsymbol{k}\neq\boldsymbol{0}}}^{\infty} \frac{\rho_c(\boldsymbol{k})}{|\boldsymbol{k}|^2} e^{\imath \boldsymbol{k}\mathfrak{R}} \\ &= \sum_{k=1}^{N} \frac{z_k}{\epsilon_0 \mathcal{V}} \sum_{\substack{\boldsymbol{k}=-\infty \\ \boldsymbol{k}\neq\boldsymbol{0}}}^{\infty} \frac{e^{\imath \boldsymbol{k}\left(\mathfrak{R} - \boldsymbol{r}_{C,k}\right)}}{|\boldsymbol{k}|^2}, \end{aligned} \tag{3.187}$$

where we have used the following expression for the Fourier representation

of the charge density [106, 171]:

$$\begin{aligned}
\rho_c(\boldsymbol{k}) &= \int_{\mathcal{V}} \rho_c(\boldsymbol{\mathfrak{R}}) e^{-\imath \boldsymbol{k}\boldsymbol{\mathfrak{R}}} d^3\mathfrak{R} \\
&= \sum_{k=1}^{N} z_k \int_{\mathcal{V}} \sum_{\boldsymbol{n}=-\infty}^{\infty} \delta(\boldsymbol{\mathfrak{R}} - \boldsymbol{r}_{C,k} + \boldsymbol{n}L) e^{-\imath \boldsymbol{k}\boldsymbol{\mathfrak{R}}} d^3\mathfrak{R} \\
&= \sum_{k=1}^{N} z_k \int_{\text{all space}} \delta(\boldsymbol{\mathfrak{R}} - \boldsymbol{r}_{C,k}) e^{-\imath \boldsymbol{k}\boldsymbol{\mathfrak{R}}} d^3\mathfrak{R} \\
&= \sum_{k=1}^{N} z_k e^{-\imath \boldsymbol{k}\boldsymbol{r}_{C,k}}.
\end{aligned} \tag{3.188}$$

The Coulomb operator can thus be represented as [198]

$$\sum_{\boldsymbol{n}=-\infty}^{\infty} \frac{1}{|\boldsymbol{\mathfrak{R}} - \boldsymbol{r}_{C,\boldsymbol{k}} + \boldsymbol{n}\boldsymbol{L}|} = \sum_{\substack{\boldsymbol{k}=-\infty \\ \boldsymbol{k}\neq\boldsymbol{0}}}^{\infty} \frac{4\pi}{\mathcal{V}|\boldsymbol{k}|^2} e^{\imath \boldsymbol{k}(\boldsymbol{\mathfrak{R}} - \boldsymbol{r}_{C,k})} \tag{3.189}$$

Our next task is to express the last term on the right-hand side of equation (3.178) in Fourier representation. We proceed as above and obtain the Fourier representation of the potential contribution from the corresponding charge density. The latter is obtained from the Poisson equation in real space. We shall work in spherical coordinates and exploit the identity $\nabla^2 f = \frac{\partial^2 f}{\partial \mathfrak{R}^2} + \frac{2}{\mathfrak{R}} \frac{\partial f}{\partial \mathfrak{R}} = \frac{1}{\mathfrak{R}} \frac{\partial^2 (\mathfrak{R} f)}{\partial \mathfrak{R}^2}$ [2, 106]. The individual steps described above will be used to show how the following result emerges. For the spherically symmetric long-ranged part to the Coulomb operator we obtain [106, 171]

$$\begin{aligned}
\Psi_{LR}(\boldsymbol{\mathfrak{R}}) &= \sum_{k=1}^{N} \frac{z_k}{4\pi\epsilon_0} \sum_{\boldsymbol{n}=-\infty}^{\infty} \frac{erf(\alpha|\boldsymbol{\mathfrak{R}} - \boldsymbol{r}_{C,k} + \boldsymbol{n}L|)}{|\boldsymbol{\mathfrak{R}} - \boldsymbol{r}_{C,k} + \boldsymbol{n}L|} \\
&= \sum_{k=1}^{N} \frac{z_k}{\epsilon_0 \mathcal{V}} \sum_{\substack{\boldsymbol{k}=-\infty \\ \boldsymbol{k}\neq\boldsymbol{0}}}^{\infty} \frac{e^{-\frac{|\boldsymbol{k}|^2}{4\alpha^2}}}{|\boldsymbol{k}|^2} e^{\imath \boldsymbol{k}(\boldsymbol{\mathfrak{R}} - \boldsymbol{r}_{C,k})}.
\end{aligned} \tag{3.190}$$

This result has been arrived at by means of the following charge density [106]:

$$\begin{aligned}
\rho_c(\mathfrak{R}) &= -\epsilon_0 \nabla^2 \Psi_{LR}(\mathfrak{R}) \\
&= -\sum_{k=1}^{N} \frac{z_k}{4\pi} \sum_{\boldsymbol{n}=-\infty}^{\infty} \frac{1}{|\mathfrak{R} - \boldsymbol{r}_{C,k} + \boldsymbol{n}L|} \frac{\partial^2 erf(\alpha|\mathfrak{R} - \boldsymbol{r}_{C,k} + \boldsymbol{n}L|)}{\partial \mathfrak{R}^2} \\
&= -\sum_{k=1}^{N} \frac{z_k}{4\pi} \sum_{\boldsymbol{n}=-\infty}^{\infty} \frac{1}{|\mathfrak{R} - \boldsymbol{r}_{C,k} + \boldsymbol{n}L|} \frac{\partial^2 \frac{2}{\sqrt{\pi}} \int_0^{\alpha|\mathfrak{R} - \boldsymbol{r}_{C,k} + \boldsymbol{n}L|} e^{-u^2} du}{\partial \mathfrak{R}^2} \\
&= -\sum_{k=1}^{N} \frac{z_k}{4\pi} \sum_{\boldsymbol{n}=-\infty}^{\infty} \frac{1}{|\mathfrak{R} - \boldsymbol{r}_{C,k} + \boldsymbol{n}L|} \frac{\partial \frac{2\alpha}{\sqrt{\pi}} e^{-\alpha^2|\mathfrak{R} - \boldsymbol{r}_{C,k} + \boldsymbol{n}L|^2}}{\partial \mathfrak{R}} \\
&= \sum_{k=1}^{N} z_k \sum_{\boldsymbol{n}=-\infty}^{\infty} \left(\frac{\alpha^2}{\pi}\right)^{\frac{3}{2}} e^{-\alpha^2|\mathfrak{R} - \boldsymbol{r}_{C,k} + \boldsymbol{n}L|^2}. \qquad (3.191)
\end{aligned}$$

As a result, the long-range part of the partitioning scheme (3.178) can be thought of as arising from a sum of Gaussian-shaped charge clouds [106,107]. The Fourier representation of this charge density reads [106, 107]

$$\begin{aligned}
\rho_c(\boldsymbol{k}) &= \int_{\mathcal{V}} \rho_c(\mathfrak{R}) e^{-\imath \boldsymbol{k}\mathfrak{R}} d^3\mathfrak{R} \\
&= \sum_{k=1}^{N} z_k \int_{\mathcal{V}} \left(\frac{\alpha^2}{\pi}\right)^{\frac{3}{2}} \sum_{\boldsymbol{n}=-\infty}^{\infty} e^{-\alpha^2|\mathfrak{R} - \boldsymbol{r}_{C,k} + \boldsymbol{n}L|^2} e^{-\imath \boldsymbol{k}\mathfrak{R}} d^3\mathfrak{R} \\
&= \sum_{k=1}^{N} z_k \int_{\text{all space}} \left(\frac{\alpha^2}{\pi}\right)^{\frac{3}{2}} e^{-\alpha^2|\mathfrak{R} - \boldsymbol{r}_{C,k}|^2} e^{-\imath \boldsymbol{k}\mathfrak{R}} d^3\mathfrak{R} \\
&= \sum_{k=1}^{N} z_k \int_{\text{all space}} \left(\frac{\alpha^2}{\pi}\right)^{\frac{3}{2}} e^{-\alpha^2\left(\mathfrak{R} + \frac{\imath \boldsymbol{k}}{2\alpha^2} - \boldsymbol{r}_{C,k}\right)^2} e^{-\alpha^2\left(\left(\frac{\imath \boldsymbol{k}}{2\alpha^2}\right)^2 + \frac{2\imath \boldsymbol{k}\boldsymbol{r}_{C,k}}{2\alpha^2}\right)} d^3\mathfrak{R} \\
&= \sum_{k=1}^{N} z_k e^{-\frac{|\boldsymbol{k}|^2}{4\alpha^2}} e^{-\imath \boldsymbol{k}\boldsymbol{r}_{C,k}}, \qquad (3.192)
\end{aligned}$$

where we have completed the square in the exponential and used the normalization of the error function.

Until now the result (3.190) has been given for an arbitrary point in space. In that case, the electrostatic potential stems from all Gaussian-shaped charge clouds in the system. However, we require the electrostatic

potential at the site of a point charge to evaluate the Coulomb potential energy [199]. As already mentioned, the electrostatic potential at this point must not include the charge density of the site where we wish to compute the electrostatic potential energy. Consequently, we subtract a term in the limit of $\mathfrak{R}$ approaching a point charge site for the central simulation cell ($\boldsymbol{n} = \boldsymbol{0}$). Mathematically we have [171]

$$\begin{aligned}
\lim_{\mathfrak{R}\to\boldsymbol{r}_{C,k}} \Psi_{LR}(\mathfrak{R}) &= \lim_{\mathfrak{R}\to\boldsymbol{r}_{C,k}} \sum_{k=1}^{N} \frac{z_k}{4\pi\epsilon_0} \frac{erf(\alpha|\mathfrak{R}-\boldsymbol{r}_{C,k}|)}{|\mathfrak{R}-\boldsymbol{r}_{C,k}|} \\
&= \sum_{k=1}^{N} \frac{z_k}{4\pi\epsilon_0} \lim_{\mathfrak{R}\to\boldsymbol{r}_{C,k}} \frac{2}{|\mathfrak{R}-\boldsymbol{r}_{C,k}|\sqrt{\pi}} \int_0^{\alpha|\mathfrak{R}-\boldsymbol{r}_{C,k}|} e^{-u^2} du \\
&= \sum_{k=1}^{N} \frac{z_k}{4\pi\epsilon_0} \lim_{\mathfrak{R}\to\boldsymbol{r}_{C,k}} \frac{2\alpha}{\sqrt{\pi}} e^{-\alpha^2|\mathfrak{R}-\boldsymbol{r}_{C,k}|^2} \\
&= \sum_{k=1}^{N} \frac{z_k}{4\pi\epsilon_0} \frac{2\alpha}{\sqrt{\pi}}. \qquad (3.193)
\end{aligned}$$

In going from the second to the third line we have used L'Hôpital's rule [2, 171]. The self-interaction term must be subtracted from the remaining contributions. In practice, the short-range part of the right-hand side of equation (3.178) will be evaluated in real space and need not be modified. Hence, we can collect all terms that contribute to the Coulomb potential energy [106, 107]:

$$\begin{aligned}
V_{ES}(\boldsymbol{r}) =& \frac{1}{2} \sum_{j=1}^{N} \sum_{k=1}^{N} \frac{z_j z_k}{4\pi\epsilon_0} \Bigg(\sum_{\boldsymbol{n}=-\infty}^{\boldsymbol{n}=\infty_*} \frac{erfc(\alpha|\boldsymbol{r}_{C,jk}+\boldsymbol{n}L|)}{|\boldsymbol{r}_{C,jk}+\boldsymbol{n}L|} \\
&+ \frac{4\pi}{\mathcal{V}} \sum_{\substack{\boldsymbol{k}=-\infty \\ \boldsymbol{k}\neq\boldsymbol{0}}}^{\infty} \frac{e^{-\frac{|\boldsymbol{k}|^2}{4\alpha^2}}}{|\boldsymbol{k}|^2} e^{\imath\boldsymbol{k}\boldsymbol{r}_{C,jk}} \Bigg) - \frac{1}{4\pi\epsilon_0} \sum_{j=1}^{N} \frac{\alpha z_j^2}{\sqrt{\pi}}. \qquad (3.194)
\end{aligned}$$

The above result holds if the surrounding medium is conducting with an infinite dielectric constant [106, 107, 197]. The following physical picture corresponds to equation (3.194): The first term on the right-hand side describes the interaction of point charges screened by a Gaussian charge density of

equal magnitude and opposite sign; the second term represents the interaction of Gaussian charge clouds with the same sign as the point charges; the last term corrects for the interaction of the Gaussian charge densities with themselves.

We now consider the case in which the system of interest is not neutral. In that case, a uniform, neutralizing background charge density is added to ensure that the overall charge in a simulation cell and thus in the entire system vanishes [197, 202]. The overall effect of the neutralizing background depends on the total charge of the system of interest $\sum_j z_j$. In particular, the following correction term can be added to equation (3.194) [203]:

$$-\frac{\pi}{2}\frac{\left(\sum_{j=1}^{N} z_j\right)^2}{\alpha^2}\frac{1}{4\pi\epsilon_0}. \tag{3.195}$$

To see how this correction arises, we consider how the potential ψ is affected by the neutralizing background. In the presence of the neutralizing background, the potential ψ becomes [197, 198, 201, 203–205]

$$\psi(\mathfrak{R}) = \sum_{\boldsymbol{n}=-\infty}^{\boldsymbol{n}=\infty} \frac{erfc(\alpha|\mathfrak{R}+\boldsymbol{n}L|)}{|\mathfrak{R}+\boldsymbol{n}L|} + \sum_{\substack{\boldsymbol{k}=-\infty \\ \boldsymbol{k}\neq\boldsymbol{0}}}^{\infty} \frac{4\pi}{\mathcal{V}|\boldsymbol{k}|^2} e^{-\frac{|\boldsymbol{k}|^2}{4\alpha^2}} e^{\imath\boldsymbol{k}\mathfrak{R}} - \frac{\pi}{\mathcal{V}\alpha^2}. \tag{3.196}$$

The last term in equation (3.196) has been omitted from equation (3.176) because it cancels due to the assumed charge neutrality condition in the final result (3.194) [197]. The term $-\frac{\pi}{\mathcal{V}\alpha^2}$ ensures that the potential ψ is independent of the parameter α and that the average potential in a unit cell vanishes [198, 203–205]. The resulting electrostatic potential energy reads [197, 198, 203, 205]

$$V_{ES}(\boldsymbol{r}) = \frac{1}{2}\sum_{j=1}^{N}\sum_{k=1}^{N}\frac{z_j z_k}{4\pi\epsilon_0}\psi(\boldsymbol{r}_{C,jk}) + \frac{1}{2}\sum_{j=1}^{N}\frac{z_j^2}{4\pi\epsilon_0}\lim_{\mathfrak{R}\to\boldsymbol{0}}\left(\psi(\mathfrak{R}) - \frac{1}{|\mathfrak{R}|}\right). \tag{3.197}$$

The last term in equation (3.197) corresponds to the Wigner potential [201, 205]. The Wigner potential gives the interaction energy of a point charge

with all its periodic images and the uniform, neutralizing background charge density [205]. Omitting the prefactors, we have [203]

$$\begin{aligned}\lim_{\mathfrak{R}\to\mathbf{0}}\left(\psi(\mathfrak{R})-\frac{1}{|\mathfrak{R}|}\right) &= \sum_{\substack{\boldsymbol{n}=-\infty\\ \boldsymbol{n}\neq\mathbf{0}}}^{\boldsymbol{n}=\infty}\frac{erfc(\alpha|\boldsymbol{n}L|)}{|\boldsymbol{n}L|}+\frac{4\pi}{\mathcal{V}}\sum_{\substack{\boldsymbol{k}=-\infty\\ \boldsymbol{k}\neq\mathbf{0}}}^{\infty}\frac{e^{-\frac{|\boldsymbol{k}|^2}{4\alpha^2}}}{|\boldsymbol{k}|^2}-\frac{\pi}{\mathcal{V}\alpha^2}\\ &\quad+\lim_{\mathfrak{R}\to\mathbf{0}}\left(\frac{erfc(\alpha|\mathfrak{R}|)}{|\mathfrak{R}|}-\frac{1}{|\mathfrak{R}|}\right)\\ &= \sum_{\substack{\boldsymbol{n}=-\infty\\ \boldsymbol{n}\neq\mathbf{0}}}^{\boldsymbol{n}=\infty}\frac{erfc(\alpha|\boldsymbol{n}L|)}{|\boldsymbol{n}L|}+\frac{4\pi}{\mathcal{V}}\sum_{\substack{\boldsymbol{k}=-\infty\\ \boldsymbol{k}\neq\mathbf{0}}}^{\infty}\frac{e^{-\frac{|\boldsymbol{k}|^2}{4\alpha^2}}}{|\boldsymbol{k}|^2}-\frac{\pi}{\mathcal{V}\alpha^2}-\frac{2\alpha}{\sqrt{\pi}}.\end{aligned} \tag{3.198}$$

According to reference [203], the correction term to Coulomb potential energy due to the Ewald sum without a uniform, neutralizing background charge density is precisely that given in equation (3.195).

Having discussed the basic theoretical framework of long-ranged interactions with cubic periodic boundary conditions, we turn to the description of the model systems in the next chapter.

Chapter 4

Model and simulation details

A physical system can be studied by experiment, computer simulation and analytical theory. Experiments study the real system, whereas simulations and theory use a representation of the real system: a *model* [106, 107]. Given a model, characterized by the interactions of the components of the model system, simulations provide essentially exact results. The outcome of the simulations can be used in two ways. On the one hand, a comparison of the simulation result and the outcome of a physical experiment provides a test of the model [106, 107]. On the other hand, an approximate *theory*, a set of consistent ideas to describe and explain a physical phenomenon [72], can be constructed from a model using assumptions. The theory then provides predictions of the properties of the system, and a comparison of those predictions with simulation results tests the assumptions of the theory [106, 107]. I shall employ computer simulations in this second sense.

Two model systems are studied in this work. The first system consists of a two-dimensional array of argon particles. This model system is used to test the transition path sampling method and the temperature control described in section 3.3.2. This procedure is adopted because the results are known [76, 164] and provide a reference. The second model system contains a classical ferrous ion solvated by classical water molecules,[15] which is oxidized in a redox half-reaction. The model system is employed for the following

[15] I shall call the $Fe^{2+}_{(aq)}/Fe^{3+}_{(aq)}$ system also iron (ion) model throughout this work.

purposes. First, the transition path sampling method is tested for a complex model because the system is (assumed to be) well described by Marcus theory. Second, the assumptions underlying Marcus theory can be tested by comparing results from Marcus theory based simulations to those from umbrella integration and (validated) transition path sampling because the latter make fewer assumptions. Third, numerical results for activation parameters and their derivatives are obtained for this model electron-transfer system.

Below, I describe the model systems and their interaction potentials. In addition, the simulation details are presented. I shall start with the argon model and turn to the iron system subsequently.

4.1 Argon

4.1.1 Argon model

The argon model system consists of nine atoms interacting via the purely repulsive Weeks-Chandler-Andersen (WCA) potential, shown in figure 4.1 (solid line):

$$V_{\mathrm{WCA}}(r) = \begin{cases} 4\,\epsilon_{LJ}\left(\left(\frac{\sigma_{LJ}}{r}\right)^{12} - \left(\frac{\sigma_{LJ}}{r}\right)^{6}\right) + \epsilon_{LJ} & \text{if } r \leq r_{\mathrm{WCA}}; \\ 0 & \text{if } r > r_{\mathrm{WCA}}. \end{cases} \tag{4.1}$$

The interaction potential corresponds to the potential of the reference system in references [206, 207]. The interaction is isotropic and depends on the distance r between two particles only. The strength ϵ_{LJ} and the range σ_{LJ} characterize the interaction potential. The repulsion is limited to distances up to $r_{\mathrm{WCA}} = 2^{1/6}\sigma_{LJ}$ [206].

In addition, two of the nine argon atoms are held together via a double-well potential [76, 164], shown in figure 4.2:

$$V_{dw}(r_{12}) = V_h \left(1 - \frac{(r_{12} - r_{\mathrm{WCA}} - r_w)^2}{r_w^2}\right)^2 . \tag{4.2}$$

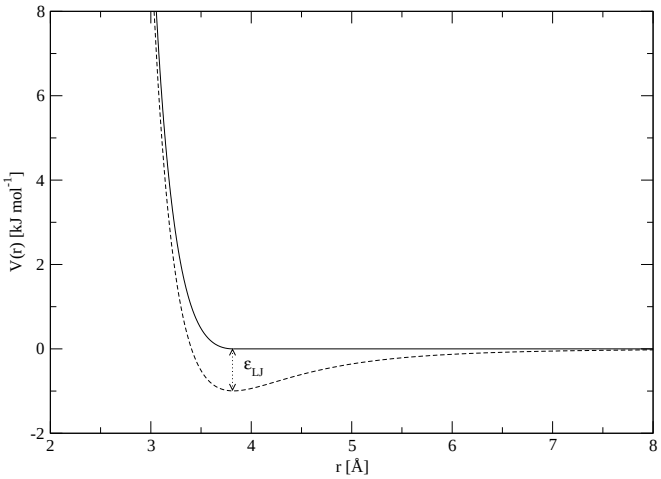

Figure 4.1: The Weeks-Chandler-Andersen (WCA) potential $V_{\mathrm{WCA}}(r)$ of equation (4.1) is shown as a function of the interparticle distance r (solid line). It is repulsive up to $r_{\mathrm{WCA}} = 2^{1/6}\sigma_{LJ}$ [206, 207]. For comparison the Lennard-Jones potential $V_{LJ}(r)$ is represented by the dashed line. The interaction strength ϵ_{LJ} is indicated at the potential energy minimum. The Lennard-Jones parameters of argon [166] are used for this figure.

The parameter r_w defines the width of the barrier separating the two stable states. The minima of the potential are located at $r_{12} = r_{\mathrm{WCA}}$ and $r_{12} = r_{\mathrm{WCA}} + 2r_w$; the maximum between the stable states is found at $r_{12} = r_{\mathrm{WCA}} + r_w$. The barrier height V_h determines how rare transitions between reactants and products are, and the bond length r_{12} of the dimer serves as reaction coordinate.

4.1.2 Previous work related to the argon model

The Weeks-Chandler-Andersen potential (4.1) was used to partition the Lennard-Jones potential and to investigate the role of repulsive and attractive forces on the structure and thermodynamics of a Lennard-Jones system [206]. It was found that the repulsive forces determined the structural and thermodynamic properties of the Lennard-Jones system at sufficiently high densities [206]. As

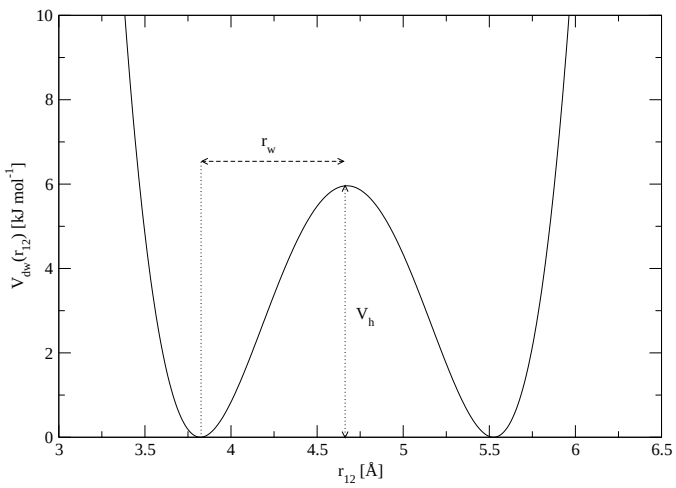

Figure 4.2: The double-well potential $V_{dw}(r_{12})$ of equation (4.2) for the argon dimer is shown. The bond length is denoted by r_{12}, whereas the height and the width of the potential barrier are V_h and r_w, as in [76,164]. The displayed barrier height corresponds to the microcanonical case: $V_h = 5.98\,\mathrm{kJ\,mol^{-1}}$ [164].

a result, the Weeks-Chandler-Andersen (WCA) potential effectively mimics the influence of a condensed phase environment. Furthermore, the Weeks-Chandler-Andersen potential is convenient in numerical simulations because it exhibits continuous forces.

The double-well potential (4.2) was employed to study the isomerization of a dimer in a WCA fluid in the microcanonical ensemble [164]. In particular, the rate constant was computed for this model system by molecular dynamics and transition path sampling simulations. In that work, Dellago, Bolhuis, and Chandler derived the rate constant (2.67) [164]

$$k_+(t) = \frac{\langle \dot{\theta}_P(x_t)\rangle^*_{RP}}{\langle \theta_P(x_{t'})\rangle^*_{RP}} \times \frac{\langle \theta_R(x_0)\theta_P(x_{t'})\rangle}{\langle \theta_R\rangle} \tag{4.3}$$

to improve the efficiency of rate constant calculations by means of transition path sampling, which does not require knowledge of the reaction mechanism. The rate constant evaluation consists of two parts. The first part evaluates

the first fraction on the right-hand side of equation (4.3), which is also done in the present work. The second part computes the second fraction on the right-hand side of equation (4.3) by means of a series of transition path sampling simulations for which the order parameter range of the final state is moved from reactants to products [164]. This procedure yields the reversible work to constrain the endpoint of the trajectories to the product region at time t' [164]. It was found that transition path sampling simulations became more efficient than molecular dynamics simulations for sufficiently high barriers separating the reactant and product states [164]. An additional conclusion was that the transition path sampling method should be applicable to chemical reactions in solution [164].

Dellago and Bolhuis studied the same isomerization reaction of the model dimer in the canonical ensemble [76]. They derived equation (2.70) [76]

$$E_a(t) = \frac{\langle \dot{\theta}_P(x_t)\, \mathcal{H}(\boldsymbol{\xi}_0)\rangle^*_{RP}}{\langle \dot{\theta}_P(x_t)\rangle^*_{RP}} - \langle \mathcal{H}(\boldsymbol{\xi}_0)\rangle_R \tag{4.4}$$

to avoid the computation of rate constants at several temperatures for the evaluation of activation energies. The calculation of activation energies could therefore be performed directly from a single transition path sampling simulation at a single temperature without knowledge of the reaction coordinate [76]. Dellago and Bolhuis foresaw the difficulty of obtaining statistically accurate activation energies for larger systems due to the increasing fluctuations in total energy with increasing system size [76].

The results of references [164] and [76] were reproduced in the present work to test the implementation of the transition path sampling method.

4.1.3 Argon simulation details

Three types of simulations have been performed for the argon model system: molecular dynamics (NVT-MD) computations in the canonical ensemble and transition path sampling simulations both in the canonical (NVT-TPS) and in the microcanonical ensemble (NVE-TPS). I shall first describe the aspects common to the three simulation set-ups and then outline the specifics for

each case.

In all cases, the simulation box is square with a length of $L = 13.19\,\text{Å}$ and periodically replicated. The Lennard-Jones parameters are taken from reference [166]; in particular, $\sigma_{LJ,Ar} = 3.405\,\text{Å}$ and $\epsilon_{LJ,Ar} = k_B T = 0.996\,\text{kJ mol}^{-1}$ with $T = 119.8\,\text{K}$. The argon mass is $m_{Ar} = 39.948\,\text{g mol}^{-1}$ and the number density $\rho_n = 0.6\,\sigma_{LJ,Ar}^{-2}$ [76, 164]. The width of the barrier is $r_w = 0.25\,\sigma_{LJ,Ar} = 0.85125\,\text{Å}$. The timescale associated with the Lennard-Jones potential for the argon system is $\tau_{LJ,Ar} = \sqrt{m_{Ar}\,\sigma_{LJ,Ar}^2/\epsilon_{LJ,Ar}} = 2.16\,\text{ps}$. The integration timestep is $2 \times 10^{-3}\,\tau_{LJ,Ar} = 4.31\,\text{fs}$ [76, 164].

Transition path sampling simulations for the argon model

Transition path sampling in the microcanonical and canonical ensembles employ trajectories of length $2\,\tau_{LJ,Ar} = 4.31\,\text{ps}$, which corresponds to 1000 timesteps, resulting in 101 time slices. A time slice comprises ten timesteps to reduce the memory requirements for storing the transition paths. The maximum shifting length amounts to 20 time slices, and the momentum change for each momentum degree of freedom in a shooting move is normally distributed with a width of $0.04\,\sqrt{m_{Ar}\,\epsilon_{LJ,Ar}}$. Shooting moves are attempted with a probability of $w_{shoot} = 0.6$. These simulation details are the same as in reference [76].

In the microcanonical case, the total energy is fixed at $E = 9\,\epsilon_{LJ,Ar} = 8.96\,\text{kJ mol}^{-1}$, and the height of the double-well potential is $V_h = 6\,\epsilon_{LJ,Ar} = 5.98\,\text{kJ mol}^{-1}$. The boundaries of the stable states are $r_{12} < 1.3\,\sigma_{LJ,Ar} = 4.4265\,\text{Å}$ for the reactants and $r_{12} > 1.45\,\sigma_{LJ,Ar} = 4.93725\,\text{Å}$ for the products. A total of 6×10^6 Monte Carlo steps are carried out, and shooting moves are accepted with a probability of 0.59, whereas shifting moves are successful in 75% of the attempted cases. The values for E, V_h and the stable state boundaries correspond to those given in reference [164].

In the case of the canonical ensemble, the height of the double-well potential is $V_h = 10\,\epsilon_{LJ,Ar} = 9.96\,\text{kJ mol}^{-1}$, and the boundaries of the stable states are $r_{12} < 1.35\,\sigma_{LJ,Ar} = 4.59675\,\text{Å}$ for the reactant state and $r_{12} > 1.45\,\sigma_{LJ,Ar} = 4.93725\,\text{Å}$ for the product state. These simulation details

coincide with those reported in reference [76]. For the 2×10^6 attempted Monte Carlo steps, shooting moves are accepted with an overall probability of 0.24. In contrast, shifting moves are accepted with a higher probability; they are successful in 81% of all cases. The probability of accepting the proposed shooting point according to the asymmetric generation probability for kinetic energies discussed in section 3.3.2 is 0.7, resulting in a conditional probability of 0.35 for accepting a shooting move given that the shooting point has been accepted.

Canonical molecular dynamics simulations for the argon model

The molecular dynamics simulation in the canonical ensemble is 10^9 timesteps long, and the velocities are scaled every 10^3 timesteps in such a way that the new kinetic energy is selected according to the canonical distribution. In particular, the new kinetic energy is proposed by the same algorithm that is employed to choose the kinetic energy of the shooting point in the transition path sampling simulations discussed in section 3.3.2. Specifically, a kinetic energy displacement ΔK is drawn from a normal distribution to yield a trial kinetic energy $K^n = K^o + \Delta K$ from the old kinetic energy K^o. The trial kinetic energy K^n is then accepted by means of a Monte Carlo procedure according to the Metropolis criterion with respect to the kinetic energy distribution in the canonical ensemble [141]. The barrier height is again $V_h = 10\,\epsilon_{LJ,Ar} = 9.96\,\mathrm{kJ\,mol^{-1}}$ [76].

All argon simulations were carried out with a purpose-written molecular dynamics program and an extended version of the transition path sampling procedure provided by Phillip Geissler. A pseudo random number generator written and provided by Nick MacLaran was employed. The iron simulations were performed with the same transition path sampling and pseudo random number generator programs. However, a modified version of the DL_POLY_2.18 program [208] was used for the molecular dynamics simulations. All programs and most analyzing tools were written in FORTRAN; the remaining analyzing scripts were written in bash.

4.2 Iron

4.2.1 Iron model

The iron model system consists of the oxidation half-reaction of the aqueous ferrous ion ($Fe^{2+}_{(aq)}$) to its ferric ($Fe^{3+}_{(aq)}$) counterpart:

$$Fe^{2+}_{(aq)} \rightarrow Fe^{3+}_{(aq)} + e^{-}_{(\mu)}. \tag{4.5}$$

As mentioned in the introduction, the iron ions are characterized by charge-localized, diabatic empirical valence bond states [105]. The mixing (γ_{el}) between the diabatic states yields adiabatic potential energies, discussed on page 139. The quantity μ represents an effective energy of the electron, which is not treated explicitly. This energy can be varied continuously and provides a means of controlling the effective reaction free energy $\Delta\mu = \mu - \mu_0$. The value $\Delta\mu = 0$, shown in figure 1.2, is reached for a vanishing reaction free energy according to the Marcus formula of equation (2.41): $\Delta_r F = \frac{1}{2}\left(\langle \Delta E \rangle_R + \langle \Delta E \rangle_P\right)$.

The electron is not treated quantum-mechanically because I focus on the statistical mechanics of the nuclear dynamics. Therefore, I describe the interaction potential determining the forces on the nuclei and the corresponding parameters for the iron ions and water molecules next. General aspects are given below, followed by the diabatic and adiabatic potential energy surfaces.

The model system involves only intermolecular interactions because the geometry of the water molecules is fixed by bond constraints. Long-ranged interactions are electrostatic, whereas short-ranged forces are derived from a Lennard-Jones potential. All interactions are pairwise additive and depend on the distance between the interaction sites only. Also, polarization effects are not taken into account.

Diabatic potential energy

The potential energy $V^{(d)}(\boldsymbol{r}_C)$ of an N-particle system with $\mathcal{N}_f$ degrees of freedom of a configuration $\boldsymbol{r}_C = \{r_{C,1}, \ldots, r_{C,\mathcal{N}_f}\} = \{\boldsymbol{r}_{C,1}, \ldots, \boldsymbol{r}_{C,N}\}$, where

$\boldsymbol{r}_{C,j}$ denotes the position vector of particle j in Cartesian coordinates, is the sum of van der Waals and electrostatic contributions:

$$V^{(d)}(\boldsymbol{r}_C) = V_{LJ}(\boldsymbol{r}_C) + V_{ES}(\boldsymbol{r}_C); \tag{4.6a}$$

$$V^{(d)}(\boldsymbol{r}) = V_{LJ}(\boldsymbol{r}) + V_{ES}(\boldsymbol{r}). \tag{4.6b}$$

Above, the set $\boldsymbol{r} = \{r_{12}, \ldots, r_{\mathcal{N}_r-1,\mathcal{N}_r}\}$ of distances $r_{jk} = |\boldsymbol{r}_{C,j} - \boldsymbol{r}_{C,k}|$ between two interaction sites j and k is introduced because the interaction potential depends on the distance between interaction sites only. The sum of interaction sites arising from all species is $\mathcal{N}_r = \mathcal{N}_O + \mathcal{N}_H + \mathcal{N}_{Fe}$. Specifically, one iron ion and 64 water molecules lead to $\mathcal{N}_r = 193$ interaction sites.

The short-range contribution is accounted for by a Lennard-Jones potential [72, 106, 107]

$$V_{LJ}(\boldsymbol{r}) = \sum_{j=1}^{\mathcal{N}_r-1} \sum_{k=j+1}^{\mathcal{N}_r} 4\,\epsilon_{LJ,jk} \left\{ \left(\frac{\sigma_{LJ,jk}}{r_{jk}} \right)^{12} - \left(\frac{\sigma_{LJ,jk}}{r_{jk}} \right)^{6} \right\}. \tag{4.7}$$

Above, the ϵ_{LJ} denotes the interaction strength of the Lennard-Jones potential, whereas σ_{LJ} measures the range of the interaction potential [106, 107]. The short-range effect of a water molecule is condensed into a single interaction site, namely the oxygen atom, so that we have $\epsilon_{HO} = \epsilon_{HFe} = \sigma_{HO} = \sigma_{HFe} = 0$. The short-ranged interaction potential thus reduces to

$$\begin{aligned} V_{LJ}(\boldsymbol{r}) = &\sum_{j=1}^{\mathcal{N}_O-1} \sum_{k=j+1}^{\mathcal{N}_O} 4\,\epsilon_{LJ,OO} \left\{ \left(\frac{\sigma_{LJ,OO}}{r_{jk}} \right)^{12} - \left(\frac{\sigma_{LJ,OO}}{r_{jk}} \right)^{6} \right\} \\ &+ \sum_{l=1}^{\mathcal{N}_O} 4\,\epsilon_{LJ,FeO} \left\{ \left(\frac{\sigma_{LJ,FeO}}{r_{Fe,l}} \right)^{12} - \left(\frac{\sigma_{LJ,FeO}}{r_{Fe,l}} \right)^{6} \right\}. \end{aligned} \tag{4.8}$$

The first term on the right-hand side of equation (4.8) above includes a sum over all unique pairs of water molecules, whereas the second term covers the interaction of the iron ion with all water molecules. The Lennard-Jones parameters for interaction potentials between unlike species j and k are con-

$\sigma_{LJ,OO}$	$\sigma_{LJ,FeFe}$	$\sigma_{LJ,FeO}$	$\epsilon_{LJ,OO}$	$\epsilon_{LJ,FeFe}$	$\epsilon_{LJ,FeO}$
3.16549	2.2	2.63895	0.65073	0.13523	0.29665

Table 4.1: The Lennard-Jones parameters for water-water interactions of the SPC [109] water model are as in [110]. The iron-iron interaction parameters are taken from reference [49]. Iron-water interaction parameters are obtained from the geometrical combination rules $\epsilon_{LJ,jk} = \sqrt{\epsilon_{LJ,jj}\,\epsilon_{LJ,kk}}$ and $\sigma_{LJ,jk} = \sqrt{\sigma_{LJ,jj}\,\sigma_{LJ,kk}}$ [49]. The Lennard-Jones interaction range parameters are in Å, whereas the interaction strength parameters are in $\mathrm{kJ\,mol^{-1}}$.

structed using the following combination rules [49, 209]:[16]

$$\epsilon_{LJ,jk} = \sqrt{\epsilon_{LJ,jj}\,\epsilon_{LJ,kk}}; \tag{4.9a}$$

$$\sigma_{LJ,jk} = \sqrt{\sigma_{LJ,jj}\,\sigma_{LJ,kk}}. \tag{4.9b}$$

The Lennard-Jones parameters used in the present work are summarized in table 4.1. It is noteworthy that the Lennard-Jones parameters for the ferrous and ferric ions are the same. Hence, the difference in interaction energy of the water molecules with each iron ion stems from the long-range interaction described below.

The electrostatic potential energy V_{ES} is given by the Coulomb interaction between unique pairs of (partially) charged interaction sites with cubic periodic boundary conditions [198], as described in section 3.5:

$$V_{ES}(\boldsymbol{r}) = \frac{1}{2}\sum_{j=1}^{\mathcal{N}_r}\sum_{k=1}^{\mathcal{N}_r}\frac{z_j z_k}{4\pi\epsilon_0}\sum_{\boldsymbol{n}=-\infty}^{\boldsymbol{n}=\infty_{**}}\frac{1}{|\boldsymbol{r}_{C,jk}+\boldsymbol{n}L|}. \tag{4.10}$$

Above, the symbol $**$ in the last sum indicates that the Coulomb interaction is omitted for interaction sites on the same molecule [208] and that the terms for $\boldsymbol{n} = \boldsymbol{0}$ are omitted if $j = k$. The distance between site j and site k is denoted by $|\boldsymbol{r}_{C,jk}|$, and the charge of particle l is z_l. The permittivity in vacuum is $\epsilon_0 = 8.854187817 \times 10^{-12}\,\mathrm{As\,(Vm)^{-1}}$, and $e_0 = 1.60217646 \times$

[16]Note that the combination rule given in references [49, 209] for the interaction range $\sigma_{LJ,jk}$ of (4.9b) differs from the conventional Lorentz-Berthelot rule [107]: $\sigma_{LJ,jk} = \frac{1}{2}(\sigma_{LJ,jj} + \sigma_{LJ,kk})$.

10^{-19} As denotes the elementary charge [1].

For the solvent a simple point charge (SPC) water model is employed [109,110]. The partial charge on the oxygen atom is $z_O = -0.82\, e_0$, that carried by hydrogen atoms is $z_H = 0.41\, e_0$. The geometry of the water molecules is determined by imposing the following bond lengths via the RATTLE algorithm described in section 3.1.5: $r_{OH} = 1.0\,\text{Å}$ and $r_{HH} = 1.63299\,\text{Å}$. The charges of the ferrous ($z_{Fe} = 2\, e_0$) and ferric ($z_{Fe} = 3\, e_0$) ions correspond to the oxidation state of the iron species. The masses of the nuclear species are $m_{Fe} = 55.845\,\text{g}\,\text{mol}^{-1}$, $m_O = 16\,\text{g}\,\text{mol}^{-1}$ and $m_H = 1\,\text{g}\,\text{mol}^{-1}$.

Adiabatic potential energy

The adiabatic potential energy of the model system is characterized by two control parameters whose effects are described below: the coupling element γ_{el}, mixing the diabatic states, and the effective energy μ, shifting the diabatic states with respect to each other. I shall first deal with the coupling element.

Above, the potential energies of the iron ions correspond to those of charge-localized, diabatic states. For the oxidation process of interest a transition between the diabatic states must occur. In addition, molecular dynamics simulations require smooth forces to ensure sufficient stability of the integration algorithm. Both requirements can be met if the diabatic states interact via a constant coupling element γ_{el}, yielding the ground state adiabatic potential energy surface $V^{(a)}$, as in reference [108]:

$$V^{(a)}(\boldsymbol{r}_C, \gamma_{el}) = \frac{V^{(d)}_{Fe^{2+}}(\boldsymbol{r}_C) + V^{(d)}_{Fe^{3+}}(\boldsymbol{r}_C)}{2} - \frac{1}{2}\sqrt{(\Delta E(\boldsymbol{r}_C))^2 + 4\,\gamma_{el}^2}. \tag{4.11}$$

As above, the variable $\boldsymbol{r}_C$ denotes the Cartesian coordinates of all particles in the system, and the diabatic potentials $V^{(d)}_{Fe^{2+}}$ and $V^{(d)}_{Fe^{3+}}$ have the form given in equations (4.6), (4.8) and (4.10). Because the energy difference ΔE is instantaneously evaluated at a fixed nuclear configuration, the kinetic energy remains unaltered, and the diabatic gap (2.30) is a function of positions only:

$$\Delta E(\boldsymbol{r}_C) = V^{(d)}_{Fe^{3+}}(\boldsymbol{r}_C) - V^{(d)}_{Fe^{2+}}(\boldsymbol{r}_C). \tag{4.12}$$

The coupling element γ_{el} not only mixes the charge-localized states, but also determines the energy difference between the diabatic and adiabatic states at the crossing point ($\Delta E = 0$).

The description of the model electron-transfer reaction in terms of adiabatic potential energy surfaces implies that the system will evolve on the ground-state potential enregy surface. At the beginning the solute will be the ferrous ion (Fe^{2+}), and after the barrier crossing the ferric ion (Fe^{3+}) is obtained. In the barrier region, the charge distribution of the solute depends on the strength of the electronic coupling γ_{el} [35]. For very weak couplings the interaction between the two diabatic states would only be important for nearly degenerate states. In the opposite limit of very strong coupling, the two diabatic states would mix significantly over a large range of energy differences so that their individual characters might not be recognizable [210]. As a consequence from the above, the coupling strength determines how close the diabatic states have to be in energy for significant mixing to occur [35]. In the present model, the coupling element is of the order of $k_B T$, which was considered by Marcus as a sufficiently weak coupling for the diabatic picture to provide a rather accurate description of the electron-transfer process [35] and by Hush as a sufficiently strong coupling to justify an adiabatic electron transfer [86]. As mentioned in the introduction, the physical situation is likely to be the following. The electronic coupling is sufficiently strong for the nuclear dynamics to occur on the ground-state potential energy surface [38]. Furthermore, the electronic coupling is sufficiently weak that the adiabatic state clearly has the character of the reactant diabatic state in the reactants and the character of the product diabatic state after the barrier crossing [35, 38]. In other words, the solute's charge distribution resembles that of the diabatic states in the corresponding regions of phase space and the solute's charge distribution is not a mixture between the reactant and product diabatic states due to strong coupling. However, in the vicinity of the barrier top the two diabatic states are close in energy and the electronic coupling between them becomes effective so that the electron transfer can occur [38]. The physical picture is then to a good approximation a transition from the reactant diabatic state to the product diabatic state enabled by

a suitable fluctuation of the solvent [35]. As mentioned earlier, the solvent configuration at which the transition occurs would be in equilibrium with the completely mixed solute charge distribution [38].

In the present model, the situation is as close as possible to the physical picture described above in the following sense. The electronic coupling is so small that it only effectively mixes the reactant and product diabatic states in the barrier region. The resulting charge distribution could be described as schematically illustrated in figure 4.3. The charge of the iron ion would essentially correspond to that of the ferrous ion in the reactant well and switch to a charge close to that of the ferric ion in the product well within a narrow energy gap range around the barrier top. The instantaneous charge on the iron ion would roughly correspond to the equivalent charge distribution that would be in equilibrium with the instantaneous solvent configuration [38]. However, due to the interaction of the system with a neutralizing, homogeneous charge density, the correspondence between the relative weight of the diabatic states and the amount of charge transferred between the reactants and products is not exact [34].

The use of the diabatic energy gap as the reaction coordinate and of the adiabatic potential energy (4.11) for the dynamics will result in the energy gap being a dynamically relevant variable. However, this does not guarantee that Marcus theory will be obeyed. As already mentioned, the validity of Marcus theory requires that the gap as the reaction coordinate is normally distributed in the reactant and product states with the same variance [68]. Hence, if the energy gap is not normally distributed or if the variances in the two states differ, Marcus theory will not be obeyed. If the aim is only to construct the free energy profile, alternative order parameters can be used. For instance, Zhou and Szabo employed a charging parameter to efficiently construct the free energy functions [48]. However, if dynamical trajectories are required, the coupling of two potential energy surfaces seems the most straightforward way unless a completely new adiabatic potential energy function is parametrized. In addition, any potential energy function would have to allow for two stable states that can be distinguished by means of an order parameter. In principle, different potential energy functions define different

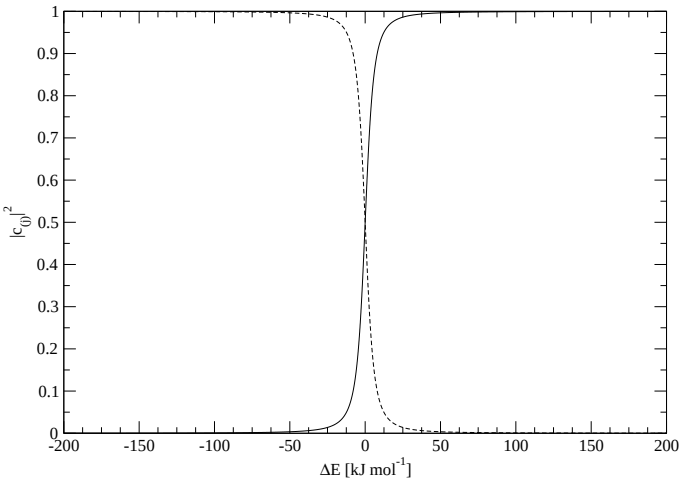

Figure 4.3: Schematic illustration of the charge distribution during the oxidation of the ferrous ion in terms of the coefficients $c_{(j)}$ of the diabatic states in the adiabatic state $|\Psi_1\rangle = c_{(R)}|\Psi_R\rangle + c_{(P)}|\Psi_P\rangle$ [85, 86]. The hypothetical charge density of the transferring electron is shown for the reactant ($|c_R|^2$; solid line) and for the product ($|c_P|^2$; dashed line) diabatic states assuming negligible overlap between the two diabatic states [15, 85, 86].

systems so that the dynamics would differ for another choice of the potential function.

The mixing of the diabatic states also affects the forces used in the molecular dynamics simulations. The force $\boldsymbol{\mathcal{F}}_j$ on particle j derived from the adiabatic potential energy (4.11) reads

$$\begin{aligned}\boldsymbol{\mathcal{F}}_j^{(a)} &= -\nabla_{\boldsymbol{r}_{C,j}} V^{(a)} \\ &= \frac{1}{2}\left(\boldsymbol{\mathcal{F}}_{R,j} + \boldsymbol{\mathcal{F}}_{P,j}\right) + \frac{1}{2}\frac{\Delta E(\boldsymbol{r}_C)}{\sqrt{(\Delta E(\boldsymbol{r}_C))^2 + 4\,\gamma_{el}^2}}\left(\boldsymbol{\mathcal{F}}_{R,j} - \boldsymbol{\mathcal{F}}_{P,j}\right), \qquad (4.13)\end{aligned}$$

where the forces derived from the diabatic potential energies of the reactant and product states are denoted by $\boldsymbol{\mathcal{F}}_{R,j}$ and $\boldsymbol{\mathcal{F}}_{P,j}$. It is seen from equation (4.13) that the forces correspond to those of the diabatic reactant state if $\Delta E \gg 0$ in which case $\Delta E\left((\Delta E)^2 + 4\gamma_{el}^2\right)^{-1/2}$ is essentially unity. Similarly,

for $\Delta E \ll 0$, $\Delta E\left((\Delta E)^2 + 4\gamma_{el}^2\right)^{-1/2}$ approaches -1, and the forces essentially coincide with those found in the diabatic product state. In the barrier region the adiabatic force on particle j has contributions from both diabatic states. This choice ensures that the forces near the barrier top are continuous. In practice, the potential energies and the forces for both diabatic states are computed at a given nuclear configuration. Then, the adiabatic potential energy and the adiabatic forces are evaluated according to equations (4.11) and (4.13). Subsequently, the integration according to the velocity Verlet algorithm proceeds as usual.

Next, I describe the effective energy μ in more detail. I shall start with a short motivation and turn to quantitative aspects subsequently. As noted above, the short-range contribution to the potential energy is the same for the present model ferric and ferrous ions. Consequently, the diabatic gap is determined by the difference in electrostatic interactions. Because the interaction among the water molecules is the same for both oxidation states, the charge of the iron ion determines the potential energy difference between the diabatic states via the difference in solvation energies. It then follows from the Born solvation (free) energy formula (4.14) [33] that the ferric ion has a lower energy than the ferrous ion for any solvent configuration:

$$E_{solvation} = -\frac{1}{4\pi\epsilon_0}\frac{z^2}{2B}\left(1 - \frac{1}{\epsilon_r}\right). \tag{4.14}$$

In equation (4.14) B and z denote the radius and the charge of the solvated ion. The permittivity in vacuum is again ϵ_0, and ϵ_r denotes the relative dielectric constant of the medium. The ferric ion is stabilized to such an extent that the reaction free energy becomes very negative and that the system is in the inverted regime of Marcus theory (dotted-dashed line in figure 4.4). However, the present work aims at investigating thermal electron-transfer processes in the normal regime (dashed line in figure 4.4) characterized by moderate reaction free energies. Hence, the energy μ is introduced to increase the potential energy of the ferric ion and to decrease that of the ferrous ion

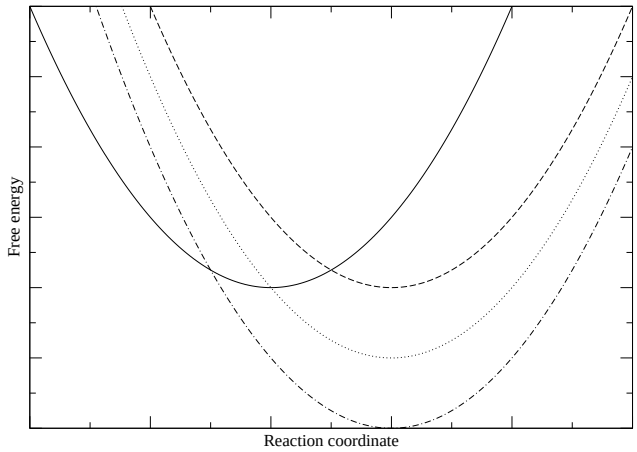

Figure 4.4: Schematic illustration of the different regimes in Marcus theory [42]. The solid line represents the free energy curve of the reactant state, whereas the three different product free energy curves are displayed. The normal regime, in which $-\Delta_r F < \lambda$, is represented by the dashed line. In contrast, the inverted regime is illustrated by the dotted-dashed line. In the inverted regime, $-\Delta_r F > \lambda$ and reactive transitions are always non-adiabatic. The normal regime is characterized by increasing rate constants as the reaction free energy decreases, whereas the free energy barrier increases with decreasing reaction free energy in the inverted regime. The rate constant reaches its maximum value if the reaction is barrierless: $-\Delta_r F = \lambda$ (dotted line). The inverted regime is a consequence of the quadratic dependence of the activation free energy on the reaction free energy.

according to equations (4.15):

$$V^{(d)}_{Fe^{2+}}(\boldsymbol{r}_C, \Delta\mu) = V^{(d)}_{Fe^{2+}}(\boldsymbol{r}_C) - \frac{\mu}{2} = V^{(d)}_{Fe^{2+}} - \frac{\mu_0}{2} - \frac{\Delta\mu}{2}; \tag{4.15a}$$

$$V^{(d)}_{Fe^{3+}}(\boldsymbol{r}_C, \Delta\mu) = V^{(d)}_{Fe^{3+}}(\boldsymbol{r}_C) + \frac{\mu}{2} = V^{(d)}_{Fe^{3+}} + \frac{\mu_0}{2} + \frac{\Delta\mu}{2}. \tag{4.15b}$$

This procedure yields a controllable effective free energy difference $\Delta\mu = \mu - \mu_0$ for the iron model system that allows for reactive transitions. If Marcus theory applies, the reaction free energy in the absence of any potential shift is $\Delta_r F(\mu = 0) = \frac{1}{2}(\langle \Delta E \rangle_R + \langle \Delta E \rangle_P) = -\mu_0$. Thus, the specific value μ_0

leads to a system with vanishing reaction free energy $\Delta\mu = 0$.

The shifting parameter μ is introduced for computational and theoretical convenience. In the case of heterogeneous electron transfer, μ might be considered as being related to the potential applied at an electrode and $\Delta\mu$ as the overpotential. This phenomenological view would then effectively incorporate the interaction of the solute species with the electrode, thereby circumventing the difficulties associated with treating the electric double layer explicitly. However, if the overpotential is non-zero, the system is not in equilibrium any longer because a net current would arise. The present work focuses on equilibrium systems and their dynamics, and the parameter μ is therefore best regarded as a tool to aid establish a suitable thermally activated process.

In practice, the shift of the reaction free energy origin to μ_0 gives for the diabatic gap

$$\Delta E(\boldsymbol{r}_C, \Delta\mu) = V^{(d)}_{Fe^{3+}}(\boldsymbol{r}_C, \Delta\mu) - V^{(d)}_{Fe^{2+}}(\boldsymbol{r}_C, \Delta\mu) = \Delta E(\boldsymbol{r}_C, 0) + \Delta\mu. \quad (4.16)$$

Also, the adiabatic potential energy surface is now characterized by

$$\begin{aligned} V^{(a)}\left(\boldsymbol{r}_C, \gamma_{el}, \Delta\mu\right) =& \frac{V^{(d)}_{Fe^{2+}}(\boldsymbol{r}_C, \Delta\mu) + V^{(d)}_{Fe^{3+}}(\boldsymbol{r}_C, \Delta\mu)}{2} \\ & - \frac{1}{2}\sqrt{\left(\Delta E(\boldsymbol{r}_C, \Delta\mu)\right)^2 + 4\,\gamma_{el}^2} \\ =& \frac{V^{(d)}_{Fe^{2+}}(\boldsymbol{r}_C, 0) + V^{(d)}_{Fe^{3+}}(\boldsymbol{r}_C, 0)}{2} \\ & - \frac{1}{2}\sqrt{\left(\Delta E(\boldsymbol{r}_C, \Delta\mu)\right)^2 + 4\,\gamma_{el}^2}. \end{aligned} \quad (4.17)$$

Above, the first term on the right-hand side is independent of the shifting potential μ. The effect of the energy μ on the second term on the right-hand side is to shift the system into the normal regime of Marcus theory. The adiabatic potential (4.17) is close to that of the ferrous and ferric ions for large positive and negative diabatic gap values. Furthermore, the largest deviation (γ_{el}) from any diabatic state occurs at the assumed transition state, where the diabatic gap vanishes, as mentioned earlier.

Below, I shall consider the effect of $\Delta\mu$ on the (diabatic) reaction and reorganization free energies according to Marcus theory. If the linear response approximation holds, the following relations are expected to be accurate:

$$\begin{aligned}\Delta_r F(\Delta\mu) &= \frac{1}{2}\left(\langle\Delta E(\Delta\mu)\rangle_R + \langle\Delta E(\Delta\mu)\rangle_P\right) \\ &= \Delta_r F(0) + \Delta\mu = \Delta\mu; \qquad (4.18a)\\ \lambda(\Delta\mu) &= \frac{1}{2}\left(\langle\Delta E(\Delta\mu)\rangle_R - \langle\Delta E(\Delta\mu)\rangle_P\right) = \lambda(0) = \lambda. \qquad (4.18b)\end{aligned}$$

As seen above, the shifting potential μ defines an effective reaction free energy $\Delta\mu$. This feature will be exploited to investigate the dependence of the activation parameters on the reaction free energy.

4.2.2 Previous work related to the iron model

Systems involving iron ions and classical water molecules have been examined previously in the literature; some examples include references [34, 45, 49, 97, 211–214]. These works have focused on different aspects of the aqueous iron ion model systems.

For instance, a realistic microscopic model for the iron ion self-exchange reaction $Fe^{2+} + Fe^{3+} \rightleftharpoons Fe^{3+} + Fe^{2+}$ in aqueous solution was constructed by Kuharski and co-workers [45]. The model consists of two classical ferric ions, 430 classical SPC water molecules and an electron that is treated quantum-mechanically [45]. The activation free energy was computed by means of umbrella sampling, and it was found that Marcus theory was valid for that model system [45]. In particular, the free energy curves were parabolas to a good approximation, and the activation free energies obtained from umbrella sampling and from extrapolation of gap fluctuations in the stable states agreed well [45]. Furthermore, the ligand structure at the transition state was studied. The average distance between the iron ions and the oxygen sites of the first solvation shell was intermediate (2.08 Å) between that of the single ferric (2.02 Å) and ferrous (2.15 Å) ions [45]. In particular, the transition state was assumed to exhibit two iron ions with a charge of $z_{Fe} = 2.5\, e_0$ [45].

The ferrous-ferric electron transfer was investigated in reference [211].

In particular, the dependence of the free energy curves on the distance of the iron ion from the electrode was considered [211]. It was found that the model system of an iron ion and 216 water molecules between two conducting walls exhibited slight non-linearities and that the curvature of the free energy functions depended weakly on the distance of the ion from the electrode [211]. The dynamics were described in the non-adiabatic limit, and free energy curves were obtained by molecular dynamics and umbrella sampling simulations [211]. In addition, Smith and Halley evaluated the electrochemical transfer coefficient, which corresponds to the charge-transfer symmetry factor for elementary reactions, and found a value of 0.6 ± 0.2 [211].

Rose and Benjamin computed the free energy curves for a series of aqueous iron ions next to an electrode compared to the bulk behaviour [212]. The resulting free energy curves for the ferrous and ferric ions obey the linear response approximation [212]. Furthermore, it was found that even the presence of an electric field did not lead to a breakdown of the linear response behaviour [212]. The focus of Rose and Benjamin was on the relative inner- and outer-shell contributions of the solvent to the free energy curves to study the effect of the electrode compared to the bulk solution [212]. Molecular dynamics and umbrella sampling simulations of both the ferrous and the ferric ion solvated by 512 flexible SPC water molecules between two parallel Pt slabs showed that the solvent contribution from inner- and outer-shell reorganization was essentially identical for the bulk and metal/solution interface [212]. Deviations from the linear response behaviour were most pronounced for the inner-shell reorganization around the neutral iron atom [212].

The adiabatic heterogeneous electron transfer from a ferrous ion to a ferric ion was investigated in reference [213]. In particular, the classical activation free energy was compared to the quantum activation free energy by means of path integral simulations [213]. The molecular dynamics and umbrella sampling simulations in the canonical ensemble involved 671 flexible SPC water molecules and an iron ion next to a Pt electrode [213]. It was found that the activation free energy in the quantum treatment was significantly larger than that in the classical case, suggesting that quantum aspects might have to be considered in the description of heterogeneous electron transfer [213].

In addition, the transition state theory framework underlying Marcus theory was tested by computing the transmission factor in the classical case. The transmission factor was found to be approximately 0.6, thereby supporting the transition state theory character of the electron transfer between the ferrous ion and the electrode [213].

The iron ion self-exchange reaction was also studied by Yelle and Ichiye [97]. They used 717 TIP3P [215] water mocules with truncated octahedral periodic boundary conditions in the microcanonical ensemble and compared molecular dynamics simulation results for the solvation free energy to a dielectric continuum model and a model taking into account dielectric saturation [97]. The solvation free energy of an ion depends on the presence and distance of another ion, thus affecting the activation free energy [97]. In particular, it was found that the free energy curves were parabolic to a good approximation and that the activation free energy decreases as the ions approach each other from an infinite separation [97]. The latter effect arises because the solvent rearranges around two ions at large separations; however, at small separations between the ions, the solvent far from the two ions remains essentially unaltered, and only the solvent molecules close to the ion pair reorganize, thereby reducing the activation free energy compared to the large separation case [97].

The effect of high-frequency intramolecular vibrations of solvent molecules in the first solvation shell on the reorganization free energy was studied by Ando [49]. The simulations were performed in the microcanonical ensemble and involved a ferrous and a ferric ion as well as 500 TIP3P [215] water molecules contained in a cubic cell that was periodically replicated [49]. It was found that the contribution from inner-shell solvent reorganization was around 40 % and that nuclear quantum effects were important to capture the full dependence of the electron-transfer rate constant on the reaction free energy [49].

Amira and co-workers investigated the solvation structure and dynamics of SPC-like water molecules around a single ferrous or ferric ion in dilute aqueous solution (512 water molecules) [214]. The iron ions were found to exhibit a six-fold first coordination shell and corresponding iron-oxygen dis-

tances of $1.96 - 1.99$ Å for the ferric ion and 2.09 Å for the ferrous ion [214]. A flexible SPC-like water model was constructed to account for the oxygen-hydrogen vibrational spectra in pure liquid water and in the presence of an iron ion [214]. Furthermore, the flexible water model enabled Amira and co-workers to observe an increase in the oxygen-hydrogen bond length and a decrease of the water bond angle for water molecules close to an iron ion compared to the pure liquid. The effect was more pronounced for the ferric ion than for the ferrous one [214]. Importantly, the structural properties of the aqueous solutions were found to be rather similar for the different SPC-based water models [214].

Ayala and Sprik investigated two half-reactions involving iron ions in aqueous solution ($Fe^{2+} \rightarrow Fe^{3+} + e^-$ and $Fe^+ \rightarrow Fe^{2+} + e^-$) [34]. Their main focus was on the dependence of oxidation free energies and reorganization free energies on system size [34]. It was found from molecular dynamics simulations involving a varying number of classical simple point charge water molecules and Ewald summation including a uniform, neutralizing background charge density that the reaction free energy was relatively insensitive to the system size; its dependence scales as the inverse volume in solvents with high static dielectric constants [34]. In contrast, the reorganization free energy varies with system size as the inverse length of the cubic simulation cell [34]. Furthermore, the iron-oxygen distance of the first solvation shell was 1.93 Å for the ferric ion (Fe^{3+}) and 2.03 Å for the ferrous ion (Fe^{2+}) [34]. Importantly, it was pointed out that the mixing of the diabatic potential energy surfaces and an increase of the charge on the ion are not equivalent if the system is treated with periodic boundary conditions [34]. In particular, a charge of $z_{Fe} = 2.5\, e_0$ on the iron ion and a Hamiltonian $\mathcal{H} = \frac{1}{2}\left(\mathcal{H}_R + \mathcal{H}_P\right)$ are not exactly equivalent [34]. It was shown that the linear response approximation was obeyed for the half-reaction involving the oxidation of the aqueous ferrous ion [34].

Free energy profiles for electron-transfer systems described by classical nuclear dynamics and force fields have been computed and discussed many times, for example in references [43–48, 91, 97, 211–213, 216]. It was found in most cases that the linear response approximation is quite robust. However,

if the charge transfer leads to neutral species, for example in charge recombination or charge separation reactions, deviations from the linear response behaviour have been observed [47, 48, 97, 212, 216].

The validity of Marcus theory has also been investigated from other viewpoints. For instance, the transmission coefficient has been evaluated for a model electron-transfer process to assess the importance of solvent dynamical effects [108]. Furthermore, the effect of electronic friction on heterogeneous electron-transfer rates [217] and the treatment of Coulomb interactions on the potential of mean force between iron ions have been studied [218]. In addition, the solvent relaxation after photoinduced electron transfer from the ferrous to the ferric ion was shown to exhibit moderate deviations from the expected linear response behaviour [219].

Although the following studies did not consider *small inorganic* solute species in polar solvents, I mention the evaluation of reorganization free energies and reorganization entropies in polar solvents in the work of references [51, 52]. These studies are examples of the comparatively infrequent effort to determine the temperature dependence of the electron-transfer activation free energy from which the activation entropy and the activation energy can be obtained [220]. Ghorai and Matyushov found a positive reorganization entropy for $p-$nitroaniline, which exhibits a large change in dipole moment upon electron transfer, in water and acetonitrile [52]. In a more complex system, which included a donor-spacer-acceptor complex solvated by TIP3P water molecules mimicking a biological intramolecular electron transfer, the reorganization entropy was also positive [51]. However, the overall activation entropy was negative, indicating that the reorganization entropy need not be the dominant factor [51]. In fact, Matyushov [220] noted that the activation entropy has contributions from the reorganization entropy and from the reaction entropy, which is in line with Marcus theory whose corresponding expression is equation (2.50) [37]:

$$\Delta_{\ddagger} S^{(d)} = \left(\frac{1}{2} + \frac{\Delta_r F}{2\,\lambda}\right) \Delta_r S + \left(\frac{1}{4} - \left(\frac{\Delta_r F}{2\,\lambda}\right)^2\right) \Delta S_{\lambda}. \tag{4.19}$$

According to reference [37], the reorganization entropy ΔS_λ is typically negligible compared to the reaction entropy. The studies of Matyushov and co-workers [51, 52, 220] go beyond this statement and provides evidence from molecular simulation and analytical theory that the reorganization entropy is positive, whereas dielectric continuum theory predicts a negative reorganization entropy for solvents with high static dielectric constant [52].

4.2.3 Iron simulation details

Four types of simulations, divided into two groups, are carried out for the iron model system. On the one hand, canonical molecular dynamics simulations are performed, which include Marcus theory (MT) based simulations on the diabatic potential energy surfaces ($\gamma_{el} = 0$) and biased molecular dynamics simulations (umbrella integration) on the adiabatic potential energy surface of equation (4.11) with an electronic coupling of $\gamma_{el} = 3\,\mathrm{kJ\,mol^{-1}}$. On the other hand, molecular dynamics simulations in the microcanonical ensemble are carried out in transition path sampling (TPS) simulations and during the committor (COM) analysis. These simulations are also performed on the adiabatic potential energy surface. The transition path sampling method also uses Monte Carlo moves, as described in section 3.3. I shall describe those features common to all simulations first and continue with the two categories of simulations mentioned above in turn.

In all simulations the SPC water model [109, 110] described earlier is employed, and the equations of motion are integrated by means of the velocity Verlet/RATTLE algorithm [166, 167, 169] with a timestep of $\delta t = 1\,\mathrm{fs}$. One iron ion is solvated by $\mathcal{N}_W = 64$ water molecules in a cubic box of side length $L = 12.69\,\text{Å}$, which is periodically replicated. As discussed in section 3.5, a neutralizing, homogeneous charge density background is added to obtain an overall neutral system. The parameters of the interaction potential have been given in the previous section. The electrostatic interactions are treated via the Ewald summation technique [106, 107, 199]. Simulations are performed at effective free energy ($\Delta\mu$) values of -10 to $40\,\mathrm{kJ\,mol^{-1}}$ in steps of $10\,\mathrm{kJ\,mol^{-1}}$, and we employ $\mu_0 = 1944\,\mathrm{kJ\,mol^{-1}}$.

Molecular dynamics simulations in the canonical ensemble

The temperature in the MT and UI simulations is controlled by a Nosé-Hoover thermostat [172–175] with a relaxation time of $\tau_{NH} = 1\,\mathrm{ps}$. Equilibration runs last 1 ns, whereas production runs are 10 ns long, yielding 10^4 uncorrelated data points for subsequent analysis. Molecular dynamics simulations in the canonical ensemble are performed at temperatures of 278.15 K, 298.15 K and 318.15 K. Marcus theory based simulations, which evaluate $\Delta_r F$, λ and $\Delta_\ddagger F^{(d)}$ from the average diabatic gaps in the stable states according to equations (2.41), (2.43) and (2.29), are also carried out at 338.15 K and 358.15 K. This approach is further used to compute the free energies of reaction according to Simpson's rule (4.20), as an application of equation (C.1):

$$\Delta_r F_{SR} = \frac{\langle \Delta E \rangle_R + 4\,\langle \Delta E \rangle_{\mathrm{CP}} + \langle \Delta E \rangle_P}{6}. \tag{4.20}$$

The subscripts indicate reactants (R), products (P) and crossing points (CP), for which the coupling parameter values of the Hamiltonian (3.156) are $\zeta = 0$, $\zeta = 1$ and $\zeta = 0.5$.

In the case of umbrella integration simulations, 27 windows have been employed. The window centres are located from $-225\,\mathrm{kJ\,mol^{-1}}$ to $225\,\mathrm{kJ\,mol^{-1}}$ in steps of $25\,\mathrm{kJ\,mol^{-1}}$. Additional windows close to the barrier top are centred at $-20\,\mathrm{kJ\,mol^{-1}}$ to $20\,\mathrm{kJ\,mol^{-1}}$ in steps of $5\,\mathrm{kJ\,mol^{-1}}$. The generalized force constant for the harmonic restraining potential of equation (3.167) is $\kappa_b = 2.5 \times 10^{-2}\,\mathrm{mol\,(kJ)^{-1}}$. Umbrella integration [65] simulations yield the free energy profile $F_L(\Delta E)$ along the diabatic gap, as described in section 3.4.4. This Landau free energy profile is employed to determine the free energy of reaction according to equation (3.150) with ΔE as order parameter and $\theta_P(\Delta E) = \theta(-\Delta E) = 1 - \theta_R(\Delta E)$. In addition, the free energy profile yields the Landau free energy of reaction (2.37) as an approximation to the reaction free energy. As mentioned in section 2.2.1, the difference between the reaction free energy and the Landau free energy of reaction for normally distributed order parameters is given by equation (2.38). Here, the curvature of the free energy profile is extracted from regions where the second derivative of the free energy curves are approximately constant. Furthermore, the

adiabatic activation free energy $\Delta_{\ddagger}F^{(a)}$ is obtained as the Landau free energy difference between the reactant minimum and the barrier top, as indicated in equation (2.45).

Internal energies are obtained from the finite difference approximation (4.22) [2] to the Gibbs-Helmholtz equation (2.49), whereas entropies result from the finite difference temperature derivative of the corresponding free energy according to equation (4.21) [2, 29, 54].

$$\Delta S(T) = -\frac{\Delta F(T+\Delta T) - \Delta F(T-\Delta T)}{T+\Delta T-(T-\Delta T)} \tag{4.21}$$

$$\begin{aligned}\Delta U(T) = &\left(\frac{\Delta F(T+\Delta T)}{T+\Delta T} - \frac{\Delta F(T-\Delta T)}{T-\Delta T}\right)\\ &\times\left(\frac{1}{T+\Delta T} - \frac{1}{T-\Delta T}\right)^{-1}\end{aligned} \tag{4.22}$$

In addition, Marcus theory based simulations employ graphical fits to extract internal energies and entropies. Graphical fits are also used to determine the charge-transfer symmetry factor and its energetic and entropic components.

Transition path sampling and committor analysis

Having outlined the simulations details for the canonical molecular dynamics calculations above, I now turn to the transition path sampling and committor simulations. In both cases, the boundaries for the stable states are $\Delta E_{R,min} = 50\,\mathrm{kJ\,mol^{-1}}$ for the reactants and $\Delta E_{P,max} = -50\,\mathrm{kJ\,mol^{-1}}$ for the products because the diabatic energy gap (4.16) is defined as $\Delta E = V_P^{(d)} - V_R^{(d)}$. These boundary values contain the vast majority of equilibrium fluctuations of the stable states. The time between two time slices amounts to two timesteps and equals 2 fs.

The transition path sampling simulations in the canonical ensemble use the kinetic energy control described in section 3.3.2 at a temperature of $T = 298.15\,\mathrm{K}$ to compute the activation energy (2.70). Initial trajectories are obtained by long molecular dynamics simulations where possible. Other-

wise, a reactive trajectory can be obtained by either increasing the electronic coupling γ_{el} or by decreasing the effective free energy of reaction $\Delta\mu$. In practice, the second route turns out to be more effective. Transition path sampling simulations at different values of $\Delta\mu$ can then yield initial trajectories at the desired effective reaction free energies. After extensive equilibration, the production run consists of 2×10^6 Monte Carlo steps, from which 200 reactive trajectories are retained for geometrical and committor analyses. The pathways consist of 101 time slices and are 200 fs long. The maximum shifting length is 100 fs, whereas the shooting probability is 0.6. Momentum changes for each Cartesian momentum degree of freedom amount to $0.1\,\sigma_{p_{C,j}}$, where $\sigma_{p_{C,j}} = \sqrt{m_j k_B T}$ denotes the width of the Maxwell-Boltzmann distribution [76]. These simulations are carried out for $\Delta\mu$ values ranging from $-10\,\mathrm{kJ\,mol^{-1}}$ to $40\,\mathrm{kJ\,mol^{-1}}$ in steps of $10\,\mathrm{kJ\,mol^{-1}}$. Shifting moves are accepted in 70% of all attempts, whereas shooting moves exhibit an acceptance probability of around 0.55. The proposed shooting points are accepted in 70 out of 100 cases.

The committor analysis consists of computing the relaxation probability w_P for all 101 configurations of the 200 harvested reactive trajectories according to equation (3.145). For each configuration random momenta are drawn from the Maxwell-Boltzmann distribution, and the system is then propagated for 40 fs. The number of fleeting trajectories is 125, and only configurations for which at least 100 trajectories reach one of the stable states are considered for the committor distribution. Configurations whose committor value lies in the range $0.4 \leq w_P \leq 0.6$ are considered to be transition states in the committor sense.

The committor analysis yields the committor of all configurations harvested. The committor as a function of the order parameter then indicates whether the latter is a good reaction coordinate. In addition, a subset of these data can be used to examine the transition state. To investigate whether the crossing points are transition states in the committor sense, configurations with a diabatic gap value lying in the range $-2\,\mathrm{kJ\,mol^{-1}} \leq \Delta E \leq 2\,\mathrm{kJ\,mol^{-1}}$ are selected to compute the committor distribution. A range of $10\,\mathrm{kJ\,mol^{-1}}$ has been used to evaluate the gap distribution of transition states, which

indicates whether dynamical transition states correspond to crossing points according to Marcus theory.

Computational effort

I shall briefly comment on the computational effort to compute the activation energy at a given reaction free energy value. Marcus theory based simulations and umbrella integration calculations are needed at three temperatures if the activation free energy is also evaluated. In contrast, transition path sampling yields the activation energy from simulations at the temperature of interest. However, the activation free energy is not available.

The computational effort will be given in the accumulated molecular dynamics time, namely the number of simulations required times the simulated time per calculation. Molecular dynamics simulations based on Marcus theory are less demanding by an order of magnitude and require an equivalent simulation time of 60 ns. Transition path sampling simulations take 400 ns and umbrella integration 810 ns. These estimates hold for the production run times. If equilibration times are also taken into account, the computational effort for transition path sampling and umbrella integration is of the same order of magnitude. I stress that the above numbers are only intended as a rough estimate to provide an overview.

4.2.4 Error estimates

In this section I shall briefly mention some of the errors that affect the results of a measurement. Errors are generally divided into systematic and statistical or random errors [1]. The former arise from a bias in the investigation so that the outcome of a measurement is shifted away from its true value [1]. This shift is reproducible. In contrast, random errors are due to the variability of individual measurements, and the deviation from the true value can have variable sign and magnitude [1,2,137]. In the following, I shall describe finite size effects as an example of a systematic error relevant to the present work. Subsequently, statistical errors are discussed.

Systematic errors

Finite size effects arise because the number of particles in a simulation is generally much smaller than Avogadro's number [106, 107]. To simulate bulk properties, periodic boundary conditions are typically applied [106,107]. However, bulk solutions are not periodic, and the enforced periodicity of the system is artificial [196,205]. Short-range interactions are usually not severely affected [106, 196]. In contrast, the accuracy of long-range electrostatic interactions is affected by artificial periodicity and finite size effects [201]. I shall focus on charged systems, described by Ewald summation, that consist of simple ions and simple point charge water molecules.

The effect of imposing artificial periodicity can be thought of as follows [201, 205]. Without periodic boundary conditions the solute interacts with the surrounding solvent molecules. When periodic boundary conditions are applied, the solute interacts with solvent molecules in the central simulation box and their periodic images further away. In addition, the solute experiences the forces from the neutralizing background charge and from its periodic images. These two aspects constitute the self-interaction energy [201, 205]. As pointed out in reference [205], the central ion is undersolvated because the solvent molecules in neighbouring boxes solvate the image solute in that box. As a result, the stabilization of the ion in the central box is lower than in a bulk environment [205].

It was shown in reference [201] that Ewald summation was responsible for finite size effects in systems containing simple ions. Because of the large dielectric constant in polar solvents the correction to the solvation free energy was found to scale as the inverse volume of the system [196,201,205]. Subsequently, the reaction free energy was shown to exhibit the same dependence on system size [34]. In contrast, the reorganization free energy scales as the inverse of the box length and is thus more sensitive to finite size effects [34].

Ayala and Sprik [34] investigated a very similar model system to the one studied in this work. It included rigid simple point charge water molecules and one ferrous or ferric ion. This enables me to estimate the finite size effects from their published data. The reaction free energy should be within

5% of the largest system (1000 water molecules) studied in [34]. In contrast, the reorganization free energy is too small by at least a factor of 2 [34] and therefore strongly system size dependent.

It is clear from the above that the activation free energies computed in this work, which are dominated by the term $\lambda/4$, will be too small. To obtain more accurate reorganization free energies, which is not the aim of the present work, a larger system would have to be employed. However, this would lead to a very large imbalance between computational cost and statistical uncertainty. As discussed in the next chapter in more detail (see page 186), the statistical uncertainty of internal energy differences, and hence of activation energies, increases with the square root of the number of particles [76, 221]. If the system size were increased to obtain reasonably accurate activation free energies (requiring at least one order of magnitude more particles [34]), no statement about the accuracy of the transition path sampling method compared to equilibrium and biased molecular dynamics simulations would be possible.

A larger system and a larger reorganization free energy would imply that the range of $\Delta\mu$ values chosen would describe situations closer to degenerate diabatic free energy states. This should not lead to significantly different results for the charge-transfer symmetry factor, however, because λ does not depend on $\Delta\mu$. Accordingly, the variation of the activation free energy with $\Delta\mu$ is governed by the reaction free energy, which is much less sensitive to the system size. Similarly, the temperature dependence of the reorganization free energy is found to be relatively weak. The error in the reorganization free energy should thus only have a minor impact on the activation energies and entropies.

In addition, a larger system would not alter the qualitative features of the system. In particular, the present purposes require a thermally activated process, and the free energy barriers are roughly one order of magnitude larger than typical thermal fluctuations. I believe that it is more important that the umbrella integration simulations are performed with exactly the same potential energy function as the one employed in the transition path sampling computations. In that case, the deficiencies of the system are the

same so that the methods can be compared. Again, the system is not realistic and does not mimic a specific physical experiment. However, the system is well-defined in the sense that it should capture the qualitative features of the nuclear dynamics of a thermally activated redox process in equilibrium.

Statistical errors

According to the ergodic hypothesis, an infinitely long simulation would yield the correct average of a dynamical observable [106]. In that case, all possible states of an ensemble would be visited, and the probability distribution function would effectively be known [137]. In practice, however, computer simulations are finite and thus subject to statistical errors [106, 107].

The central idea to estimating the statistical uncertainty of a (computer) experiment is to regard data points as realizations of a random variable [137]. In that sense, computer simulations yield a random sample from a population, namely the set of all possible outcomes of a given random experiment. This sample is used to infer the properties of the population [137]. Now, one sample is obtained from one computer experiment. Another simulation would yield a different sample and so on. Hence, not only is one data point the realization of a random variable, but also a sample mean is the realization of a random variable [137]. Because sample means are the common observables of computer experiments, it is necessary to obtain information on their sampling variation. In other words, the variance of the sample mean (and, in principle, of the sample variance) should be determined [106, 107, 222]. Different methods for estimating the variance of the sample mean will be described in the context of specific simulation techniques.

The error estimation described below will focus on the direct output of simulations. If the simulation data are used as input to derive composite quantities, their statistical error can also be estimated. In particular, the statistical error of a parameter y that depends on the observables u_j is obtained by the propagation of the statistical errors associated with the observables

according to equation (4.23) [1, 223]:

$$\sigma^2(y) = \sum_j \left(\frac{\partial y}{\partial u_j}\right)^2 \sigma^2(u_j). \tag{4.23}$$

Above, $\sigma^2(u)$ denotes the variance of the random variable u, whose unbiased estimator is the sample variance [2, 137, 222],

$$s^2 = \frac{1}{\mathcal{N}_d - 1} \sum_{j=1}^{j=\mathcal{N}_d} (y_j - M)^2, \tag{4.24}$$

where we have used the mean of a sample of size $\mathcal{N}_d$ [2, 137, 222]:

$$M = \frac{1}{\mathcal{N}_d} \sum_{j=1}^{j=\mathcal{N}_d} y_j. \tag{4.25}$$

Below, I turn to specific estimates of the sampling variation.

Flyvbjerg and Petersen reviewed a particularly convenient method for estimating the variance of a sample mean containing correlated data [224]. The idea is to start with a sample of a given size and to compute its mean and variance. Next, a *blocking transformation* [224] is performed that groups the mean of two successive data points of the original sample into a new data point of the new sample. This new sample formally contains half the number of data points of the old sample. However, the mean and the variance of the mean remain the same for all data sets [224]. As the number of blocking transformations increases, the correlation between transformed data points decreases, and the estimate of the variance of the sample mean becomes more and more accurate until it reaches a fixed point [224]. This method is employed to estimate the variance of sample means computed from canonical molecular dynamics and transition path sampling simulations. In the former case, the original data set consists of 10^4 harvested data points. In the latter case, the activation energy estimates from 20 transition path sampling simulations of 10^5 Monte Carlo moves constitute the initial data set.

The statistical error from umbrella integration simulations is estimated as

in references [66, 225]. This error estimate requires trend-free, uncorrelated and normally distributed input data. As a result, the following statistical tests are performed for every window of the biased molecular dynamics procedure. First, the Mann-Kendall test for trend in the sample mean and sample variance is performed [66, 225, 226] to ensure that the data set is well equilibrated. Next, the shape test for normality [225,227,228], which employs the sample skewness and kurtosis, is carried out. Then, the von Neumann test for serial correlation [225, 229, 230] is used to establish that data points are uncorrelated. Given these characteristics of the data in each window, the variance of the sample mean and variance are estimated by dividing the data points into segments [66]. These estimates constitute the statistical input quantities that are propagated to yield an error estimate of Landau free energy differences [66].

All errror estimates are given in terms of one standard deviation. Due to their approximate nature they are likely to be lower than the true statistical error. Within the estimated errors, the models and simulation details described in this chapter lead to the following results.

Chapter 5

Results

This chapter presents the results for the studied argon and iron model systems. The simulations for the argon model system have been performed to validate the methodology, which is subsequently applied to the more complex iron model system.

5.1 Argon

One aim of this work is to compute the activation energy of a given system by means of transition path sampling. To ensure that the method works correctly, the results presented in references [164] and [76] are reproduced for the microcanonical case and for the activation energy in the canonical ensemble. The first case demonstrates that the transition path sampling procedure works accurately in the microcanonical ensemble; the second example shows that the temperature control method from reference [141] implemented here yields the same results for the activation energy as in reference [76]. These two examples are presented below.

5.1.1 Microcanonical transition path sampling results

The path average $\langle \theta_P(x_t) \rangle^*_{RP}$ obtained according to the procedure outlined in section 4.1.3 in the microcanonical case is displayed in figure 5.1. It is seen that the path average enters the linear regime after about $\tau_{LJ,Ar}$ and

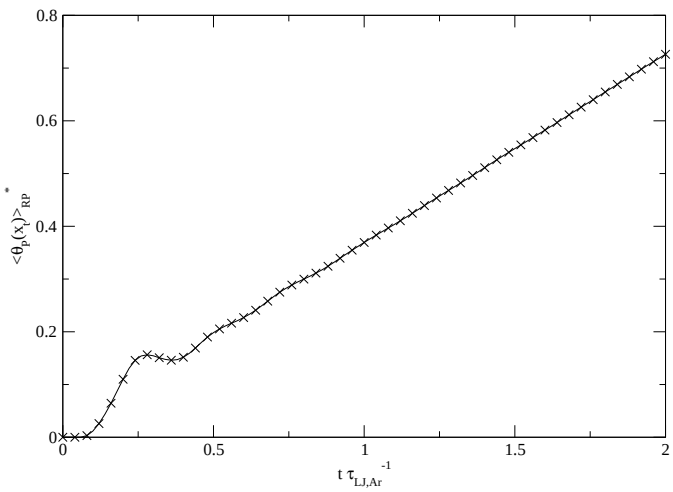

Figure 5.1: The path average $\langle\theta_P(x_t)\rangle^*_{RP}$ is shown as a function of time, measured in units of $\tau_{LJ,Ar} = 2.16\,\mathrm{ps}$, for the argon model system in the microcanonical ensemble. The total energy is $E = 9\,\epsilon_{LJ,Ar} = 8.96\,\mathrm{kJ\,mol^{-1}}$, and the barrier height separating the stable states is $V_h = 6\,\epsilon_{LJ,Ar} = 5.98\,\mathrm{kJ\,mol^{-1}}$. The transition path sampling simulation consists of 6×10^6 Monte Carlo steps and reproduces the results of reference [164].

reaches a value of about 0.73 for $t = 2\,\tau_{LJ,Ar}$. Comparison to the upper panel of figure 2 of reference [164] shows that the qualitative behaviour is the same. The quantitative agreement is also satisfactory because the path average reaches a value of about 0.74 after $2\,\tau_{LJ,Ar}$. The error is thus within about two percent.

The quantity $\kappa_r = 1 - \langle\,\theta_P(x_t)\rangle^*_{RP}$, which can be extracted from figure 5.1, is interpreted as the fraction of reactive trajectories that recross within the path length $2\,\tau_{LJ,Ar}$, showing that the argon model system exhibits recrossings. The recrossings indicate that transition state theory might not hold for the present model system.

Next, the dimensionless quantity $\langle\,\dot{\theta}_P(x_t)\rangle^*_{RP} \times \tau_{LJ,Ar}$ is shown in figure 5.2. The two curves correspond to how the numerical derivative is evaluated. The solid line and crosses are obtained from the forward finite difference

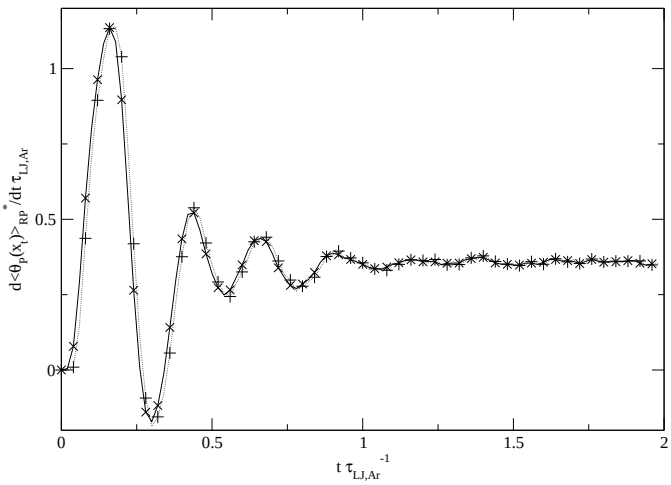

Figure 5.2: The path average $\langle \dot{\theta}_P(x_t) \rangle^*_{RP} \, \tau_{LJ,Ar}$ is shown as a function of time, measured in units of $\tau_{LJ,Ar} = 2.16\,\mathrm{ps}$, for the argon model system in the microcanonical ensemble. The total energy is $E = 9\,\epsilon_{LJ,Ar} = 8.96\,\mathrm{kJ\,mol^{-1}}$, and the barrier height separating the stable states is $V_h = 6\,\epsilon_{LJ,Ar} = 5.98\,\mathrm{kJ\,mol^{-1}}$. The dotted line and the plus signs indicate that the time derivative has been obtained from the forward finite difference scheme of equation (5.1), whereas the solid line and the crosses represent the time derivative resulting from the central finite difference scheme of equation (5.2). The transition path sampling simulation consists of 6×10^6 Monte Carlo steps and reproduces the results of reference [164].

scheme (2.69)

$$\dot{\mathcal{A}} = \frac{d\mathcal{A}}{dt} \approx \frac{\mathcal{A}(t + \Delta t) - \mathcal{A}(t)}{\Delta t}. \tag{5.1}$$

and the dotted line and the plus signs result from the central finite difference scheme (2.68):

$$\dot{\mathcal{A}} = \frac{d\mathcal{A}}{dt} \approx \frac{\mathcal{A}(t + \Delta t) - \mathcal{A}(t - \Delta t)}{2\Delta t}. \tag{5.2}$$

It is clear from figure 5.2 that the uncertainty for the time derivative is larger than for the fraction of transmitted reactive trajectories in figure 5.1. The larger error arises from the finite difference scheme used to compute the derivative because the number of time slices is only moderately dense to

minimize memory requirements. However, a plateau value can be identified for the time derivatives whose values are 0.36 and 0.35 for the forward and central finite difference schemes. The value extracted from the lower panel of figure 2 of reference [164] is about 0.38. Consequently, the present results agree to within about five percent. Most importantly, the qualitative behaviour is well reproduced.

The above results indicate that the transition path sampling method implemented here works accurately. Next, the implementation of the asymmetric generation probability, introduced in section 3.3.2, is tested for the momentum displacements in the canonical case.

5.1.2 Canonical molecular dynamics calculations

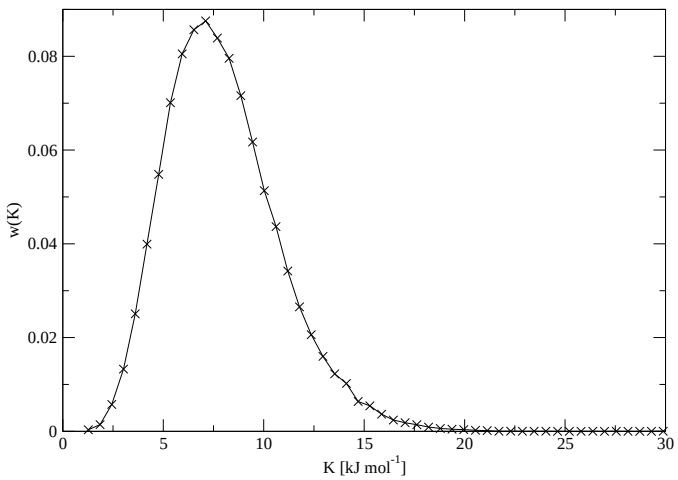

Figure 5.3: The kinetic energy histogram from an equilibrium constant temperature ($T = 119.8\,\mathrm{K}$) simulation for the argon model is displayed. It is obtained from a simulation of 10^9 timesteps by scaling the momenta every 10^3 timesteps (see text). The kinetic energies are selected from the canonical ensemble according to the same Monte Carlo procedure that controls the temperature in the transition path sampling method, as discussed in section 3.3.2 and in reference [141].

State	$\langle r_{12} \rangle$	$\langle \mathcal{H} \rangle$	$\langle K \rangle$	$\langle V \rangle$
R	3.84	10.04	7.97	2.07
P	5.50	10.19	7.98	2.21
$R+P$	4.55	10.10	7.97	2.13
TS	4.66	19.48	8.65	10.82

Table 5.1: State-specific averages of the argon dimer bond length ($\langle r_{12} \rangle$ in Å) as well as of the total ($\langle \mathcal{H} \rangle$), kinetic ($\langle K \rangle$) and potential ($\langle V \rangle$) energies (in $\mathrm{kJ\,mol^{-1}}$) are shown for the reactants (R: $r_{12} \leq 4.59675\,\text{Å}$), products ($P$: $r_{12} \geq 4.93725\,\text{Å}$), all states ($R+P$) and transition state (TS: $\min(|r_{12} - 4.67323\,\text{Å}|)$). The results are obtained for the argon model system from a $4.3\,\mu s$-equilibrium molecular dynamics simulation at constant temperature ($k_B T = \epsilon_{LJ,Ar}$).

I shall first present the computation of the average total energy in the reactant state from molecular dynamics simulations in the canonical ensemble. Then, the numerical results of the transition path sampling simulations are described. Combining the two yields the activation energy according to equation (2.70): $E_a(t) = \langle \dot{\theta}_P(x_t)\mathcal{H}(\boldsymbol{\xi}_0)\rangle^*_{RP} \left(\langle \dot{\theta}_P(x_t)\rangle^*_{RP}\right)^{-1} - \langle H \rangle_R$.

The simulation details for the molecular dynamics calculations have been given in section 4.1.3. In particular, the system is propagated according to Hamilton's equations of motion for 10^9 timesteps; one timestep is 4.31 fs long. The momenta are scaled every 10^3 timesteps to sample the canonical ensemble. To this end, the new kinetic energy $K^n = K^o + \Delta K$ is obtained from the old kinetic energy K^0 according to the Monte Carlo procedure described in section 3.3.2. The kinetic energy displacement ΔK is drawn from a normal distribution, and the new kinetic energy is accepted according to the Metropolis criterion [141, 179], as in equation (3.132) with $\mathcal{N}_f = 16$:

$$w_a(K^o \to K^n) = \min\left\{1,\, e^{-\beta(K^n - K^o)} \left(\frac{K^n}{K^o}\right)^{\mathcal{N}_f/2-1}\right\}. \tag{5.3}$$

This procedure leads to a time evolution on energy hypersurfaces that are distributed according to the canonical ensemble. As can be seen from figure 5.3, the temperature control employed generates a kinetic energy distribution

whose shape is that expected for the canonical ensemble; in particular, it is skewed to the right [137]. The average kinetic energy also coincides with that expected from classical thermodynamics [15], namely $\langle K \rangle = \frac{\mathcal{N}_f}{2} k_B T = 7.97\,\mathrm{kJ\,mol^{-1}}$, where $\mathcal{N}_f = 16$ denotes the number of degrees of freedom. This result provides an independent test of the accuracy of the temperature control method.

In table 5.1 the average properties for each region of phase space are summarized. The kinetic (K), potential (V), and total (E) energies vary by less than two percent between reactants (R) and products (P). Although only five data points have been collected near the barrier top (TS), the data are presented here as a first indication that the reactive parts of the equilibrium trajectory exhibit a higher total energy than that accessible via typical fluctuations ($\sigma_E = 3.2\,\mathrm{kJ\,mol^{-1}}$) in the stable states. It is noted that the exact boundaries of the stable states do not affect the averages of the observables as long as most fluctuations of the phase space region under consideration are included. The relevant number entering the evaluation of the activation energy is the average total energy in the reactant state: $\langle \mathcal{H} \rangle_R = 10.04\,\mathrm{kJ\,mol^{-1}}$.

5.1.3 Transition path sampling in the canonical ensemble

I now turn to the transition path sampling simulations of the argon model system in the canonical ensemble. The procedure is described in section 3.3, and the simulation parameters are given in section 4.1.3.

The kinetic energy distribution $w(K)$ from transition path sampling (TPS) and molecular dynamics (MD) simulations in the canonical ensemble are compared in figure 5.4. It is seen that the kinetic energy histogram near the barrier top (dashed line and plus signs) from TPS calculations is very close to that obtained from equilibrium MD simulations (solid line and crosses). In contrast, the histogram resulting from the kinetic energies of the initial time slice of reactive trajectories is broader with a larger mean (dotted line and triangles). The differences in the average energetic properties are furthermore displayed in tables 5.1 and 5.2.

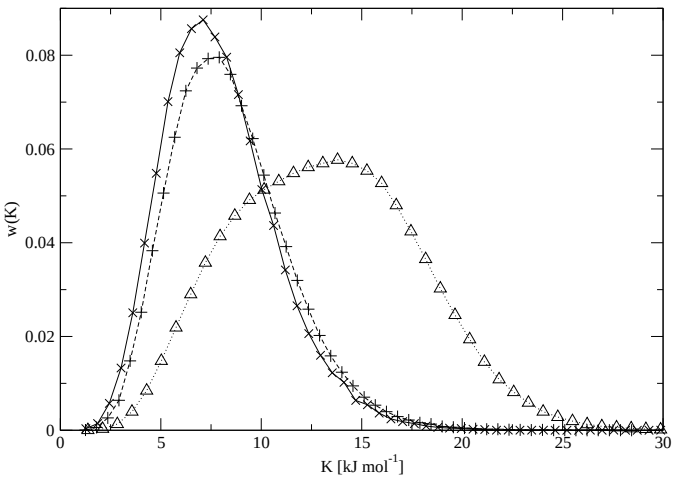

Figure 5.4: Kinetic energy histograms $w(K)$ from molecular dynamics (MD) and transition path sampling (TPS) simulations are displayed for the argon model system. The simulations were performed in the canonical ensemble, and the temperature was set to $T = 119.8\,\mathrm{K}$. The solid line with the crosses indicate equilibrium MD simulation results in the reactant state. The dashed line and the plus signs correspond to the kinetic energy distribution of the transition states from TPS simulations, whereas the kinetic energy histogram of the initial time slice of all reactive trajectories in the transition path ensemble is shown by the dotted line and the triangles.

The average energetic properties in the stable states are hardly sufficient to overcome the barrier in the molecular dynamics simulations, whereas the average kinetic and total energies in the stable state portions of the transition path ensemble are larger than the barrier height V_h. That the average total energy of the reactive trajectories (dashed line and plus signs) is roughly twice as large as that in the stable states of a long molecular dynamics simulation (solid line and crosses) is shown in figure 5.5. The difference in average total energies between the reactant (R) and product (P) states in table 5.2 arises because the number of phase space points in each state need not be the same for a given trajectory. For instance, if more time slices are in the reactant region than in the product region for a pathway

State	$\langle r_{12} \rangle$	$\langle \mathcal{H} \rangle$	$\langle K \rangle$	$\langle V \rangle$
R	4.03	20.21	13.41	6.80
P	5.42	20.18	14.34	5.84
$R+P$	4.57	20.16	13.21	6.94
TS	4.67	20.06	8.45	11.62
BR	4.76	19.79	8.59	11.20

Table 5.2: State-specific averages of the argon dimer bond length ($\langle r_{12} \rangle$ in Å) as well as of the total ($\langle \mathcal{H} \rangle$), kinetic ($\langle K \rangle$) and potential ($\langle V \rangle$) energies (in $\mathrm{kJ\,mol^{-1}}$) are shown for the reactants (R: $r_{12} \leq 4.59675\,\text{Å}$), products ($P$: $r_{12} \geq 4.93725\,\text{Å}$), all states ($R+P$), transition state (TS: $\min(|r_{12} - 4.67323\,\text{Å}|)$) and barrier region (BR: $4.59675\,\text{Å} < r_{12} < 4.93725\,\text{Å}$). The results are obtained for the argon model from reactive trajectories obtained from transition path sampling simulations in the canonical ensemble ($k_B T = \epsilon_{LJ,Ar}$) according to reference [76] with 2×10^6 attempts.

with a high total energy, a higher average total energy for the reactant state is expected from the contribution of that specific trajectory. As a result, the displayed energetic averages can only indicate the energy partitioning close to the rare event. This representation assumes that the transition time slice is uniformly distributed over the trajectory length. Importantly, the sum of average kinetic and potential energies in table 5.2 equals the average total energy for each region in phase space for the transition path sampling simulations because every pathway has a constant total energy.

As mentioned above, the average kinetic energy from the equilibrium molecular dynamics calculations is smaller than the barrier height V_h. Even the average total energy in the reactant state in equilibrium is barely higher, thus preventing the system from crossing the barrier on average. Consequently, only a small fraction of trajectories would cross the barrier if the kinetic energy were fixed in the stable states. Here, I observe that the kinetic energy is selected near the barrier top in the transition path sampling procedure. It then follows from the constant energy nature of the trajectories and the lower potential energies in the stable states that the average kinetic energy is significantly higher in the reactant and product wells than in the barrier region. This leads to a higher energy reservoir in the stable states so

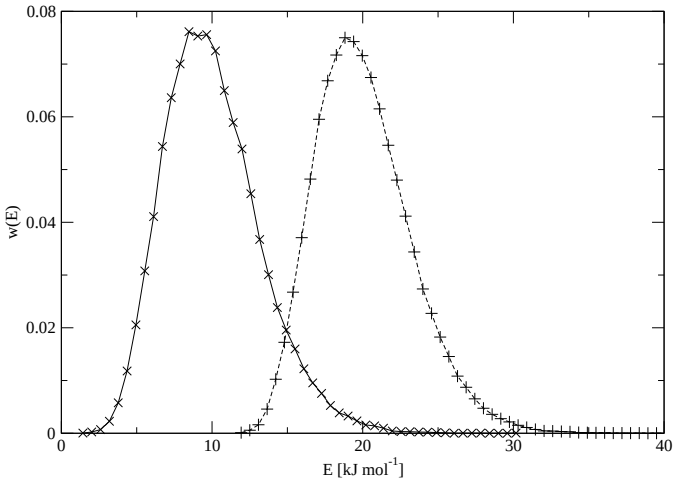

Figure 5.5: Total energy histograms for the argon model system are shown for molecular dynamics (crosses and solid line) and transition path sampling (plus signs and dashed line) simulations in the canonical ensemble at a temperature of $T = 119.8\,\mathrm{K}$.

that transitions become more likely from an energetic point of view.

A canonical distribution of phase space points can be obtained from a canonical distribution of initial conditions and the Hamiltonian time evolution of all initial phase space points because Hamiltonian dynamics conserve the phase space distribution [165]. However, the transition path ensemble does not yield a canonical distribution of trajectories; it yields the subensemble of reactive trajectories. This means that the non-reactive trajectories, which are required to describe the entire canonical ensemble, are not taken into account. If the non-reactive trajectories were considered with their proper statistical weight, the average kinetic energy according to the defined temperature would be recovered in the stable states.

An alternative would consist in employing thermostatted dynamical trajectories. These should yield a similar average kinetic energy in the stable states and at the transition state. However, typical relaxation times of the solvent in a condensed phase are on the order of picoseconds [33]. This means

State	$\langle r_{12} \rangle$	$\langle \mathcal{H} \rangle$	$\langle K \rangle$	$\langle V \rangle$
R	4.01	20.13	13.64	6.48
P	5.42	20.04	14.45	5.60
$R + P$	4.61	20.06	13.54	6.52
TS	4.67	20.06	8.45	11.62
BR	4.76	19.70	8.54	11.16

Table 5.3: State-specific averages of the argon dimer bond length ($\langle r_{12} \rangle$ in Å) as well as of the total ($\langle \mathcal{H} \rangle$), kinetic ($\langle K \rangle$) and potential ($\langle V \rangle$) energies (in $\mathrm{kJ\,mol^{-1}}$) are shown for the reactants (R: $r_{12} \leq 4.59675\,\text{Å}$), products ($P$: $r_{12} \geq 4.93725\,\text{Å}$), all states ($R + P$), transition state (TS: $\min(|r_{12} - 4.67323\,\text{Å}|)$) and barrier region (BR: $4.59675\,\text{Å} < r_{12} < 4.93725\,\text{Å}$). The results are obtained for the argon model from the initial time slice of all Monte Carlo attempts, reactive and non-reactive, obtained from transition path sampling simulations in the canonical ensemble ($k_B T = \epsilon_{LJ,Ar}$) according to reference [76] with 2×10^6 attempts.

that the thermostatting effect for a given trajectory would be relatively small unless a very fast-relaxing thermostat would be employed. In the iron model system, the trajectories are only 200 fs long, and the use of thermostatted dynamics would seem rather artificial. Consequently, the choice has been made to keep the system's underlying Hamiltonian dynamics to avoid sampling the thermostat's dynamics even if this limits the sampling to the reactive trajectory part of the canonical ensemble.

Another way of seeing this is to consider reactive trajectories harvested from transition path sampling as cut from a long equilibrium molecular dynamics trajectory. Transition path sampling focuses on the reactive event itself; however, this is only possible if an equilibrium fluctuation has brought the system in a suitable situation to actually cross the barrier. In other words, the activation might already have happened (in part) prior to the reactive event. Hence, a small perturbation of the system by a momentum change is likely to leave the system (partially) activated and in a state suitable for reaction.

A comparison of the average properties displayed in tables 5.2 and 5.3 further indicates that reactive trajectories have a higher total energy than

most parts of an equilibrium pathway. Specifically, the average total energy for all phase space regions $(R+P)$ in table 5.2 is higher than the corresponding average total energy in table 5.3. This difference is not expected to be large because the non-reactive trajectories are obtained by modifying successful pathways that have a relatively high energy. In other words, it is unlikely that the energetics of the non-reactive paths are close to the energetics of the equilibrium simulation in the canonical ensemble probing the stable states alone. Alongside higher total energies, reactive trajectories exhibit, on average, higher potential energies and lower kinetic energies than their non-reactive counterparts. This becomes especially obvious when contrasting averages from the transition path ensemble with those from molecular dynamics simulations, as seen above.

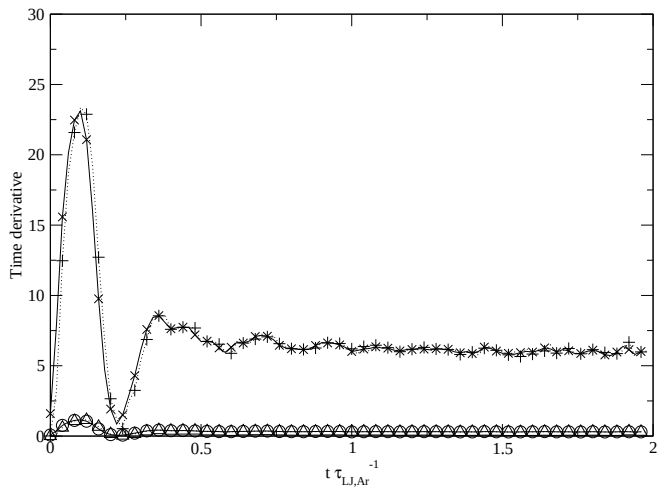

Figure 5.6: For the argon model system, the time derivative, multiplied by $\tau_{LJ,Ar}$ of the path averages $\langle\theta_P(x_t)\mathcal{H}(\boldsymbol{\xi}_0)\rangle^*_{RP}$ (crosses and plus signs) and $\langle\theta_P(x_t)\rangle^*_{RP}$ (triangles and circles) are shown as obtained from the numerator and denominator of the first term on the right-hand side of equation (5.4) from transition path sampling simulations in the canonical ensemble at $T = 119.8\,\mathrm{K}$. The solid lines represent time derivatives from the central finite difference scheme of (5.2), and the dotted lines indicate the use of the forward finite difference scheme given in equation (5.1).

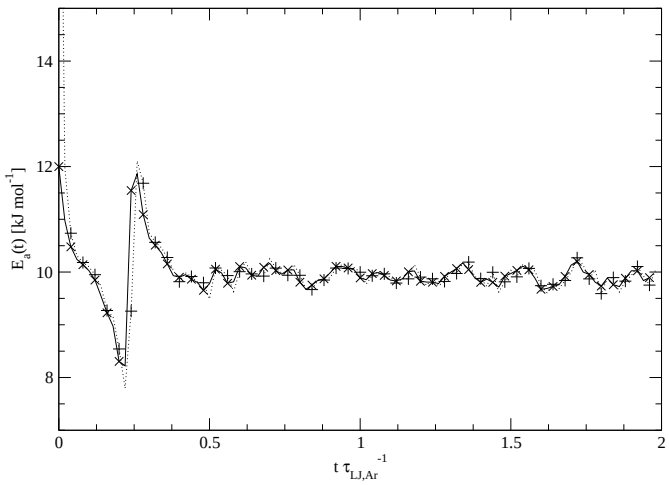

Figure 5.7: The activation energy (5.4) for the argon model system is displayed as obtained from transition path sampling and molecular dynamics simulations in the canonical ensemble ($T = 119.8\,\mathrm{K}$; $\tau_{LJ,Ar} = 2.16\,\mathrm{ps}$). Activation energies obtained from the central (5.2) and forward (5.1) finite difference schemes are indicated by the solid line through the crosses and by the dotted line through the plus signs. The computed activation energies are in good agreement with the potential barrier $V_h = 10\,\epsilon_{LJ,Ar} = 9.96\,\mathrm{kJ\,mol^{-1}}$ of the model. The transition path sampling simulation consists of 2×10^6 attempts and accurately reproduces the results of reference [76].

From a technical point of view, the influence of the stable state boundaries on the average values of the observables is considered. It is seen from table 5.2 that the averages at the barrier top (TS) differ from those obtained from phase space points in the entire barrier region (BR). The latter phase space points can have any order parameter value that does not belong to the stable states, whereas the former are restricted to order parameter values that deviate minimally from that corresponding to the barrier top at $r_{12} = r_{WCA} + r_w = 4.67\,\text{Å}$. However, the effect is moderate and below 10%. In addition, although the number of points near the barrier top from equilibrium molecular dynamics simulations is very small, the average values of the computed properties are in rough agreement with those obtained from the

$\frac{\langle\dot{\theta}_P(x_t)\mathcal{H}(\boldsymbol{\xi}_0)\rangle^*_{RP}}{\langle\dot{\theta}_P(x_t)\rangle^*_{RP}}$	$\langle\mathcal{H}\rangle_R$	E_a
19.93	10.04	9.89
20.07	10.04	10.04

Table 5.4: The activation energy E_a is displayed for the argon model system. According to equation (5.4), the activation energy is obtained from an average over the transition path ensemble (first column) and the equilibrium total energy in the reactant state ($\langle\mathcal{H}\rangle_R$) from molecular dynamics simulations. The simulations are performed in the canonical ensemble at a temperature of $k_BT = \epsilon_{LJ,Ar}$. The path average requires a numerical time derivative, which has been computed according to the central finite difference scheme of equation (5.2) in the first data row and by means of the forward finite difference scheme of equation (5.1). All quantities are in $\mathrm{kJ\,mol^{-1}}$.

transition path ensemble. The transition path sampling method thus seems rather robust with respect to the exact choice of the stable state boundaries as long as the latter do not overlap [21].

The transition time for a reactive event is at most $0.4\,\tau_{LJ,Ar}$ so that it is anticipated that the activation energy reaches a plateau value within the length of the trajectories. Indeed, the time derivatives $\langle\dot{\theta}_P(x_t)\rangle^*_{RP}$ and $\langle\dot{\theta}_P(x_t)\mathcal{H}(x_0)\rangle^*_{RP}$ shown in figure 5.6 are in qualitative and quantitative agreement with figure 1 of reference [76]. As in the microcanonical case, the time derivative in figure 5.6 is obtained from the forward (dotted lines) and central (solid lines) finite difference schemes of equations (5.1) and (5.2). The ratio of their plateau values is given in table 5.4. The difference between the ratio of time derivatives of path averages and the average total energy of the reactant state from an equilibrium molecular dynamics simulation yields the activation energy (2.70) [76]

$$E_a(t) = \frac{\langle\dot{\theta}_P(x_t)\mathcal{H}(\boldsymbol{\xi}_0)\rangle^*_{RP}}{\langle\dot{\theta}_P(x_t)\rangle^*_{RP}} - \langle H\rangle_R \tag{5.4}$$

whose plateau value is displayed in figure 5.7. Both the procedure employing the finite difference scheme and that using the central difference scheme yield activation energies very close to the barrier height of $10\,\epsilon_{LJ,Ar}$.

It may be concluded from the kinetic energy histograms of figure 5.4, from the transition path sampling simulation in the microcanonical ensemble and from the activation energies obtained here that the temperature control and the transition path sampling implementation work satisfactorily. In particular, the present implementation of the transition path sampling method is capable of reproducing the activation energy values and graphs published in reference [76] accurately. It is thus believed that the tools and analysis protocols developed here allow for the investigation of a more complex case, namely the oxidation of the classical aqueous ferrous ion, which I shall describe next.

5.2 Iron

As mentioned in the introduction, the present work aims at investigating activation parameters controlling electron-transfer dynamics by means of molecular simulation. The activation parameters are computed by (biased) canonical molecular dynamics computations, which exploit knowledge of the reaction coordinate for the present Marcus model. These simulations serve as a reference for transition path sampling results, which is used as a more general alternative because it does not require any knowledge of the reaction coordinate. To check the validity of the reference data, the assumptions underlying the simulation methods and the model system are tested first.

Hence, the results for the model oxidation half-reaction of the classical ferrous ion are structured as follows. I shall describe the validation of the methodologies first and turn to the physical results afterwards. In particular, the validity of Marcus theory for the iron model is initially assessed by means of unrestricted and biased canonical molecular dynamics simulations. Next, I outline the validation of the transition path sampling method. Then, a test of the reaction coordinate and the transition state is presented. The properties of the transition state provide a bridge to the physical results, which include the activation parameters and their dependence on the reaction free energy, namely the charge-transfer symmetry factor and its entropic and energetic components.

5.2.1 Validity of Marcus theory

Marcus theory applies whenever the underlying assumptions are fulfilled. As detailed in section 2.2.1, Marcus theory assumes that the diabatic energy gap (ΔE) corresponds to the reaction coordinate [38] and that the crossing point ($\Delta E = 0$) characterizes the transition state [35,42]. These assumptions are equivalent to the knowledge of the reaction coordinate and the transition state assumed in transition state theory and will be discussed in section 5.2.3. In the present section I shall consider Marcus's additional assumption, namely the linear response approximation [30, 42].

The linear response approximation holds if the diabatic gap is normally

distributed *and* if the variance of the diabatic gap is the same for reactants and products. A breakdown of linear response could then be due to diabatic gap variables that are not normally distributed or to normally distributed gap variables whose variance is state-dependent [141,231,232]. I shall investigate the validity of the linear response approximation by testing the two conditions mentioned above, starting with the state-independence of the gap variances.

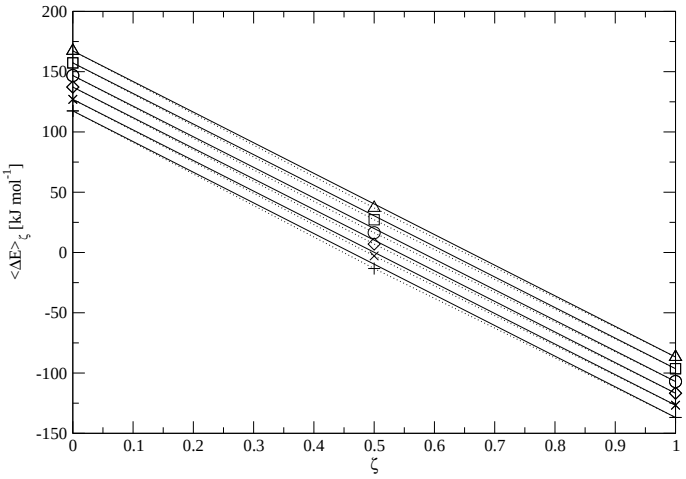

Figure 5.8: The reaction free energies from canonical equilibrium simulations at a temperature of $T = 298.15\,\mathrm{K}$ are displayed as the integral of the average diabatic gap $\langle \Delta E \rangle_\zeta$ over the coupling parameter ζ using the Hamiltonian (5.5). Dotted lines show the reaction free energy according to Simpson's rule (5.8), whereas solid lines indicate the corresponding Marcus theory result (5.7). The reaction free energies have been obtained for effective free energy of reaction values (in $\mathrm{kJ\,mol^{-1}}$) of -10 (plus signs), 0 (crosses), 10 (diamonds), 20 (circles), 30 (squares) and 40 (triangles).

Here, I assume that the diabatic gap is normally distributed and compare the variances of the stable states from Marcus theory based molecular dynamics simulations. In particular, 10 ns-long simulations are performed in the canonical ensemble by employing a Nosé-Hoover thermostat for both the

$\Delta\mu$	-10	0	10	20	30	40
$\Delta_r F$	-9.7	0.2	10.3	19.9	30.5	40.3
$\Delta_r F_{SR}$	-12.1	-1.8	8.1	17.6	28.2	38.1
$\Delta(\Delta_r F)$	2.4	2.0	2.2	2.3	2.2	2.2
$-k_B T\, ln\, \frac{\sigma_P}{\sigma_R}$	0.1	0.2	0.1	0.2	0.1	0.2
$\Delta_r U$ (GF)	-41.5	-31.9	-22.7	-13.4	-1.9	7.6
$\Delta_r U$ (FD)	-40.7	-28.7	-21.3	-9.1	1.2	11.7
$-T\Delta_r S$ (GF)	31.9	32.7	33.4	34.1	32.5	33.1
$-T\Delta_r S$ (FD)	31.0	29.2	31.8	29.5	29.0	28.6

Table 5.5: The reaction free energies computed from canonical equilibrium molecular dynamics simulations at a temperature of $T = 298.15\,\mathrm{K}$ according to equations (5.7) and (5.8) are shown as a function of the effective free energy of reaction $\Delta\mu$ for the iron model. In the third data row, the difference between the reaction free energy from Marcus's formula and that from Simpson's rule (SR) is reported: $\Delta(\Delta_r F) = \Delta_r F - \Delta_r F_{SR}$. This difference is compared to the non-linearity arising from the difference in the variances between the stable states given in the fourth data row. All quantities are in $\mathrm{kJ\,mol^{-1}}$, and computations used the diabatic Hamiltonian (5.5) with coupling parameter values of $\zeta = 0$ for the reactants, $\zeta = 1$ for the products and $\zeta = 0.5$ for the crossing point. In addition, the entropies and internal energies of reaction are shown, which are obtained from the temperature-dependence of $\Delta_r F$ both via the finite difference (FD) schemes of equations (5.14) and (5.13) and from graphical fits (GF). The estimated statistical uncertainty of the entropies and internal energies of reaction is around $2\,\mathrm{kJ\,mol^{-1}}$ and thus an order of magnitude larger than that for the reaction free energies.

reactant and product diabatic states. Specifically, the Hamiltonian (3.156)

$$\begin{aligned}\mathcal{H}(\boldsymbol{\xi},\zeta) &= \mathcal{H}(\boldsymbol{\xi},0) + \zeta\ (\mathcal{H}(\boldsymbol{\xi},1) - \mathcal{H}(\boldsymbol{\xi},0)) \\ &= \mathcal{H}_R(\boldsymbol{\xi}) + \zeta\Delta E(\boldsymbol{\xi}) \end{aligned} \tag{5.5}$$

is used with the diabatic potential energy functions corresponding to the ferrous (R; $\zeta = 0$) and ferric (P; $\zeta = 1$) ions. From these simulations the gap variances are estimated from the sample variances of the time series of the gap. The ratio of the gap variances σ_P/σ_R for different $\Delta\mu$ values lies between 0.9 and 0.95, and the corresponding free energy difference is displayed in the fourth data row of table 5.5. An alternative way of investigating the state-independence of the Gaussian distribution of gap variables is to use equation (3.159)

$$\begin{aligned}\Delta_r F = F(\zeta=1) - F(\zeta=0) &= \int_{\zeta=0}^{\zeta=1} \left\langle \frac{\partial\mathcal{H}(\boldsymbol{\xi},\zeta')}{\partial\zeta'} \right\rangle_{\zeta'} d\zeta' \\ &= \int_{\zeta=0}^{\zeta=1} \langle\Delta E\rangle_{\zeta'}\ d\zeta' \end{aligned} \tag{5.6}$$

for different numbers of intermediate states to compute the reaction free energy. If the system obeys linear response, the reaction free energy is independent of the number of intermediate states. The first three data rows of table 5.5 and figures 5.8 and 5.11 (top left panel) compare the results from no intermediate point, which corresponds to Marcus's formula (2.41)

$$\Delta_r F = \frac{1}{2}\left(\langle\Delta E\rangle_R + \langle\Delta E\rangle_P\right), \tag{5.7}$$

to those with one intermediate point, namely Simpson's rule (4.20):

$$\Delta_r F_{SR} = \frac{1}{6}\left(\langle\Delta E\rangle_R + 4\langle\Delta E\rangle_{CP} + \langle\Delta E\rangle_P\right). \tag{5.8}$$

In practice, the sample means of the diabatic gap from canonical equilibrium simulations employing the Hamiltonian (5.5) at ζ values of 0 (reactants), 1 (products) and 0.5 (crossing points) were used to estimate the reaction free

energies from Marcus theory and from Simpson's rule. It is seen that the reaction free energies obtained from Simpson's rule (second data row of table 5.5) differ from those obtained from Marcus's formula (first data row of table 5.5) by less than k_BT (third data row of table 5.5). Although this result indicates a non-linearity, the effect is relatively small, and Marcus theory might still provide a good approximation.

$\Delta\mu$	-10	0	10	20	30	40
$\Delta_r F$	-11.9	-2.0	7.6	17.5	27.5	37.7
$\Delta_r F_L$	-12.0	-2.2	7.5	17.3	27.3	37.5
$\Delta(\Delta_r F)$	0.1	0.2	0.2	0.2	0.2	0.2
$-k_BT\, ln\, \frac{\sigma_P}{\sigma_R}$	0.2	0.2	0.2	0.2	0.2	0.2
$\Delta_r U$	-34.7	-26.7	-18.8	-12.6	2.8	13.8
$\Delta_r U_L$	-34.4	-26.3	-18.7	-12.6	3.3	14.1
$-T\Delta_r S$	22.9	24.9	26.8	30.3	25.1	24.0
$-T\Delta_r S_L$	22.4	24.4	26.5	30.2	24.4	23.5

Table 5.6: The reaction free energies $\Delta_r F$ (5.10) and the Landau free energies of reaction $\Delta_r F_L$ (5.9) for the iron model from umbrella integration simulations at a temperature of $T = 298.15\,\mathrm{K}$ are shown as a function of the effective free energy of reaction $\Delta\mu$. In the third data row, the difference between the reaction free energy and the Landau free energy of reaction is reported: $\Delta(\Delta_r F) = \Delta_r F - \Delta_r F_L$. This difference is compared to the data in the fourth data row obtained from equation (5.11) and quadratic fits (dotted lines) to the free energy profiles of figure (5.9). All quantities are in $\mathrm{kJ\,mol^{-1}}$, and the estimated standard deviation for the Landau free energy of reaction is $\sigma = 0.6\,\mathrm{kJ\,mol^{-1}}$. In addition, the entropies and internal energies of reaction are shown, and their standard error is an order of magnitude larger than that for the corresponding free energy differences.

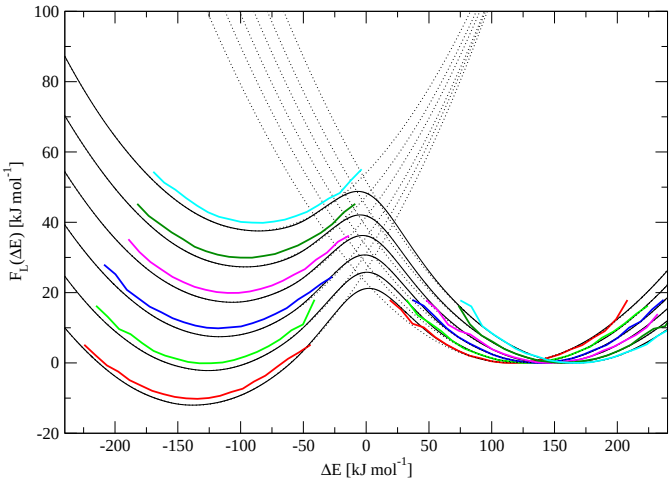

Figure 5.9: Free energy profiles from umbrella integration and canonical equilibrium simulations are shown for the model oxidation half-reaction of the aqueous ferrous ion at a temperature of $T = 298.15$ K. The free energy profiles obtained from umbrella integration are represented by solid black lines for all values of the effective reaction free energy $\Delta\mu$. The free energy profiles from Marcus theory based canonical equilibrium simulations result from the logarithm of the diabatic energy gap histograms. The line colours red (-10), green (0), blue (10), magenta (20), dark green (30) and cyan (40) correspond to the $\Delta\mu$ values in brackets in $\mathrm{kJ\,mol^{-1}}$. The dotted black lines are fits to the umbrella integration results in regions where the second derivative of the Landau free energy is approximately constant. The free energy profiles have been shifted so that the reactant minimum for all $\Delta\mu$ values is set to zero. The diabatic energy gap is positive for reactants; hence, the forward reaction (oxidation) proceeds from right to left in the present figure.

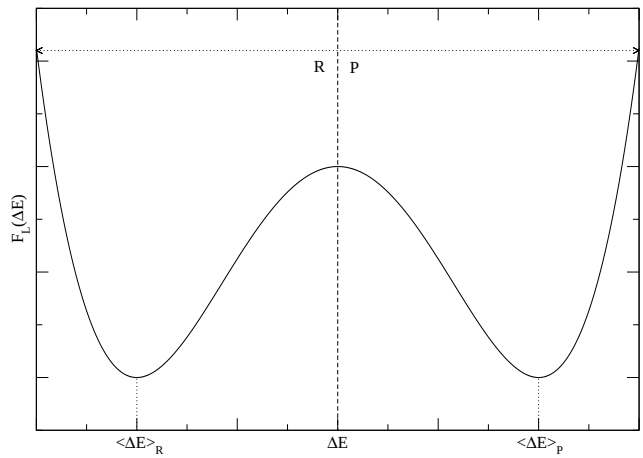

Figure 5.10: A schematic free energy profile is displayed. The barrier top separating the reactant (R) and product (P) regions is indicated by the dashed line. The Landau free energy of reaction (5.9) is evaluated as the difference between the Landau free energy values at the minima of the stable states (indicated by the dotted lines at $\langle \Delta E \rangle_R$ and $\langle \Delta E \rangle_P$). The reaction free energy (5.10) is obtained as the difference between the reactant and product state free energies by summing $e^{-\beta F(\Delta E)}$ from the transition state over the entire reactant and product wells, respectively (as indicated by the horizontal dotted arrows).

Next, the normal distribution of the energy gaps is assessed indirectly. To this end, I compare the Landau free energies of reaction $\Delta_r F_L$ (2.37)

$$\Delta_r F_L = F_{L,P}(\langle \Delta E \rangle_P) - F_{L,R}(\langle \Delta E \rangle_R) \tag{5.9}$$

and the reaction free energies $\Delta_r F$ (3.150)

$$\Delta_r F = F_P - F_R = -k_B T \, ln \, \frac{Q_P}{Q_R} = -k_B T \, ln \, \frac{\int e^{-\beta F_L(\Delta E)} \, \theta_P(\Delta E) \, d\Delta E}{\int e^{-\beta F_L(\Delta E)} \, \theta_R(\Delta E) \, d\Delta E} \tag{5.10}$$

from umbrella integration given in the first and second data row of table 5.6, which are related by equation (2.38)

$$\Delta_r F = \Delta_r F_L - k_B T \, ln \frac{\sigma_P}{\sigma_R} \tag{5.11}$$

if the energy gap is normally distributed [48, 68]. For each value of the effective reaction free energy $\Delta\mu$, biased molecular dynamics simulations with harmonic restraining potentials were carried out in 27 overlapping windows. In each window, 10^4 independent data points were collected from 10 ns-long molecular dynamics simulations coupled to a Nosé-Hoover thermostat. The data points from all windows were combined by the umbrella integration analysis [65, 66] to yield the free energy profile as a function of the diabatic energy gap. The Landau free energy of reaction (5.9) is extracted as the difference between the lowest free energy in the product and reactant wells. In contrast, the reaction free energy (5.10) is obtained by numerically integrating the exponentials of the Landau free energy in the entire region of a given stable state, as indicated in figure 5.10. The data in table 5.6 reveal that the difference in Landau free energies and free energies of reaction from direct simulation and from equation (5.11) agree well. This supports the assumption of the first test above that the diabatic gap is normally distributed to a good approximation.

In addition, it can be noted that the ratio of variances obtained from Marcus theory based equilibrium simulations and from umbrella integration exhibit the same sign and are of the same order of magnitude. Another indication for this is provided by the similarity of the curvatures of the free energy profiles shown in figure 5.9. We also see that the reaction free energies from umbrella integration and from Simpson's rule agree within statistical uncertainty. Although these results show that there are slight non-linearities, the two independent methods yield similar results, thus indicating that the description of the model oxidation half-reaction is reasonable and that Marcus theory provides a good representation because the system responds approximately linearly.[17]

[17]The extent to which simulation results indicate linear response or deviations from it

The above discussion shows that the control parameter $\Delta\mu$ is a suitable effective reaction free energy. In particular, a given $\Delta\mu$ value is within k_BT of the reaction free energy. More importantly, if the reaction free energies from Marcus theory based molecular dynamics and umbrella integration simulations shown in tables 5.5 and 5.6 are considered for different values of $\Delta\mu$, the change in $\Delta_r F$ is the same as that in $\Delta\mu$, as expected from equation (4.18a)

$$\Delta_r F(\Delta\mu) = \frac{1}{2}\left(\langle\Delta E(\Delta\mu)\rangle_R + \langle\Delta E(\Delta\mu)\rangle_P\right) = \Delta\mu, \tag{5.12}$$

within statistical uncertainty. The latter is about $0.6\,\mathrm{kJ\,mol^{-1}}$ for umbrella integration and $0.2\,\mathrm{kJ\,mol^{-1}}$ for molecular dynamics simulations in the stable states.

I now turn to the results regarding the internal energies and entropies of reaction, displayed in the right and left panel of the bottom row of figure 5.11, which are obtained from the temperature dependence of the reaction free energies (top left panel of figure 5.11). In particular, Marcus theory based molecular dynamics simulations on the diabatic potential energy surfaces in the reactant and product minima were performed at temperatures of 278.15 and 318.15 K. The reaction free energies (5.7) at 278.15 and 318.15 K were then used to estimate the internal energy of reaction via a finite-difference approximation to the Gibbs-Helmholtz equation (4.22)

$$\begin{aligned}\Delta_r U(T) = &\left(\frac{\Delta_r F(T+\Delta T)}{T+\Delta T} - \frac{\Delta_r F(T-\Delta T)}{T-\Delta T}\right)\\ &\times\left(\frac{1}{T+\Delta T} - \frac{1}{T-\Delta T}\right)^{-1}\end{aligned} \tag{5.13}$$

and the reaction entropy according to equation (4.21)

$$\Delta_r S(T) = -\frac{\Delta_r F(T+\Delta T) - \Delta_r F(T-\Delta T)}{T+\Delta T-(T-\Delta T)}. \tag{5.14}$$

involves subjective elements. For instance, simulation results from reference [45] have been described as showing non-linear behaviour by Zhou and Szabo [48]. In contrast, Geissler and Chandler [141] characterize the same findings as results exhibiting linear response.

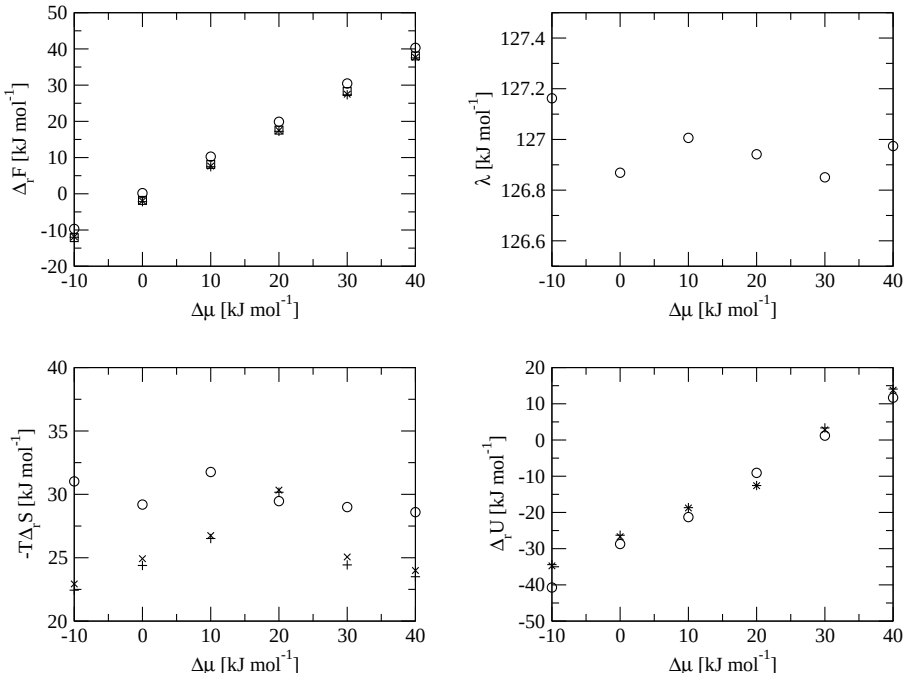

Figure 5.11: Reaction free energies (top left), entropies (bottom left), internal energies (bottom right) and reorganization free energies (top right) are shown as a function of the effective reaction free energy $\Delta\mu$. Results from Marcus theory based simulations are indicated by circles, whereas umbrella integration results are represented by plus signs (for Landau free energies and the corresponding energetic and entropic components) and crosses (for free energies obtained according to equation (5.10) and the corresponding energetic and entropic components). In the top left panel, the reaction free energy according to Simpson's rule is indicated by squares. The reorganization free energy was only estimated from Marcus theory based simulations (top right panel). All displayed results correspond to canonical ensemble averages at a temperature of 298.15 K.

Umbrella integration simulations on the adiabatic potential energy surface also yielded reaction free energies at 278.15 and 318.15 K, shown in figure 5.12, which were used in equations (5.13) and (5.14) to estimate the internal energies and entropies of reaction. It is seen from figure 5.12 that the reaction free energies increase approximately linearly in the temperature range

considered, thereby showing that the finite difference approximations (5.13) and (5.14) should be reasonable.

It is seen from the internal energies and entropies of reaction presented in figure 5.11 and in tables 5.5 and 5.6 that the control parameter $\Delta\mu$ mainly affects the internal energy of reaction. The variation of the internal energies of reaction obtained from both Marcus theory based molecular dynamics simulations and umbrella integration over the entire range of $\Delta\mu$ values follows that of $\Delta\mu$, as seen in tables 5.5 and 5.6 and in the bottom right panel of figure 5.11. In contrast, the reaction entropies show no systematic variation with $\Delta\mu$ if the statistical uncertainties are taken into account: $2.0\,\mathrm{kJ\,mol^{-1}}$ for Marcus theory based simulations and $6.0\,\mathrm{kJ\,mol^{-1}}$ for umbrella integration. It is expected that the variation of $\Delta\mu$ only affects the energies (and not the entropies) for equilibrium molecular dynamics simulations on the diabatic potential energy surface because a change in $\Delta\mu$ simply results in a shift in potential and total energy. However, the forces remain unaltered, and the dynamics does not change. Consequently, the temperature dependence of the average gaps in the stable states, which determine the reaction free energy (5.7), is not affected, and the reaction entropy is independent of $\Delta\mu$ to a good approximation. Because $\Delta\mu$ is linearly related to the reaction free energy, it can be concluded that the reaction energy is most sensitive to that control parameter. In the case of umbrella integration simulations on the adiabatic potential energy surface the situation is slightly different. Specifically, a variation of the parameter $\Delta\mu$ alters not only the relative energies but also the forces acting on the system at a given nuclear configuration because the diabatic states are coupled, as can be seen from equation (4.13):

$$\boldsymbol{\mathcal{F}}_j^{(a)} = \frac{1}{2}\left(\boldsymbol{\mathcal{F}}_{R,j} + \boldsymbol{\mathcal{F}}_{P,j}\right) + \frac{1}{2}\frac{\Delta E(\boldsymbol{r}_C, \Delta\mu)}{\sqrt{(\Delta E(\boldsymbol{r}_C), \Delta\mu)^2 + 4\,\gamma_{el}^2}}\left(\boldsymbol{\mathcal{F}}_{R,j} - \boldsymbol{\mathcal{F}}_{P,j}\right). \tag{5.15}$$

It follows from the coupling between the two diabatic states that the dynamics will be altered if the temperature is varied. Consequently, the entropy is likely to change. However, the change in entropy is expected to be small as long as the qualitative nature of the force acting on the system remains

the same. In that case, the translational, vibrational and rotational degrees of freedom will explore a similar volume in phase space, and the major influence of $\Delta\mu$ on the reaction free energy will be due to the internal energy of reaction. Hence, the parameter $\Delta\mu$ might be interpreted as an effective electrode potential regarding the equilibrium reaction energetics because it alters the force acting on the donor solute species if the coupling to the (virtual) electron acceptor does not vanish. Overall, the variation of the reaction free energy with $\Delta\mu$ is more regular than that of its components discussed here. This might be attributed to the statistical uncertainty of the latter, which is an order of magnitude larger than the standard error of the reaction free energies for both simulation methods.

The observation that the statistical uncertainty of internal energy differences is about an order of magnitude larger that that for free energy differences is not new [191, 221]. The statistical challenge in computing internal energy differences arises because we need to compute the difference of two ensemble averages, each of which tends to be a relatively large number [191,221]. The associated fluctuations depend on the square root of the particle number [76, 221]. As a result, the difference in internal energy, which is typically small compared to the individual contributions from which it is computed, exhibits a large statistical uncertainty [221]. This challenge becomes severer as the system size increases [76]. In contrast, the statistical uncertainty for free energy differences is smaller because a free energy difference involves, in principle, a single average over that part of phase space where the initial and final states differ [191, 221]. The fluctuations from the remainig regions of phase space do not affect the computation of free energy differences because they are the same for the initial and final states [191, 221].

An additional observation from the reaction energetics data considered above concerns the energy-entropy partitioning of the reaction free energy. For instance, the internal energy of reaction at $\Delta\mu = 0$ is negative, which reflects the stronger Coulombic interaction with the water molecules of the ferric ion compared to the ferrous ion. This interaction also leads to the negative reaction entropy for all $\Delta\mu$ values because the Fe^{3+} ion limits the orientational and translational freedom of the surrounding solvent dipoles,

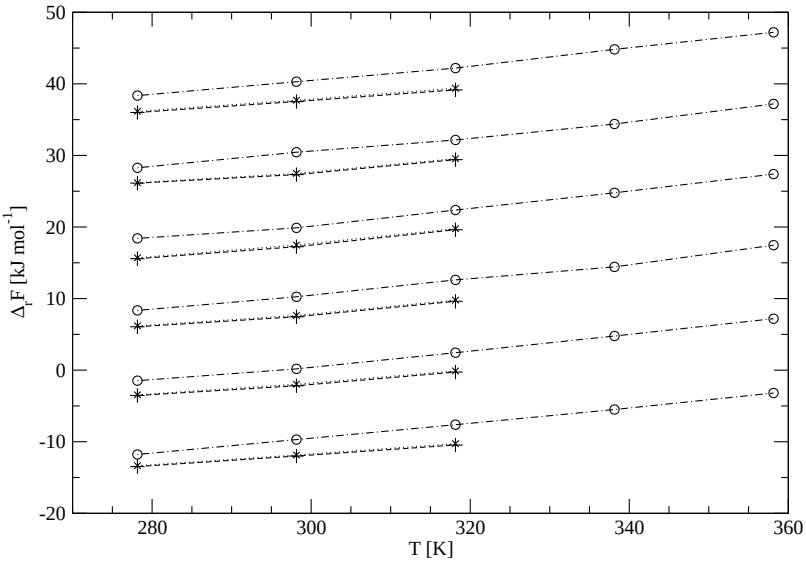

Figure 5.12: The temperature dependence of the reaction free energy is displayed for the iron ion system at a temperature of $T = 298.15\,\mathrm{K}$. Results from umbrella integration (UI) are indicated by plus signs connected by dashed lines ($\Delta_r F_L$ according to (5.9)) and by crosses connected by dotted lines ($\Delta_r F$ according to (5.10)), whereas canonical equilibrium molecular dynamics (MT) simulation results are marked by circles connected by dashed-dotted lines. The effective free energy $\Delta\mu$ increases from bottom to top from -10 to $40\,\mathrm{kJ\,mol^{-1}}$.

thereby decreasing the entropy relative to the reactant state. It is noted that the same physical phenomenon is responsible for the smaller gap variances in the product state compared to the reactant state, which leads to the slight non-linear effects discussed above.

In summary, Marcus theory provides a good description of the present model system so that predictions from this theory should prove useful for rationalizing further aspects of this work.

5.2.2 Validation of transition path sampling

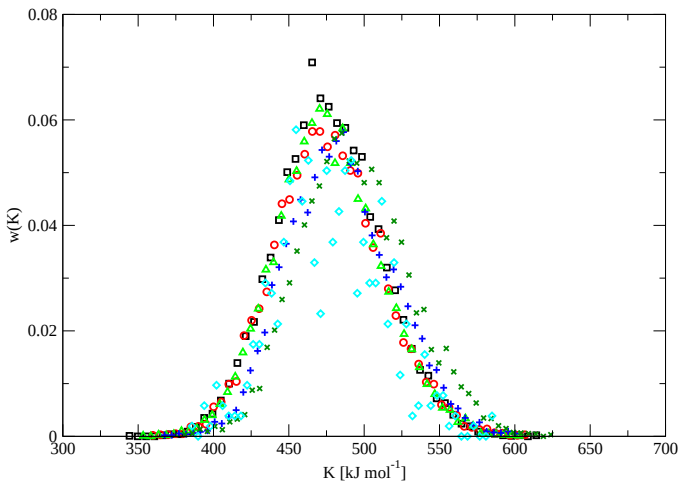

Figure 5.13: The kinetic energy histograms $w(K)$ are shown for the reactant (R), product (P) and crossing point (CP) configurations sampled from both Marcus theory based molecular dynamics (MT) and transition path sampling (TPS) simulations for the model oxidation half-reaction $Fe^{2+}_{(aq)} \rightarrow Fe^{3+}_{(aq)} + e^{-}_{(\mu)}$. The symbols corresponding to MT simulations are black squares (R), red circles (P) and green triangles (CP), whereas TPS results are represented by blue plus signs (R), dark green crosses (P) and cyan diamonds (CP). The temperature is set to $T = 298.15\,\mathrm{K}$, and the corresponding expected average kinetic energy is $\langle K \rangle = 476\,\mathrm{kJ\,mol^{-1}}$.

This section discusses the validity of the transition path sampling method. The discussion comprises the temperature control, the definition of the stable states, the path length and the accuracy of the activation energy. I start with the temperature control below.

The effectiveness of the temperature control described in section 3.3.2 for the transition path sampling method whose simulation parameters are given in section 4.2.3 is discussed. To this end, the average kinetic energies from molecular dynamics and transition path sampling simulations are compared in table 5.7 for $\Delta\mu = 0$. It is seen that the Nosé-Hoover thermostat employed for the molecular dynamics simulations maintains a stable average

Method	$\langle K \rangle_R$	$\langle K \rangle_P$	$\langle K \rangle_{\mathrm{CP}}$
MT	476.3±0.3	476.4±0.3	475.9±0.3
TPS	484.3±0.3	493.5±0.3	477.4±0.3

Table 5.7: State-specific average kinetic energies of the reactants (R), products (P) and crossing point (CP) for $\Delta\mu = 0$ are shown for the aqueous iron model. The first data row displays average kinetic energies obtained from Marcus theory (MT) based canonical equilibrium molecular dynamics simulations (10 ns) on diabatic potential energy surfaces characterized by coupling parameter values of $\zeta = 0$ (reactants), $\zeta = 0.5$ (crossing point) and $\zeta = 1$ (products) in the Hamiltonian (5.5). The second data row shows average kinetic energies from transition path sampling computations in the canonical ensemble consisting of 2×10^6 Monte Carlo attempts. The temperature is set to $T = 298.15$ K, and all values are given in kJ mol^{-1}.

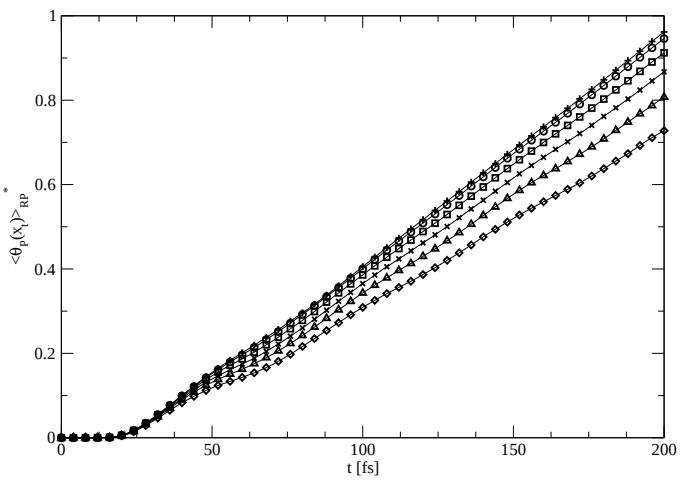

Figure 5.14: The path average $\langle \theta_P(x_t) \rangle^*_{RP}$ obtained from transition path sampling simulations in the canonical ensemble at a temperature of $T = 298.15$ K is shown as a function of time for various values of the effective reaction free energy $\Delta\mu$ (in kJ mol^{-1}): -10 (plus signs); 0 (circles); 10 (squares); 20 (crosses); 30 (triangles); 40 (diamonds). The linear regime is reached after about 120 fs for the aqueous iron ion model system.

kinetic energy for all states. In contrast, the average kinetic energy from transition path sampling at the crossing point is lower than in the stable

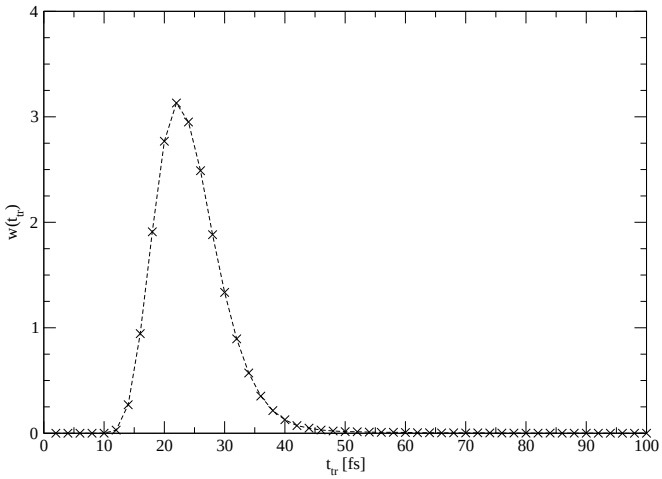

Figure 5.15: The transition time histogram $w(t_{tr})$ (in relative probability units) is shown for 200 fs trajectories from transition path pampling simulations in the canonical ensemble at a temperature of $T = 298.15\,\mathrm{K}$ and an effective reaction free energy of $\Delta\mu = 0$ for the oxidation of the model aqueous ferrous ion.

states. As in the case of the argon model system, the kinetic energy of the crossing point corresponds to that of the imposed temperature. Here, the agreement with the average kinetic energy of the molecular dynamics simulations is better. This is probably due to the larger number of degrees of freedom in the iron model system. The higher energies in the stable states are caused by the constant-energy nature of the reactive trajectories in the transition path ensemble, as discussed for the argon system in section 5.1. The same behaviour is illustrated in figure 5.13. In particular, the kinetic energy histogram is skewed to the right as expected. Furthermore, the average kinetic energy is higher in the product state than in the reactant state, which is consistent with the negative internal energy of reaction reported in tables 5.5 and 5.6. It should be noted that the data for the transition path sampling at the crossing point in figure 5.13 are rather noisy. This noise arises because the number of data points available at the crossing point in the transition path ensemble is lower than for the stable states. In particular,

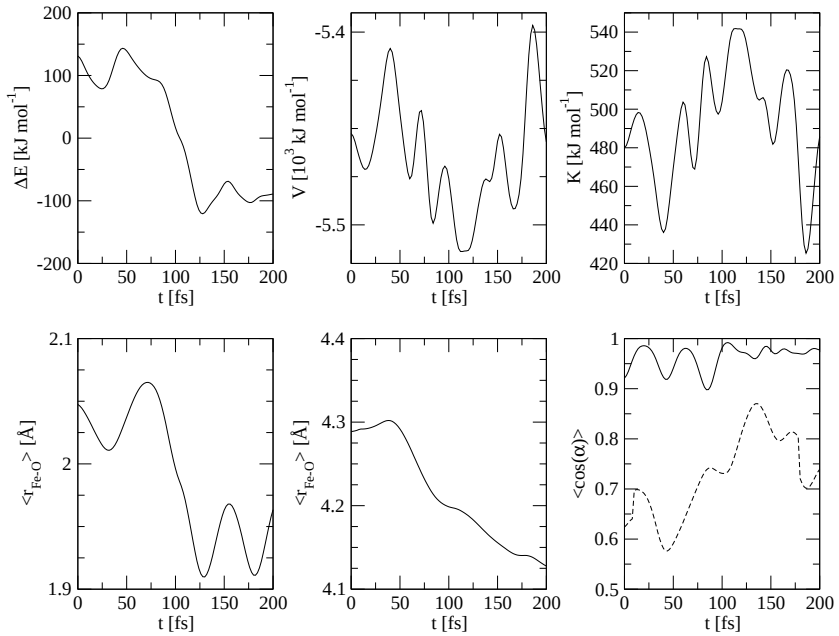

Figure 5.16: The energetic and structural changes during a typical 200 fs reactive transition (top left panel) are shown for the oxidation of the aqueous ferrous ion at a temperature of $T = 298.15\,\mathrm{K}$ and an effective reaction free energy of $\Delta\mu = 0$. The top row displays the potential (middle) and kinetic (right) energies. The bottom row shows the average $Fe - O$ distance in the first (left) and second (middle) solvation shells. The bottom right panel displays the average of the scalar product ($\langle cos(\alpha)\rangle$) of the unit vectors characterizing the water dipole moment and the internuclear separation pointing from the oxygen to the iron site.

not every reactive trajectory yields a configuration that corresponds to the crossing point in the following sense. A reactive trajectory is represented by a sequence of time slices that are stored. Because configurations are not saved at every timestep along the trajectory and because the energy gap is a rapidly varying function of phase space coordinates, the resolution of energy gap values in the barrier region is limited. Accordingly, some trajectories do not exhibit a configuration satisfying the criterion characterizing crossing poins ($|\Delta E| < 2\,\mathrm{kJ\,mol^{-1}}$). These results provide supporting evidence that the method proposed in reference [141] provides an effective means of controlling the temperature in the canonical transition path ensemble. As already

mentioned, the constant energy nature of the dynamical trajectories and the focus on the ensemble of reactive trajectories lead to different temperatures in the stable states compared to the barrier top region. The inclusion of non-reactive trajectories would most likely lead to a constant temperature in all regions of phase space. Alternatively, the propagation of dynamical trajectories could be achieved by means of thermostatted dynamics. However, due to the short trajectories (200 fs) compared to typical relaxation times in a condensed phase environment ($1 - 10$ ps) I chose to focus on the Hamiltonian dynamics of the system rather than on the dynamics of a (strong) heat bath. For larger systems, the ability of the system to distribute energy over many degrees of freedom might decrease the effect that the average kinetic energies from different regions of phase space differ if the focus is on reactive trajectories. Indeed, the relative deviation from the target kinetic energy are significantly smaller for the iron ion system than for the argon model.

The reactive trajectories of the transition path ensemble connect the stable states. As mentioned in section 4.2.3, a barrier region ranging from $-50\,\mathrm{kJ\,mol^{-1}}$ to $50\,\mathrm{kJ\,mol^{-1}}$ separates reactants and products. This definition of the stable states ensures that the vast majority of data points sampled from equilibrium trajectories fall outside the barrier region, as can be seen from the coloured curves in figure 5.9.

As an illustration, the energetic and structural properties of a typical reactive trajectory are shown in figure 5.16. The top left panel shows that the transition from reactants to products is fast. The middle and right panels in the top row indicate that typical variations of the potential and kinetic energy are of the order of $100\,\mathrm{kJ\,mol^{-1}}$ along a given trajectory. The bottom row displays the average $Fe{-}O$ distance in the first (left) and second (middle) solvation shell, whereas the right panel compares the orientational structure for the first (solid line) and second (dashed line) solvation shells. As expected, the average iron-oxygen distance decreases upon oxidation of the ferrous ion. In addition, the Coulombic forces also lead to a higher alignment of the water dipole moments along the $Fe - O$ connection line for the ferric ion compared to the ferrous ion. For both structural parameters considered here, the effect is much less pronounced beyond the second solvation shell.

The evaluation of the activation energy from transition paths requires that the process is activated. As mentioned earlier, a process is activated if a plateau time is observed for the rate constant, or equivalently, if a linear regime is reached for the population decay. Such a behaviour is observed for the path average $\langle \theta_P(x_t) \rangle^*_{RP}$ in figure 5.14, thus indicating that the model oxidation half-reaction is thermally activated. The linear regime is reached after about 120 fs. This observation is further supported by the histogram of transition times displayed in figure 5.15. In particular, reactive trajectories cross the barrier region within 40 fs, which will be exploited in the committor analysis of section 5.2.3. Given that the process is activated and the path length suitably chosen, I shall discuss the accuracy of the activation energy below.

Anticipating the results for $\Delta\mu = 0$, I compare the activation energy obtained from transition path sampling (TPS) with those from Marcus theory based simulations (MT) and umbrella integration (UI). Contrary to the activation energies obtained from equilibrium and biased canonical molecular dynamis simulations, the activation energy was obtained from a transition path sampling simulation at a single temperature $T = 298.15\,\mathrm{K}$ according to equation (2.70) [76]:

$$E_a(t) = \frac{\langle \dot{\theta}_P(x_t)\mathcal{H}(\boldsymbol{\xi}_0) \rangle^*_{RP}}{\langle \dot{\theta}_P(x_t) \rangle^*_{RP}} - \langle H \rangle_R. \tag{5.16}$$

The second term on the right-hand side of equation (5.16) is obtained from a long canonical equilibrium molecular dynamics simulation, whereas the first term on the right-hand side is extracted from the transition path ensemble of 200 fs-long reactive trajectories in the canonical ensemble. The time derivative of the path averages was taken numerically according to the central (2.68)

$$\dot{\mathcal{A}} = \frac{d\mathcal{A}}{dt} \approx \frac{\mathcal{A}(t+\Delta t) - \mathcal{A}(t-\Delta t)}{2\Delta t} \tag{5.17}$$

or the forward finite difference schemes (2.69)

$$\dot{\mathcal{A}} = \frac{d\mathcal{A}}{dt} \approx \frac{\mathcal{A}(t+\Delta t) - \mathcal{A}(t)}{\Delta t}. \tag{5.18}$$

The timestep was 1 fs, and the barrier region separating the stable states extended from -50 to $50\,\mathrm{kJ\,mol^{-1}}$. The resulting activation energies from transition path sampling (TPS: $10.2\,\mathrm{kJ\,mol^{-1}}$) agree within statistical uncertainty with reference calculations (UI: $15.2\,\mathrm{kJ\,mol^{-1}}$; MT: $15.7\,\mathrm{kJ\,mol^{-1}}$). The standard deviations from TPS, UI and MT are $2.1\,\mathrm{kJ\,mol^{-1}}$, $3.0\,\mathrm{kJ\,mol^{-1}}$, $1.2\,\mathrm{kJ\,mol^{-1}}$. As a result, transition path sampling provides reasonably accurate estimates of the activation energy for the present, moderately complex activated process.

A consequence of practical importance for the present work is that the transition path ensemble obtained here seems representative of the studied redox process. Thus, the harvested reactive trajectories can be analyzed by means of a committor analysis to obtain information about the reaction coordinate and the transition state, which have been assumed known in the discussion of the validity of Marcus theory above. I shall describe the committor analysis in the next section.

5.2.3 Reaction coordinate and transition state

After the validation of the transition path sampling method and the linear response approximation I study the remaining assumptions of Marcus theory. In particular, I investigate whether the transition state in the committor sense corresponds to the ensemble of configurations with vanishing gap, as predicted by Marcus theory, and whether the energy gap constitutes the reaction coordinate. I shall discuss the accuracy of the reaction coordinate first and the characteristics of the transition state and crossing points subsequently.

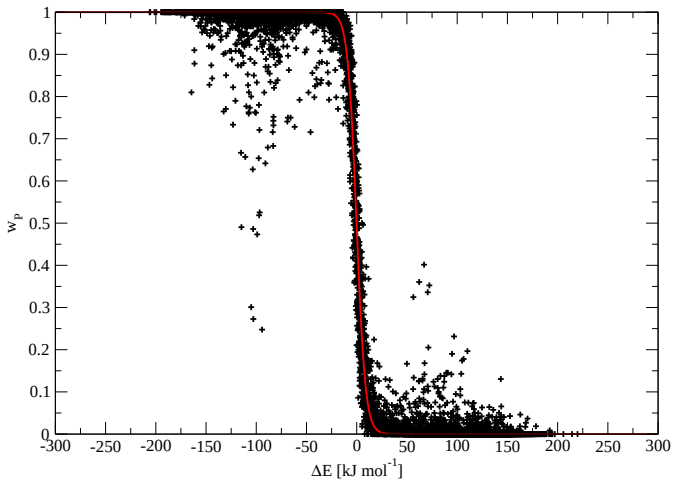

Figure 5.17: The committor w_P, which is the probability of reaching the product state prior to the reactant state for a given configuration [21, 22, 79], is displayed as a function of the diabatic energy gap ΔE. The datapoints represent the committor values of all configurations of 200 representative trajectories harvested from transition path sampling in the canonical ensemble at a temperature of $T = 298.15\,\mathrm{K}$. The red line is a fit using the function $f(y) = \frac{1}{2} - \frac{1}{2}(tanh(\mathcal{C}_1(y - \mathcal{C}_2))$ as described in reference [185], where $\mathcal{C}_1$ and $\mathcal{C}_2$ are fitting parameters and y is the order parameter whose suitability as a reaction coordinate is tested.

A committor analysis as described in section 3.3.4 is carried out to test whether the diabatic energy gap is a suitable reaction coordinate. The simu-

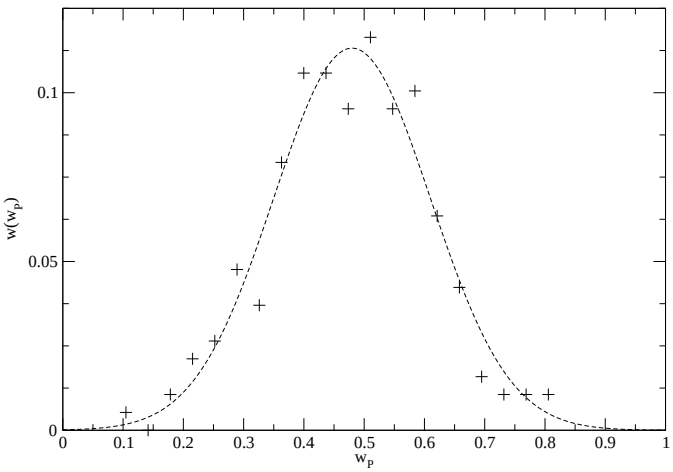

Figure 5.18: The committor distribution for the aqueous iron model is displayed for crossing points defined as lying in an order parameter range of $2\,\mathrm{kJ\,mol^{-1}}$ around the Marcus theory prediction for the transition state: $\Delta E = 0$. The dashed line is a Gaussian fit to the data points, whose mean is 0.47. The calculations were performed at $\Delta\mu = 0$ and $T = 298.15\,\mathrm{K}$.

$\Delta\mu$	-10	0	10	20	30	40
$F_L(\Delta E_{max})$	21.2	25.8	30.7	36.2	42.1	48.8
ΔE_{max}	2.3	0.6	-1.2	-2.9	-4.8	-6.7

Table 5.8: The maxima of the free energy profiles extracted from figure 5.9 and obtained from umbrella integration simulations at $T = 298.15\,\mathrm{K}$ are displayed for all values of the effective free energy of reaction $\Delta\mu$. The Landau free energy values in the first row and the corresponding diabatic energy gap values ΔE_{max} in the second row are given in $\mathrm{kJ\,mol^{-1}}$ for the iron model system.

lation details are given in section 4.2.3, and the resulting plot of the committor against the diabatic gap is shown in figure 5.17. This figure exhibits all the characteristics described in section 3.3.4 because the diabatic gap decreases during the reaction and the figure should thus be read from right to left. In particular, the committor increases steeply as a function of the diabatic gap in the barrier region, namely for gap values from around $-50\,\mathrm{kJ\,mol^{-1}}$

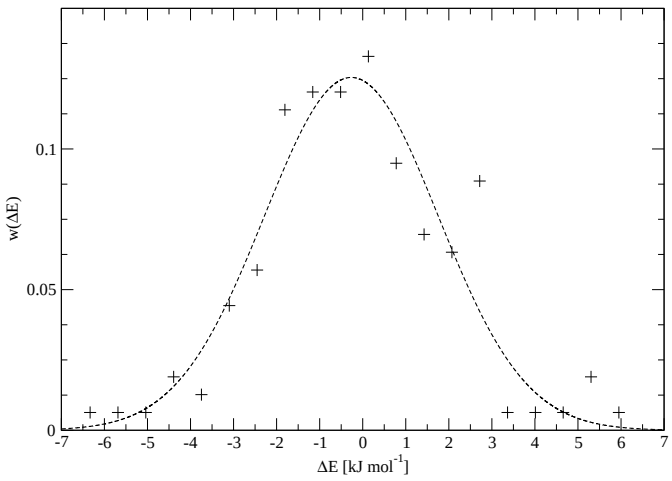

Figure 5.19: The gap distribution is shown for transition states identified from transition path sampling simulations according to the committor criterion. The data points for the aqueous ferrous-ferric ion model system at $\Delta\mu = 0$ and $T = 298.15\,\mathrm{K}$ are indicated by plus signs, and the dotted line is a Gaussian fit to the data points. The mean of the diabatic energy gap is $-0.2\,\mathrm{kJ\,mol^{-1}}$ for dynamical transition states in the range $-10\,\mathrm{kJ\,mol^{-1}}$ to $10\,\mathrm{kJ\,mol^{-1}}$.

$\Delta\mu$ [kJ mol^{-1}]	-10	0	10	20	30	40
κ_r	0.96	0.95	0.91	0.87	0.81	0.73

Table 5.9: The transmission coefficient κ_r from the reactive trajectories contained in the transition path ensemble is shown as a function of the effective free energy of reaction $\Delta\mu$ for the aqueous iron ion model system at $T = 298.15\,\mathrm{K}$.

to $50\,\mathrm{kJ\,mol^{-1}}$. From the behaviour in the barrier region it would be concluded that the diabatic gap constitutes a good reaction coordinate for the present model system, as would be expected from Marcus theory. However, the present committor analysis indicates that a few configurations outside the barrier region are also dynamical transition states. A similar observation was made in a study of ion pair dissociation pathways [233] and indicates that degrees of freedom orthogonal to the diabatic gap contribute to the ex-

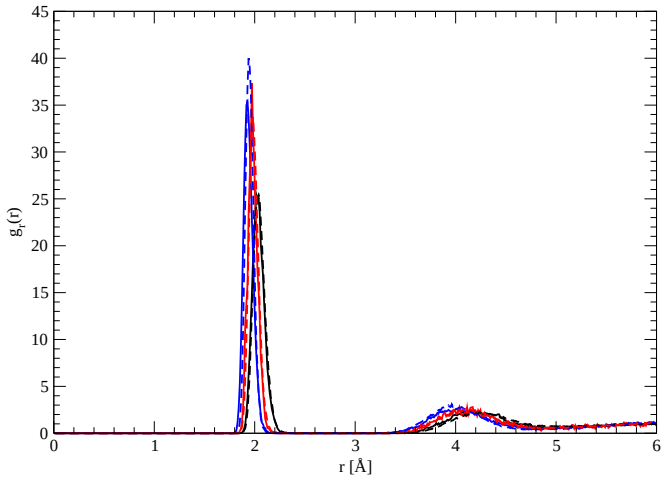

Figure 5.20: The Fe-O radial distribution functions for reactants (black), products (blue), and crossing points (red) are displayed. Solid lines represent configurations from the transition path ensemble, whereas dashed lines denote configurations from Marcus theory based molecular dynamics simulations. The latter employ diabatic potential energies corresponding to coupling parameter values of $\zeta = 0$ (reactants), $\zeta = 0.5$ (transition states) and $\zeta = 1$ (products) in equation (5.5). All simulations are performed at a temperature of $T = 298.15\,\mathrm{K}$.

act reaction coordinate. All attempts to understand why there are dynamical transition states characterized as stable states by the order parameter failed (as in reference [233]). In particular, these configurations exhibit neither particularly high potential nor kinetic energies. Furthermore, evaluating the committor for those configurations by means of fleeting trajectories coupled to a strong heat bath did not change the committor value compared to using Hamiltonian dynamics and momenta drawn from a Boltzmann distribution. In other words, a lack of relaxation of energy from important degrees of freedom to bath or spectator modes in the present system does not seem to be the cause for dynamical transition states to lie outside the barrier region according to the order parameter criterion. However, the vast majority of configurations of the transition path ensemble shows the expected behaviour.

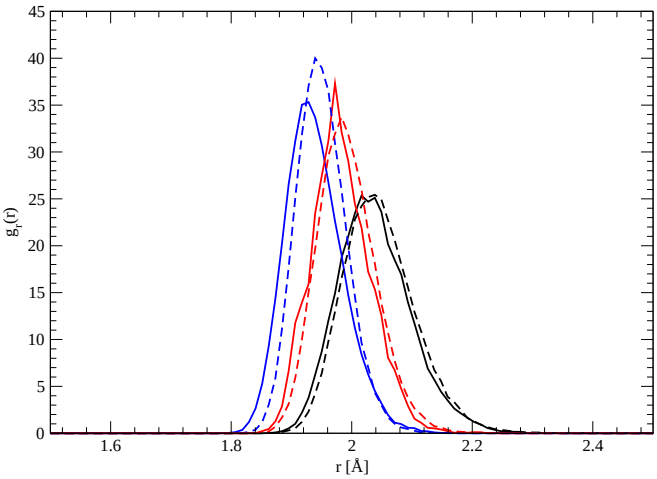

Figure 5.21: The first peaks of the Fe-O radial distribution functions for reactants (black), products (blue), and crossing points (red) are displayed. Solid lines represent configurations from the transition path ensemble, whereas dashed lines denote configurations from Marcus theory based molecular dynamics simulations. The latter employ diabatic potential energies corresponding to coupling parameter values of $\zeta = 0$ (reactants), $\zeta = 0.5$ (transition states) and $\zeta = 1$ (products) in equation (5.5). All simulations are performed at a temperature of $T = 298.15\,\mathrm{K}$.

It is thus concluded that the present committor analysis supports the diabatic gap as a suitable reaction coordinate for the model oxidation half-reaction of the aqueous ferrous ion.

Below, the relation between the crossing point configurations and the transition state is investigated. As already mentioned in section 3.3.4, dynamical transition states are configurations whose committor value is 0.5. In practice, a range of 0.4 to 0.6 is chosen to describe transition state configurations in the committor sense. In contrast, the maximum of the free energy profile may be called a static transition state according to transition state theory if the reaction coordinate is known. Given the above results from the reaction coordinate study of the diabatic gap, this is considered a valid approach. I thus ask what the relation between the dynamical and

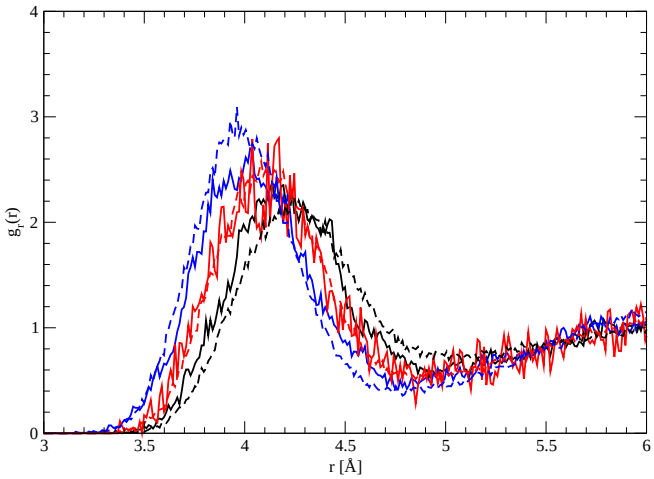

Figure 5.22: The second peaks of the Fe-O radial distribution functions for reactants (black), products (blue), and crossing points (red) are displayed. Solid lines represent configurations from the transition path ensemble, whereas dashed lines denote configurations from Marcus theory based molecular dynamics simulations. The latter employ diabatic potential energies corresponding to coupling parameter values of $\zeta = 0$ (reactants), $\zeta = 0.5$ (transition states) and $\zeta = 1$ (products) in equation (5.5). All simulations are performed at a temperature of $T = 298.15\,\mathrm{K}$.

static transition state configurations and the set of crossing points in Marcus theory is.

To answer this question three pieces of information are taken into account. First, the location of the maximum of the free energy profile will be compared to the vanishing gap value. Second, the committor distribution is computed for a set of configurations with order parameter values satisfying $|\Delta E| \leq 2\,\mathrm{kJ\,mol^{-1}}$ obtained from transition path sampling simulations at $\Delta\mu = 0$ and $T = 298.15\,\mathrm{K}$. Third, the gap distribution for dynamically determined transition states is calculated.

A detailed analysis of the free energy profiles from umbrella integration, displayed in figure 5.9, reveals that the location of the maximum of the free energy profile, which corresponds to the transition state in transition state

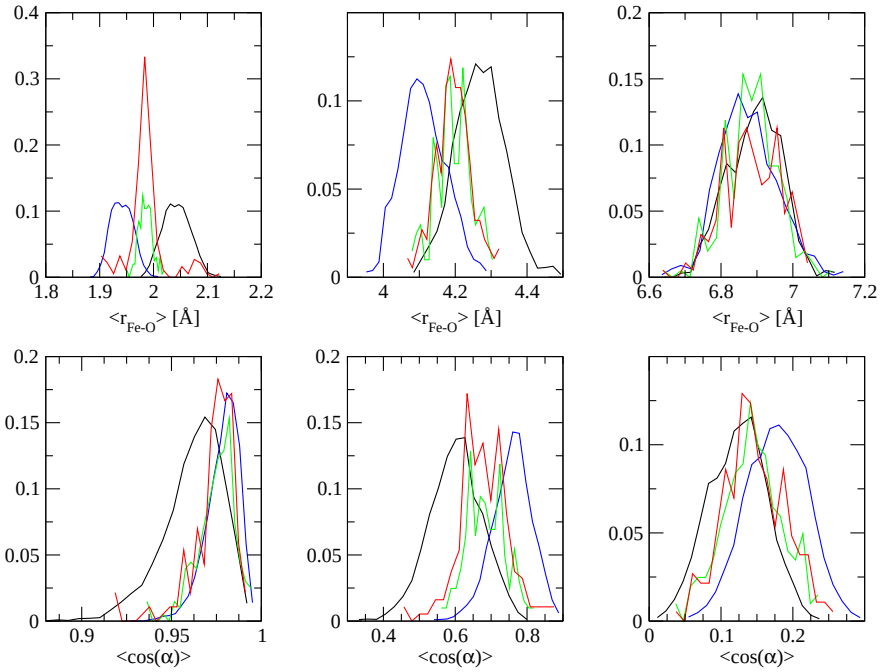

Figure 5.23: The histograms of structural properties of the iron ion model system are shown for reactants (black), products (blue), crossing points (green; $|\Delta E| < 2\,\mathrm{kJ\,mol^{-1}}$) and transition states (red) harvested by transition path sampling. In each row, the structural properties are given for the first (left), second (middle) and remaining (right) solvation shells around the iron ion. The first row shows the average iron-oxygen distance, whereas the second row displays the average of $cos(\alpha)$, where α is the angle between the water dipole moment and the connection line from the oxygen to the iron site.

theory if the reaction coordinate is known, shifts towards more product-like configurations for increasing reaction free energies. The numerical values are given in table 5.8. This trend is in agreement with the Leffler-Hammond postulate [17, 18] and Marcus theory predictions [158].

I now turn to the committor distribution of the crossing points, which are defined as those phase space points for which the diabatic gap vanishes. In contrast to an earlier study [108] that constrained the system to a phase space hypersurface with vanishing diabatic gap, the time resolution of the dynamical transitions from transition path sampling does not allow for collecting exact crossing points. Instead, a range of the order parameter around

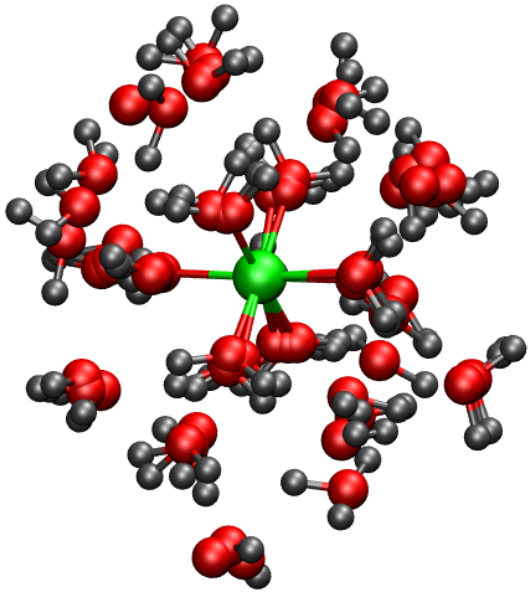

Figure 5.24: An overlay of snapshots of a reactant, a product, and a transition state configuration along a typical reactive trajectory (see top left panel of figure 5.16) are shown. Oxygen atoms are displayed in red; hydrogen atoms are shown in gray. The green sphere denotes the iron ion. For clarity, only the first two solvation shells are shown.

zero is employed to identify approximate crossing points. It is found that the precise numerical value of the order parameter range has little quantitative influence on the resulting committor distribution. In practice, a histogram of relaxation probabilities from all crossing points approximates the committor distribution of equation (3.147). The committor distribution resulting from

a gap range of $2\,\mathrm{kJ\,mol^{-1}}$ around zero is shown in figure 5.18. The mean committor value is 0.47, and its standard error is estimated to be 0.10. This result provides support for the crossing points to be dynamical transition states within statistical uncertainty.

The finding from the committor distribution of the crossing points is compared to the distribution of the diabatic gap for dynamical transition states. All configurations whose committor lies between 0.4 and 0.6 are considered transition states. Their average committor is 0.50 ± 0.05, and their gap distribution is shown in figure 5.19. It is seen that this gap distribution for transition states in the barrier region ($|\Delta E| \leq 10\,\mathrm{kJ\,mol^{-1}}$) is peaked at around $-0.2\,\mathrm{kJ\,mol^{-1}}$, which is close to Marcus theory predictions. If all dynamical transition states are included in the present analysis, the mean diabatic gap becomes $-2.9\,\mathrm{kJ\,mol^{-1}}$. This finding might indicate that dynamical transition states tend to be more product-like (according to the diabatic energy gap value) on average than crossing point configurations. This observation is consistent with the above result from the committor distribution that crossing points might be slightly more reactant-like according to the committor criterion. However, the statistical uncertainty is too large for these observations to be conclusive. Overall, the crossing points from Marcus theory and the dynamical transition states according to the committor description are in satisfactory agreement with each other and with the maximum of the free energy profile at $\Delta\mu = 0$.

Further support for the validity of Marcus theory is provided by the iron-oxygen radial distribution function displayed in figures 5.20, 5.21 and 5.22 because they show that the crossing point configurations from transition path sampling and from Marcus theory based molecular dynamics simulations have properties in between those of the reactants and products. In particular, the average iron-oxygen distance of the first solvation shell corresponds to an equivalent charge distribution of the iron ion of approximately $z_{Fe} = 2.5\,e_0$ at the transition state, as predicted by Marcus and Hush [38, 85, 86]. This result reflects the symmetry of the free energy barrier for $\Delta\mu = 0$ shown in figure 5.9.

In figure 5.23, the histograms of structural properties are displayed ac-

cording to different categories of configurations sampled via transition path sampling. The top row provides essentially the same information as the radial distribution functions of figures 5.20, 5.21 and 5.22. However, it focuses on the transition path ensemble and distinguishes between the dynamical transition state configurations and crossing point configurations. The former (red) have a committor between 0.4 and 0.6, whereas the latter configurations satisfy $|\Delta E| < 2\,\mathrm{kJ\,mol^{-1}}$ (green). Results corresponding to configurations of the reactant (black; $\Delta E > 50\,\mathrm{kJ\,mol^{-1}}$) and product (blue; $\Delta E < -50\,\mathrm{kJ\,mol^{-1}}$) states are also shown. The bottom row of figure 5.23 displays the average orientational structure for the first (left panel), second (middle panel) and remaining (right panel) solvation shells. Compared to the average $Fe-O$ distance, the orientational structure seems to persist beyond the second solvation shell to a certain extent. The results for the 202 crossing points and 186 transition states according to the committor criterion from 200 reactive trajectories are statistically indistinguishable. The statistics are better for the stable states because about 43 configurations per stable state are available on average from each reactive event. Although the oxidation of the ferrous ion leads to a higher alignment of the water molecules relative to the iron ion and to a decrease of the radii of the first and second solvation shells (electrostriction), the effect is not very pronounced. Indeed, an overlay of the first, the last and the transition state configurations of a typical reactive trajectory in figure 5.24 shows that the structural changes are relatively small. This is a further indication for the outer-sphere character of the present model system. In particular, the first solvation shell remains almost unchanged.

In addition, the low fraction of recrossings shown in table 5.9 for reactive trajectories might point to the validity of transition state theory underlying Marcus theory. This observation is only indicative in nature because the exact transmission coefficient also includes unreactive trajectories that cross and recross the dividing surface, which are not collected in this study.

In summary, the results presented here for the oxidation half-reaction of the aqueous ferrous ion provide supporting evidence for the accuracy and approximate validity of transition state theory and Marcus theory for outer-

sphere electron-transfer reactions. Hence, I shall employ Marcus theory predictions in the discussion of the activation parameters, of the charge-transfer symmetry factor and of its energetic and entropic components below.

5.2.4 Activation parameters

Until now, I have discussed reaction energetics and the suitability of the effective reaction free energy. In this section I shall focus on activation parameters including the reorganization free energy and entropy as well as the effect of the coupling element, which does not appreciably affect the stable states, as shown in section 5.2.1. I start with the discussion of the results on the reorganization free energy and entropy below.

$\Delta\mu$	-10	0	10	20	30	40
$\Delta_r F\,(T = 278.15\,\mathrm{K})$	-11.8	-1.5	8.4	18.4	28.3	38.4
$\Delta_r F\,(T = 298.15\,\mathrm{K})$	-9.7	0.2	10.3	19.9	30.5	40.3
$\Delta_r F\,(T = 318.15\,\mathrm{K})$	-7.6	2.4	12.6	22.4	32.2	42.2
$\Delta_r F\,(T = 338.15\,\mathrm{K})$	-5.5	4.8	14.4	24.8	34.4	44.8
$\Delta_r F\,(T = 358.15\,\mathrm{K})$	-3.2	7.2	17.5	27.4	37.2	47.2
$\Delta_\ddagger F^{(d)}\,(T = 278.15\,\mathrm{K})$	26.0	30.9	35.9	41.6	47.4	53.7
$\Delta_\ddagger F^{(d)}\,(T = 298.15\,\mathrm{K})$	27.1	31.8	37.1	42.5	48.8	55.1
$\Delta_\ddagger F^{(d)}\,(T = 318.15\,\mathrm{K})$	28.1	33.0	38.5	44.0	49.9	56.4
$\Delta_\ddagger F^{(d)}\,(T = 338.15\,\mathrm{K})$	29.1	34.3	39.6	45.5	51.4	58.2
$\Delta_\ddagger F^{(d)}\,(T = 358.15\,\mathrm{K})$	30.3	35.6	41.4	47.2	53.3	60.0
$\lambda\,(T = 278.15\,\mathrm{K})$	126.6	126.3	126.3	126.8	126.7	126.4
$\lambda\,(T = 298.15\,\mathrm{K})$	127.2	126.9	127.0	126.9	126.9	127.0
$\lambda\,(T = 318.15\,\mathrm{K})$	127.4	126.9	127.4	127.5	127.3	127.0
$\lambda\,(T = 338.15\,\mathrm{K})$	127.3	127.6	127.7	127.6	127.6	127.2
$\lambda\,(T = 358.15\,\mathrm{K})$	127.9	127.8	128.2	128.0	128.1	128.3

Table 5.10: The free energies of reaction $\Delta_r F$, of activation $\Delta_\ddagger F^{(d)}$ and of reorganization λ are shown as a function of temperature T and effective reaction free energy $\Delta\mu$ for the aqueous iron ion system. The results are obtained from Marcus's relations (5.22), (5.21) and (5.19) with canonical equilibrium simulation data as input. All quantities are in $\mathrm{kJ\,mol^{-1}}$, and the statistical error for activation free energies ($0.1\,\mathrm{kJ\,mol^{-1}}$) is half that for reorganization or reaction free energies.

$\Delta\mu$	-10	0	10	20	30	40
$\Delta_r F\,(T = 278.15\,\mathrm{K})$	-13.3	-3.5	6.2	15.7	26.2	36.2
$\Delta_r F\,(T = 298.15\,\mathrm{K})$	-11.9	-2.0	7.6	17.5	27.5	37.7
$\Delta_r F\,(T = 318.15\,\mathrm{K})$	-10.3	-0.1	9.8	19.8	29.6	39.4
$\Delta_r F_L\,(T = 278.15\,\mathrm{K})$	-13.5	-3.5	6.1	15.6	26.1	36.0
$\Delta_r F_L\,(T = 298.15\,\mathrm{K})$	-12.0	-2.2	7.5	17.3	27.3	37.5
$\Delta_r F_L\,(T = 318.15\,\mathrm{K})$	-10.5	-0.3	9.6	19.6	29.4	39.2
$\Delta_\ddagger F^{(a)}\,(T = 278.15\,\mathrm{K})$	20.5	25.1	29.8	35.1	41.4	47.7
$\Delta_\ddagger F^{(a)}\,(T = 298.15\,\mathrm{K})$	21.2	25.8	30.7	36.2	42.1	48.8
$\Delta_\ddagger F^{(a)}\,(T = 318.15\,\mathrm{K})$	22.1	26.9	32.1	37.6	43.6	50.1

Table 5.11: For the $Fe^{2+}_{(aq)}/Fe^{3+}_{(aq)}$ system the effective free energy of reaction dependence of the Landau free energies of reaction ($\Delta_r F_L$) and activation ($\Delta_\ddagger F^{(a)}$) as well as free energies of reaction ($\Delta_r F$) obtained from umbrella integration simulations at different temperatures are shown in $\mathrm{kJ\,mol^{-1}}$. The statistical uncertainty of reaction free energies is $0.6\,\mathrm{kJ\,mol^{-1}}$ and about twice that for activation free energies. These data underlie the evaluation of entropies and internal energies according to equations (5.29) and (5.23).

$\Delta\mu$	-10	0	10	20	30	40
$\Delta_\ddagger F^{(d)}$ (MT)	27.1	31.8	37.1	42.5	48.8	55.1
$\Delta_\ddagger U^{(d)}$ (MT-GF)	11.1	14.1	17.3	21.8	27.3	31.9
$\Delta_\ddagger U^{(d)}$ (MT-FD)	11.3	16.2	17.9	24.5	29.7	35.2
$-T\Delta_\ddagger S^{(d)}$ (MT-GF)	16.0	18.0	20.1	21.2	21.7	23.5
$-T\Delta_\ddagger S^{(d)}$ (MT-FD)	15.7	15.7	19.3	18.4	19.0	19.8
λ (MT)	127.2	126.9	127.0	126.9	126.9	127.0
$-T\Delta S_\lambda$ (MT-GF)	4.1	5.3	6.8	4.7	5.3	6.0
$-T\Delta S_\lambda$ (MT-FD)	5.5	4.3	8.5	5.2	4.5	4.3
$\Delta_\ddagger F^{(a)}$ (UI)	21.2	25.8	30.7	36.2	42.1	48.8
$\Delta_\ddagger U^{(a)}$ (UI)	10.3	12.7	14.9	17.8	26.7	31.0
$-T\Delta_\ddagger S^{(a)}$ (UI)	11.0	13.3	16.0	18.5	15.8	17.9
$\Delta_\ddagger F^{(d)}$ (UI)	24.4	29.6	34.5	40.3	46.2	53.2

Table 5.12: For the $Fe^{2+}_{(aq)}/Fe^{3+}_{(aq)}$ system the activation parameters obtained from umbrella integration (UI; adiabatic: (a)) and Marcus theory (MT; diabatic: (d)) based simulations are shown in $\mathrm{kJ\,mol^{-1}}$. The last row displays hypothetical diabatic activation free energies from the curve crossings of the dotted lines in figure 5.9.

Estimates of the reorganization free energy and entropy have been obtained from Marcus theory based simulations on diabatic potential energy surfaces in the canonical ensemble at 298.15 K. In particular, the reorganization free energies were computed from the average gaps in the reactant and product states according to equation (2.43)

$$\lambda = \frac{1}{2}\left(\langle \Delta E \rangle_R - \langle \Delta E \rangle_P\right). \tag{5.19}$$

The reorganization entropies were calculated from additional evaluations of the reorganization free energy at 278.15 and 318.15 K (so that $\Delta T = 20\,\mathrm{K}$) as follows

$$\Delta S_\lambda = -\left(\frac{\partial \lambda}{\partial T}\right)_{N,\mathcal{V}} \approx -\frac{\lambda(T+\Delta T) - \lambda(T-\Delta T)}{2\Delta T}. \tag{5.20}$$

The dependence of the free energies of reaction, activation and reorganization on temperature and reaction free energy for unbiased molecular dynamics simulations is displayed in table 5.10. The resulting reorganization entropies are reported in table 5.12. It is observed that the reorganization free energy λ itself is remarkably insensitive to changes in the effective free energy of reaction $\Delta\mu$ (see also figure 5.11). This result is in agreement with the expectation from equation (4.18b): $\lambda \neq f(\Delta\mu)$. The temperature-dependence of the reorganization free energy, reported in the right panel of figure 5.25 is weak, thus resulting in small values for the reorganization entropy ΔS_λ. It is found that the reorganization entropy is negative for the present model system. According to Ghorai and Matyushov [52], recent numerical simulations and molecular theories predict that the reorganization entropy should be positive. In particular, their work of *p*-nitroaniline in acetonitrile and SPC/E water indicated small positive reorganization entropies ($T\Delta S_\lambda \approx k_B T$). However, they also indicate that negative reorganization entropies have been observed for charged solute species [52]. Furthermore, dielectric continuum theory predicts negative reorganization entropies for high solvent polarities and positive reorganization entropies for low solvent polarities [52]. Accordingly, the sign obtained for $-T\Delta S_\lambda$ in this work would

be in agreement with dielectric continuum theory [52]. Given the controversy in the literature about which sign is expected, I shall restrict myself to the observation that the reorganization entropy is small and negative in the present case. It is seen from table 5.12 that the variation of the reorganization entropy with $\Delta\mu$ is within $1\,\mathrm{kJ\,mol^{-1}}$ except for $\Delta\mu = 10\,\mathrm{kJ\,mol^{-1}}$. This outlier value is within 2σ of the remaining $-T\Delta S_\lambda$ results, where the statistical error is $\sigma = 2.0\,\mathrm{kJ\,mol^{-1}}$.

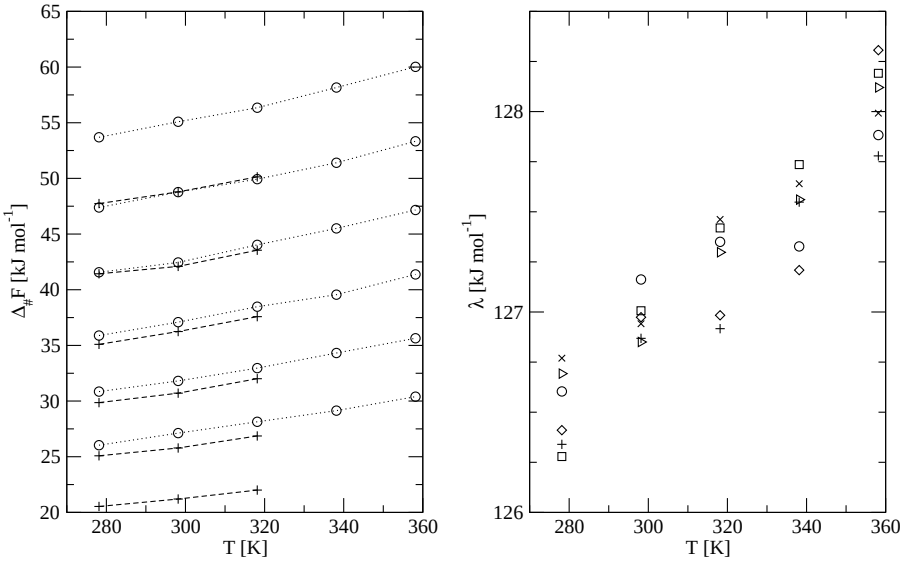

Figure 5.25: The temperature dependence of the activation (left panel) and reorganization (right panel) free energies is displayed for the model oxidation of the ferrous ion in aqueous solution at a temperature of $T = 298.15\,\mathrm{K}$. In the left panel, results from umbrella integration (UI) are indicated by plus signs connected by dashed lines, whereas canonical equilibrium molecular dynamics (MT) simulations on the diabatic potential energy surface are marked by circles connected by dotted lines. The effective free energy $\Delta\mu$ increases from bottom to top from -10 to $40\,\mathrm{kJ\,mol^{-1}}$. The right panel shows reorganization free energies from MT simulations for the following $\Delta\mu$ values (in $\mathrm{kJ\,mol^{-1}}$): -10 (circles), 0 (plus signs), 10 (squares), 20 (crosses), 30 (triangles) and 40 (diamonds).

In the following, I describe the free energy barrier and its energetic and entropic components; I shall start with the activation free energies below. The activation free energies obtained from Marcus theory (MT) based molecular dynamics simulation and umbrella integration (UI) are reported in table 5.12 (see also tables 5.10 and 5.11). The activation free energies according to Marcus theory (2.29)

$$\Delta_{\ddagger} F^{(d)} = \frac{(\lambda + \Delta_r F)^2}{4\lambda} \tag{5.21}$$

were computed from 10 ns-long canonical equilibrium molecular dynamics. The reorganization free energy (5.19) and the reaction free energy (2.41)

$$\Delta_r F = \frac{1}{2} \left(\langle \Delta E \rangle_R + \langle \Delta E \rangle_P \right) \tag{5.22}$$

were extracted from the difference and the sum of the average diabatic gaps $\langle \Delta E \rangle_j$ in the stable states $j = R, P$.

It is seen from table 5.12 and from figures 5.9 and 5.26 that the diabatic activation free energy $\Delta_{\ddagger} F^{(d)}$ (MT) is larger than the adiabatic one $\Delta_{\ddagger}^{(a)} F$ (UI) by about $6\,\mathrm{kJ\,mol^{-1}}$. To understand this difference, two aspects are considered. First, as outlined in section 2.2.5, the dominant effect of the electronic coupling is to lower the adiabatic free energy of the transition state with respect to the diabatic case by γ_{el}, which equals $3\,\mathrm{kJ\,mol^{-1}}$ in the present study. Second, the results of section 5.2.1 indicate that the reaction free energy from umbrella integration and Simpson's rule is lower by $-2\,\mathrm{kJ\,mol^{-1}}$ than the corresponding $\Delta\mu$ value and Marcus theory estimate. According to equation (5.21), this reduces the diabatic activation free energy by $1\,\mathrm{kJ\,mol^{-1}}$. Hence, the adiabatic activation free energy is lower by around $k_B T$ compared to Marcus theory predictions. This difference might be due to non-linear effects. Support for this hypothesis stems from the crossing points of the dotted lines in figure 5.9, which characterize the quadratic free energy curves with state-dependent curvatures from umbrella integration simulations. The resulting hypothetical "diabatic" activation free energies displayed in the last row of table 5.12 are about $k_B T$

smaller than those predicted from the equal curvature parabolas of Marcus theory. Hence, if the corrections due to finite-size effects did not affect the deviation from linear response, the non-linear behaviour due to the different curvatures in the stable states could be one contribution to the difference between Marcus theory based and umbrella integration simulations. In that case, the difference between Marcus's diabatic activation free energies and the adiabatic activation free energies from umbrella sampling would arise from two contributions: the first would be due to non-linear effects, and the second would be caused by the electronic coupling.

$\Delta\mu$	-10	0	10	20	30	40	$\langle\sigma\rangle$
$E_a(UI)$	12.8	15.2	17.4	20.3	29.2	33.5	3.4
E_a (MT-GF)	10.6	13.6	16.7	21.3	26.8	31.4	-
E_a (MT-FD)	10.9	15.7	17.4	23.9	29.1	34.7	1.3
$E_{a,ctr}(t)$ (TPS)	9.6	10.2	20.6	21.0	25.1	33.7	2.4
$E_{a,fwd}(t)$ (TPS)	10.0	8.8	20.0	20.6	22.7	37.5	2.8

Table 5.13: Activation energies for the aqueous iron model system in the canonical ensemble at $T = 298.15\,\mathrm{K}$ are compared for transition path sampling (TPS) simulations, umbrella integration (UI) and Marcus theory (MT) based molecular dynamics simulations. The two latter methods use equations (5.24) and (5.25) to relate the internal energy of activation $\Delta_\ddagger U$, obtained from equilibrium simulations at various temperatures via the finite difference scheme (FD) of equation (5.23), to the activation energy. Marcus theory based simulations also employ graphical fits (GF) and yield the adiabatic activation energy $E_a = \Delta_\ddagger U^{(d)} + k_B T - \gamma_{el}$ by assuming that the electronic coupling γ_{el} affects the potential energy only. The activation energies from transition path sampling results from the central (ctr) and forward (fwd) finite difference schemes (5.27) and (5.28) employed to compute (5.26). The average standard deviation is indicated by $\langle\sigma\rangle$, and all quantities are given in $\mathrm{kJ\,mol^{-1}}$.

Having discussed the activation free energies above, I turn to its components next, starting with the activation energies. The activation energies

from Marcus theory (MT) based equilibrium simulations and from umbrella integration (UI) calculations are obtained from the corresponding activation free energies at 278.15 K and 318.15 K, displayed in figure 5.25, according to (4.22)

$$\Delta_{\ddagger}U(T) = \left(\frac{\Delta_{\ddagger}F(T+\Delta T)}{T+\Delta T} - \frac{\Delta_{\ddagger}F(T-\Delta T)}{T-\Delta T}\right) \times \left(\frac{1}{T+\Delta T} - \frac{1}{T-\Delta T}\right)^{-1} \tag{5.23}$$

with $\Delta T = 20\,\mathrm{K}$. As already mentioned, equation (5.23) is an approximation to equation (2.49):

$$\Delta_{\ddagger}U = \left(\frac{\partial \frac{\Delta_{\ddagger}F}{T}}{\partial \frac{1}{T}}\right)_{N,\mathcal{V}}. \tag{5.24}$$

The computed internal energies of activation are then converted to activation energies via equation (2.24):

$$E_a = \Delta_{\ddagger}U + k_B T. \tag{5.25}$$

Transition path sampling activation energies are computed according to equation (2.70)

$$E_a(t) = \frac{\langle \dot{\theta}_P(x_t)\mathcal{H}(\boldsymbol{\xi}_0)\rangle^*_{RP}}{\langle \dot{\theta}_P(x_t)\rangle^*_{RP}} - \langle H\rangle_R, \tag{5.26}$$

where the time derivative is performed numerically according to the central (2.68)

$$\dot{\mathcal{A}} = \frac{d\mathcal{A}}{dt} \approx \frac{\mathcal{A}(t+\Delta t) - \mathcal{A}(t-\Delta t)}{2\Delta t} \tag{5.27}$$

or the forward finite difference schemes (2.69)

$$\dot{\mathcal{A}} = \frac{d\mathcal{A}}{dt} \approx \frac{\mathcal{A}(t+\Delta t) - \mathcal{A}(t)}{\Delta t}. \tag{5.28}$$

Similar to the activation energy, the activation entropy from MT and UI simulations is obtained from the temperature dependence of the activation

free energies according to equation (4.21):

$$\Delta_{\ddagger} S(T) = -\frac{\Delta_{\ddagger} F(T + \Delta T) - \Delta_{\ddagger} F(T - \Delta T)}{2\Delta T}. \tag{5.29}$$

It is seen from table 5.12 that the activation entropies computed from Marcus theory (MT) based simulations and umbrella integration (UI) agree within their statistical errors for $-T\Delta_{\ddagger} S$. The latter range from 1.1 to 1.4 kJ mol^{-1} for MT and from 2.4 to 4.4 kJ mol^{-1} for UI with increasing $\Delta\mu$.[18] Importantly, the activation entropy significantly contributes to the free energy barrier. For bimolecular processes this is expected because the reactants approach to form the transition state, thereby decreasing the translational freedom. However, the present model system describes a unimolecular process so that this argument does not apply. Nonetheless, Marcus theory provides a means to rationalize these findings.

As emphasized by Weaver [58], half-reactions are asymmetric, and the reaction entropies are therefore expected to be non-vanishing, as already noted. In addition, a comparison of the reaction entropies shown in tables 5.5 and 5.6 with the activation entropies reported in table 5.12 illustrates that the latter are well approximated by equation (2.50):

$$\Delta_{\ddagger} S^{(d)} = \left(\frac{1}{2} + \frac{\Delta_r F}{2\,\lambda}\right) \Delta_r S + \left(\frac{1}{4} - \left(\frac{\Delta_r F}{2\,\lambda}\right)^2\right) \Delta S_{\lambda}. \tag{5.30}$$

This means that the activation entropies are mainly determined by half the reaction entropies if the reorganization free energy is large, as in the present case. Accordingly, only for symmetrical reactions is the reorganization entropy expected to dominate the activation entropy. From a physical point of view, the lower activation entropy for symmetrical reactions compared to asymmetrical reactions can be rationalized as follows. In particular, the overall charge of the solute does not change for symmetric reactions, and the solvent experiences similar forces due to the solute. In contrast, for asymmetric

[18] The variance of the umbrella integration results increases because the reactant minimum and the transition state become more separated as $\Delta\mu$ increases (see figure 5.9). Accordingly, the variance of more windows enters the error propagation formula (4.23).

reactions, for example for a charge separation reaction ($D + A \rightarrow D^+ + A^-$), the solute changes from approximately non-polar to strongly dipolar (ion-pair) within the first solvation shell. As a result, the orientational restrictions are likely to be higher in the ion-pair state compared to the less polar initial state, resulting in a negative activation entropy. A physical explanation for the non-vanishing activation entropy considers the effective transition state charge. As seen from the iron-oxygen radial distribution functions, this effective charge lies between that of the reactants and the products. Specifically, the transition state behaves as if it carried a higher positive charge than the reactant ferrous ion. This leads to a reduced translational and orientational freedom at the transition state compared to the reactants and thus explains why the activation entropy is negative. It is approximately half that of the reaction entropy if the transition state is half-way between the reactant and product states.

It is clear from the above results for the activation entropy and for the activation free energy that the activation energy is smaller than the latter. To compare the different methods, the internal energies of activation from Marcus theory based simulations and umbrella integration have been transformed into adiabatic activation energies as obtained from transition path sampling. In particular, equation (5.25) relates internal energies of activation and activation energies. In addition, the electronic coupling, which is assumed to affect the energy only, is subtracted from the diabatic estimate obtained from Marcus theory [108, 158]. The resulting activation energies and their average standard deviations are reported in table 5.13. The statistical uncertainty of Marcus theory based simulations is smaller than that of umbrella integration and transition path sampling simulations, which are around $k_B T$ for the latter. The estimated activation energies are in reasonable agreement and within statistical uncertainty. Hence, the transition path sampling method implemented here is capable of providing the activation energy without prior knowledge of the reaction coordinate.

It is noteworthy that the calculation of the activation energy in the transition path ensemble employed here [76] differs from a more recent approach in reference [185]. There [185], the activation enthalpy was determined along

a given trajectory as the difference between the average enthalpies of the transition state and of the reactant state. This single-path activation energy was then averaged over all harvested reactive trajectories [185]. During the development stage of the present work the activation energy computed according to equation (5.26) was compared to the difference in average total energies of crossing points in the transition path ensemble and configurations sampled from molecular dynamics simulations in the reactant state. This approach is similar to that employed in reference [185] and yielded activation energies comparable to those reported in table 5.13.

Having presented the activation parameters in this section, I shall next describe their variation with the effective reaction free energy.

5.2.5 Charge-transfer symmetry factor and its components

In this section I shall describe the charge-transfer symmetry factor (β_{ct}) as well as its entropic ($T\beta_{ct,S}$) and energetic ($\beta_{ct,U}$) components.

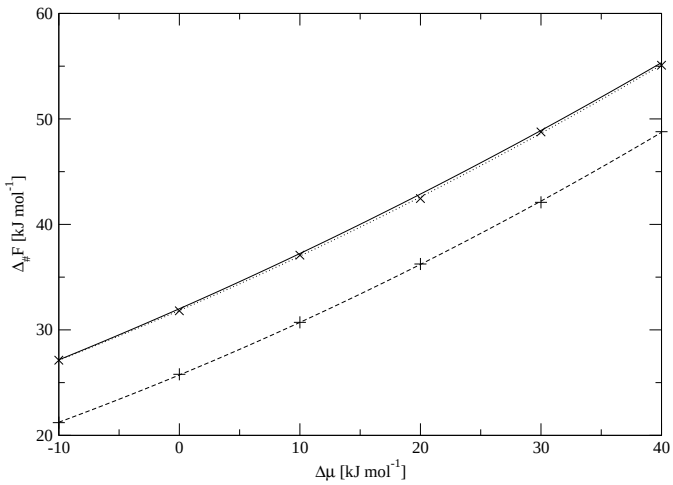

Figure 5.26: The activation free energies $\Delta_\ddagger F$ are illustrated as a function of the effective reaction free energy$\Delta\mu$ for the model oxidation of the ferrous ion in aqueous solution at a temperature of $T = 298.15\,\mathrm{K}$. Results from umbrella integration (UI) are indicated by plus signs, whereas canonical equilibrium molecular dynamics (MT) simulations on the diabatic potential energy surface are marked by crosses. Quadratic fits to the data (dashed line: UI; dotted line: MT) yield a charge-transfer symmetry factor value of 0.47 for the former method and 0.49 for the latter. The solid line represents the Marcus theory prediction for a reorganization free energy of $\lambda = 127\,\mathrm{kJ\,mol^{-1}}$ according to $\Delta_\ddagger F^{(d)} = \frac{(\lambda+\Delta\mu)^2}{4\lambda}$.

As noted previously, the charge-transfer symmetry factor β_{ct} (2.56)

$$\beta_{ct} = \frac{\partial \Delta_\ddagger F}{\partial \Delta_r F} \tag{5.31}$$

determines how the activation free energy varies with the reaction free energy. Although the numerical values of the activation free energies computed

	TPS	TPS (fwd)	UI	MT (FD)	MT (GF)
β_{ct}	-	-	0.47 ±0.005	0.49 ±0.007	0.49 ±0.007
$\beta_{ct,U}$	0.39 ±0.16	0.28 ±0.23	0.23 ±0.08	0.38 ±0.06	0.33 ±0.02
$T\beta_{ct,S}$	-	-	0.25 ±0.08	0.13 ±0.06	0.18 ±0.02

Table 5.14: The charge-transfer symmetry factor for the oxidation half-reaction $Fe^{2+}_{(aq)} \rightarrow Fe^{3+}_{(aq)} + e^{-}_{(\mu)}$, denoted by β_{ct}, and its energetic ($\beta_{ct,U}$) and entropic ($\beta_{ct,S}$) components are shown for transition path sampling (TPS), umbrella integration (UI) and Marcus theory (MT) based equilibrium canonical simulations at $T = 298.15\,\mathrm{K}$. The error estimates stem from the asymptotic standard error calculated by the gnuplot program. For the charge-transfer symmetry factor, no temperature derivative is required so that Marcus theory based equilibrium simulations yield the same estimate from graphical fits (GF) and finite difference (FD) schemes. The transition path sampling calculations performed in this work yield the energetic component of the charge-transfer symmetry factor only.

	UI	MT
β_{ct}	0.47 ±0.005	0.49 ±0.007
$\left(\frac{\partial \beta_{ct}}{\partial T}\right)$ [K^{-1}]	0.0008 ±0.00025	0.0004 ±0.00016
$T\left(\frac{\partial \beta_{ct}}{\partial T}\right)$	0.25 ±0.08	0.13 ±0.05

Table 5.15: The charge-transfer symmetry factor β_{ct} and its temperature-dependence are shown for umbrella integration (UI) and Marcus theory (MT) based equilibrium canonical simulations for the model aqueous ferrous-ferric oxidation half-reaction at $T = 298.15\,\mathrm{K}$.

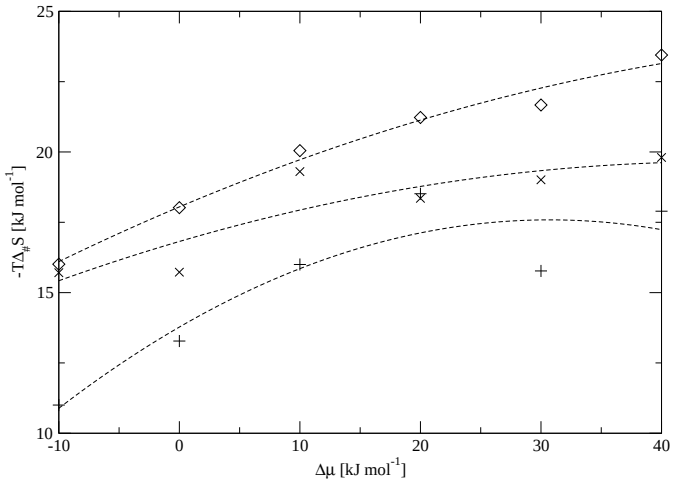

Figure 5.27: The activation entropies ($-T\Delta_{\ddagger}S$) are illustrated as a function of the effective reaction free energy $\Delta\mu$ for the aqueous ferrous-ferric model system at $T = 298.15\,\mathrm{K}$. Results from umbrella integration (UI) are indicated by plus signs, whereas canonical equilibrium simulations on the diabatic potential energy surface are marked by crosses for values obtained from the finite difference scheme (FD) and diamonds for values resulting from graphical fits (GF). Quadratic fits to the data (dashed lines) yield entropic components of the charge-transfer symmetry factor of 0.25 (UI), 0.13 (FD) and 0.18 (GF), which are also reported in table 5.14.

from Marcus theory based simulations and umbrella integration differ by an amount discussed in section 5.2.4, their variation with reaction free energy is very similar, as seen from tables 5.12 and 5.14. Likewise, a quadratic fit to figure 5.26 yields $\beta_{ct} = 0.47$ for umbrella integration and $\beta_{ct} = 0.49$ for Marcus theory based molecular dynamics simulations for $\Delta\mu = 0$.[19] These values are in good agreement with Marcus theory predictions according to

[19]The activation free energy as well as the activation entropy and the activation energy are expected to depend quadratically on the reaction free energy. Therefore, I employ quadratic fits of the activation parameters as a function of $\Delta\mu$. An alternative would consist in evaluating the derivative of the symmetry factor (and its components) numerically and fitting the result to a linear function. However, the numerical derivative is expected to be very noisy so that the approach employed here seems more reliable.

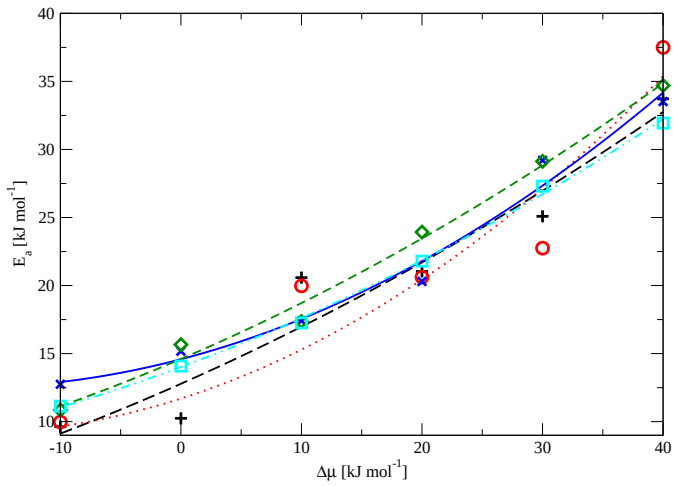

Figure 5.28: The variation of the activation energy with the effective reaction free energy $\Delta\mu$ as obtained from transition path sampling (TPS), umbrella integration (UI) and Marcus theory (MT) based molecular dynamics simulations is shown for the model oxidation reaction $Fe^{2+}_{(aq)} \rightarrow Fe^{3+}_{(aq)} + e^{-}_{(\mu)}$ at a temperature of $T = 298.15\,\mathrm{K}$. The green diamonds and cyan squares denote activation energies obtained from MT based molecular dynamics simulations by means of the finite difference (FD) scheme (5.23) and from graphical fits (GF). Activation energies computed from MT based canonical molecular dynamics simulations result from $E_a = \Delta_{\ddagger} U^{(d)} + k_B T - \gamma_{el}$ because of equation (5.25) ($+k_B T$) and because of the correction due to the difference between the diabatic and the adiabatic activation energies ($-\gamma_{el}$). The transition path sampling simulations yield activation energies obtained from central (ctr: black plus signs) and forward (fwd: red circles) finite difference schemes (5.27) and (5.28). Activation energies from umbrella integration are indicated by blue crosses. The lines are quadratic fits to the data points shown here and also reported in table 5.13. The fits yield the energetic component of the charge-transfer symmetry factor given in table 5.14: 0.39 (TPS,ctr), 0.28 (TPS,fwd), 0.23 (UI), 0.38 (MT-FD) and 0.33 (MT-GF).

equation (2.57)

$$\beta_{ct,MT} = \frac{1}{2} + \frac{\Delta_r F}{2\lambda}. \tag{5.32}$$

In addition, the charge-transfer symmetry factor is an indicator of the relative location of the transition state with respect to the stable states. It agrees with the average committor of crossing point configurations and with the $Fe - O$ radial distribution functions discussed in section 5.2.3. It is thus found that the charge-transfer symmetry factors computed from umbrella integration and molecular dynamics calculations are in qualitative and good quantitative agreement with Marcus theory predictions.

In contrast, the variation of the activation entropy with reaction free energy is less regular. Nonetheless, table 5.12 shows that the activation entropy ($-T\Delta_{\ddagger}S$) increases over the entire range of $\Delta\mu$ values. Although the quantitative agreement from Marcus theory based simulations and umbrella integration is smaller for $T\beta_{ct,S}$ than for β_{ct}, the sign and the order of magnitude of $T\beta_{ct,S}$ are the same, as can be seen from tables 5.12 and 5.14 and from figure 5.27. In particular, $T\beta_{ct,S} > 0$.

That the entropic component of the charge-transfer symmetry factor is positive can be understood from Marcus theory in two ways. First, the entropic component of the charge-transfer symmetry factor is given by equation (2.59)

$$T\beta_{ct,S,MT} = -T\frac{\partial\Delta_{\ddagger}S^{(d)}}{\partial\Delta_r F} = -T\frac{\Delta_r S}{2\,\lambda} + T\Delta S_{\lambda}\frac{\Delta_r F}{2\,\lambda^2}. \tag{5.33}$$

From tables 5.5 and 5.12 it is seen that the reaction entropy ($-T\Delta_r S$) is larger than the reorganization entropy ($-T\Delta S_{\lambda}$) by about a factor of five. Moreover, the prefactor of the reorganization entropy ($-T\Delta S_{\lambda}$) is significantly smaller than unity for the range of reaction free energies considered here. Thus, $T\beta_{ct,S}$ is expected to be positive. Its numerical value is estimated from the first term of equation (5.33) to be around 1/8 with $-T\Delta S \approx 30\,\mathrm{kJ\,mol^{-1}}$ and $\lambda \approx 120\,\mathrm{kJ\,mol^{-1}}$. Table 5.14 illustrates that the simulation results are in reasonable agreement with this order of magnitude estimate.

Second, as already noted, the transition state in Marcus theory can be thought of as carrying an equivalent charge intermediate between that of the reactant and product states. As the free energy of reaction increases, the

transition state is expected to become more product-like [17, 18, 30, 85, 86]. In the present case, the equivalent charge of the transition state becomes more positive, thus decreasing the entropy of the transition state by an argument similar to that given in section 5.2.4. If the entropy of the reactant state remains approximately the same, the activation entropy decreases, and $T\beta_{ct,S}$ is larger than zero. In summary, Marcus theory provides a means of rationalizing the sign and the order of magnitude of the entropic component of the charge-transfer symmetry factor for the model oxidation half-reaction studied in this work.

I now turn to the description of the energetic component of the charge-transfer symmetry factor, which, from the above argument that $T\beta_{ct,S}$ is positive, is expected to be smaller than β_{ct} itself. In fact, this is found independently from transition path sampling, umbrella integration, and Marcus theory based molecular dynamics simulation results reported in tables 5.13 and 5.14 and shown in figure 5.28. Specifically, $\beta_{ct,U}$ is positive and larger than $T\beta_{ct,S}$. Quadratic fits to the activation energies against $\Delta\mu$ in figure 5.28 yield energetic components of the charge-transfer symmetry factor as reported in table 5.14. Although the range of the $\beta_{ct,U}$ values amounts to 0.16, this is still within the estimated errors. This situation arises because the uncertainty on the activation energy leads to a large range of possible slopes for the variation of E_a with the effective reaction free energy. Importantly, the three methods are in qualitative agreement with one another and consistent with the estimates of $T\beta_{ct,S}$ in the sense that the charge-transfer symmetry factor of the present model reaction is predicted to be temperature-dependent. This temperature-dependence is discussed next.

The Marcus theory expression for the charge-transfer symmetry factor (5.32) indicates that the reorganization free energy λ and the reaction free energy $\Delta_r F$ might depend on temperature. The temperature-dependence of the reorganization free energy is small, as seen from table 5.10. Therefore, the temperature-dependence of β_{ct} reported in table 5.15 is mainly due to the reaction free energy dependence on temperature. In fact, the present simulations are carried out under equilibrium conditions at different reaction free energies. At a given temperature $\Delta_r F$ governs the equilibrium

constant and the equilibrium populations. From classical thermodynamics these properties are expected to depend on temperature if the internal energy of reaction does not vanish, which is the case in this work. In particular, the temperature-dependence of the charge-transfer symmetry factor and its entropic component displayed in tables 5.15 and 5.14 contain the same information for the present model system. As a result, the dependence of the charge-transfer symmetry factor on temperature does not contradict Marcus theory.

In summary, Marcus theory provides a good approximation for the model system studied both from a qualitative and from a quantitative point of view. The computation of the energetic component of the charge-transfer symmetry factor by means of transition path sampling, umbrella integration and molecular dynamics simulations yields results of the same order of magnitude. It is found that the energetic component is smaller than the charge-transfer symmetry factor, thus indicating that the latter is temperature-dependent. This conclusion is supported by the non-vanishing and positive values obtained for $T\beta_{ct,S}$.

Chapter 6

Conclusion

The aims of this work have been to determine the activation parameters governing outer-sphere electron-transfer dynamics and to investigate whether transition path sampling calculations of the activation energy, as reported in reference [76], can be carried out accurately for a moderately complex system: the model oxidation half-reaction of the classical aqueous ferrous ion.

This system has been chosen because it has been expected and confirmed to be well described by Marcus theory. Therefore, Marcus theory has served as a reference to evaluate the results obtained from transition path sampling simulations. After its validation the transition path sampling method has been applied to compute the energetic component of the charge-transfer symmetry factor to gain insight into the activation process of outer-sphere electron-transfer reactions.

To validate the transition path sampling implementation used here, literature results of a nine-atom argon system have been reproduced [76, 164]. Specifically, path averages in the microcanonical ensemble reported in [164] have been calculated within statistical uncertainty. In addition, the activation energy in the canonical ensemble for the same model argon system has been computed and compares favorably with the original values reported in [76]. This provided supporting evidence that the temperature control for the canonical ensemble proposed in reference [141] is correctly implemented. Overall, the results obtained from the argon model system indicate that the

transition path sampling method implemented in this work produces accurate activation energies.

The validated methodology has then been used to compute the activation energy for the model oxidation of the aqueous ferrous ion. Comparison of the activation energy to umbrella integration and Marcus theory based molecular dynamics simulations shows satisfactory agreement if the standard errors for the activation energies are taken into account. The comparison of the activation energy to the activation free energies computed from umbrella integration and Marcus theory based equilibrium simulations indicates that the activation entropy significantly contributes to the free energy barrier of the present model system. This result agrees qualitatively with experimental investigations of one-electrode processes [58].

Transition path sampling has also been applied to the computation of the energetic component of the charge-transfer symmetry factor. The charge-transfer symmetry factor itself from both umbrella integration and equilibrium molecular dynamics simulations is in excellent agreement with Marcus theory predictions. The energetic component of the charge-transfer symmetry factor ranges from 0.2 to 0.4 and is thus lower than the charge-transfer symmetry factor, which is around 0.5. This result suggests that a change in the reaction free energy is not completely reflected by a corresponding change in the internal energy of activation. Instead, the activation entropy also varies with the reaction free energy. Such a variation of the activation entropy with reaction free energy indicates a temperature-dependent charge-transfer symmetry factor [58]. The present work indeed finds that the charge-transfer symmetry factor is temperature-dependent, thereby reflecting how the equilibrium constant depends on temperature.

Furthermore, the validity of Marcus theory has been tested by various approaches. The traditional investigation of the linear response approximation shows that fluctuations of the diabatic energy gap in the stable states are Gaussian and that the variances differ only slightly. In addition, a committor analysis has shown that the diabatic gap is a good reaction coordinate. However, the committor analysis also reveals that the short-time dynamics of activated portions of equilibrium trajectories might be richer than expected

from Marcus theory. The crossing points of Marcus theory correspond to transition states in the committor sense to a good approximation, and the maximum of the free energy profile computed from umbrella integration also indicates that the transition state theory approximations underlying Marcus theory are reasonable. In particular, the transmission factor of trajectories in the transition path ensemble is close to unity. Furthermore, the geometry of the crossing points is intermediate between reactants and products, as indicated by the iron-oxygen radial distribution function computed from transition path sampling and equilibrium molecular dynamics simulations. This result is in agreement with the (equivalent) charge distribution at the transition state predicted by Marcus and Hush [38, 85, 86].

In summary, transition path sampling, umbrella integration and Marcus theory based molecular dynamics simulations show that the present aqueous ferrous ion model system is accurately described by Marcus theory.

The present work is limited by two major factors. First, the system size is so small that finite-size effects are relatively large. Second, the artificial aspects of the model do not provide a realistic description of an experimental electron-transfer reaction. Nevertheless, this work has considered an activated process for which energetic and entropic factors are important. It therefore captures the essential features of a barrier crossing problem in terms of classical nuclear motion and the associated statistical mechanics.

In particular, the present work has shown that the computation of activation energies by means of transition path sampling is possible for moderately complex systems. Transition path sampling and other methods will always face the intrinsic statistical challenge of computing activation energies [76, 191, 221]. However, if the reaction coordinate of the system under consideration is unknown, transition path sampling computations of the activation energy might provide a first insight into the mechanism. One possible extension of this work could therefore be the investigation of systems for which the reaction coordinate is unknown.

Another way to extend this work would be to replace the virtual electrode by an explicit electron acceptor. If the electron acceptor were a chemical species in solution, it might be possible to construct diabatic states with

the empirical valence bond approach [105], as in this work. This would allow for an investigation of the distance dependence between the donor and acceptor species of the activation parameters. Alternatively, the electron acceptor could be an electrode. In that case, the electronic structure would have to be treated at a more sophisticated level. The advantage of such an approach might be to get insight into the temperature dependence of the charge-transfer symmetry factor in electrochemical systems, for which the driving force can be controlled by an external electric potential [103]. Such an approach would then require the treatment of a non-equilibrium system for non-vanishing net current densities [33].

Appendix A

Random variables and probability

In this appendix we shall introduce some notions of probability theory. The central concept of probability theory and statistics is a random variable. Before we can define random variables, we need to discuss random experiments, events and probabilities. In doing this, our presentation is inspired by reference [2].

A.1 Random experiment and probability

We call a random experiment an experiment whose outcome we cannot predict. With this definition it does not matter whether we could do so in principle. The important feature is that we cannot predict the outcome of the experiment in practice. An example of a random experiment is rolling a fair dice.

A random experiment has a result or outcome [2]. We shall call any possible outcome of a random experiment an elementary event. The set of all elementary events is the certain event $\mathbb{E}$. In our example of rolling a fair dice the elementary events are 1, 2, 3, 4, 5, 6, and the certain event is the set $\mathbb{E} = \{1, 2, 3, 4, 5, 6\}$ [2].

From set theory [2] we can combine elementary events to new events. For instance, the union $\mathbb{A} \cup \mathbb{B}$ of events $\mathbb{A}$ and $\mathbb{B}$ means that the events $\mathbb{A}$ or $\mathbb{B}$ or both occur. In contrast, the cut of $\mathbb{A}$ and $\mathbb{B}$ is $\mathbb{A} \cap \mathbb{B}$ and denotes the event

that both $\mathbb{A}$ and $\mathbb{B}$ occur. We also define the complementary event $\bar{\mathbb{A}}$ to the event $\mathbb{A}$ such that $\bar{\mathbb{A}} \cup \mathbb{A} = \mathbb{E}$. As a special case, the complementary event to the certain event $\mathbb{E}$ is the impossible event $\oslash = \bar{\mathbb{E}}$.

We now associate a number $w(\mathbb{A})$ with the event $\mathbb{A}$ and call it the probability that the event $\mathbb{A}$ is observed in a random experiment. Probabilities obey the following axioms [2]:

1. Every event $\mathbb{A}$ has a probability $0 \leq w(\mathbb{A}) \leq 1$.

2. The certain event $\mathbb{E}$ has probability $w(\mathbb{E}) = 1$.

3. If two events $\mathbb{A}$ and $\mathbb{B}$ are mutually exclusive, that is if $\mathbb{A} \cap \mathbb{B} = \oslash$, then $w(\mathbb{A} \cup \mathbb{B}) = w(\mathbb{A}) + w(\mathbb{B})$; in words, the probability of observing $\mathbb{A}$ or $\mathbb{B}$ is the sum of probabilities $w(\mathbb{A})$ and $w(\mathbb{B})$ if the cut of $\mathbb{A}$ and $\mathbb{B}$ is the empty set $\oslash$.

A.2 Random variables and probability functions

Having introduced the concepts of random experiments and probability above, we now turn to random variables and probability functions. A random variable is a function that assigns a real number to every possible event. In other words, the outcome of a random experiment is transformed into a finite, real number [2].

Consequently, the probability $w(Y = y)$ of observing a given value y of the random variable Y equals the probability of observing the possible event associated with that particular value y. The set of all possible probabilities $w(Y = y)$ defines the probability distribution. The probability distribution function or distribution function characterizing the probability distribution is defined as the probability $W_Y(y) = w(Y \leq y)$ that the random variable Y assumes a value smaller than or equal to the real number y. From this definition we obtain the probability of observing the values $y_1 < y \leq y_2$ of the random variable Y [2]:

$$w(y_1 < Y \leq y_2) = w(Y \leq y_2) - w(Y \leq y_1) = W_Y(y_2) - W_Y(y_1). \qquad \text{(A.1)}$$

We distinguish between two kinds of random variables: discrete and continuous ones. Discrete random variables can take only particular values, often integers. The probability distribution function for a discrete random variable Y is given by [2]

$$W_Y(y) = \sum_{y_j \leq y} w(Y = y_j). \tag{A.2}$$

The sum of the probabilities of all events corresponds to the probability of the certain event [2]:

$$\sum_j w(Y = y_j) = 1. \tag{A.3}$$

On the other hand, continuous random variables can have any real number as their values. The probability distribution function $\Omega_Y(y)$ for a continuous random variable Y is defined as the integral over the corresponding probability density $\omega(Y)$ [2]:

$$\Omega_Y(u) = \int_{-\infty}^{u} \omega(y)\, dy. \tag{A.4}$$

We see that the probability density $\omega(Y)$ is normalized [2]:

$$\int_{-\infty}^{\infty} \omega(y)\, dy = 1. \tag{A.5}$$

At all points where the probability distribution function $\Omega_Y(y)$ is differentiable, we have for the probability density [2]

$$\omega(y) = \frac{d}{dy}\Omega_Y(y). \tag{A.6}$$

A.3 Conditional probability

The conditional probability of observing event $\mathbb{B}$ given that event $\mathbb{A}$ has already occurred is the probability of observing the events $\mathbb{A}$ and $\mathbb{B}$ divided

by the probability of observing $\mathbb{A}$ (if this probability does not vanish) [2]:

$$w(\mathbb{B}|\mathbb{A}) = \frac{w(\mathbb{B} \cap \mathbb{A})}{w(\mathbb{A})}. \tag{A.7}$$

Mutually exclusive events have no outcome of a random experiment in common. Because of $w(\mathbb{B} \cap \mathbb{A}) = 0$ we have [2]

$$w(\mathbb{B}|\mathbb{A}) = \frac{w(\mathbb{B} \cap \mathbb{A})}{w(\mathbb{A})} = 0. \tag{A.8}$$

Independent events are events that do not influence each other. For instance, when we roll a fair dice twice, the outcome of the first roll and that of the second are independent. For independent events the conditional probability becomes [2]

$$w(\mathbb{B}|\mathbb{A}) = \frac{w(\mathbb{B} \cap \mathbb{A})}{w(\mathbb{A})} = \frac{w(\mathbb{B})w(\mathbb{A})}{w(\mathbb{A})} = w(\mathbb{B}). \tag{A.9}$$

Appendix B

Expectation values, moments and cumulants

The present appendix defines expectation values of a function of a random variable as well as moments and cumulant-generating functions of a probability distribution. We shall discuss continuous random variables first and turn to discrete random variables in the following. In section B.3 the cumulant expansion of a Gaussian probability density is derived. Our presentation follows references [2, 137].

B.1 Continuous random variables

We consider a continuous random variable Y and its probability density $\omega(Y)$. Then, the expectation value of a function $f(Y)$ of the random variable Y is given by [2]

$$\langle f(Y) \rangle = \int f(y)\, \omega(y)\, dy. \tag{B.1}$$

For the special choice $f(Y) = Y^k$ with $k = 0, 1, 2, \ldots$ the raw moments $\mu_k^{(r)}$ of the probability density are obtained [137]:

$$\mu_k^{(r)} = \left\langle Y^k \right\rangle = \int y^k\, \omega(y)\, dy. \tag{B.2}$$

Most important for the present document are the cases $k = 0$ and $k = 1$. The case $k = 0$ corresponds to the normalization of the probability density [2]:

$$\mu_0^{(r)} = \int \omega(y)\, dy = 1. \tag{B.3}$$

The population mean is obtained for $k = 1$ [2]:

$$\mu_1^{(r)} = \int y\, \omega(y)\, dy. \tag{B.4}$$

Contrary to raw moments, central moments $\mu_k^{(c)}$ are expectation values around the arithmetic mean $\mu_1^{(r)}$ [137]:

$$\mu_k^{(c)} = \left\langle \left(Y - \mu_1^{(r)} \right)^k \right\rangle = \int \left(y - \mu_1^{(r)} \right)^k \omega(y)\, dy. \tag{B.5}$$

In particular, the variance σ^2 is defined as the second central moment [137]:

$$\sigma^2 = \mu_2^{(c)} = \mu_2^{(r)} - \left(\mu_1^{(r)} \right)^2 = \langle Y^2 \rangle - \langle Y \rangle^2. \tag{B.6}$$

Having introduced expectation values and moments above, we now turn to moment-generating functions and cumulants. The moment-generating function $\mathbb{M}(u)$ of a continuous random variable Y is defined as [137]

$$\mathbb{M}(u) = \left\langle e^{u\,Y} \right\rangle = \int e^{u\,y}\, \omega(y)\, dy. \tag{B.7}$$

To see why $\mathbb{M}(u)$ is called moment-generating function, we consider the kth derivative with respect to u [137]:

$$\frac{d^{(k)}\mathbb{M}(u)}{du^{(k)}} = \left\langle Y^k\, e^{u\,Y} \right\rangle = \int y^k\, e^{u\,y}\, \omega(y)\, dy. \tag{B.8}$$

For $u = 0$ this reduces to the raw moments given by equation (B.2).

For the present work it is more convenient to employ cumulant-generating

functions $\mathbb{K}(u)$. They are related to moment-generating functions by [137]

$$\mathbb{K}(u) = ln\,\mathbb{M}(u) = ln\,\left\langle e^{u\,Y}\right\rangle = ln\int e^{u\,y}\,\omega(y)\,dy. \tag{B.9}$$

The kth cumulant κ_k^c is given by the kth derivative with respect to u at $u = 0$ [137]:

$$\kappa_k^c = \langle Y^k\rangle_c = \left.\frac{d^k\,\mathbb{K}(u)}{du^k}\right|_{u=0}. \tag{B.10}$$

In particular, the first two cumulants equal the population mean $\kappa_1^c = \mu_1^{(r)}$ and variance $\kappa_2^c = \sigma^2$ [137]. To show this, the first two derivatives of the cumulant-generating function $\mathbb{K}(u)$ are expressed in terms of the moment-generating functions and their derivatives [137]:

$$\frac{d\mathbb{K}(u)}{du} = \frac{d\,ln\,\mathbb{M}(u)}{du} = \frac{\mathbb{M}'(u)}{\mathbb{M}(u)}; \tag{B.11}$$

$$\frac{d^2\mathbb{K}(u)}{du^2} = \frac{d}{du}\left(\frac{\mathbb{M}'(u)}{\mathbb{M}(u)}\right) = \frac{\left(\mathbb{M}''(u)\right)\left(\mathbb{M}(u)\right) - \left(\mathbb{M}'(u)\right)^2}{\left(\mathbb{M}(u)\right)^2}. \tag{B.12}$$

Using equation (B.8) and setting u to zero for equations (B.11) and (B.12) establishes the first and second cumulants [137].

B.2 Discrete random variables

In this seciton we consider a discrete random variable Y with associated probability distribution function $W(Y \leq y)$. Furthermore, the probability that the random variable takes the value $Y = y_j$ is denoted by $w(Y = y_j) = w(y_j)$. The expectation value of a function $f(Y)$ of the random variable Y is given by [2]

$$\langle f(Y)\rangle = \sum_j w(y_j)\,f(y_j). \tag{B.13}$$

The special choice $f(Y) = Y^k$ with $k = 0, 1, 2, \ldots$ yields the raw moments

of the probability distribution function [137]:

$$\mu_k^{(r)} = \langle Y^k \rangle = \sum_j w(y_j)\, y_j^k. \tag{B.14}$$

As in the case of continuous random variables, the cases $k = 0$ and $k = 1$ correspond to the normalization of the probability distribution function and the expected value of the random variable Y.

For the central moments $\mu_k^{(c)}$ around the mean $\mu_1^{(r)}$ we find [137]

$$\mu_k^{(c)} = \left\langle \left(Y - \mu_1^{(r)}\right)^k \right\rangle = \sum_j w(y_j)\, \left(y_j - \mu_1^{(r)}\right)^k. \tag{B.15}$$

The first non-vanishing central moment defines the variance σ^2 [137]:

$$\begin{aligned}\sigma^2 = \mu_2^{(c)} &= \left\langle \left(Y - \mu_1^{(r)}\right)^2 \right\rangle = \mu_2^{(r)} - \left(\mu_1^{(r)}\right)^2 = \sum_j w(y_j)\, \left(y_j - \mu_1^{(r)}\right)^2 \\ &= \sum_j w(y_j)\, y_j^2 - \left(\sum_{y_j} w(y_j) y_j\right)^2 . \end{aligned} \tag{B.16}$$

B.3 Gaussian probability density and cumulants

The relations introduced above hold for arbitrary probability densities. Here, the important special case of a Gaussian probability density will be considered. Most notably, it is shown that all cumulants beyond the second vanish for a Gaussian probability density of a random variable Y with mean $\mu_1^{(r)}$ and variance σ^2 [137]:

$$\omega(Y) = \frac{1}{\sqrt{2\pi\,\sigma^2}} e^{-\frac{\left(Y-\mu_1^{(r)}\right)^2}{2\sigma^2}}. \tag{B.17}$$

Evaluating the cumulant-generating function by substituting (B.17) into (B.9) yields [137]

$$
\begin{aligned}
\mathbb{K}(u) &= ln \int e^{u\,y}\,\omega(y)\,dy \\
&= ln \int e^{u\,y}\,\frac{1}{\sqrt{2\pi\,\sigma^2}} e^{-\frac{\left(y-\mu_1^{(r)}\right)^2}{2\sigma^2}}\,dy \\
&= ln \int \frac{1}{\sqrt{2\pi\,\sigma^2}} e^{-\frac{\left(y-\mu_1^{(r)}\right)^2-2\sigma^2 uy}{2\sigma^2}}\,dy \\
&= ln \int \frac{1}{\sqrt{2\pi\,\sigma^2}} e^{-\frac{\left(y-\left(\mu_1^{(r)}+\sigma^2 u\right)\right)^2+\left(\mu_1^{(r)}\right)^2-\left(\mu_1^{(r)}+\sigma^2 u\right)^2}{2\sigma^2}}\,dy \\
&= ln \int \frac{1}{\sqrt{2\pi\,\sigma^2}} e^{-\frac{\left(y-\left(\mu_1^{(r)}+\sigma^2 u\right)\right)^2}{2\sigma^2}} e^{\mu_1^{(r)}u+\frac{1}{2}\sigma^2 u^2}\,dy \\
&= \mu_1^{(r)}\,u + \frac{1}{2}\sigma^2\,u^2. \qquad \text{(B.18)}
\end{aligned}
$$

Proceeding from the third to the fourth line involves completing the square in the argument of the exponential. To reach the last line, we note that the second exponential in the integrand does not depend on Y and can be taken out of the integral. The remaining integral evaluates to unity since the first exponential is a Gaussian with a different mean, but with the same variance as the original one. It is seen from equation (B.18) that the cumulant-generating function of a Gaussian probability distribution is a parabola in u. Consequently, the third and higher derivatives with respect to u vanish, and so do the third and higher cumulants [137].

Appendix C

Mathematical relations

In this appendix we present mathematical relations used in this work. Importantly, our discussion is operational and not mathematically rigorous. It merely serves as an internal reference.

C.1 Simpson's rule

Given a function $f(y)$, the integral over the range $y_b - y_a$ can be approximated by means of Simpson's rule [2]:

$$\int_{y_a}^{y_b} f(u)\,du \approx \frac{\Delta y}{3}\left(f(y_a) + 4\,f\left(\frac{y_a + y_b}{2}\right) + f(y_b)\right). \tag{C.1}$$

Above, $\Delta y = \frac{y_b - y_a}{2}$ divides the range $y_b - y_a$ into two equal segments.

An extended version of Simpson's rule imposes an odd number $\mathcal{N}_d$ of y-values to approximate the integral over the function $f(y)$ [2, 66]:

$$\int_{y_a}^{y_b} f(u)\,du \approx \frac{\Delta y}{3}\sum_{j=1}^{\mathcal{N}_d} \mathcal{C}_j f(y_j). \tag{C.2}$$

Here, the function values are equidistant, and the separation is $\Delta y = \frac{y_b - y_a}{\mathcal{N}_d - 1}$. The coefficients $\mathcal{C}_j$ assume the values 4 for even j, 2 for odd j, and 1 for the first and last coefficients [66].

C.2 δ-distribution

Following reference [2], we present an operational definition and selected properties of the δ-distribution. The δ-distribution is a linear functional acting on test functions $f(y)$. A function associates a number with a number, whereas a functional $\Phi(f)$ assigns a number to a function f. Given the constants $\mathcal{C}_j$ and test functions $f_j(y)$ with $j = 1, 2$, a linear functional has the following property [2]:

$$\Phi[\mathcal{C}_1 f_1(y) + \mathcal{C}_2 f_2(y)] = \mathcal{C}_1 \Phi[f_1(y)] + \mathcal{C}_2 \Phi[f_2(y)]. \tag{C.3}$$

The δ-distribution is defined as [2, 170]

$$\int_{u_a}^{u_b} f(y)\, \delta(y - y_0)\, dy = \begin{cases} f(y_0) & \text{for } u_a < y_0 < u_b; \\ 0 & \text{otherwise.} \end{cases} \tag{C.4}$$

Its domain of definition is that of the test function $f(y)$.

Derivatives of the δ-distribution are given by [2]

$$\int_{u_a}^{u_b} f(y)\, \delta^{(n)}(y - y_0)\, dy = \begin{cases} (-1)^n f^{(n)}(y_0) & \text{for } u_a < y_0 < u_b; \\ 0 & \text{otherwise.} \end{cases} \tag{C.5}$$

If the argument of the δ-distribution is a function $f(y)$, we have [2]

$$\int_{-\infty}^{\infty} \delta\left(f(y)\right)\, dy = \int_{-\infty}^{\infty} \sum_{y_j : f(y_j)=0} \frac{\delta(y - y_j)}{\left|\frac{\partial f}{\partial y}|_{y_j}\right|}\, dy. \tag{C.6}$$

The sum is over all roots of the function $f(y)$.

The δ-distribution can also be represented as a Fourier transform [170]:

$$\delta(y - y_0) = \frac{1}{2\pi} \int_{-\infty}^{\infty} e^{\imath u (y - y_0)}\, du. \tag{C.7}$$

C.3 Γ-function, hypersphere and canonical kinetic energy distribution

The Γ-function is defined as [2, 170, 234]

$$\begin{aligned}\Gamma(n) &= \int_0^\infty e^{-y} y^{n-1} dy \\ &= 2\int_0^\infty e^{-y^2} y^{2n-1} dy. \end{aligned} \tag{C.8}$$

According to reference [234], we can define an n-sphere or hypersphere of radius $\mathbb{R}$ as the set of n-tuples satisfying

$$\sum_{j=1}^{n} y_j^2 = \mathbb{R}^2. \tag{C.9}$$

In particular, for a hypersphere of unit radius, the following relation holds [234]:

$$\begin{aligned}\int_{-\infty}^{\infty} e^{-\sum_{j=1}^{n} y_j^2} dy_1 \cdots dy_n &= \left(\int_{-\infty}^{\infty} e^{-y^2} dy\right)^n \\ &= \mathbb{S}_n \int_0^\infty e^{-y^2} y^{n-1} dy \\ &= \frac{1}{2}\mathbb{S}_n \int_0^\infty e^{-y} y^{\frac{n}{2}-1} dy. \end{aligned} \tag{C.10}$$

Above, $\mathbb{S}_n$ denotes the hypersurface area of an n-sphere with unit radius.

The properties of the hypersphere will be used below to rationalize the Boltzmann distribution of the kinetic energy in a many-particle system. Specifically, the Maxwell-Boltzmann distribution of Cartesian momenta in the canonical ensemble is normalized (with $\beta^{-1} = k_B T$):

$$\int_{-\infty}^{\infty} e^{-\beta \sum_{j=1}^{\mathcal{N}_f} \frac{p_{C,j}^2}{2m_j}} \prod_{j=1}^{\mathcal{N}_f} \left(\sqrt{\frac{\beta}{2\pi m_j}}\right) dp_{C,1} \cdots dp_{C,\mathcal{N}_f} = 1. \tag{C.11}$$

The masses m_j are eliminated from equation (C.11) with the following change

of variables:

$$p_{C,j}^{(m)} = p_{C,j}\sqrt{\frac{\beta}{2\,m_j}}. \tag{C.12}$$

Then, equation (C.11) is proportional to equation (C.10). In particular, if we identify the y_j of (C.10) with the $p_{C,j}^{(m)}$ of (C.12) and replace y in the last line of equation (C.10) by βK, we obtain the kinetic energy distribution in the canonical ensemble for a system with $\mathcal{N}_f$ degrees of freedom to within a constant $\mathcal{C}$ [141]:

$$\mathcal{C}\int_0^\infty e^{-\beta K}\,K^{\frac{\mathcal{N}_f}{2}-1}\,dK = 1. \tag{C.13}$$

Appendix D

Statistical mechanics

This appendix introduces some of the basic results of statistical mechanics. These results are well-known and stated here for reference, but no attempt is made to derive these relationships. Our presentation is inspired by the following textbooks [33, 72, 113].

D.1 Fundamentals

Statistical mechanics deals with how macroscopic observables can be obtained from microscopic properties [113]. Suppose we know the properties of microscopic particles, how they interact and evolve in time. We then ask how a macroscopically large number of particles behaves on average [72].

To evaluate the average of any dynamical variable, two ingredients are needed. First, we need to know the possible values of the dynamical variable under consideration. Second, the probability is required for the system to have a given value of the dynamical variable. In mathematical terms, the average $\mathcal{A}_{obs}$ of a macroscopic observable $\mathcal{A}$ is [72]

$$\mathcal{A}_{obs} = \langle \mathcal{A} \rangle = \sum_j w_j \, \mathcal{A}_j. \tag{D.1}$$

The sum in equation (D.1) is over all possible microstates j of the system, which are characterized by their microscopic mechanical properties, whether

quantum or classical. A dynamical variable $\mathcal{A}$ is a quantity that depends on the microstate of the system and fluctuates as the system evolves. The possible values $\mathcal{A}_j$ of the dynamical variable can be evaluated, in principle, from quantum or classical mechanics. To determine the probability w_j of finding a system in a given microstate j is the role of statistical mechanics.

The weight w_j depends on the ensemble under consideration. An ensemble is characterized by all possible microstates that fulfill the constraints imposed upon the system. The constraints are external control parameters that we have at our disposal to describe the system macroscopically [72, 113].

From quantum and classical mechanics we know that the time evolution of a microscopic system is deterministic if its initial state is completely specified [33, 72]. In the quantum case, the time evolution is governed by Schrödinger's equation [235]; Newton's equations of motion determine the future dynamics of a classical system [33]. Given the deterministic dynamics, one may ask why we need any statistical tool.

The reason for employing statistical methods lies in our incapacity to know or control the microstate of a system completely when the number of particles becomes macroscopically large [113]. Even for small systems Heisenberg's uncertainty principle prevents us from determining arbitrary observables simultaneously in principle [113]. In addition, perturbations are ubiquitous so that dynamical properties fluctuate. Although the system's time evolution is still deterministic, our *description* of the system's dynamics contains randomness because we cannot even characterize the initial state exactly [33]. This randomness allows us to treat dynamical variables as random variables. Despite that randomness, it is assumed that our description of the system's microstate is representative or close to any relevant physical state of the system [106]. Consequently, we believe that the average behaviour of the system under consideration can be described accurately if sufficient representative microstates enter the ensemble average (D.1).

According to the *ergodic hypothesis*, the time average of a dynamical variable approaches the ensemble average in equation (D.1) for long times [72, 113]. Another way of describing ergodicity is that the system approaches every possible microstate arbitrarily closely for long trajectories. This means

that there are two ways of estimating the average behaviour of a macroscopic system. On the one hand, we can observe a system for a long time and measure the dynamical variable of interest at various times. Alternatively, we can determine the instantaneous state of a large number of subsystems simultaneously, thus obtaining an ensemble average.

For any prediction to be accurate the individual measurements should be independent. This will be the case if they are separated by times longer than the relaxation time of the system in the case of the time average. Similarly, the (macroscopic) subsystems must be larger than the correlation length for their averages to approach the ensemble average [72].

Until now, we have not specified the nature of microstates. Consequently, we briefly describe what is meant by this expression. In the quantum case, a microstate is a pure quantum-mechanical state characterized by the linear combination of any complete set of basis functions in Hilbert space [235]. In the classical world, the microstate of a system is characterized by all positions and momenta of all particles. The system's microstate is a point in phase space, which is spanned by all possible values of positions and momenta of all particles [113]. This results in $6\,N$ dimensions, where N is the number of particles. The factor 6 arises from the possible variation of the components of the Cartesian coordinates and momenta for each particle.

D.2 Ensembles

Having set the scene of the general role of statistical mechanics, we now proceed to introduce some useful and fundamental relationships. As announced above, statistical mechanics provides the probability functions for observing microstates according to the ensemble under consideration. As we will be concerned with the microcanonical and canonical ensembles in this work, we shall restrict our attention to these cases.

First, we consider the microcanonical ensemble, which is characterized by constant volume $\mathcal{V}$, fixed particle number N and constant energy E [72, 113]. According to the fundamental assumption of statistical mechanics, all microstates of an isolated system in thermodynamical equilibrium (microcanon-

ical ensemble) are equally likely [72, 113]. The probability of finding the system in any microstate is the inverse of the microcanonical partition function $\Xi_{N\mathcal{V}E}$, which counts all microstates consistent with the constraints of the ensemble. For an isolated system the number of microstates is related to the entropy [113]:

$$S = k_B \, ln \, \Xi_{N\mathcal{V}E}. \tag{D.2}$$

Next, we turn to the canonical ensemble in which the particle number N, the volume $\mathcal{V}$ and the temperature T are imposed upon the system. The probability of finding a system in quantum state j with energy eigenvalue E_j is [72]

$$w_j = \frac{e^{-\beta E_j}}{\sum_j e^{-\beta E_j}}. \tag{D.3}$$

For a classical phase space point $\boldsymbol{\xi} = \{r_{C,1}, \ldots, r_{C,3N}, p_{C,1}, \ldots, p_{C,3N}\}$ the corresponding expression is given by [72]

$$\rho(\boldsymbol{\xi}) = \frac{e^{-\beta \mathcal{H}(\boldsymbol{\xi})}}{\int e^{-\beta \mathcal{H}(\boldsymbol{\xi})} d\boldsymbol{\xi}}. \tag{D.4}$$

The integral is over phase space, and $\beta^{-1} = k_B T$, where T denotes the absolute temperature and k_B the Boltzmann constant. Furthermore, $\mathcal{H}$ is the classical Hamiltonian.

From the above equations we see that different microstates have different probabilities in the canonical ensemble. Hence, the partition function in the canonical ensemble is defined as a weighted counting of all microstates consistent with the constraints of fixed particle number, volume and temperature. The quantum partition function reads [113]

$$Q = \sum_j e^{-\beta E_j}. \tag{D.5}$$

Similarly, the classical limit in three physical dimensions yields equation (D.6) [113]:

$$Q = \frac{1}{N! h^{3N}} \int e^{-\beta \mathcal{H}(\boldsymbol{\xi})} d\boldsymbol{\xi}. \tag{D.6}$$

Here, h denotes Planck's constant, and h^{3N} is a measure of the phase space volume occupied by a microstate [106]. The central quantity in the canonical ensemble is the Helmholtz free energy. For instance, it determines whether a system is in equilibrium or how much reversible work is needed for a particular chemical transformation. The Helmholtz free energy F is defined as [33, 72]

$$F = -k_B\, T\, ln\, Q. \tag{D.7}$$

We see that the partition function and the Helmholtz free energy are related to the volume of phase space. Such quantities are referred to as thermal quantities [106].

We now turn to averages of a dynamical variable $\mathcal{A}$ in the canonical ensemble. With the quantum (D.3) and classical (D.4) probability functions we obtain the following expressions for the quantum and classical canonical ensemble averages [72]:

$$\langle \mathcal{A} \rangle = \sum_j w_j\, \mathcal{A}_j = \frac{\sum_j e^{-\beta E_j} \mathcal{A}_j}{\sum_j e^{-\beta E_j}}; \tag{D.8}$$

$$\langle \mathcal{A} \rangle = \int \mathcal{A}(\boldsymbol{\xi})\, \rho(\boldsymbol{\xi})\, d\boldsymbol{\xi} = \frac{\int e^{-\beta \mathcal{H}(\boldsymbol{\xi})}\, \mathcal{A}(\boldsymbol{\xi})\, d\boldsymbol{\xi}}{\int e^{-\beta \mathcal{H}(\boldsymbol{\xi})}\, d\boldsymbol{\xi}}. \tag{D.9}$$

The quantum ensemble average can also be computed via the trace of the product formed by the operator associated with the observable of interest and the density operator $\hat{\rho}$. The trace is the sum of all diagonal elements of a matrix representing an operator. It is invariant under basis transformations and thus does not depend on the representation chosen [170]. The density operator for a statistical mixture of pure quantum states $|\Psi_k\rangle$ occurring with probability w_k is [235]

$$\hat{\rho} = \sum_k w_k \hat{\rho}_k = \sum_k w_k |\Psi_k\rangle\langle\Psi_k|, \tag{D.10}$$

where $|\Psi_k\rangle\langle\Psi_k|$ is the projection operator onto the pure state $|\Psi_k\rangle$. Conse-

quently, the expectation value of the observable $\mathcal{A}$ is [33, 113, 235]

$$\begin{aligned}\langle\mathcal{A}\rangle &= Tr(\hat{\rho}\mathcal{A}) = \sum_j \langle j|\hat{\rho}\mathcal{A}|j\rangle \\ &= \sum_{j,k} \langle j|w_k|\Psi_k\rangle\langle\Psi_k|\mathcal{A}|j\rangle = \sum_{j,k} w_k\langle\Psi_k|\mathcal{A}|j\rangle\langle j|\Psi_k\rangle \\ &= \sum_k w_k\langle\Psi_k|\mathcal{A}|\Psi_k\rangle = \sum_k w_k\langle\mathcal{A}\rangle_k. \end{aligned} \tag{D.11}$$

We see from equation (D.11) that the trace operation is equivalent to performing a weighted sum over expectation values $\langle\mathcal{A}\rangle_k$ arising from individual pure states for a given observable. In the last line, we have used the closure relation of the complete set of functions $\{|j\rangle\}$ [235]:

$$I = \sum_j |j\rangle\langle j|. \tag{D.12}$$

D.3 Restricted phase space functions

The partition function provides the entire information of a system characterized by external control parameters. Equivalently, it describes the complete phase space accessible to the system. However, it does not allow for the distinction of different regions in phase space such as chemical composition or native contacts of a protein. To distinguish regions of phase space, we need internal constraints. Formally, internal constraints are introduced by means of an order parameter $x^{'}(\boldsymbol{\xi})$, restricted to a particular value $x^{'}(\boldsymbol{\xi}) = x$ by means of a δ-distribution [68]. The restricted partition function then reads [161]

$$Q(x) = \frac{1}{N!h^{3N}} \int \delta\left(x^{'}(\boldsymbol{\xi}) - x\right) e^{-\beta\mathcal{H}(\boldsymbol{\xi})}\, d\boldsymbol{\xi}. \tag{D.13}$$

Equation (D.13) comprises all microstates consistent with the external constraints of the ensemble and with the internal constraint, namely those phase space points for which the order parameter has the value x. The unrestricted

partition function is recovered by integrating the restricted ones over the order parameter [33]:

$$Q = \int Q(x)\, dx. \tag{D.14}$$

As seen above, the unrestricted partition function is associated with the Helmholtz free energy. Similarly, we use the restricted partition function to define the Landau free energy [68], also called the free energy profile or the potential of mean force:[20]

$$\begin{aligned} F(x) &= -k_B T\, ln\, Q(x) \\ &= -k_B T\, ln\, \frac{1}{N! h^{3N}} \int \delta(x^{'}(\boldsymbol{\xi}) - x)\, e^{-\beta \mathcal{H}(\boldsymbol{\xi})}\, d\boldsymbol{\xi}. \end{aligned} \tag{D.15}$$

An equivalent expression, often encountered in the literature, uses the restricted phase space density $\rho(x) = \frac{Q(x)}{Q}$ of observing a given value of the order parameter to write the potential of mean force as [33, 68, 118]

$$\begin{aligned} F(x) &= F - k_B T\, ln\, \rho(x) = F - k_B T\, ln\, \frac{Q(x)}{Q} \\ &= F - k_B T\, ln\, \frac{\int \delta(x^{'}(\boldsymbol{\xi}) - x)\, e^{-\beta \mathcal{H}(\boldsymbol{\xi})}\, d\boldsymbol{\xi}}{\int e^{-\beta \mathcal{H}(\boldsymbol{\xi})}\, d\boldsymbol{\xi}} \\ &= F - k_B T\, ln\, \langle \delta(x^{'}(\boldsymbol{\xi}) - x) \rangle. \end{aligned} \tag{D.16}$$

D.4 Validity of classical limit

Above, statistical mechanical results most relevant to the present work have been described. We focused on equilibrium classical statistical mechanics because this framework is used in the vast majority of expressions encountered. We close the discussion recalling under what circumstances classical statistical mechanics is valid.

[20] In principle, a factor with the dimension of x should multiply the restricted partition function $Q(x)$ to render the argument of the logarithm dimensionless. For notational brevity it is omitted here and throughout this document.

Classical statistical mechanics is a good approximation if the particles involved are sufficiently heavy and the temperature sufficiently high. As a rule of thumb, particles heavier than Helium at temperatures above 4 K can be treated classically. In that case, the thermal wavelength $\Lambda = \sqrt{\frac{h^2}{2\pi\, m\, k_B T}}$, indicating the spread of the quantum wavepacket, is smaller than atomic dimensions so that quantum interference effects become negligible [113]. If the hydrogen atoms are considered to be part of a larger compound, namely a rigid water molecule carrying a dipole moment, the mass of the water molecules and room temperature ensure that classical statistical mechanics is reasonably accurate for the phenomena treated in this document.

Appendix E

Linear response theory

Equilibrium statistical mechanics provides a general description for time-independent, reversible equilibrium properties. For time-dependent, irreversible non-equilibrium processes no such general theory exists [33, 72]. The reason for this is as follows. There is a unique equilibrium state for a system subject to external constraints, whereas a system can deviate from equilibrium in many different ways [148]. As a result, the description of the non-equilibrium state will depend on the specific process investigated.

However, if the system is close to equilibrium, the non-equilibrium properties of the system can be described by *linear response theory*. Linear response theory is a statistical-mechanical perturbation theory around equilibrium. Our short presentation of it in this appendix follows the lines of references [33, 72, 106] and will focus on classical linear response theory.

Before beginning the quantitative description, we shall specify what is meant by "weakly perturbed," "close to equilibrium" or "small deviations from equilibrium." A system is considered close to equilibrium if the perturbation is so small that an accurate description of the non-equilibrium behaviour is obtained by retaining only linear terms in the perturbative expansion. In other words, the deviations from equilibrium are linearly related to the disturbance driving the system away from equilibrium [72].

Below, we shall consider in turn the response of a system to a time-independent perturbation, the relaxation from a prepared non-equilibrium

state to the unperturbed equilibrium state and the general dynamic response to an arbitrary, small perturbation.

E.1 Static response

We consider an equilibrium system characterized by the Hamiltonian $\mathcal{H}$. The ensemble average of a dynamical variable $\mathcal{A}$ is given by [72]

$$\langle \mathcal{A} \rangle = \frac{\int \mathcal{A}(\boldsymbol{\xi}) e^{-\beta \mathcal{H}(\boldsymbol{\xi})} d\boldsymbol{\xi}}{\int e^{-\beta \mathcal{H}(\boldsymbol{\xi})} d\boldsymbol{\xi}}, \tag{E.1}$$

where $\boldsymbol{\xi}$ denotes a point in phase space and integration is carried out over the entire phase space.

Adding a perturbation $\mathcal{F}$ coupling to another dynamical variable $\mathcal{B}$ yields the Hamiltonian of the perturbed system $\mathcal{H}_p = \mathcal{H} + \Delta\,\mathcal{H} = \mathcal{H} - \mathcal{F}\,\mathcal{B}$. We now ask how the average value of the dynamical variable $\mathcal{A}$ is affected by the perturbation $\Delta\,\mathcal{H}$. Here we consider the system after it has relaxed to the perturbed Hamiltonian. In other words, we compare two equilibrium states; the first one is characterized by $\mathcal{H}$, and the second one by $\mathcal{H}_p$. To this end, we express the ensemble average of $\mathcal{A}$ governed by the Hamiltonian $\mathcal{H}_p$ in terms of ensemble averages governed by the unperturbed Hamiltonian $\mathcal{H}$. The exponential of the perturbed Hamiltonian $\mathcal{H}_p$ can be expanded around the unperturbed Hamiltonian $\mathcal{H}$ because the perturbation $\Delta\mathcal{H}$ is small: $e^{-\beta\mathcal{H}_p} = e^{-\beta\mathcal{H}} e^{-\beta\Delta\mathcal{H}} \approx e^{-\beta\mathcal{H}}(1-\beta\Delta\mathcal{H})$. Also, $(1-\beta\Delta\mathcal{H})^{-1} \approx 1+\beta\Delta\mathcal{H}$ for small $\Delta\mathcal{H}$ around $\Delta\mathcal{H} = 0$. We obtain [33, 72]

$$\begin{aligned}
\langle \mathcal{A} \rangle_p &= \frac{\int \mathcal{A}(\boldsymbol{\xi}) e^{-\beta \mathcal{H}_p(\boldsymbol{\xi})} d\boldsymbol{\xi}}{\int e^{-\beta \mathcal{H}_p(\boldsymbol{\xi})} d\boldsymbol{\xi}} \\
&= \frac{\int \mathcal{A}(\boldsymbol{\xi}) e^{-\beta \mathcal{H}(\boldsymbol{\xi})} (1-\beta\Delta\mathcal{H}) d\boldsymbol{\xi}}{\int e^{-\beta \mathcal{H}(\boldsymbol{\xi})} (1-\beta\Delta\mathcal{H}) d\boldsymbol{\xi}} + O\left[(\Delta\mathcal{H})^2\right] \\
&= \frac{\langle \mathcal{A} \rangle - \beta \langle \mathcal{A}\Delta\mathcal{H} \rangle}{1 - \beta\langle \Delta\mathcal{H} \rangle} + O\left[(\Delta\mathcal{H})^2\right] \\
&= \left(\langle \mathcal{A} \rangle - \beta\langle \mathcal{A}\Delta\mathcal{H} \rangle\right)\left(1 + \beta\langle \Delta\mathcal{H} \rangle\right) + O\left[(\Delta\mathcal{H})^2\right] \\
&= \langle \mathcal{A} \rangle - \beta\left(\langle \mathcal{A}\Delta\mathcal{H} \rangle - \langle \mathcal{A} \rangle\langle \Delta\mathcal{H} \rangle\right) + O\left[(\Delta\mathcal{H})^2\right].
\end{aligned} \tag{E.2}$$

To reach the third line from the second, we have divided the numerator and denominator by the phase space integral $\int e^{-\beta\mathcal{H}(\boldsymbol{\xi})}d\boldsymbol{\xi}$ to obtain averages characteristic of the unperturbed system.

Expressing the deviation in the averages of the dynamical variable $\mathcal{A}$ as $\mathcal{D}_p\langle\mathcal{A}\rangle = \langle\mathcal{A}\rangle_p - \langle\mathcal{A}\rangle$ and substituting $\Delta\mathcal{H} = -\mathcal{F}\mathcal{B}$ yields to first order in $\mathcal{F}$ [33, 72]

$$\begin{aligned}\mathcal{D}_p\langle\mathcal{A}\rangle &= \beta\,\mathcal{F}\left(\langle\mathcal{A}\mathcal{B}\rangle - \langle\mathcal{A}\rangle\langle\mathcal{B}\rangle\right)\\ &= \beta\,\mathcal{F}\,\langle\mathcal{D}\mathcal{A}\,\mathcal{D}\mathcal{B}\rangle. \end{aligned} \tag{E.3}$$

The last line of the above equation is obtained on noting that every dynamical variable $\mathcal{A}$ can be expressed as $\mathcal{A} = \langle\mathcal{A}\rangle + \mathcal{D}\mathcal{A}$ and on realizing that the fluctuations $\mathcal{D}\mathcal{A}$ vanish on average; namely, $\langle\mathcal{D}\mathcal{A}\rangle = 0$.

E.2 Relaxation

We now turn to the phenomenon of relaxation. Relaxation is the time-dependent evolution of a system from a non-equilibrium state towards equilibrium. Let the equilibrium state be characterized by the unperturbed Hamiltonian $\mathcal{H}$. As in the static response case, we consider a perturbation $\Delta\mathcal{H} = -\mathcal{F}\mathcal{B}$ driving the system from its original equilibrium state to a state characterized by the Hamiltonian $\mathcal{H}_p = \mathcal{H} + \Delta\mathcal{H}$. The equilibrium state with respect to the perturbed Hamiltonian corresponds to a non-equilibrium state with respect to the original, unperturbed Hamiltonian $\mathcal{H}$. We now ask how the system prepared in the non-equilibrium state characterized by $\mathcal{H}_p$ relaxes back to its equilibrium state when the static perturbation is suddenly turned off. We follow the time evolution of the dynamical variable $\mathcal{A}$ to monitor the relaxation [33, 72].

To quantify this process, we note that the initial non-equilibrium distribution with respect to $\mathcal{H}$ corresponds to the equilibrium distribution associated with $\mathcal{H}_p$, whereas the time evolution of the system is governed by the unperturbed Hamiltonian $\mathcal{H}$ [33, 72]. Denoting the non-equilibrium ensemble average of $\mathcal{A}$ by $\langle\mathcal{A}(t)\rangle_{ne}$ and performing similar mathematical operations as

in the static response case above, we obtain [33, 72]

$$\begin{aligned}\langle \mathcal{A}(t)\rangle_{ne} &= \frac{\int \mathcal{A}(\boldsymbol{\xi},t)e^{-\beta\mathcal{H}_p(\boldsymbol{\xi})}d\boldsymbol{\xi}}{\int e^{-\beta\mathcal{H}_p(\boldsymbol{\xi})}d\boldsymbol{\xi}} \\ &= \frac{\int \mathcal{A}(\boldsymbol{\xi},t)e^{-\beta\mathcal{H}(\boldsymbol{\xi})}(1-\beta\Delta\mathcal{H})d\boldsymbol{\xi}}{\int e^{-\beta\mathcal{H}(\boldsymbol{\xi})}(1-\beta\Delta\mathcal{H})d\boldsymbol{\xi}} + O\left[(\Delta\mathcal{H})^2\right] \\ &= \left(\langle\mathcal{A}(t)\rangle - \beta\langle\mathcal{A}(t)\Delta\mathcal{H}\rangle\right)\left(1+\beta\langle\Delta\mathcal{H}\rangle\right) + O\left[(\Delta\mathcal{H})^2\right] \\ &= \langle\mathcal{A}(t)\rangle - \beta\left(\langle\mathcal{A}(t)\Delta\mathcal{H}\rangle - \langle\mathcal{A}(t)\rangle\langle\Delta\mathcal{H}\rangle\right) + O\left[(\Delta\mathcal{H})^2\right]. \end{aligned} \tag{E.4}$$

As equilibrium averages are independent of reference time t, we have $\langle\mathcal{A}(t)\rangle = \langle\mathcal{A}\rangle$. Inserting the perturbing field $\mathcal{F}$ coupling to the dynamical variable $\mathcal{B}$ according to $\Delta\mathcal{H} = -\mathcal{F}\mathcal{B}$ yields the time-dependent relaxation $\mathcal{D}_{ne}\langle\mathcal{A}(t)\rangle = \langle\mathcal{A}(t)\rangle_{ne} - \langle\mathcal{A}\rangle$ [33, 72]:

$$\mathcal{D}_{ne}\langle\mathcal{A}(t)\rangle = \beta\,\mathcal{F}\,\langle\mathcal{D}\mathcal{A}(t)\mathcal{B}(0)\rangle. \tag{E.5}$$

In equation (E.5) the instantaneous fluctuations of the dynamical variables $\mathcal{A}$ and $\mathcal{B}$ are $\mathcal{D}\mathcal{A}(t) = \mathcal{A}(t) - \langle\mathcal{A}\rangle$ and $\mathcal{D}\mathcal{B}(0) = \mathcal{B}(0) - \langle\mathcal{B}\rangle$.

We see that the relaxation of a macroscopic non-equilibrium perturbation towards equilibrium occurs on the same timescale as the decay of correlations between microscopic spontaneous fluctuations in equilibrium [33, 72, 236]. In other words, for small deviations from equilibrium, one cannot distinguish whether the system has been prepared in a non-equilibrium state by an external perturbation or whether the system has undergone a spontaneous fluctuation. Equation (E.5) is known as the *fluctuation-dissipation theorem.* This theorem is a formal proof of Onsager's regression hypothesis [145, 147] and yields the remarkable result that relaxation is governed by equilibrium dynamics [72].

E.3 Dynamic response and response functions

In the discussion above we have restricted our attention to time-independent perturbations. We now turn to a time-dependent perturbation $\mathcal{F}(t)$ that

couples to the dynamical variable $\mathcal{B}$. In the linear regime the response of the system $\mathcal{D}_{ne}\langle\mathcal{A}(t;\mathcal{F})\rangle$ is linear in the disturbance $\mathcal{F}$ [72]:

$$\mathcal{D}_{ne}\langle\mathcal{A}(t;\alpha\mathcal{F})\rangle = \alpha\mathcal{D}_{ne}\langle\mathcal{A}(t;\mathcal{F})\rangle. \tag{E.6}$$

The most general linear relationship satisfying equation (E.6) is [33, 72, 106]

$$\mathcal{D}_{ne}\langle\mathcal{A}(t)\rangle = \int_{-\infty}^{\infty} \mathcal{F}\left(t^{'}\right)\chi\left(t,t^{'}\right)dt^{'}. \tag{E.7}$$

In equation (E.7) above the macroscopic non-equilibrium response of the system is written as an integral over the history of perturbations $\mathcal{F}$ and the *response function* χ, which has the following characteristics. Since the response function is a property of the equilibrium system, it does not depend on the time-dependent perturbation $\mathcal{F}$. In addition, the absolute time origin is not relevant for equilibrium systems so that χ is a function of the time difference $t - t^{'}$ between the response and the perturbation only [72, 106]:

$$\chi\left(t,t^{'}\right) = \chi\left(t-t^{'}\right). \tag{E.8}$$

Finally, the principle of causality demands that the response function vanishes before any disturbance is applied. This yields [72, 106]

$$\chi\left(t-t^{'}\right) = \begin{cases} 0 & \text{for } t \leq t^{'}; \\ \theta\left(t-t^{'}\right) & \text{for } t > t^{'}. \end{cases} \tag{E.9}$$

Above, $\theta(y)$ is the indicator function. In summary, the response function $\chi(t-t^{'})$ determines the response of the equilibrium system (in absence of any disturbance) at time t to a perturbation at an earlier time $t^{'}$.

As mentioned above, the response function is independent of the disturbance applied. As a consequence, we can choose any form of $\mathcal{F}$ to find the

general form of the response function. We choose [72]

$$\mathcal{F}\left(t^{'}\right) = \begin{cases} \mathcal{F} & \text{for } t^{'} < 0; \\ 0 & \text{for } t^{'} \geq 0. \end{cases} \tag{E.10}$$

Inserting (E.10) and the response function properties (E.8) and (E.9) into equation (E.7) yields [72]

$$\mathcal{D}_{ne}\langle \mathcal{A}(t)\rangle = \mathcal{F}\int_{-\infty}^{0} \chi\left(t - t^{'}\right) dt^{'}. \tag{E.11}$$

Changing variables to $t - t^{'}$, we obtain [72]

$$\mathcal{D}_{ne}\langle \mathcal{A}(t)\rangle = \mathcal{F}\int_{t}^{\infty} \chi\left(t^{'}\right) dt^{'}. \tag{E.12}$$

To proceed, we note that our choice of disturbance given by equation (E.10) coincides with that of the relaxation case studied in the previous section. In particular, the non-equilibrium state is prepared with the Hamiltonian $\mathcal{H} - \mathcal{F}\mathcal{B}$, the disturbance is turned off at $t = 0$, and the system relaxes back to equilibrium with dynamics governed by the unperturbed Hamiltonian $\mathcal{H}$. The relaxation dynamics is given by equation (E.5). Comparing this result to equation (E.12) above, we obtain [33, 236]

$$\int_{t}^{\infty} \chi(t^{'})dt^{'} = \beta\langle \mathcal{D}\mathcal{A}(t)\, \mathcal{D}\mathcal{B}(0)\rangle. \tag{E.13}$$

We take the time derivative using "Leibniz's rule" to obtain the response function (E.14) [33, 72, 106]:

$$\chi(t) = -\theta(t)\beta\langle \mathcal{D}\dot{\mathcal{A}}(t)\, \mathcal{D}\mathcal{B}(0)\rangle = \theta(t)\beta\langle \mathcal{D}\mathcal{A}(t)\mathcal{D}\dot{\mathcal{B}}(0)\rangle. \tag{E.14}$$

This completes our brief outline of linear response theory.

Appendix F

Time correlation functions

Time correlation functions are an important tool for investigating the dynamics of a system [33, 72]. They play a crucial role in linear response theory (see appendix E), which is employed to express rate constants. Our presentation of time correlation functions is guided by references [33, 72]. We shall restrict ourselves to stationary systems and classical mechanics because of their central importance to the present document.

In stationary systems all times are equivalent because macroscopic observables are time-independent. However, it is meaningful to consider the relation between a dynamical variable $\mathcal{A}(t_0)$ at time t_0 and another dynamical variable $\mathcal{B}(t_0+t)$ at time t_0+t on average. This is exactly the information contained in a time correlation function [33].

In the realm of classical mechanics the time evolution of a system in phase space can be described by Hamiltonian dynamics [165]. In particular, a dynamical variable $\mathcal{A}(t) = \mathcal{A}(\boldsymbol{\xi}(t)) = \mathcal{A}(\boldsymbol{\xi}; t)$ depends on time via the time evolution of the phase space variables $\boldsymbol{\xi}(t)$, which is determined by a given set of initial conditions $\boldsymbol{\xi}$. Averaging over initial conditions in phase space $\rho(\boldsymbol{\xi})$ then yields the time correlation function [33, 72]:

$$\begin{aligned} C_{AB}(t_0, t_0+t) &= \langle \mathcal{A}(t_0)\, \mathcal{B}(t_0+t) \rangle \\ &= \int \mathcal{A}\left(\boldsymbol{\xi}, t_0\right)\, \mathcal{B}\left(\boldsymbol{\xi}, t_0+t\right) \rho(\boldsymbol{\xi})\, d\boldsymbol{\xi}. \end{aligned} \tag{F.1}$$

Below, we introduce some properties of time correlation functions. First, the time origin is arbitrary because we consider stationary systems. Hence, only the time difference between observations is relevant $t = (t_0 + t) - t_0$ [33, 72]:

$$\begin{aligned} C_{AB}(t_0, t_0 + t) &= \langle \mathcal{A}(t_0)\, \mathcal{B}(t_0 + t) \rangle \\ &= \langle \mathcal{A}(-t)\, \mathcal{B}(0) \rangle \\ &= \langle \mathcal{A}(0)\, \mathcal{B}(t) \rangle = C_{AB}(t). \end{aligned} \tag{F.2}$$

Second, it follows from equation (F.2) that the time derivative of the time correlation function has the following property [33]:

$$\begin{aligned} \left\langle \mathcal{A}(0)\, \dot{\mathcal{B}}(t) \right\rangle &= \frac{d}{dt} C_{AB}(t) = \left\langle \mathcal{A}(0)\, \frac{d}{dt} \mathcal{B}(t) \right\rangle = \frac{d}{dt} \langle \mathcal{A}(0)\, \mathcal{B}(t) \rangle \\ &= \frac{d}{dt} \langle \mathcal{A}(-t)\, \mathcal{B}(0) \rangle = \left\langle \frac{d}{dt} \mathcal{A}(-t)\, \mathcal{B}(0) \right\rangle = - \left\langle \dot{\mathcal{A}}(-t)\, \mathcal{B}(0) \right\rangle \\ &= - \langle \dot{\mathcal{A}}(0)\, \mathcal{B}(t) \rangle. \end{aligned} \tag{F.3}$$

Third, if the dynamical variables are identical $\mathcal{A} = \mathcal{B}$, we have [33, 72]

$$\begin{aligned} C_{AA}(t) &= \langle \mathcal{A}(0)\, \mathcal{A}(t) \rangle \\ &= \langle \mathcal{A}(-t)\, \mathcal{A}(0) \rangle \\ &= \langle \mathcal{A}(0)\, \mathcal{A}(-t) \rangle \\ &= C_{AA}(-t). \end{aligned} \tag{F.4}$$

Above, the second line follows from a shift in time origin, and the third line is obtained by exchanging the order of the dynamical variables, which is permissible for classical systems [72].

The properties presented here are the most relevant for this work. As mentioned earlier, they are used in section 2.1 and in appendix E.

Appendix G

Non-Hamiltonian dynamics

The natural time evolution of a classical mechanical system is characterized by Hamilton's canonical equations of motion and generates the microcanonical ensemble [165]. We have seen in section 3.1 that the time evolution of a Hamiltonian system is generated by the Hamiltonian as a canonical transformation that is continuous in time. The consequences of such Hamiltonian dynamics include the conservation of an arbitrary phase space volume element and the Liouville theorem [165].

G.1 Phase space compressibility

In contrast, the generation of other ensembles from a single long trajectory requires non-Hamiltonian dynamics. In that case, the equations of motion are not canonical and cannot be derived from the Hamiltonian [106]. Furthermore, the symplectic condition does not hold in general, and the magnitude of a volume element in phase space is not conserved under dynamical propagation [106].

However, generalizations of the Hamiltonian formalism to non-Hamiltonian systems have been obtained, for example, in references [176, 177]. We shall follow the lines of these presentations to introduce some of the concepts used in non-Hamiltonian dynamics and their relation to classical statistical mechanics. To limit the scope of the present document, the reader is referred

to references [176, 177] for derivations of the relations presented.

As pointed out in reference [165], the time evolution of a system can be viewed as a continuous coordinate transformation. For any coordinate transformation ($\boldsymbol{\xi}_0 \rightarrow \boldsymbol{\xi}_t$) the volume element of the new coordinates $d\boldsymbol{\xi}_t$ is related to that of the old coordinates $d\boldsymbol{\xi}_0$ by the absolute value $|\mathcal{J}|$ of the determinant $\mathcal{J}(\boldsymbol{\xi}_t; \boldsymbol{\xi}_0)$ of the Jacobian matrix $\boldsymbol{\mathcal{J}}$, whose elements are $\mathcal{J}_{jk} = \frac{\partial \xi_t^j}{\partial \xi_0^k}$ [2, 176, 177]:

$$d\boldsymbol{\xi}_t = |\mathcal{J}(\boldsymbol{\xi}_t; \boldsymbol{\xi}_0)|\, d\boldsymbol{\xi}_0. \tag{G.1}$$

For Hamiltonian systems the absolute value of the Jacobian determinant is unity [165]. An equivalent way of expressing this property is to state that the phase space compressibility κ, given in equation (G.2) below, vanishes [106, 176, 177]:

$$\kappa(\boldsymbol{\xi}_t, t) = \nabla_{\boldsymbol{\xi}} \dot{\boldsymbol{\xi}}_t = \sum_j \frac{\partial \dot{\xi}_j}{\partial \xi_j}. \tag{G.2}$$

In contrast, the phase space compressibility does not generally vanish for non-Hamiltonian systems.

G.2 Generalized invariant measure

However, there exists an invariant measure under dynamical propagation in the case of non-Hamiltonian dynamics as well. It has been reported in reference [176] that the absolute value of the determinant of the Jacobian matrix equals the ratio of the metric determinant factors $\sqrt{g}$ [176, 177] of the old and new sets of coordinates:

$$\mathcal{J}(\boldsymbol{\xi}_t; \boldsymbol{\xi}_0) = \frac{\sqrt{g(\boldsymbol{\xi}_0)}}{\sqrt{g(\boldsymbol{\xi}_t)}}. \tag{G.3}$$

Using equation (G.3) and the time derivative of the Jacobian determinant and its inverse $\mathcal{J}^{-1}$ [176],

$$\frac{d\mathcal{J}(\boldsymbol{\xi}_t;\boldsymbol{\xi}_0)}{dt} = \mathcal{J}(\boldsymbol{\xi}_t;\boldsymbol{\xi}_0)\,\kappa(\boldsymbol{\xi}_t,t); \tag{G.4a}$$

$$\frac{d\mathcal{J}^{-1}(\boldsymbol{\xi}_0;\boldsymbol{\xi}_t)}{dt} = -\mathcal{J}^{-1}(\boldsymbol{\xi}_0;\boldsymbol{\xi}_t)\,\kappa(\boldsymbol{\xi}_t,t), \tag{G.4b}$$

it has been shown [176] that the generalized invariant measure under dynamical evolution for non-Hamiltonian systems is given by equation (G.5) below:

$$\sqrt{g(\boldsymbol{\xi}_0)}\,d\boldsymbol{\xi}_0 = \sqrt{g(\boldsymbol{\xi}_t)}\,d\boldsymbol{\xi}_t. \tag{G.5}$$

We note for reference that the metric determinant factor is related to the phase space compressibility (assumed here not to be explicitly time-dependent) as follows [176, 177]:

$$\mathcal{J}(\boldsymbol{\xi}_t;\boldsymbol{\xi}_0) = \frac{\sqrt{g(\boldsymbol{\xi}_0)}}{\sqrt{g(\boldsymbol{\xi}_t)}} = e^{\Upsilon(\boldsymbol{\xi}_t,t)-\Upsilon(\boldsymbol{\xi}_0,0)} = e^{\int_0^t \kappa(\boldsymbol{\xi}_u,u)du}. \tag{G.6}$$

The phase space compressibility is related to Υ by [176]

$$\kappa = \dot{\Upsilon}. \tag{G.7}$$

G.3 Generalized Liouville equation

Given the generalized invariant measure in equation (G.5) above, the following generalized version of the Liouville equation can be derived [176, 177]:

$$\frac{\partial(\rho\sqrt{g})}{\partial t} + \nabla_{\boldsymbol{\xi}}(\rho\sqrt{g}\dot{\boldsymbol{\xi}}) = 0. \tag{G.8}$$

We combine the generalized invariant measure (G.5) and the time derivative of the Jacobian determinant (G.4) to show that the phase space density ρ is

conserved for non-Hamiltonian systems:

$$\begin{aligned}\frac{\partial\left(\rho\sqrt{g}\right)}{\partial t}+\nabla_{\boldsymbol{\xi}}\left(\rho\sqrt{g}\dot{\boldsymbol{\xi}}\right)=&\sqrt{g}\left(\frac{\partial\rho}{\partial t}+\dot{\boldsymbol{\xi}}\nabla_{\boldsymbol{\xi}}\rho\right)\\&+\rho\left(\frac{\partial\sqrt{g}}{\partial t}+\dot{\boldsymbol{\xi}}\nabla_{\boldsymbol{\xi}}\sqrt{g}+\sqrt{g}\nabla_{\boldsymbol{\xi}}\dot{\boldsymbol{\xi}}\right)\\=&\sqrt{g}\left(\frac{d\rho}{dt}\right)+\rho\left(\frac{d\sqrt{g}}{dt}+\sqrt{g}\kappa\right)=0.\end{aligned}\tag{G.9}$$

According to reference [176], the time evolution of the metric factor reads

$$\frac{d\sqrt{g(\boldsymbol{\xi}_t)}}{dt}=-\sqrt{g(\boldsymbol{\xi}_t)}\,\kappa(\boldsymbol{\xi}_t,t).\tag{G.10}$$

We thus see that the second bracket on the right-hand side in the last line of equation (G.9) vanishes. Hence, the first bracket must also vanish. As a consequence, the phase space density is time-independent even if the system's motion is governed by non-Hamiltonian dynamics [176,177]. This result leads to the following expression for the ensemble average of any dynamical variable $\mathcal{A}$ [176, 177]:

$$\langle\mathcal{A}\rangle=\frac{\int\mathcal{A}(\boldsymbol{\xi})\rho(\boldsymbol{\xi})\sqrt{g(\boldsymbol{\xi})}\,d\boldsymbol{\xi}}{\int\rho(\boldsymbol{\xi})\sqrt{g(\boldsymbol{\xi})}\,d\boldsymbol{\xi}}.\tag{G.11}$$

G.4 Generalized distribution function

As discussed in reference [177], conservation laws restrict the system to explore a given subspace of phase space. If all conservation laws are identified by the set of conserved quantities $\{C_{c,k}\}$, the phase space available to the system can be specified by a generalized microcanonical-like partition function [177],

$$\Xi(\mathcal{C}_k)=\int\prod_k\delta(C_{c,k}(\boldsymbol{\xi})-\mathcal{C}_k)\sqrt{g(\boldsymbol{\xi})}\,d\boldsymbol{\xi},\tag{G.12}$$

where $\mathcal{C}_k$ denotes a set of constants. To obtain the correct phase space density, it is essential to specify all conservation laws [106, 177].

Following reference [177], we present a general procedure for obtaining the equilibrium phase space density describing a non-Hamiltonian system. First, all conservation quantities need to be identified so that the microcanonical-like partition function of equation (G.12) can be determined. Second, linearly dependent variables are eliminated using the equations of motion and the conservation laws. Third, the phase space compressibility κ is evaluated and used to obtain the phase space metric $\sqrt{g(\boldsymbol{\xi})}$ yielding the invariant measure $\sqrt{g(\boldsymbol{\xi})}\, d\boldsymbol{\xi}$. Fourth, we construct the generalized microcanonical partition function according to equation (G.12). If the system under consideration contains artificial coordinates that extend the size of the phase space, integration over these variables in equation (G.12) enables us to obtain the phase space density for the physical variables in the system.

In the present work the outline given in this appendix is used in section 3.1 to discuss molecular dynamics simulations in the canonical ensemble using the Nosé-Hoover thermostat.

Bibliography

[1] D. Meschede, *Gerthsen Physik*, Springer, Berlin, twenty-third edition, 2006.

[2] C. B. Lang and N. Pucker, *Mathematische Methoden in der Physik*, Elsevier Spektrum Akademischer Verlag, München, second edition, 2005.

[3] M. Matsumoto, S. Saito, and I. Ohmine, Nature **416**, 409 (2002).

[4] L. Vrbka and P. Jungwirth, J. Phys. Chem. B **110**, 18126 (2006).

[5] T. E. Graedel and R. P. Frankenthal, J. Electrochem. Soc. **137**, 2385 (1990).

[6] P. Refait, M. Abdelmoula, and J.-M. R. Génin, Corros. Sci. **40**, 1547 (1998).

[7] P. Karlson, *Kurzes Lehrbuch der Biochemie für Mediziner und Naturwissenschaftler*, Georg Thieme Verlag, Stuttgart, eleventh edition, 1980.

[8] J. P. Hosler, S. Ferguson-Miller, and D. A. Mills, Annu. Rev. Biochem. **75**, 165 (2006).

[9] D. Chandler, J. Chem. Phys. **68**, 2959 (1978).

[10] S. H. Northrup and J. T. Hynes, J. Chem. Phys. **73**, 2700 (1980).

[11] D. Chandler, J. Stat. Phys. **42**, 49 (1986).

[12] P. Hänggi, P. Talkner, and M. Borkovec, Rev. Mod. Phys. **62**, 251 (1990).

[13] E. Pollak and P. Talkner, Chaos **15**, 026116 (2005).

[14] R. D. Levine, *Molecular reaction dynamics*, Cambridge University Press, Cambridge, 2005.

[15] P. W. Atkins and J. de Paula, *Atkins' Physical Chemistry*, Oxford University Press, Oxford, ninth edition, 2009.

[16] T. W. Swaddle, Chem. Rev. **105**, 2573 (2005).

[17] J. E. Leffler, Science **117**, 340 (1953).

[18] G. S. Hammond, J. Am. Chem. Soc. **77**, 334 (1955).

[19] D. H. Paik, D.-S. Yang, I.-R. Lee, and A. H. Zewail, Angew. Chem. Int. Ed. **43**, 2830 (2004).

[20] E. Neria, S. Fischer, and M. Karplus, J. Chem. Phys. **105**, 1902 (1996).

[21] C. Dellago, P. G. Bolhuis, and P. Geissler, Adv. Chem. Phys. **123**, 1 (2002).

[22] G. Hummer, J. Chem. Phys. **120**, 516 (2004).

[23] P. G. Bolhuis, D. Chandler, C. Dellago, and P. L. Geissler, Annu. Rev. Phys. Chem. **53**, 291 (2002).

[24] W. H. Miller, N. C. Handy, and J. E. Adams, J. Chem. Phys. **72**, 99 (1980).

[25] W. J. Albery, Annu. Rev. Phys. Chem. **31**, 227 (1980).

[26] R. C. Patel and J. F. Endicott, J. Am. Chem. Soc. **90**, 6364 (1968).

[27] H. Eyring, J. Chem. Phys. **3**, 107 (1935).

[28] M. J. Weaver and E. L. Yee, Inorg. Chem. **19**, 1936 (1980).

[29] M. Strajbl, Y. Y. Sham, J. Villà, Z.-T. Chu, and A. Warshel, J. Phys. Chem. B **104**, 4578 (2000).

[30] R. A. Marcus, J. Chem. Phys. **43**, 679 (1965).

[31] M. D. Newton and N. Sutin, Annu. Rev. Phys. Chem. **35**, 437 (1984).

[32] R. A. Marcus and N. Sutin, Biochim. Biophys. Acta **811**, 265 (1985).

[33] A. Nitzan, *Chemical dynamics in condensed phases: relaxation, transfer, and reactions in condensed molecular systems*, Oxford University Press, Oxford, New York, 2006.

[34] R. Ayala and M. Sprik, J. Phys. Chem. B **112**, 257 (2008).

[35] R. A. Marcus, J. Chem. Phys. **24**, 966 (1956).

[36] R. A. Marcus, J. Chem. Phys. **26**, 867 (1957).

[37] R. A. Marcus, J. Chem. Phys. **26**, 872 (1957).

[38] R. A. Marcus, Discuss. Faraday Soc. **29**, 21 (1960).

[39] R. A. Marcus, J. Phys. Chem. **67**, 853 (1963).

[40] R. A. Marcus, J. Phys. Chem. **67**, 2889 (1963).

[41] R. A. Marcus, Annu. Rev. Phys. Chem. **15**, 155 (1964).

[42] R. A. Marcus, Rev. Mod. Phys. **65**, 599 (1993).

[43] A. Warshel, J. Phys. Chem. **86**, 2218 (1982).

[44] J.-K. Hwang and A. Warshel, J. Am. Chem. Soc. **109**, 715 (1987).

[45] R. A. Kuharski et al., J. Chem. Phys. **89**, 3248 (1988).

[46] E. A. Carter and J. T. Hynes, J. Phys. Chem. **93**, 2184 (1989).

[47] G. King and A. Warshel, J. Chem. Phys. **93**, 8682 (1990).

[48] H.-X. Zhou and A. Szabo, J. Chem. Phys. **103**, 3481 (1995).

[49] K. Ando, J. Chem. Phys. **114**, 9470 (2001).

[50] D. W. Small, D. V. Matyushov, and G. A. Voth, J. Am. Chem. Soc. **125**, 7470 (2003).

[51] A. A. Milischuk, D. V. Matyushov, and M. D. Newton, Chem. Phys. **324**, 172 (2006).

[52] P. K. Ghorai and D. V. Matyushov, J. Phys. Chem. A **110**, 8857 (2006).

[53] W. F. van Gunsteren, X. Daura, and A. E. Mark, Helv. Chim. Acta **85**, 3113 (2002).

[54] C. Peter, C. Oostenbrink, A. van Dorp, and W. F. van Gunsteren, J. Chem. Phys. **120**, 2652 (2004).

[55] R. A. Marcus, J. Phys. Chem. **72**, 891 (1968).

[56] R. A. Marcus, J. Am. Chem. Soc. **91**, 7224 (1969).

[57] J. O. Bockris and Z. Nagy, J. Chem. Educ. **50**, 839 (1973).

[58] M. J. Weaver, J. Phys. Chem. **83**, 1748 (1979).

[59] J. C. R. Reis, J. Electrochem. Soc. **144**, 2404 (1997).

[60] E. Gileadi and E. Kirowa-Eisner, Corros. Sci. **47**, 3068 (2005).

[61] B. E. Conway and D. F. Wilkinson, J. Electroanal. Chem. **214**, 633 (1986).

[62] B. E. Conway, D. F. Tessier, and D. P. Wilkinson, J. Electroanal. Chem. **199**, 249 (1986).

[63] B. E. Conway, D. F. Tessier, and D. P. Wilkinson, J. Electrochem. Soc. **136**, 2486 (1989).

[64] A. Damjanovic, A. T. Walsh, and D. B. Sepa, J. Phys. Chem. **94**, 1967 (1990).

[65] J. Kästner and W. Thiel, J. Chem. Phys. **123**, 144104 (2005).

[66] J. Kästner and W. Thiel, J. Chem. Phys. **124**, 234106 (2006).

[67] J. Blumberger and M. Sprik, Theor. Chem. Acc. **115**, 113 (2006).

[68] J. Blumberger and M. Sprik, Lect. Notes Phys. **704**, 477 (2006).

[69] E. Wigner, Trans. Faraday Soc. **34**, 29 (1938).

[70] W. H. Miller, Acc. Chem. Res. **9**, 306 (1976).

[71] R. F. Grote and J. T. Hynes, J. Chem. Phys. **73**, 2715 (1980).

[72] D. Chandler, *Introduction to modern statistical mechanics*, Oxford University Press, Oxford, New York, 1987.

[73] C. Dellago, P. G. Bolhuis, and P. L. Geissler, Lect. Notes Phys. **703**, 349 (2006).

[74] C. Dellago, P. G. Bolhuis, F. S. Csajka, and D. Chandler, J. Chem. Phys. **108**, 1964 (1998).

[75] C. Dellago, P. G. Bolhuis, and D. Chandler, J. Chem. Phys. **108**, 9236 (1998).

[76] C. Dellago and P. G. Bolhuis, Mol. Simul. **30**, 795 (2004).

[77] R. B. Best and G. Hummer, Proc. Natl. Acad. Sci. U. S. A. **102**, 6732 (2005).

[78] W. E, W. Ren, and E. Vanden-Eijnden, Chem. Phys. Lett. **413**, 242 (2005).

[79] W. E and E. Vanden-Eijnden, J. Stat. Phys. **123**, 503 (2006).

[80] P. Metzner, C. Schütte, and E. Vanden-Eijnden, J. Chem. Phys. **125**, 084110 (2006).

[81] L. Maragliano, A. Fischer, E. Vanden-Eijnden, and G. Ciccotti, J. Chem. Phys. **125**, 024106 (2006).

[82] B. Peters and B. L. Trout, J. Chem. Phys. **125**, 054108 (2006).

[83] B. Peters, G. T. Beckham, and B. L. Trout, J. Chem. Phys. **127**, 034109 (2007).

[84] R. A. Marcus, J. Chem. Phys. **24**, 979 (1956).

[85] N. S. Hush, J. Chem. Phys. **28**, 962 (1958).

[86] N. S. Hush, Trans. Faraday Soc. **57**, 557 (1961).

[87] T. Van Voorhis et al., Annu. Rev. Phys. Chem. **61**, 149 (2010).

[88] M. J. Rosker, T. S. Rose, and A. H. Zewail, Chem. Phys. Lett. **146**, 175 (1988).

[89] W. Heitler and F. London, Zeitschrift für Physik **44**, 455 (1927).

[90] L. Song and J. Gao, J. Phys. Chem. A **112**, 12925 (2008).

[91] M. Tachiya, J. Phys. Chem. **93**, 7050 (1989).

[92] M. Tachiya, J. Phys. Chem. **97**, 5911 (1993).

[93] Y. Tateyama, J. Blumberger, M. Sprik, and I. Tavernelli, J. Chem. Phys. **122**, 234505 (2005).

[94] R. A. Marcus, J. Chem. Phys. **125**, 194504 (2006).

[95] R. A. Marcus, J. Phys. Chem. B **111**, 6643 (2007).

[96] J. T. Hynes, J. Phys. Chem. **90**, 3701 (1986).

[97] R. B. Yelle and T. Ichiye, J. Phys. Chem. B **101**, 4127 (1997).

[98] D. V. Matyushov and G. A. Voth, J. Chem. Phys. **113**, 5413 (2000).

[99] T. Simonson, Proc. Natl. Acad. Sci. U. S. A. **99**, 6544 (2002).

[100] J. Blumberger and M. Sprik, J. Phys. Chem. B **109**, 6793 (2005).

[101] J. Blumberger, I. Tavernelli, M. L. Klein, and M. Sprik, J. Chem. Phys. **124**, 064507 (2006).

[102] J. Blumberger, J. Am. Chem. Soc. **130**, 16065 (2008).

[103] E. Gileadi, J. Electrochem. Soc. **134**, 117 (1987).

[104] E. Gileadi, J. Electrochem. Soc. **137**, 3870 (1990).

[105] A. Warshel and R. M. Weiss, J. Am. Chem. Soc. **102**, 6218 (1980).

[106] D. Frenkel and B. Smit, *Understanding molecular simulation: From algorithms to applications*, Academic Press, San Diego, second edition, 2002.

[107] M. P. Allen and D. J. Tildesley, *Computer simulation of liquids*, Clarendon Press, Oxford, 1989.

[108] D. A. Zichi, G. Ciccotti, J. T. Hynes, and M. Ferrario, J. Phys. Chem. **93**, 6261 (1989).

[109] H. J. C. Berendsen, J. P. Postma, W. F. van Gunsteren, and J. Hermans, Interaction models for water in relation to protein hydration, in *Intermolecular forces*, edited by B. Pullman, pages 331–342, Reidel, Dordrecht, 1981.

[110] Y. Wu, H. L. Tepper, and G. A. Voth, J. Chem. Phys. **124**, 024503 (2006).

[111] A. Warshel and J.-K. Hwang, J. Chem. Phys. **84**, 4938 (1986).

[112] M. E. Tuckerman and G. J. Martyna, J. Phys. Chem. B **104**, 159 (2000).

[113] D. A. McQuarrie, *Statistical mechanics*, University Science Books, Sausalito, 2000.

[114] G. M. Torrie and J. P. Valleau, Chem. Phys. Lett. **28**, 578 (1974).

[115] G. M. Torrie and J. P. Valleau, J. Comput. Phys. **23**, 187 (1977).

[116] A. M. Ferrenberg and R. H. Swendsen, Phys. Rev. Lett. **63**, 1195 (1989).

[117] S. Kumar, D. Bouzida, R. H. Swendsen, P. A. Kollman, and J. M. Rosenberg, J. Comput. Chem. **13**, 1011 (1992).

[118] B. Roux, Comput. Phys. Commun. **91**, 275 (1995).

[119] M. N. Kobrak, J. Comput. Chem. **24**, 1437 (2003).

[120] R. W. Zwanzig, J. Chem. Phys. **22**, 1420 (1954).

[121] J. G. Kirkwood, J. Chem. Phys. **3**, 300 (1935).

[122] M. Berkowitz, J. D. Morgan, J. A. McCammon, and S. H. Northrup, J. Chem. Phys. **79**, 5563 (1983).

[123] L. R. Pratt, J. Chem. Phys. **85**, 5045 (1986).

[124] R. J. Allen, D. Frenkel, and P. R. ten Wolde, J. Chem. Phys. **124**, 194111 (2006).

[125] J. B. Anderson, J. Chem. Phys. **58**, 4684 (1973).

[126] C. H. Bennett, Exact defect calculations of model substances, in *Diffusion in solids: Recent developments*, edited by A. S. Nowick and J. J. Burton, page 73, Academic Press, New York, 1975.

[127] C. H. Bennett, Molecular dynamics and transition state theory: The simulation of infrequent events, in *Algorithms for computation*, edited by R. E. Christoffersen, page 63, Washington, D. C., 1977, American Chemical Society.

[128] G. E. Crooks and D. Chandler, Phys. Rev. E **64**, 026109 (2001).

[129] P. G. Bolhuis, J. Phys.: Condens. Matter **15**, S113 (2003).

[130] T. S. van Erp, D. Moroni, and P. G. Bolhuis, J. Chem. Phys. **118**, 7762 (2003).

[131] D. Moroni, P. G. Bolhuis, and T. S. van Erp, J. Chem. Phys. **120**, 4055 (2004).

[132] M. Grünwald, C. Dellago, and P. L. Geissler, J. Chem. Phys. **129**, 194101 (2007).

[133] J. Rogal and P. G. Bolhuis, J. Chem. Phys. **129**, 224107 (2008).

[134] H. A. Posch and W. G. Hoover, Phys. Rev. A **38**, 473 (1988).

[135] R. J. Allen, P. B. Warren, and P. R. ten Wolde, Phys. Rev. Lett. **94**, 018104 (2005).

[136] R. J. Allen, D. Frenkel, and P. R. ten Wolde, J. Chem. Phys. **124**, 024102 (2006).

[137] A. C. Davison, *Statistical models*, Cambridge University Press, Cambridge, 2003.

[138] B. Peters, J. Chem. Phys. **125**, 241101 (2006).

[139] W. E, W. Ren, and E. Vanden-Eijnden, Phys. Rev. B **66**, 052301 (2002).

[140] A. Ma and A. R. Dinner, J. Phys. Chem. B **109**, 6769 (2005).

[141] P. L. Geissler and D. Chandler, J. Chem. Phys. **113**, 9759 (2000).

[142] R. A. Marcus and N. Sutin, Inorg. Chem. **14**, 213 (1975).

[143] J. A. Montgomery, Jr., D. Chandler, and B. J. Berne, J. Chem. Phys. **70**, 4056 (1979).

[144] N. Wiberg, *Lehrbuch der Anorganischen Chemie*, Walter de Gruyter, Berlin, New York, thirty-fourth edition, 1995.

[145] L. Onsager, Phys. Rev. **37**, 405 (1931).

[146] D. A. McQuarrie and J. D. Simon, *Physical Chemistry: A molecular approach*, University Science Books, Sausalito, 1997.

[147] L. Onsager, Phys. Rev. **38**, 2265 (1931).

[148] R. Zwanzig, *Nonequilibrium statistical mechanics*, Oxford University Press, New York, 2001.

[149] I. N. Bronstein, K. A. Semandjajew, G. Musiol, and H. Mühlig, *Taschenbuch der Mathematik*, Verlag Harri Deutsch, Frankfurt am Main, fourth edition, 1999.

[150] H. Waalkens, R. Schubert, and S. Wiggins, Nonlinearity **21**, 1 (2008).

[151] R. Kapral, S. Hudson, and J. Ross, J. Chem. Phys. **53**, 4387 (1970).

[152] D. J. Tannor and D. Kohen, J. Chem. Phys. **100**, 4932 (1994).

[153] G. K. Schenter, B. C. Garrett, and D. G. Truhlar, J. Chem. Phys. **119**, 5828 (2003).

[154] H. A. Kramers, Physica **7**, 284 (1940).

[155] C. M. Elliott, D. L. Derr, D. V. Matyushov, and M. D. Newton, J. Am. Chem. Soc. **120**, 11714 (1998).

[156] R. A. Marcus, J. Chem. Phys. **81**, 4494 (1984).

[157] A. Houmam, Chem. Rev. **108**, 2180 (2008).

[158] B. S. Brunschwig and N. Sutin, Coord. Chem. Rev. **187**, 233 (1999).

[159] C. Dellago, Transition path sampling and the calculation of free energies, in *Free energy calculations*, edited by C. Chipot and A. Pohorille, volume 86 of *Springer Series in Chemical Physics*, page 249, Springer, Berlin, 2007.

[160] V. B. Luzhkov, Chem. Phys. Lett. **452**, 72 (2008).

[161] D. Trzesniak, A.-P. E. Kunz, and W. F. van Gunsteren, ChemPhysChem **8**, 162 (2007).

[162] D. Branduardi, F. L. Gervasio, and M. Parrinello, J. Chem. Phys. **126**, 054103 (2007).

[163] G. Sutmann, Classical molecular dynamics, in *Quantum simulations of complex many-body systems: From theory to algorithms*, edited by J. Grotendorst, D. Marx, and A. Muramatsu, page 211, NIC-Directors, 2002.

[164] C. Dellago, P. G. Bolhuis, and D. Chandler, J. Chem. Phys. **110**, 6617 (1999).

[165] H. Goldstein, C. P. Poole, Jr., and J. L. Safko, *Classical mechanics*, Addison-Wesley Publishing Company, Inc., San Francisco, third edition, 2002.

[166] L. Verlet, Phys. Rev. **159**, 98 (1967).

[167] W. C. Swope, H. C. Andersen, P. H. Berens, and K. R. Wilson, J. Chem. Phys. **76**, 637 (1982).

[168] J.-P. Ryckaert, G. Ciccotti, and H. J. C. Berendsen, J. Comput. Phys. **23**, 327 (1977).

[169] H. C. Andersen, J. Comput. Phys. **52**, 24 (1983).

[170] F. W. Byron, Jr. and R. W. Fuller, *Mathematics of classical and quantum physics*, Dover Publications, Inc., New York, 1992.

[171] M. E. Tuckerman, *Statistical mechanics: Theory and molecular simulation*, Oxford University Press, Oxford, New York, 2010.

[172] S. Nosé, Mol. Phys. **52**, 255 (1984).

[173] S. Nosé, J. Chem. Phys. **81**, 511 (1984).

[174] S. Nosé, Mol. Phys. **57**, 187 (1986).

[175] W. G. Hoover, Phys. Rev. A **31**, 1695 (1985).

[176] M. E. Tuckerman, C. J. Mundy, and G. J. Martyna, Europhys. Lett. **45**, 149 (1999).

[177] M. E. Tuckerman, Y. Liu, G. Ciccotti, and G. J. Martyna, J. Chem. Phys. **115**, 1678 (2001).

[178] M. Lewerenz, Monte Carlo methods: Overview and basics, in *Quantum simulations of complex many-body systems: From theory to algorithms*, edited by J. Grotendorst, D. Marx, and A. Muramatsu, page 1, NIC-Directors, 2002.

[179] N. Metropolis, A. W. Rosenbluth, M. N. Rosenbluth, A. N. Teller, and E. Teller, J. Chem. Phys. **21**, 1087 (1953).

[180] L. Casetti, M. Pettini, and E. G. D. Cohen, Physics Reports **337**, 237 (2000).

[181] C. Dellago and H. A. Posch, Physica A **230**, 364 (1996).

[182] G. Benettin, L. Galgani, A. Giorgilli, and J.-M. Strelcyn, Meccanica **15**, 9 (1980).

[183] M. Pettini and R. Valdettaro, Chaos **5**, 646 (1995).

[184] P. L. Geissler, C. Dellago, and D. Chandler, Phys. Chem. Chem. Phys. **1**, 1317 (1999).

[185] M. Grünwald and C. Dellago, J. Chem. Phys. **131**, 164116 (2009).

[186] C. H. Bennett, J. Comput. Phys. **22**, 245 (1976).

[187] C. Jarzynski, Phys. Rev. Lett. **78**, 2690 (1997).

[188] G. E. Crooks, J. Stat. Phys. **90**, 1481 (1998).

[189] G. Hummer and A. Szabo, J. Chem. Phys. **105**, 2004 (1996).

[190] M. Sprik and G. Ciccotti, J. Chem. Phys. **109**, 7737 (1998).

[191] P. Kollman, Chem. Rev. **93**, 2395 (1993).

[192] D. A. Kofke and P. T. Cummings, Mol. Phys. **92**, 973 (1997).

[193] F. M. Ytreberg, R. H. Swendsen, and D. M. Zuckerman, J. Chem. Phys. **125**, 184114 (2006).

[194] M. Souaille and B. Roux, Comput. Phys. Commun. **135**, 40 (2001).

[195] T. C. Beutler and W. F. van Gunsteren, Chem. Phys. Lett. **237**, 308 (1995).

[196] C. Peter, W. F. van Gunsteren, and P. H. Hünenberger, J. Chem. Phys. **119**, 122205 (2003).

[197] D. J. Adams and G. S. Dubey, J. Comput. Phys. **72**, 156 (1987).

[198] G. Hummer, L. R. Pratt, and A. E. García, J. Phys. Chem. A **102**, 7885 (1998).

[199] P. P. Ewald, Ann. Phys. **64**, 253 (1921).

[200] S. W. de Leeuw, J. W. Perram, and E. R. Smith, Proc. R. Soc. Lond. A **373**, 27 (1980).

[201] G. Hummer, L. R. Pratt, and A. E. García, J. Phys. Chem. **100**, 1206 (1996).

[202] S. G. Brush, H. L. Sahlin, and E. Teller, J. Chem. Phys. **45**, 2102 (1966).

[203] T. Darden, D. Pearlman, and L. G. Pedersen, J. Chem. Phys. **109**, 10921 (1998).

[204] F. Figueirido, G. S. Del Buono, and R. M. Levy, J. Chem. Phys. **103**, 6133 (1995).

[205] P. H. Hünenberger and J. A. McCammon, J. Chem. Phys. **110**, 1856 (1999).

[206] J. D. Weeks, D. Chandler, and H. C. Andersen, J. Chem. Phys. **54**, 5237 (1971).

[207] D. Chandler, J. D. Weeks, and H. C. Andersen, Science **220**, 787 (1983).

[208] W. Smith, T. R. Forester, and I. T. Todorov, *The DL_POLY_2 user manual version 2.18*, STFC Daresbury Laboratory, Daresbury, Warrington WA4 4AD, Cheshire, UK.

[209] K. Ando, J. Chem. Phys. **106**, 116 (1997).

[210] H. J. Kim and J. T. Hynes, J. Chem. Phys. **96**, 5088 (1992).

[211] B. B. Smith and J. W. Halley, J. Chem. Phys. **101**, 10915 (1994).

[212] D. A. Rose and I. Benjamin, Chem. Phys. Lett. **234**, 209 (1995).

[213] J. B. Straus, A. Calhoun, and G. A. Voth, J. Chem. Phys. **102**, 529 (1995).

[214] S. Amira, D. Spångberg, M. Probst, and K. Hermansson, J. Phys. Chem. B **108**, 496 (2004).

[215] W. L. Jorgensen, J. Chandrasekhar, J. D. Madura, R. W. Impey, and M. L. Klein, J. Chem. Phys. **79**, 926 (1983).

[216] C. Hartnig and M. T. M. Koper, J. Chem. Phys. **115**, 8540 (2001).

[217] B. B. Smith and J. T. Hynes, J. Chem. Phys. **99**, 6517 (1993).

[218] J. S. Bader and D. Chandler, J. Phys. Chem. **96**, 6423 (1992).

[219] J. S. Bader and D. Chandler, Chem. Phys. Lett. **157**, 501 (1989).

[220] D. V. Matyushov, Chem. Phys. **174**, 199 (1993).

[221] N. Lu, D. A. Kofke, and T. B. Woolf, J. Phys. Chem. B **107**, 5598 (2003).

[222] P. L. Douillet, Sampling distribution of the variance, in *Proceedings of the 2009 Winter Simulation Conference*, edited by M. D. Rossettti, R. R. Hill, B. Johansson, A. Dunkin, and R. G. Ingalls, page 403, 2009.

[223] A. A. Clifford, *Multivariate error analysis: A handbook of error propagation and calculation in many-parameter systems*, Applied Science Publishers Ltd, London, 1973.

[224] H. Flyvbjerg and H. G. Petersen, J. Chem. Phys. **91**, 461 (1989).

[225] S. K. Schiferl and D. C. Wallace, J. Chem. Phys. **83**, 5203 (1985).

[226] H. B. Mann, Econometrica **13**, 245 (1945).

[227] F. E. Croxton and D. J. Cowden, *Applied general statistics*, Isaac Pitman, London, second edition, 1963.

[228] E. S. Pearson, Biometrika **22**, 239 (1930).

[229] J. von Neumann, Annals Math. Stat. **12**, 367 (1941).

[230] J. von Neumann, R. H. Kent, H. R. Bellinson, and B. I. Hart, Annals Math. Stat. **12**, 153 (1941).

[231] E. R. Barthel, I. B. Martini, and B. J. Schwartz, J. Phys. Chem. B **105**, 12230 (2001).

[232] A. E. Bragg, M. C. Cavanagh, and B. J. Schwartz, Science **321**, 1817 (2008).

[233] P. L. Geissler, C. Dellago, and D. Chandler, J. Phys. Chem. B **103**, 3706 (1999).

[234] E. W. Weisstein, Hypersphere, 24 August 2010, From MathWorld – A Wolfram Web Resource, `http://mathworld.wolfram.com/Hypersphere.html`.

[235] C. Cohen-Tannoudji, B. Diu, and F. Laloë, editors, *Mécanique quantique*, volume I & II, Hermann, Paris, 1997.

[236] R. Kubo, Rep. Prog. Phys. **29**, 255 (1966).